



HAL
open science

Local Spectroscopy of two-dimensional correlated materials

Mohammadmehdi Torkzadeh

► **To cite this version:**

Mohammadmehdi Torkzadeh. Local Spectroscopy of two-dimensional correlated materials. Physics [physics]. Sorbonne Université, 2023. English. NNT : 2023SORUS103 . tel-04135029

HAL Id: tel-04135029

<https://theses.hal.science/tel-04135029v1>

Submitted on 20 Jun 2023

HAL is a multi-disciplinary open access archive for the deposit and dissemination of scientific research documents, whether they are published or not. The documents may come from teaching and research institutions in France or abroad, or from public or private research centers.

L'archive ouverte pluridisciplinaire **HAL**, est destinée au dépôt et à la diffusion de documents scientifiques de niveau recherche, publiés ou non, émanant des établissements d'enseignement et de recherche français ou étrangers, des laboratoires publics ou privés.



Sorbonne Université

Institut des NanoSciences de Paris

École doctorale de Physique en Île de France - ED 564

Local Spectroscopy of two-dimensional correlated materials

Thèse de doctorat de Physique
par Mohammadmehdi Torkzadeh

Composition du Jury:

Pascale Diener	Rapporteuse
Jean-Yves Veillen	Rapporteur
Bertrand Kierren	Examineur
Herve Aubin	Examineur
Michele Casula	Examineur
Tristan Cren	Directeur de thèse
Christophe Brun	Co-directeur de thèse

ABSTRACT

Most of the recently discovered so-called “unconventional superconductors,” such as the quasi-one-dimensional (Q1D) organic superconductors, or quasi-two-dimensional (Q2D) copper oxides superconductors share a unifying property: they exhibit a general phase diagram where superconductivity has a common border with a magnetically ordered phase. One way is to apply pressure in order to induce superconductivity like in (Q1D) organic superconductors. The other way is to induce superconductivity by doping like in Cuprates and in α -Sn/Si(111). In this framework we have studied the properties of α -Sn/Si(111) and organic superconductor, $(\text{TMTSF})_2\text{ClO}_4$ using scanning tunneling microscopy and spectroscopy (STM and STS) techniques. Starting with α -Sn/Si(111), there is an ongoing attention drawn to a class of correlated surface crystals called α -phase. They consist in a low density single-layer ($1/3$ monolayer) of metal atoms (Pb or Sn) grown on semiconducting substrates like Si (111) or Ge (111). Recently α -Sn/Si(111) was shown to have superconducting properties with a Mott insulator to Superconductor phase transition upon doping, which resembles the one occurring in the more complex high temperature cuprates superconductors. While the structure of α -Sn/Si(111) is very simple, making it a very good candidate to understand the physics of cuprates, its Mott insulating ground state is still debated. In this framework, by using STM and STS at low temperatures we have shown that the ground state of this material is an insulator with a gap of 650 meV, more than 10 times higher than previously reported values, driven by exchange interaction between the Sn atoms and the substrate surface atoms. Moreover this is accompanied by a colinear row-wise antiferromagnetic order deduced from quasi-particle interferences (QPI) measurements and advanced density functional theory (DFT) calculations. In addition, we have also studied by STS α -Pb/Ge(111) as another example of 2d correlated materials and indeed, we have found a large depletion of the density of states around the Fermi level indicating a correlated metallic ground state close to an insulating state. Regarding $(\text{TMTSF})_2\text{ClO}_4$, we have measured the excitation spectrum of this Q1D superconductor, using STS for the first time. $(\text{TMTSF})_2\text{ClO}_4$ is an ambient pressure superconductor below 1.2 K exhibiting a quantum critical point with a competition between spin density wave (insulating) and superconducting ordering. In the bulk these ground states can coexist with each other by playing with the cooling speed. We showed that the surface cleavage offers another way to probe this phase coexistence for nominally bulk superconducting samples, leading to surface granular electronic properties. Lastly in the context of unconventional superconductivity, we have performed for the first time STM/STS measurements on the superconducting 2D Electron Gas (2-DEG) formed at the interface of KTO/ Al_2O_3 . We developed a new method to perform STS maps on this 2-DEG layer which is buried under the surface.

Keywords: *Unconventional superconductors, quasi-one-dimensional, quasi-two-dimensional, organic superconductor, scanning tunneling microscopy and spectroscopy, insulator, density functional theory, Mott insulator, exchange interaction, quasi-particle interference, spin density wave.*

Résumé

La plupart des "supraconducteurs non conventionnels" découverts récemment, tels que les supraconducteurs organiques quasi unidimensionnels (Q1D) ou les supraconducteurs d'oxydes de cuivre quasi bidimensionnels (Q2D), partagent une propriété commune : ils présentent un diagramme de phase général où la supraconductivité a une frontière commune avec une phase magnétiquement ordonnée. L'une des méthodes consiste à appliquer une pression afin d'induire la supraconductivité comme dans les supraconducteurs organiques (Q1D). L'autre façon est d'induire la supraconductivité par dopage comme dans les Cuprates et dans α -Sn/Si(111). Dans ce cadre, nous avons étudié les propriétés de l' α -Sn/Si(111) et du supraconducteur organique, $(\text{TMTSF})_2\text{ClO}_4$ en utilisant les techniques de microscopie à effet tunnel et de spectroscopie (STM et STS). En commençant par α -Sn/Si(111), une classe de cristaux de surface corrélés appelée phase α fait l'objet d'une attention soutenue. Ils consistent en une monocouche de faible densité (1/3 de monocouche) d'atomes de métal (Pb ou Sn) cultivés sur des substrats semi-conducteurs comme Si (111) ou Ge (111). Récemment, il a été démontré que l' α -Sn/Si(111) possède des propriétés supraconductrices avec une transition de phase de l'isolant de Mott au supraconducteur par dopage, qui ressemble à celle qui se produit dans les cuprates, des supraconducteurs plus complexes à haute température. Alors que la structure de α -Sn/Si(111) est très simple, ce qui en fait un très bon candidat pour comprendre la physique des cuprates, son état fondamental d'isolation de Mott est encore débattu. Dans ce cadre, en utilisant le STM et le STS à basse température, nous avons montré que l'état fondamental de ce matériau est un isolant à bande avec un gap de 650 meV, plus de 10 fois supérieur aux valeurs précédemment rapportées, piloté par une interaction d'échange entre les atomes de Sn et les atomes de la surface du substrat. De plus, cet état est accompagné d'un ordre antiferromagnétique en rangées déduit de mesures d'interférences quasi-particulaires (QPI) et de calculs avancés de théorie fonctionnelle de la densité (DFT). En outre, nous avons également étudié par STS α -Pb/Ge(111) comme un autre exemple de matériaux corrélés 2d et, en effet, nous avons trouvé un grand appauvrissement autour de la densité d'états du niveau de Fermi indiquant un mauvais état fondamental métallique. En ce qui concerne $(\text{TMTSF})_2\text{ClO}_4$, nous avons mesuré le spectre d'excitation supraconducteur de ce supraconducteur Q1D, en utilisant le STS pour la première fois. Le $(\text{TMTSF})_2\text{ClO}_4$ est un supraconducteur à pression ambiante qui présente un point critique quantique avec une compétition entre l'onde de densité de spin (isolant) et l'ordre supraconducteur. Dans le bulk, ces états fondamentaux peuvent coexister l'un avec l'autre en jouant sur la vitesse de refroidissement. Nous avons montré que le clivage de surface offre un autre moyen de sonder cette coexistence de phases pour des échantillons supraconducteurs nominalemt massifs, conduisant à des propriétés électroniques granulaires de surface. Enfin, dans le contexte de la supraconductivité non conventionnelle, nous avons effectué pour la première fois des mesures STM/STS sur le gaz d'électrons 2D supraconducteur (2-DEG) formé à l'interface de KTO/ Al_2O_3 . Nous avons développé une nouvelle méthode pour réaliser des cartes STS sur cette couche 2-DEG qui est enterrée sous la surface.

Keywords: *Supraconducteurs non conventionnel, quasi unidimensionnels, quasi bidimensionnels, supraconducteurs organique, microscopie à l'effet tunnel et de spectroscopie, isolant à bande, fonctionnelle de la densité e , l'isolant de Mott, interaction d'échange, quasi-particle interférences, l'onde de densité e de spin.*

TABLE OF CONTENTS

Abstract	i
Résumé	i
General introduction	1
1 Introduction	4
1.1 Introduction	4
1.2 Superconductivity	4
1.2.1 Ginzburg-Landau Theory	5
1.2.2 BCS theory	7
1.2.3 Unconventional superconductivity	10
1.2.4 Impurity effect in superconductors	11
1.2.5 Chiral Superconductivity (a brief introduction)	13
1.3 Density waves	13
1.3.1 Charge density wave	13
1.3.2 Spin density wave	15
1.4 Insulators	15
1.4.1 Mott insulators	16
1.4.2 Comparison between band-insulator and Mott-insulator	18
2 Devices and Experimental methods	24
2.1 Introduction	24
2.2 Surfaces and Wood's notation	24
2.3 Low Energy Electron Diffraction (LEED)	25
2.4 Scanning Tunneling Microscopy/Spectroscopy	28
2.4.1 Surface topography imaging	28
2.5 Scanning Tunneling Spectroscopy	31
2.5.1 Local Density of States Measurements	31
2.5.2 Spectroscopic Grid Measurement	33
2.6 Lock-in Technique	34

2.7	Spin polarized STM	35
2.8	Quasiparticle interferences and Fourier Transform STS	36
2.9	Experimental setups	41
2.9.1	M3 setup	41
2.9.2	Cooling system	42
2.9.3	variable temperature STM	44
2.10	preparation of the samples	44
2.10.1	$(\text{TMTSF})_2\text{ClO}_4$	44
2.10.2	Sn/Si(111) (highly n doped)	46
2.10.3	Shadowing effect	47
2.10.4	Sn/Si (111) (highly P doped)	50
2.10.5	Pb/Ge(111)	52
2.10.6	Tip preparations	56
2.10.7	Nanonis electronics calibration	58
3	Electronic properties of correlated diluted 2d layers of tetravalent metals on semiconducting surfaces	61
3.1	Introduction	61
3.2	Previous studies	62
3.3	Sn/Si(111) (highly n-doped)	63
3.3.1	Is Sn/Si(111) a Mott insulator?	65
3.3.2	possible spin ordering in $\text{Sn} - \sqrt{3}$	68
3.3.3	Chiral superconductivity observed in Sn/Si(111) (highly p-doped)	68
3.3.4	Spectroscopy measurements	70
3.3.5	Artificial molecules induced by defects	81
3.3.6	Edge states	83
3.3.7	Multifractal electronic wave functions at the gap edge of $\text{Sn} - \sqrt{3}$	84
3.3.8	Conclusion	91
3.4	Pb/Ge(111)	92
4	Granular superconductivity at cleaved $(\text{TMTSF})_2\text{ClO}_4$	97
4.1	Bechgard salts	97
4.2	Results and discussion	101
4.2.1	surface spectroscopy	102
4.2.2	near bulk spectroscopy	105

4.2.3	Magnetic field dependence	108
4.2.4	discussion	108
4.2.5	conclusion	110
5	Superconductivity in $\text{KTaO}_3/\text{Al}_2\text{O}_3$	112
5.1	Introduction	112
5.2	Buried 2-d superconductivity in $\text{KTaO}_3/\text{Al}_2\text{O}_3$	112
5.2.1	Topography and Point spectroscopy measurement	113
5.2.2	spectroscopic map	114
5.2.3	discussion	117
	Conclusion	118
	REFERENCES	119

General introduction

Superconductivity has been discovered a century ago but it still remains one of the active research topics in condensed matter physics. After the discovery of high-temperature superconductivity in 1986 by IBM researchers Bednorz and Müller, who were awarded the Nobel Prize in physics in 1987, a huge research activity has been devoted to find new high temperature superconductors and to find an appropriate theoretical description of high temperature superconductivity. The very complex nature of cuprate materials exhibiting high temperature superconductivity has added some complexity to this problem. One strategy that we would expect quite efficient would be to identify some class of material which share some similarities with High Tc superconductors but with much simpler structures. For instance, would be very exciting to find some very simple materials that would be 2d Mott insulators in their undoped structure but which become superconducting upon doping with either electron or holes.

In this thesis, we have decided to investigate one of the best candidate for such Mott-insulator physics. Our system is the α -phase of Sn or Pb on Si(111) or Ge(111), which is believed to have a correlated ground state similar to that of the Cuprates. to study the undoped ground state and its transition to a superconducting state upon doping. Here we couldn't perform experiments in the heavy hole doped regime where superconductivity has been found recently. However, we have conducted experiments in the undoped regime for Sn/Si(111) and Pb/Ge(111) and we have revealed an insulating ground state for α -Sn/Si(111) and a correlated metallic phase for α -Pb/Ge(111).

The transition between a magnetically ordered phase to a superconductor is observed not only in cuprates. It has been shown that $(\text{TMTSF})_2\text{ClO}_4$ is an ambient pressure superconductor exhibiting a quantum critical point with a competition between spin density wave (insulating) and superconducting ordering. In my thesis indeed we have seen that a plausible d-wave superconducting state develops at the surface of $(\text{TMTSF})_2\text{ClO}_4$. In addition we could show that this state is not homogeneous at the surface but also presents spin-density-wave phase regions as well as correlated metallic areas.

This thesis is organized in 5 chapters. The first chapter is devoted to a general introduction to superconductivity, Charge density and spin density waves and Mott and Band insulators. The second chapter is devoted to experimental setups and devices used during this thesis, namely, scanning tunneling microscopy and spectroscopy, explaining several techniques that can be implemented by using them. Chapter 3 is devoted to presenting and discussing our results on Sn/Si(111) and Pb/Ge(111). In Chapters 4 and 5 we discuss our results on $(\text{TMTSF})_2\text{ClO}_4$ and $\text{KTO}/\text{Al}_2\text{O}_3$.

Chapter 1: In this chapter, we explain the theoretical background of superconductivity and how it relates to insulators. At first, the phenomenological approach of Ginzburg-Landau in describing superconductivity is explained and then the microscopic approach of Bardeen-Cooper-Schrieffer is used to describe conventional superconductors. Then we give a short description on unconventional superconductivity and chiral superconductivity and we explain how impurities

can be used as a tool to find the nature of superconductivity. We then continue our discussion by explaining Charge Density Wave and Spin Density Wave states. Finally, we give a short introduction to Mott insulators and we explain how the Upper Hubbard Band and Lower Hubbard Band evolve as function of doping or correlations. Furthermore we show that a band insulator and a Mott insulator have different properties in electron or hole doped regimes.

Chapter 2: In this chapter first the theoretical background behind Scanning Tunneling Microscopy and Scanning Tunneling Spectroscopy (STM/STS) is explained. We then discuss how this exceptional tool can be used to not only probe the surface topography on atomic scale but also give us information about the local density of states. After, we show how a grid spectroscopic map can be measured in order to record the local density of states. Then, we introduce several techniques that can be implemented using STM/STS, such as lock-in, Spin Polarized STM (SPSTM), and Quasi Particle Interferences (QPIs). Finally, a description of the microscope “M3” and “VT-STM”, the two main devices that have been used during thesis, is given. At the end we explain the preparation of the samples and the tips. Furthermore, we will see how the VT-STM is used in parallel to M3 in order to find optimized parameters for sample preparation.

Chapter 3: This chapter, which contains the main results of this thesis, is dedicated to the study of α -phase of Sn/Si(111) and Pb/Ge(111). In the case of α -Sn/Si(111) we start by explaining the literature and the state of the art research that indicates a Mott insulating ground state with row wise antiferromagnetic order. However, while our contaminated samples show similar results as in the literature, our results on the clean samples using STS maps together with QPIs calculations predict a ground state which is of Slater-type insulator. Our results are in good agreement with density functional theory calculations by considering the exchange interaction between the Sn atoms and the underlying Si atoms, carried out by carried out by Amitayush Thakur, helped by Cesare Tresca and Matteo Calandra. Afterwards,

several interesting phenomena like artificial molecules and edge states in this phase are discussed. Finally, we introduce the concept of multifractality and we show how it can be used as a tool in order to determine Anderson criticality in phase transitions between extended states and localized states depending on the energy of the electronic states while keeping the same disorder. In the end, we will give a short discussion about our preliminary spectroscopy results on different phases of Pb/Ge(111).

Chapter 4: This chapter is devoted to our studies on $(\text{TMTSF})_2\text{ClO}_4$, a Quasi-1-dimensional organic material that shows ambient pressure superconductivity with a critical temperature of 1.2 K. This sample was prepared by cleaving inside the STM chamber which is maintained in ultra-high vacuum. We have measured a V-shaped superconducting gap using STS at 300 mK that is consistent with a d wave symmetry gap. Furthermore, we show the results of magnetic dependent STS measurements revealing a gap filling at high perpendicular magnetic fields. Also, we have found that superconductivity is not homogenous throughout the sample, regions with metallic, bad and/or correlated metal and insulating behavior were observed, which, can be due in part to the predicted granularity of the superconductivity by previous XRD results or due to the defects induced by the cleavage process. At the end, we will show that our measured excitation spectra fit very well with the results of renormalization group calculations in the framework

of a quasi-1D electron gas model experiencing a d-wave superconducting pairing. Importantly, this ground state is very close to a quantum critical point which explains also part of the strong V-shape measured in the dI/dV spectra. These calculations were carried out by Abdel Sedeki and Claude Bourbonnais.

Chapter 5: In this chapter, we present briefly our results on STS measurements of a buried superconducting 2-Dimensional Electron Gas at the interface of KTiO_3 and Al_2O_3 . We present the measured superconducting gap together with a magnetic field dependent point spectroscopy measurement.

CHAPTER 1

Introduction

1.1 Introduction

In this chapter, we are going to start by introducing superconductivity, specifically high temperature superconductivity which is mostly seen in Cuprates and believed to be the result of doping Mott insulators with either electrons or holes. The motivation behind this thesis is to better understand this transition by studying a simple system of $1/3$ ML of Sn on Si(111) surface which is long believed to be a classic Mott-insulator (proved to be wrong by us), and recently shown to transition to a superconducting phase. To understand better these phenomena we are going to give a basic knowledge of conventional and unconventional superconductivity and how to characterize them and after we are going to explain Mott insulators and Band-insulators, all by keeping track of our system in favor which is the aforementioned $\text{Sn/Si}(111) - \sqrt{3} \times \sqrt{3} - \text{R}^\circ$ structure.

1.2 Superconductivity

In 1911, the Dutch physicist Heike Kamerlingh Onnes and his team discovered that the electrical resistance of mercury goes to zero below a certain temperature (Fig. 1.1), while studying the properties of materials at low temperatures. This was the first observation of a phenomenon called superconductivity. There are a majority of chemical compounds that become superconductors at sufficiently low temperatures.

The superconducting state is characterized by two main properties; first, there is no resistance to the passage of the electrical current, so the current can circulate in a closed superconducting wire infinitely without any dissipation. Second, at a sufficiently low magnetic field, the field cannot penetrate the superconductor; it remains at its surface. This field exclusion phenomenon was observed by Meissner in 1933.

In the beginning stages of the discovery of superconductivity, the critical temperature was below 20K, the uses of superconductors required cooling using liquid helium. It was in 1986 that high-temperature superconductivity in Cuprates [1] was discovered, and the rapid rise of the temperature to well above the boiling point of nitrogen [2] started a great era of excitement in the field of condensed matter.

Today superconductors have a vast application in industry; they are used in generators, particle acceleration, transportation, electric motors, computing, medicine, etc. However, one main drawback of superconductors is that despite the discovery of high T_c superconductors,

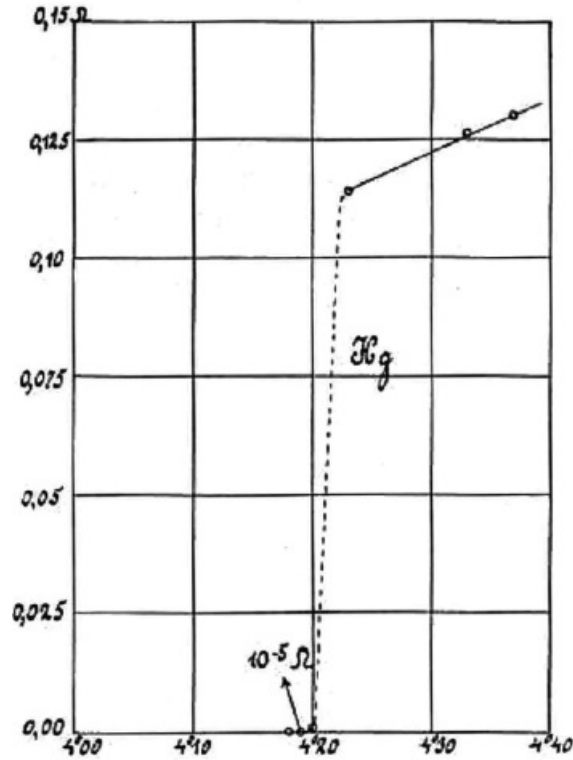


Fig. 1.1 Resistivity of Mercury in terms of temperature

their relatively low operating temperature makes them costly and difficult to use; that is why understanding deeply high- T_c superconductivity could make it easier to find systems with much higher T_c than what is available now.

Although there are hundreds of high T_c compounds, they all share the same layered compound made up of one or more copper oxygen planes and have the same universal phase diagram as shown in Fig. 1.2. An undoped cuprate compound, which has one electron per unit cell, should be a metal under conventional band theory; however, strong on-site repulsion prevents electron motion and turns it into a Mott insulator, a strongly correlated phase discovered by Mott in 1949 [3]. The Mott physics will be explained in more details further in this chapter; however, the main important note here is that the physics behind the transition from a Mott insulator to a superconductor upon doping is still not perfectly understood and there are many efforts to ease the pathway to a clear picture behind this phenomenon. One of them is to introduce a much simpler model compared to the Cuprates which is also the main motivation behind this thesis and it is explained in chapter 3 of this thesis.

1.2.1 Ginzburg-Landau Theory

We will not delve deep in to the details of the underlying microscopic mechanism for the formation of a superconducting state, a phenomenological description given by the Ginzburg-Landau theory captures the key features of a superconducting phase transition. Near the phase transition from normal state to superconducting state, the free energy can be expressed as an expansion of a complex order parameter, $\psi = \sqrt{n_s} \exp(i\theta)$, where n_s is the superfluid density and θ is the

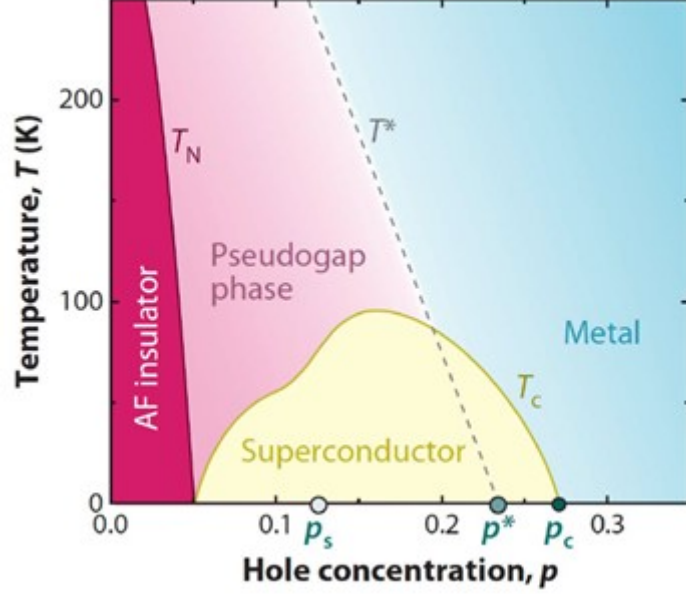


Fig. 1.2 Schematic phase diagram of cuprate superconductors as a function of hole doping concentration p . The Mott insulator phase near $p = 0$ shows antiferromagnetic (AF) order below T_N , which vanishes rapidly with doping [3]. Then for higher p doping a superconducting dome emerges with a maximum T_C at the optimal doping surrounded by an underdoped side at low p and overdoped side at large p . For large p , above T_C the cuprates are metallic. However, on the underdoped side, a badly understood pseudogap phase develops.

phase of the order parameter [4].

$$F = \alpha|\psi|^2 + \frac{\beta}{2}|\psi|^4 + \frac{1}{2m_s}|(-i\hbar\Delta - q_s A)\psi|^2 + \frac{|B|^2}{2\mu_0} \quad (1.1)$$

Where α and β are constants, m_s is the density of the superfluid, q_s is the charge of the superfluid, A is the magnetic vector potential, $B = \nabla \times A$ is the magnetic field and μ_0 is the permeability of the free space. By minimizing the free energy with respect to ψ and A , we have:

$$\begin{aligned} \frac{1}{2m_s}(-i\hbar\Delta + q_s A)^2\psi + (\alpha + \beta|\psi|^2)\psi &= 0 \\ J_s = \frac{iq_s\hbar}{2m_s}(\psi^*\Delta\psi - \psi\Delta\psi^*) - \frac{q_s^2}{m_s}A\psi^*\psi &= -\frac{q_s n_s}{m_s}(\hbar\Delta\theta + q_s A) \end{aligned} \quad (1.2)$$

Where J_s is the supercurrent density. Two characteristic length scales can be deduced from these two equations, the penetration depth λ and the coherence length ξ , which are important for classifying the superconducting behavior. λ is a measure of how far the magnetic field can penetrate into a superconductor and ξ is the coherence length of the superconductor which is the typical length-scale over which the superconducting order evolves.

There are two classes of superconductors that are defined according to the dimensionless Ginzburg-Landau parameters:

$$\kappa = \lambda/\xi \quad (1.3)$$

For $\kappa < 1/\sqrt{2}$, we have a 'type-1' superconductor, in which magnetic flux coming from an external magnetic field is expelled until the superconductivity is suddenly destroyed at a single critical field H_c (Fig. 1.3). When $\kappa > 1/\sqrt{2}$, we have a "type-II" superconductor where, instead of a sudden change from a Meissner state (expelling the magnetic flux completely) to a normal state, a vortex state with an arrangement of quantized magnetic flux line is reached above a lower critical field H_{C1} . The superconducting state totally vanishes at the upper critical field H_{C2} (Fig. 1.3).

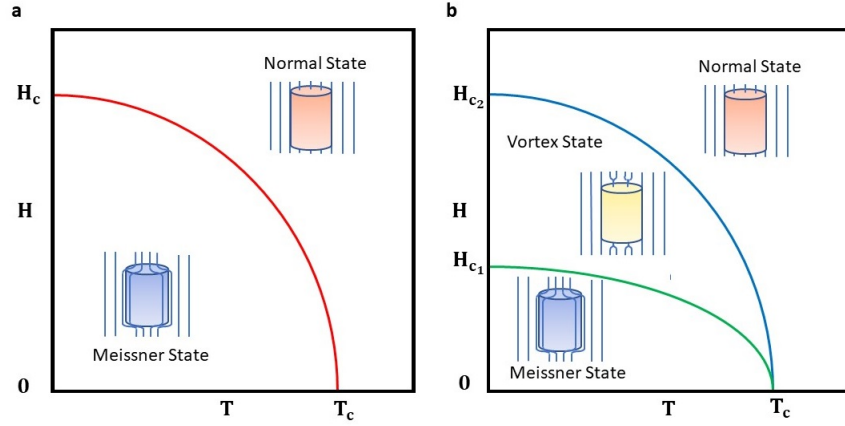


Fig. 1.3 Phase diagram of superconductivity with illustration on the magnetic penetration for a. Type 1 and b. Type 2 superconductors.

1.2.2 BCS theory

The modern understanding of the superconducting state and its microscopic mechanism started with the brilliant formalism proposed by Bardeen, Cooper and Schrieffer (BCS) [5]. They showed that a weak arbitrary attractive interaction between electrons can result in the formation of a coherent many-body state which could be interpreted as a condensate of cooper pairs. The excitations of this condensate are separated from its ground state by an energy gap of Δ . In the BCS picture the formation of Cooper pairs arises from an attractive interaction mediated through the vibrations of the ionic lattice (phonons). Let's go through this phenomenon from a classical picture: an electron moving in a conductor will attract the nearby lattice ions which are positively charged, which move slower due to their higher mass. It hence leaves behind a region with higher positive charges; thus, another electron with opposite spin is attracted to such a region, resulting in an effective attraction between the two electrons. This type of phonon-mediated superconductivity is called conventional superconductivity.

To derive the ground state properties, in a second-quantized form, the pairing Hamiltonian can be expressed as:

$$H_{BCS} = \sum_{k,\sigma} \xi_k c_{k,\sigma}^\dagger c_{k,\sigma} + \sum_{k,k',q,\sigma,\sigma'} V(k,k',q) c_{k+q,\sigma}^\dagger c_{k'-q,\sigma'}^\dagger c_{k',\sigma'} c_{k,\sigma} \quad (1.4)$$

Where k is the momentum of an electron and σ is its spin ($\uparrow\downarrow$) and $\xi_k = \epsilon_k - \mu$, where ϵ_k is the electron dispersion relation and μ is the chemical potential.

It was suggested in the original article by Barden, Cooper, and Shrieffer [5] that the exchange interaction energetically favors electrons interacting with opposite spins such that the following follows:

$$H_{BCS} = \sum_{k,\sigma} \xi_k c_{k,\sigma}^\dagger c_{k,\sigma} + \sum_{k,k',q} V(k, k', q) c_{k+q,\uparrow}^\dagger c_{k'-q,\downarrow}^\dagger c_{k',\downarrow} c_{k,\uparrow} \quad (1.5)$$

The matrix element $V(k, k', q) c_{k+q,\uparrow}^\dagger c_{k'-q,\downarrow}^\dagger c_{k',\downarrow} c_{k,\uparrow}$ term indicates destroying a $(k' \downarrow, k, \uparrow)$ pair of states and create a new pair of states $(k' - q \downarrow, k + q \uparrow)$ while conserving the total momentum $k + k'$. By using a mean field approximation proposed by Bogoliubov in 1958 [6] the gap function can be written as follows:

$$\Delta_k = - \sum_{k'} V_{kk'} \langle c_{-k',\downarrow} c_{k',\uparrow} \rangle \quad (1.6)$$

In a conventional superconductor, the electrons of a cooper pair have opposite momenta and spins. Since the interactions between the electrons in a Cooper pair is mediated by the phonons only electrons within an energy window $\hbar\omega_D$ around the Fermi level contribute to form Cooper pairs, where ω_D is the Debye frequency which is the maximum vibrational frequency in a crystal lattice.

$V_{kk'}$ is taken equal to a constant V_0 for energies lower than $\hbar\omega_D$ from Fermi level, thus $k \cong k' \cong k_F$ where k_F is the momenta of an electron close at the Fermi level, hence:

$$\begin{cases} \Delta, & \text{for } |\xi_k| < \hbar\omega_D \\ 0, & \text{for } |\xi_k| > \hbar\omega_D \end{cases} \quad (1.7)$$

The Eqn. 1.7 can be diagonalized using a Bogoliubov transformation (for more information see Ref [7]), and after it can be solved using the BSC coherent ground state, which leads to the following energy spectrum of the excited states:

$$E_k = \pm \sqrt{\xi_k^2 + |\Delta_k|^2} \quad (1.8)$$

The density of states of $N(E_k)$ of the low-energy excitations can be defined as $N(E_k)dE_k = N(0)d\xi_k$ where $N(0)$ is the electronic density of states at the Fermi level. Close to the Fermi energy, we have:

$$N(E_k) = N_0 \frac{|E_k|}{\sqrt{E_k^2 - |\Delta|^2}} \quad (1.9)$$

The density of states shown in Eqn.1.9 is presented in Fig. 1.4 as it can be seen that there is no excitation of energy lower than the absolute gap Δ . It can be interpreted as the fact that an energy higher than 2Δ is needed to break a Cooper pair.

The energy gap function can be determined by the self-consistent equation:

$$\Delta_k = -1/2 \sum_{k'} \frac{\Delta_{k'}}{\sqrt{\xi_{k'}^2 + |\Delta_{k'}|^2}} V_{kk'} \quad (1.10)$$

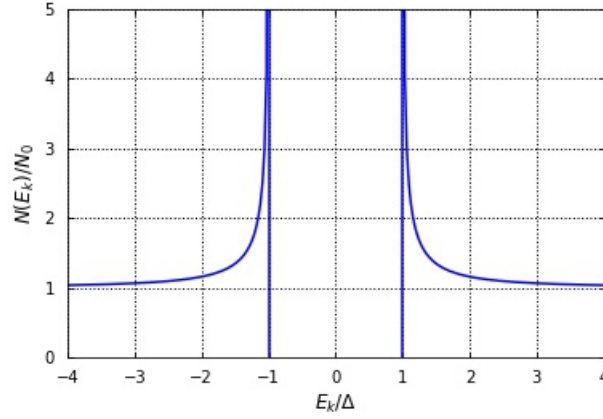


Fig. 1.4 Density of states of the low-energy excitation of a conventional superconductor.

By replacing the aforementioned equation by an integration from $-\hbar\omega_c$ to $\hbar\omega_c$, and noting the symmetry between $\pm\xi$, we can get the following:

$$\frac{1}{N(0)V} = \int_0^{\hbar\omega_c} \frac{d\xi}{\sqrt{\Delta^2 + \xi^2}} = \sinh^{-1} \hbar\omega_c / \Delta \quad (1.11)$$

Which gives:

$$\Delta = \frac{\hbar\omega_c}{\sinh[\frac{1}{N(0)V}]} \approx 2\hbar\omega_c e^{-1/N(0)V} \quad (1.12)$$

At finite temperature, considering the excitations of quasiparticles and their probability distribution, the temperature dependence of the BCS gap function, $\Delta(T)$, can be calculated by solving the self-consistent equation [4]:

$$\frac{1}{N[0]V} = \int_0^{\hbar\omega_c} \frac{d\xi}{\sqrt{\xi^2 + |\Delta(T)|^2}} \tanh\left(\sqrt{\frac{\xi^2 + |\Delta(T)|^2}{2k_B T}}\right) \quad (1.13)$$

the ratio between the value of the energy gap at zero temperature and the superconducting critical temperature takes a universal form as follows:

$$\Delta(T = 0) = 1.764 K_B T_c \quad (1.14)$$

The microscopic BCS theory was very successful in describing the s-wave superconductors, where the origin of the pairing of the electrons is the electron-phonon interaction, however, there are other materials that have interactions that lead to non s-wave superconductivity. Among the various possibilities, one could mention singlet d-wave pairing, like in cuprates, or triplet p-wave and f-wave pairing like in heavy fermions compounds. Such materials are called unconventional superconductors. Unconventional superconductivity will be described in the following subsection.

1.2.3 Unconventional superconductivity

Since a Cooper pair is a two-particles fermionic state, its wave function $\psi(\mathbf{k}, -\mathbf{k}, \sigma_1, \sigma_2)$ (where \mathbf{k} is the momenta and σ denotes the spin of the electrons) must be antisymmetric under the exchange of the two electrons, so $\psi(\mathbf{k}, -\mathbf{k}, \sigma_1, \sigma_2) = -\psi(-\mathbf{k}, \mathbf{k}, \sigma_2, \sigma_1)$. Now lets consider the gap function explained in the previous section for conventional superconductivity with a notation that displays explicitly the spin dependence:

$\Delta_{\mathbf{k},\uparrow,\downarrow} = -\sum_{\mathbf{k}'} V_{-\mathbf{k},\mathbf{k}'} \langle c_{-\mathbf{k},\downarrow}, c_{\mathbf{k}',\uparrow} \rangle$. In the following, we will compare $\Delta_{\mathbf{k},\uparrow,\downarrow}$ to $\Delta_{-\mathbf{k},\uparrow,\downarrow}$ to see if the gap function possesses the same antisymmetric properties as the wave function of the Cooper pair, by placing $-\mathbf{k}'$ instead of \mathbf{k}' in the formula aforementioned we have:

$$\Delta_{-\mathbf{k},\uparrow,\downarrow} = -\sum_{\mathbf{k}'} V_{-\mathbf{k},-\mathbf{k}'} \langle c_{-\mathbf{k}',\uparrow}, c_{\mathbf{k}',\downarrow} \rangle \quad (1.15)$$

Assuming a time-reversal symmetry potential $V_{-\mathbf{k},-\mathbf{k}'}$ and because of the anticommutation relation of the fermionic operators: $V_{-\mathbf{k},-\mathbf{k}'} = V_{\mathbf{k},\mathbf{k}'}$ and $\langle c_{\mathbf{k}',\uparrow}, c_{-\mathbf{k}',\downarrow} \rangle = -\langle c_{-\mathbf{k}',\downarrow}, c_{\mathbf{k}',\uparrow} \rangle$, we have:

$$\Delta_{-\mathbf{k},\uparrow,\downarrow} = +\sum_{\mathbf{k}'} V_{\mathbf{k},\mathbf{k}'} \langle c_{-\mathbf{k}',\downarrow}, c_{\mathbf{k}',\uparrow} \rangle = -\Delta_{\mathbf{k},\downarrow,\uparrow} \quad (1.16)$$

As can be seen, the gap function of a superconductor which is a function of \mathbf{k} and the spins of electrons is also antisymmetric under particle exchange like what we had for the Cooper pairs wave function. The gap function has both a spin part and a spatial part, so if one of them is antisymmetric the other one should be necessarily symmetric. As we have seen in the case of conventional superconductors: $V_{\mathbf{k},\mathbf{k}'} = \begin{cases} V_0, & \text{for } |\xi_{\mathbf{k}}| \leq \hbar\omega_D \\ 0, & \text{for } else \end{cases}$, it can be clearly seen that the gap function is even in k ; hence, the spatial part of the gap function is symmetric, which means that the spin part should be antisymmetric. Separating the spin part and the spatial part of the gap function we have:

$$\Delta_{S_1,S_2}(\mathbf{k}) = \Delta(\mathbf{k})\chi_{s_1 s_2} \quad (1.17)$$

Where $\Delta_{S_1,S_2}(\mathbf{k})$ is the gap function for any arbitrary type of superconductivity, $\Delta(\mathbf{k})$ is the spatial part of the gap function, and $\chi_{s_1 s_2}$ is the spin part of the gap function, with s_1 and s_2 being the indices for the spin part of the paired states. Following the aforementioned arguments, there are two different possibilities that respect the antisymmetric character of the gap function ($\Delta_{S_1,S_2}(\mathbf{k}) = -\Delta_{S_1,S_2}(-\mathbf{k})$):

$$\begin{cases} \chi_{s_1 s_2} = -\chi_{s_2 s_1}, & \text{and } \Delta(\mathbf{k}) = \Delta(-\mathbf{k}) \\ \chi_{s_1 s_2} = \chi_{s_2 s_1}, & \text{and } \Delta(\mathbf{k}) = -\Delta(-\mathbf{k}) \end{cases} \quad (1.18)$$

The first case refers to a spin singlet since the total spin of the pair is equal to zero ($S = 0$) and the second case refers to a spin-triplet pairing since in that case: $S = 1$. Depending on the total angular momentum of the cooper pairs (L), they have different properties and different classes. If the total angular momentum is equal to 0, which is the case of conventional superconductivity, the Cooper pairs will be referred to as 's-wave'. A Cooper pair with angular momentum L

$= 1$ is a spin triplet and superconductivity is called the 'p wave'. In the case of $L = 2$ the pairing will be singlet and the superconducting order parameter is d-wave. As mentioned earlier this kind of superconductivity is seen in cuprate-based high temperature superconductors [8]. Lastly, $L = 3$ represents a triplet pairing. Generally, an even (symmetric) angular momentum characterizes a singlet pairing, while an odd (antisymmetric) angular momentum corresponds to an even pairing.

1.2.4 Impurity effect in superconductors

One of the most important questions in solid state physics is to understand how impurities are going to change the electronic properties of correlated materials.

Indeed, real materials inevitably contain impurities and lattice defects. In 1961 Anderson showed that non-magnetic impurities in a BCS superconductor have no effect on T_c due to time-reversal symmetry [9]. However, the magnetic impurity can strongly affect both the T_c and energy gap in an s-wave superconductor.

It was shown in a seminal work by Abrikosov and Gorkov that the presence of magnetic disorder in s-wave superconductors is able to reduce the superconducting BCS gap and may ultimately destroy the coherence of the superconducting state [10]. Abrikosov and Gorkov have shown the dependence of T_c on the magnetic scattering rate Γ using Green's function method.

A few years later, it was predicted that a single classical spin is able to create a localized state, named Yu-Shiba-Rusinov bound state, within the BCS gap [11, 12, 13, 14, 15].

These bound states were observed recently using scanning tunneling spectroscopy (STS) [16] as indicated in green and red curves in Fig. 1.5.d and Fig. 1.5.g which show Shiba states induced by a single Mn atom deposited on SIC and $\sqrt{7} \times \sqrt{3}$ phases of Pb/Si(111), respectively. (Fig. 1.5.a shows a schematic of how the Mn atom is positioned and Fig. 1.5.c and Fig. 1.5.f show a spectroscopic map for the SIC and $\sqrt{7} \times \sqrt{3}$ phases of Pb/Si(111), respectively.

In 3D materials, the spatial extension of the Shiba bound states was shown to be limited to a few Å around the magnetic impurities. It was shown in my team that in 2H-NbSe₂ the spatial extent of the Shiba bound states was up to 8 nm as shown in Fig. 1.6 [17], and even up to 50 nm in Pb/Si(111) Monolayers as shown in Fig. 1.5. This very large extent of the Shiba states is a dimensionality effect due to the fact that at a scale inferior to the coherence length the wave function of Yu-Shiba-Rusinov bound states decay like $1/\sqrt{r}$ in 2D while the decay is like $1/r$ in a 3D system. Hence, in the low dimensionality systems I studied during my thesis, such defects were expected to give strong signatures even quite remotely from the impurities.

A finite concentration of magnetic impurities can form an impurity band from the overlapping Shiba states, within the superconducting gap as first demonstrated experimentally in manganese implanted lead by Bauriedl et al. in 1981 [13]. This impurity band merges with the continuum as the concentration exceeds a critical value [14, 18] and the system recovers an Abrikosov-Gork'ov like behavior.

The physics of magnetic impurities in a classical s-Wave superconductor can be linked to the effect on non-magnetic impurities in unconventional superconductors. Indeed, in Anderson's theorem it was assumed that a non-magnetic disorder has mainly the effect of homogenizing a weakly anisotropic order parameter. However, for unconventional superconductors with a sign

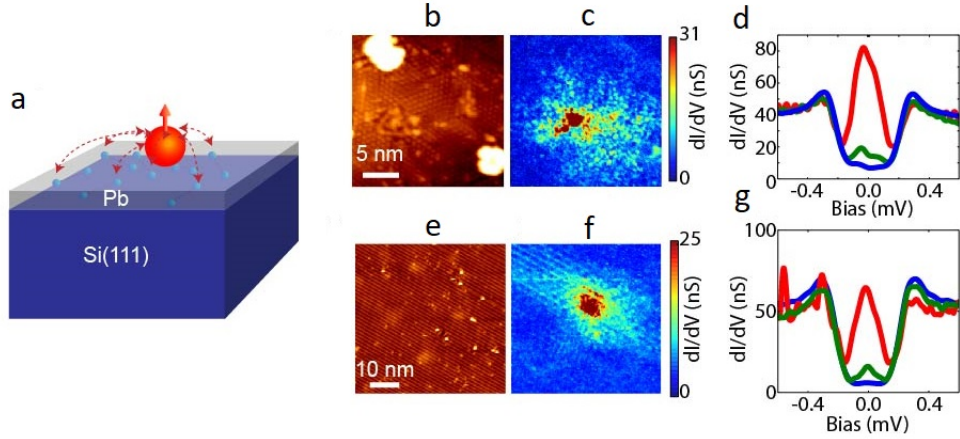


Fig. 1.5 High-resolution spectroscopy of an individual magnetic impurity in a disordered superconducting Pb/Si(111) Monolayer: a Schematics of the physical situation for an individual magnetic impurity (YSR bound state case). b. Topography of the $21 \times 21 \text{ nm}^2$ scanned area with atomic resolution in the SIC phase. c. Conductance map integrated over the superconducting gap showing the spatial dependence of the YSR bound state. d. Selected spectra taken at the largest conductance point (red), 7 nm away (green) and on the side of the measurement area (blue). e, f, g Same as a. b. and c. for the $\sqrt{7} \times \sqrt{3}$ phase of Pb/Si(111) [16].

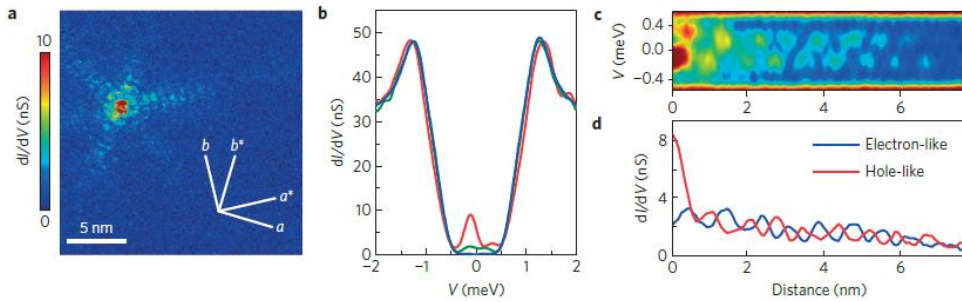


Fig. 1.6 a, Experimental conductance map taken at -0.13 meV . The a and b lines indicate the crystallographic axes of $2\text{H-NbSe} - 2$, whereas the a^* and b^* lines indicate the directions in the reciprocal space. b, Characteristic experimental spectra taken on top of the impurity (red), on the right branch, 4 nm from the centre of the impurity (green), and far from the impurity (blue). c, Spatial and energy evolution of the experimental tunnelling conductance spectra, $dI/dV(x, V)$ along one branch of the star. The left side of the figure corresponds to the centre of the star and the right side to the top-right corner of the scanning area. The colour conductance scale is the same as that used in a. d, Conductance profiles of the electron- and hole-like YSR states as a function of the distance to the impurity along the same line as for c [17].

changing order parameter, such as a d-wave pairing, the disorder averaged order parameter will vanish! This is not a small effect. Hence, the pair breaking theory was later generalized and non-magnetic impurities were shown to have pair-breaking properties for unconventional superconductors like the magnetic impurities in conventional superconductors [19, 20].

Finally, in the case of higher orbital momentum pairing state, like a d-wave superconductor, a single non-magnetic defect might also give rise to the formation of Yu-Shiba-Rusinov bound states. And looking at the presence or absence of bound states around non-magnetic defect might

help elucidating the underlying symmetry of the order parameter. For instance in Fig. 1.5 no Yu-Shiba-Rusinov bound states are observed above a non magnetic impurity like a Si substitution, while magnetic impurities give rise to the appearance of bound states. By contrast, a non-magnetic Zn impurity in substitution to Cu in the Cuprate superconductor $\text{Bi}_2\text{Sr}_2\text{CaCu}_2\text{O}_{7-\delta}$ leads to the formation of a zero energy bound state within the gap, with a four fold shape that reflects the $d_{x^2-y^2}$ symmetry of the underlying superconducting order parameter [21]. The effect of defects in superconducting systems has played an important role in understanding the symmetry of the order parameter in heavy-Fermion superconductors and Cuprates [18].

1.2.5 Chiral Superconductivity (a brief introduction)

Chiral superconductivity is a striking quantum phenomenon in which an unconventional superconductor lower its free energy by eliminating nodes in the gap while spontaneously developing an angular momentum [22]. A chiral superconducting phase happens when the complex superconducting gap function $\overline{\Delta}(\vec{k})$ winds in a clockwise or counterclockwise manner when \vec{k} is rotating around some axis on the Fermi surface of the underlying metallic phase [22] for example the chiral gap function $k_x \pm k_y$ will presses by $\pm 2\pi$ as \vec{k} follows a closed path enclosing the k_z axis. Chiral superconductivity is kind of a topological state and the Chiral superconducting gap breaks the time reversal symmetry while being degenerate with its time reversal mate. In highly correlated materials and in the presence of coulomb repulsion, as in the case of high temperature superconductors (Cuprates), the superconducting state favours a d-wave state. For a honeycomb lattice the two d-wave solutions, d_{xy} and $d_{x^2-y^2}$ are dictated to be degenerate by group theory while they become a fully gaped Chiral superconducting state of the form $d_{x^2-y^2} \pm d_{xy}$ wave below the critical temperature whose absolute squared value will be isotropic [23]. The system however should choose between one of the \pm signs in the $\pm i$, the result is a spontaneous symmetry breaking [22]. Triangular lattices naturally allow for Chiral d-wave superconductivity with topological edge states [23, 22] if the repulsive interaction dominates the pairing.

1.3 Density waves

1.3.1 Charge density wave

The aim of this part of the chapter is to give an introduction to the fundamentals of charge density wave (CDW) formation and the phenomena associated to this order phase of a compound. Deeper insights mainly in the theoretical aspects can be found in [24, 25]. In general, CDW is the appearance of a periodic modulation of the conduction electron density in a metal accompanied by a distortion of the atomic lattice. In 1955 Peierls proposed a mechanism which explained CDWs as a Fermi surface nesting effect in a one-dimensional electron gas. One-dimensional compounds, such as for example $K_2\text{Pt}(\text{CN})_4$, predominantly show CDW phases, while there are many examples of CDW in higher dimensions like Transition Metal Dichalcogenides (TMDCs) [26, 27]. A one-dimensional chain as a model system is presented in Fig. 1.7 for the explanation of the Peierls distortion. Considering an atomic chain of atoms with an equal distance of 'a', the unit cell in the reciprocal space is in the interval:

$$-\pi/a < k < \pi/a \quad (1.19)$$

If every n th atom in the unit cell is distorted by δ in one direction, we have the following:

$$-\pi/na < k < \pi/na \quad (1.20)$$

Since the reciprocal space is reduced, the band structure opens a gap at the Fermi level at the intersection points of the bands. For example, moving every second atom results in a doubling of the unit cell or reducing the reciprocal unit cell by half. When the energy gain due to the lowering of occupied bands is larger than the strain energy costs for the lattice distortion, a stable state will be formed for a finite values of the lattice distortion [28].

This effect will be noticeable only when the electrons are arranged close to their ground state, meaning that thermal excitation should be minimized. That is why the Peierls transition is observed most of the time at low temperatures.

The resulting modulation of the charge density is called the charge density wave with the wave vector of the lattice distortion having the absolute value of $2\pi/2a$ in the case of doubled periodicity of $2a$ in real space. In the new BZ a gap opens naturally, as can be seen in Fig. 1.7 through the formation of standing waves. The CDW wavevector $q_{\text{CDW}} = 2k_f$ naturally produces the CDW wavelength of $2a$ by $2\pi/q_{\text{CDW}}$.

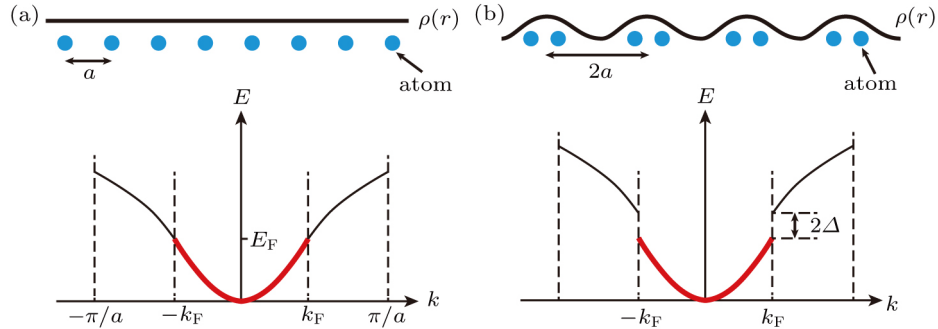


Fig. 1.7 Schematic illustration of one-dimensional periodic metallic lattice and Peierls distorted insulating lattice. a. Without electron–phonon interaction, the lattice with a period of “ a ” exhibits a constant charge density and filled electron states up to Fermi level. b. Considering the electron–phonon interaction, the Peierls distortion results in the periodically modulated charge density and an energy gap at the Fermi level [29].

In 1D there are exactly two points in the Fermi surface that always connect through, which makes the Fermi surface completely nested by q_{SDW} (Fig. 1.7.c). In a 2D free-electron system the Fermi surface is cylindrical as can be seen in Fig. 1.8.a, only two points, an infinitesimal part, are connected for a given q_{SDW} , however electron–electron interactions can cause the Fermi surface of 1-D and 2-D systems to differ from its isotropic shapes resulting in different nesting properties as can be seen in Fig. 1.8.d and Fig. 1.8.b for quasi 1-D and anisotropic 2-D systems, respectively where nesting can happen in specific directions, stabilizing CDW in those directions. Fig. 1.8.a is a circular Fermi surface of subbands of isotropic 2D quantum well states of an ultrathin Ag film prepared on Si(111) – 7×7 . Fig. 1.8.b is the hexagonal Fermi

surface for $\text{Ge}(111)\sqrt{3} \times \sqrt{3} - \text{Sn}$. Fig. 1.8.c is 1-dimensional Fermi surface and Fig. 1.8.d is the Fermi surface of $\text{Si}(111) - 4 \times 1 - \text{In}$ which resembles wavy sheets and satisfies nesting conditions.

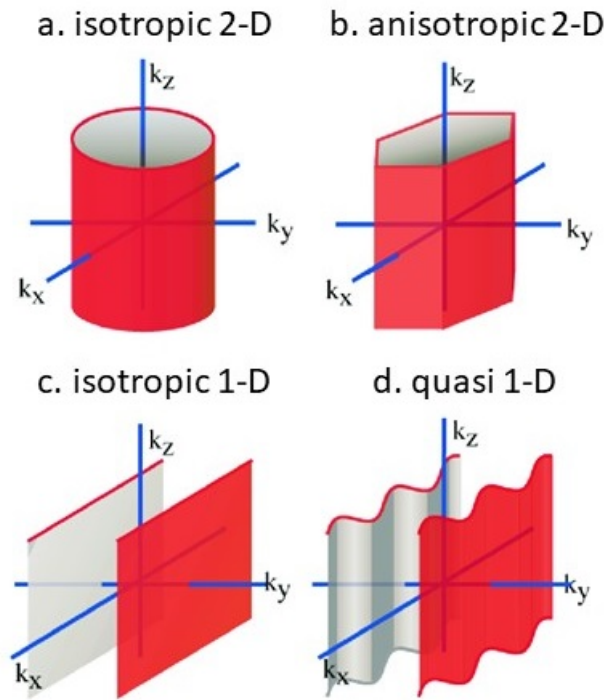


Fig. 1.8 Fermi surfaces in various dimensions a. Isotropic two-dimensional (2D) cylinder b. Anisotropic (hexagonal) 2D cylinder c. One-dimensional (1D) sheet and d. quasi-1D sheet.

1.3.2 Spin density wave

Like CDW, the spin density wave (SDW) is also a low-energy ordered phase of solids; however, in the spin density wave, the modulation of the density of states is derived by spins of the electrons rather than charges.

1.4 Insulators

In the basic conception of solid states physics one can see insulators in the semiconductor viewpoint than can be described by a two band model, a valence band and a conduction band. In this simple picture, a material with a fully occupied valence band and unoccupied conduction band is an insulator. However, this picture is far too simplistic and many other kind of insulators are possible. For instance, some materials with a half filled valence band should normally be a metal, however, we are going to explain below, the electron-electron Coulomb repulsion can lead to a Mott insulating state instead of a metallic one. The very same material with half filling can also become an insulator if a magnetic order appear below a critical temperature. In addition, a strong disorder might also induce some Anderson Localization and drive the system from a metallic to insulating state, in particular in low dimensional systems. In some cases, when an

insulating state is found instead of an expected metallic one, it is not an easy task to understand which mechanism is the correct one. Part of my thesis was devoted to such effort. In this section, I will recap some basic features about Mott insulators and (magnetic) band insulators and I will also explain a recent study that made an effort to find characteristics to distinguish between a Mott and band Insulator.

1.4.1 Mott insulators

Mott insulators are strongly correlated systems that cannot be described by the conventional Fermi liquid theory. The elementary excitations are no more single particle excitations like, but instead collective excitations, this is why a simple description of the Mott insulators, and more particularly the doped Mott insulators is rather difficult. Here, we will carry a basic explanation of Mott physics, by starting with a lattice of atoms with one valence electron per atom (unit cell). The atoms are very close to each other and their electronic orbitals will overlap between the nearest neighbors, creating a set of available states for the electrons which are called the 'bands'; while the bands are the allowed states for the electrons, the space between the bands is forbidden energies for the electrons, they are the so called 'forbidden bands'. For a single electron per atom, in our simple model, the Fermi level should lie in the middle of a band, thus, electrons can easily be mobilized with low energy excitation contrary to insulators in which, the Fermi level (or more precisely the chemical potential) lies within a forbidden band. The band theory treat the single electron states for simplicity by not considering electron-electron interactions, however, in some cases it has been discovered that some materials which should be metallic in the framework of band theory show insulating behaviour, which can only be understood by exploring deeper than the band theory and taking into consideration the electronic correlations or better said Coulomb repulsion between the electrons. In the case of a Mott insulator which ought to be a half filled metal, the on site Coulomb repulsion, if strong enough, will forbid two electrons from sitting on the same lattice site. In order to have conduction, the electrons should jump from one site to the neighbouring one which would lead to double occupancy which is prohibited. Therefore, if the Coulomb repulsion is dominant over the nearest neighbour hopping, the electrons can be frozen with one electron per lattice site, this is a Mott insulating state. Adding dopants, such as hole doping, one will have free atomic lattice site in which an electron from a nearest neighbour site will be allowed to jump, this mechanism will break the Mott insulating state and lead to metallicity.

In order to illustrate this mechanism, we will try to understand the Mott insulating phase from a tight-binding lattice model with N electrons distributed over $L = N$ Lattice sites in a square lattice. Now by considering both the kinetic part which is hopping to the nearest neighbor and also on-site Coulomb repulsion we can write the Hamiltonian as follows for the Hubbard model in a general form as:

$$H = H_{kin} + H_{int} = \sum_{ij\sigma} -t_{ij}c_{i\sigma}^\dagger c_{j\sigma} + \frac{1}{2} \sum_{ijkl\sigma\sigma'} c_{i\sigma}^\dagger c_{i\sigma'}^\dagger U_{ijkl\sigma\sigma'} c_{k\sigma'} c_{l\sigma} \quad (1.21)$$

Where $c_{\alpha\beta}^\dagger$ is the electronic creation operator on the site α with spin β and $c_{\alpha\beta}$ is the annihilation

operator on the site α with spin β . The parameter t_{ij} is the hopping amplitude between sites i and j and U is the on-site coulomb repulsion.

To proceed further to simplify the Hubbard model, it is assumed that there is only one band at the Fermi energy and that all the other bands are energetically far from the Fermi energy. This is termed as the single band Hubbard model and means that the intra-atomic coulomb repulsion is the same for all the lattice sites. The process of hopping of the electrons does not undergo any spin flip. The Pauli exclusion principle state that for the electrons to be on the same site, they should have anti-parallel spins, so, the simplified Hubbard model can be rewritten as follows:

$$H = \sum_{ij\sigma} -t_{ij} c_{i\sigma}^\dagger c_{j\sigma} + U \sum_i n_{i\uparrow} n_{i\downarrow} \quad (1.22)$$

Here, $n_i = c_i^\dagger c_i$ are number operators.

In the case of no on-site coulomb repulsion which means $U = 0$, the energy dispersion can be computed by diagonalizing the Hamiltonian in the k -space, which gives: $E_k = -2t(\cos k_x a + \cos k_y a)$. Since there is only one electron per site and the band is half filled, in the absence of U the system is metallic.

Now let us turn on the on-site coulomb repulsion $U \neq 0$ and let us consider a simple two-lattice sites Hubbard model and for simplicity we will consider all the hopping parameters to be the same $t_{ij} = t$, So we have:

$$H = -t(c_{1\uparrow}^\dagger c_{2\uparrow} + c_{1\downarrow}^\dagger c_{2\downarrow} + c_{2\uparrow}^\dagger c_{1\uparrow} + c_{2\downarrow}^\dagger c_{1\downarrow}) + U(n_{1\uparrow} n_{1\downarrow} + n_{2\uparrow} n_{2\downarrow}) \quad (1.23)$$

To simplify the notation for the possible states corresponding to this Hamiltonian we will consider the following notation called Foch states: $|n_{1\uparrow}, n_{1\downarrow}, n_{2\uparrow}, n_{2\downarrow}\rangle$ since both the number and the spins of the electron are conserved. To understand better this notation, consider that there is a single electron on the first site then the corresponding Foch states will be $|1, 0, 0, 0\rangle$ for spin up and $|0, 1, 0, 0\rangle$ for spin down configuration and the corresponding wave function will be: $\psi = a|1, 0, 0, 0\rangle + b|0, 1, 0, 0\rangle$, where a and b are complex numbers.

Since there is only one electron there is no Coulomb term in the Hubbard Hamiltonian. In the $\{|1, 0, 0, 0\rangle, |0, 1, 0, 0\rangle, |0, 0, 1, 0\rangle, |0, 0, 0, 1\rangle\}$ basis the Hamiltonian can be written as:

$$H = \begin{bmatrix} 0 & 0 & -t & 0 \\ 0 & 0 & 0 & -t \\ -t & 0 & 0 & 0 \\ 0 & -t & 0 & 0 \end{bmatrix} \quad (1.24)$$

Solving this Hamiltonian one obtains two ground state eigenstates:

$|\psi_1\rangle = \frac{1}{\sqrt{2}}(|1, 0, 0, 0\rangle + |0, 0, 1, 0\rangle)$ and $|\psi_2\rangle = \frac{1}{\sqrt{2}}(|0, 1, 0, 0\rangle + |0, 0, 0, 1\rangle)$ with energy $E = -t$ and two excited states $|\psi_3\rangle = \frac{1}{\sqrt{2}}(|1, 0, 0, 0\rangle - |0, 0, 1, 0\rangle)$ and $|\psi_4\rangle = \frac{1}{\sqrt{2}}(|0, 1, 0, 0\rangle - |0, 0, 0, 1\rangle)$ with energy $E = t$ (assuming $t > 0$).

Now let us consider the case of two-particles states having the same spins. The subspace will be composed of $|1, 0, 1, 0\rangle$ and $|0, 1, 0, 1\rangle$. The eigenvalue corresponding to this subspace will be 0, however, in the two-particle case the spins can also be opposite, in this case the subspace can be described by the basis $\{|1, 1, 0, 0\rangle, |0, 1, 1, 0\rangle, |1, 0, 0, 1\rangle, |0, 0, 1, 1\rangle\}$. The

corresponding Hamiltonian will be:

$$H = \begin{bmatrix} U & -t & -t & 0 \\ -t & 0 & 0 & -t \\ -t & 0 & 0 & -t \\ 0 & -t & -t & U \end{bmatrix} \quad (1.25)$$

After diagonalization of the matrix, the following four eigenvalues can be found: $E = 0, U, \frac{U}{2} \pm \sqrt{4t^2 + \frac{U^2}{4}}$. Since we are only interested in half filled band the two particle states mentioned above will be of interest. In this case, there are a total number of 6 states available for this subspace with energies equal to $0, U, \frac{U}{2} \pm \sqrt{4t^2 + \frac{U^2}{4}}$. Now let us see what happens if the on-site Coulomb repulsion is very high $U \gg 0$, in this case $\frac{U}{2} \pm \sqrt{4t^2 + \frac{U^2}{4}}$ will be approximately equal to 0 or U and we will end up with 4 states having 0 energy and 2 states having energy U . What we have mentioned until now was that in the case of a two-site system. Now, scaling up the system to an infinite network, the two sets of states separated by U in the limit of $U \gg 0$ will turn into two sets of bands separated roughly by a gap equal to U . The bands with lower energy are called the lower Hubbard band and the sets of bands with higher energy are called the upper Hubbard band.

In our simple two site Hubbard model, the ratio U/t plays a very important role in deciding the electronic properties of the system if $U = 0$ the ground state energy will be $-2t$ and the system is metallic; however, if $U/t \gg 1$ then the system will become an insulator with a ground state energy of $-4t^2/U$, and a ground state eigenstate identical to the one of a two sites Heisenberg Hamiltonian with antiferromagnetic coupling [30]. In the case of an infinite network the same happens and for large U the system will also display an antiferromagnetic ordering, at least in 1D and square 2D lattices. In order to illustrate this point better we will present the results of Monte Carlo simulations done by Rozenberg et al. [31] and presented in Fig. 1.9 as it can be seen, the DOS is finite at the Fermi level in low U , but becomes zero as the insulating gap opens at large U , with the existence of a peak at the intermediate U values which is called the quasi-particle peak.

In the case of a triangular lattice I studied during my thesis, the situation is more complex since magnetic frustration will show up.

1.4.2 Comparison between band-insulator and Mott-insulator

A band insulator and a Mott insulator may differ when comparing their spectral weight transfer properties. In a "good" metal the low energy excitations are electron like quasiparticles, and well described by the Landau Fermi liquid theory. However, in a strongly correlated material, the excitations cannot anymore be accounted for by a simple Fermi liquid with well defined quasiparticles; in the limit of very large U , no such quasiparticles exist anymore. Starting from a metal and adding some Coulomb repulsion some spectral weight of the quasiparticles will be transferred progressively to collective modes in a broad spectral background, when all the spectral weight of the quasiparticles will have been transferred to the spectral background the system will become a Mott insulator. A more accurate explanation of the difference between a Mott insulator and a Band insulator in term of spectral weight is given by Menders et al. [32].

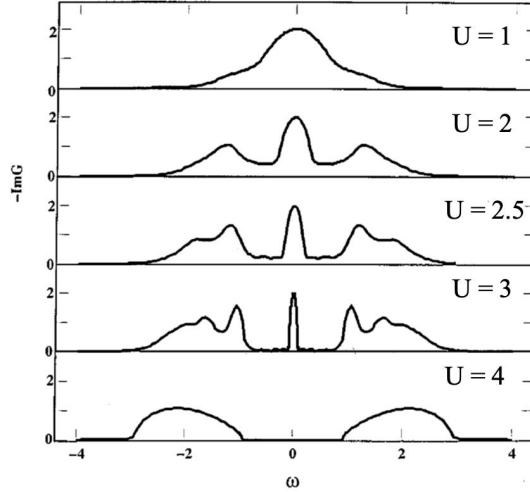


Fig. 1.9 DOS (ω) of the HM at $T = 0$ for increasing values of U . The quasiparticle peak narrows as U increases until it collapses at the critical value U_{c2} .

In the following, the physical arguments will be reproduced and we refer to the original article [32] for more details.

First, we start with a band-insulator with a filled valence band and an empty conduction band separated by a band gap E_G . For the undoped band insulator, the total removal and addition of electrons is illustrated in Fig. 1.10. If N is the total number of sites, then there are $2N$ occupied states and $2N$ unoccupied states available, taking the spin into account. If we chemically dope the band insulator by adding one hole, the chemical potential will shift into the former occupied band, if we neglect the chemical potential of the dopant. The total spectral weight for electron removal will be $2N-1$ (the number of electrons in the ground state) and the total spectral weight for electron addition will be $2N+1$ (the number of holes in the ground state) [1.10]. The electron addition spectrum can be divided into two parts, the conduction band and the unoccupied part of the valence band (Fig. 1.10) it can be seen that the Low Energy Spectral Weight (LESW) is equal to 1: one state available for an additional electron at low energy in the valence band. In contrast the High Energy Spectral Weight (HESW) will remain $2N$, the number of available states in the conduction band.

The same is also true for an electron-doped band insulator, thus when doping a band insulator, the total spectrum will be formed by just the repositioning of the chemical potential and the LESW will grow with x (x is the number of dopants). The spectral weight of the high-energy band will remain unchanged. Therefore, there will be no redistribution of the spectral intensities upon doping a simple semiconductor 1.10. Considering now a correlated system, we are going to investigate a Mott insulator in its localized regime with N sites. The total photoelectron and inverse photoelectron spectrum at half-filling are shown in Fig. 1.10. While the total number of electron addition spectral weights is equal to the number of unoccupied states, the total number of electron removal spectral weights is equal to the number of occupied states Fig. 1.10. Therefore, the intensity of both will be equal to N . If the system is doped with one hole, there will be $N-1$ singly occupied sites; therefore, the total electron removal spectral weight will be equal to

$N-1$. When an electron is added to the system now there are $N-1$ possibilities to add an electron and get a doubly occupied site, therefore the Upper Hubbard Band (UHB) will have $N-1$ states (not N), this process will cost at least U and will contribute to the high energy spectral weight. Now, one empty site remain and there are two possibilities to add an electron to this site (spin up and spin down), both belonging to LHB Fig. 1.10. As, in this case, there is no U to pay, this process will contribute to the low energy spectral weight. In summary, there will be $N-1$ electron removal states near the Fermi level, two electron addition levels near the Fermi level, and $N-1$ electron addition states at the UHB. The same also holds for the electron doped case.

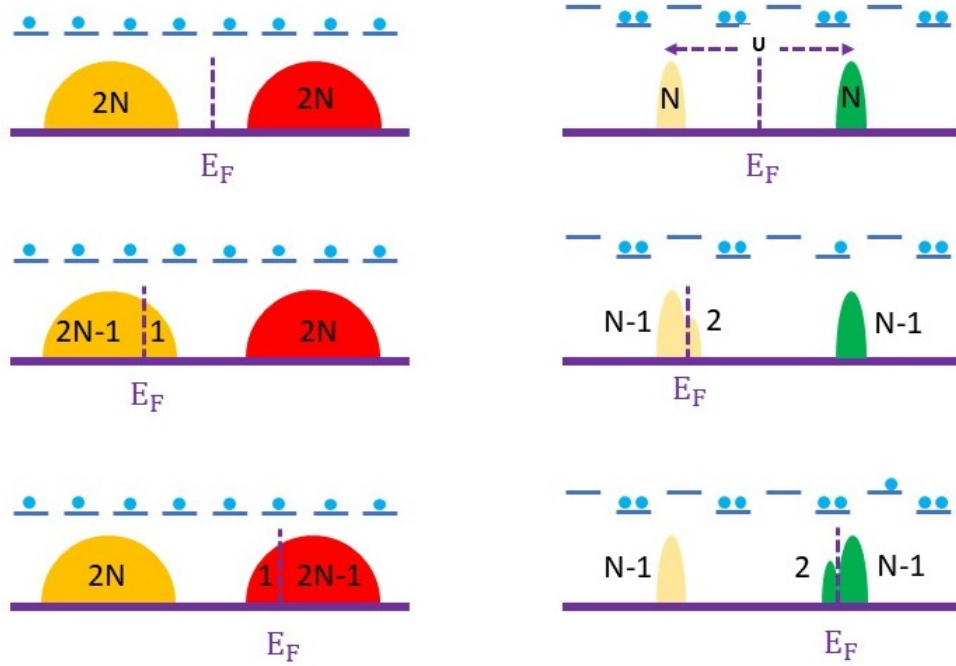


Fig. 1.10 A schematic drawing of the electron-removal and electron-addition spectra for a semiconductor (left) and a Mott- Hubbard system in the localized limit (right). a. Undoped (half filling), b. One-electron doped, and c. One-hole doped. The bars just above the figures represent the sites and the dots represent the electrons. The on-site repulsion U and the charge-transfer energy Δ are also indicated.

Menders et al. [32] have done some calculation for a Mott-Hubbard model with on-site Coulomb repulsion $U = 10$ eV. In Fig. 1.11 the total electron removal and addition spectra are plotted for a 10-site one-dimensional ring with $t = -1.0$ eV and for various number of electrons N . The hole(electron) doping concentration is given by $(N - N')/N'$ with the number of sites $N' = 10$ ($N < N'$ corresponds to hole doping and $N > N'$ corresponds to electron doping).

As can be seen in Fig. 1.11 going from the one-hole-doped to one-electron-doped case, the chemical potential shifts by the amount of the insulating gap.

However the mentioned Monte Carlo calculations are done only for a finite chain of atoms in the case of infinite lattice more powerful calculation like Dynamical Mean Field Theory is needed to illustrate more precisely. Such calculations are done by Camjayi et al. [33] they have shown that the Mott insulating phase can be destabilized by hole doping and thus changing the

particle occupation δ (at $T = 0.1$ K and strong enough U). A narrow quasi particle peak at Fermi level can be seen in Fig. 1.12 with an intensity that depends on the doping level.

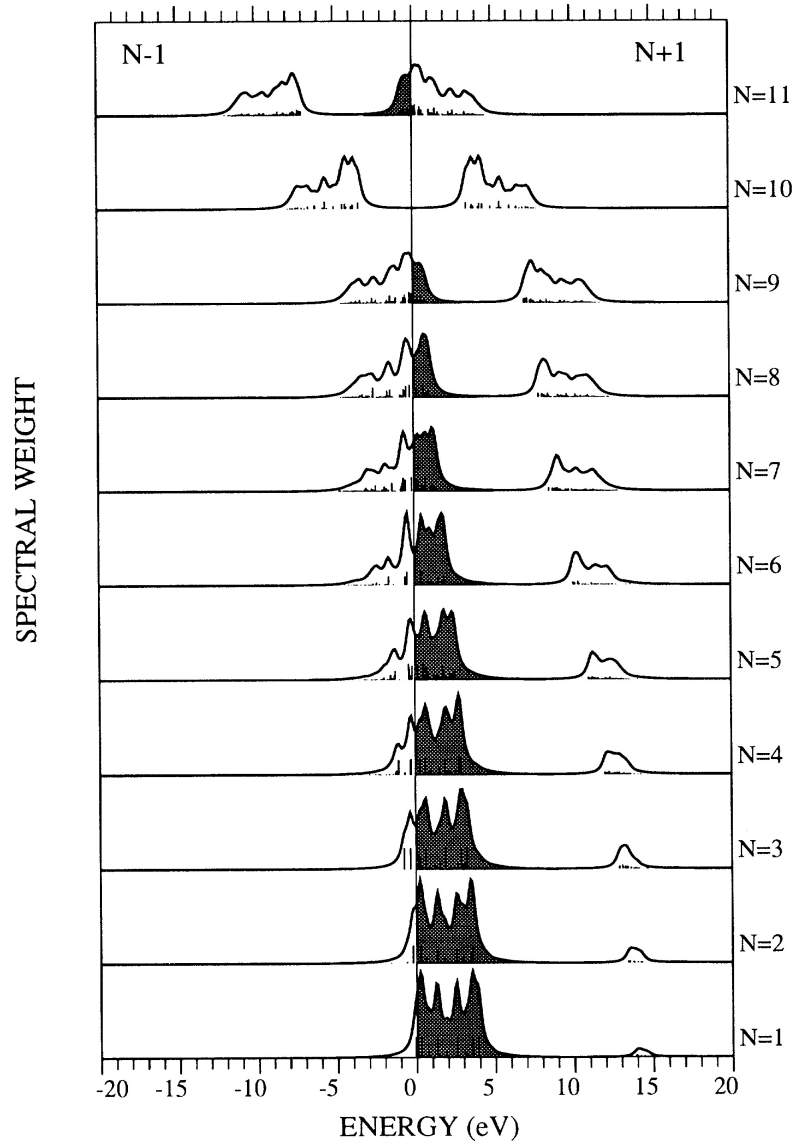


Fig. 1.11 One-particle Green's function for a one-dimensional Hubbard-ring of $X=10$ sites for $U = 10$ eV and $t=1$ eV. The number of electrons in the ground state X are indicated. The low energy electron-addition spectral weight is obtained by integration over the shaded area [32].

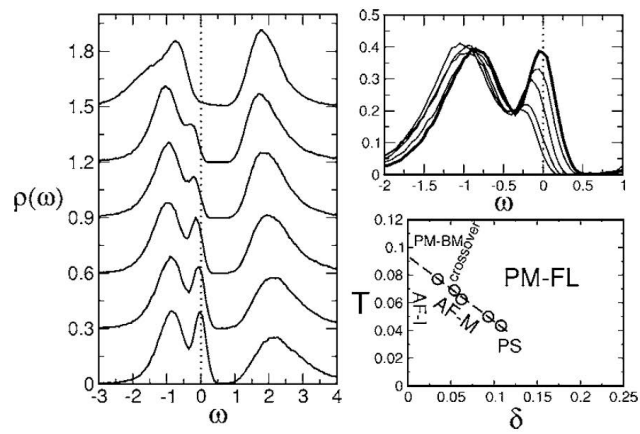


Fig. 1.12 Left: Paramagnetic Density of states ($\text{DOS}(\omega)$) of a lightly hole-doped Hubbard model at $U = 3.125$, $T = 0.1$, and increasing $\delta = 0.003, 0.0076, 0.0114, 0.022, 0.038$, and 0.055 , from top to bottom. Top right: Detail of the evolution of the quasiparticle peak in the previous results. Bottom right: Phase diagram as a function of δ and T for $U > U_{\text{critical}}$. [33]

CHAPTER 2

Devices and Experimental methods

2.1 Introduction

In this Chapter first the principles of Low Energy Electron Diffraction (LEED), Scanning Tunneling Microscopy/Spectroscopy (STM/STS) are explained together with various methods that can be implemented using STS measurements including, Spin-Polarized STM (SPSTM), Lock-in technique and Quasi Particle Interference measurements. After the setups used in this thesis, including the VT-STM and M3, will be presented in detail. And at the end the methods and parameters that has been used to prepare the samples and also the tips together with a detailed description of the steps that lead us to find optimized parameters to prepare for both the Sn/Si(111) – $\sqrt{3} \times \sqrt{3}$ – R30° and the Pb/Ge(111) samples are explained.

2.2 Surfaces and Wood's notation

At the surface of bulk material, many bonds between atoms are broken, which implies a new electronic distribution together with an increase in the total energy. This energy can be compensated by means of a reconstruction of the top layer or the top few layers of the material. The reconstructed surface may exhibit a superstructure with a different periodicity from the one of the bulk. A very famous notation to describe this superstructure is the Woods notation. In this notation, the primitive vectors of the superstructure are written as the multiples of the ones from the bulk terminated unreconstructed structure, as follows:

$$|a_s| = m|a|, \quad |b_s| = n|b| \quad (2.1)$$

If the superstructure is rotated with respect to the unreconstructed surface the angle of rotation is noted in the formalism, which leads to the following general notation:

$$X(hkl) - m \times n - R\alpha \quad (2.2)$$

Where hkl are the notation of the unreconstructed surface, m and n are the proportionality between the primitive vectors of the superstructure and the bulk and α is the angle of rotation.

For example, Si-7 × 7 means that the superstructure primitive cell is 7 times higher than that of the Si (111) surface and in the same direction.

When a new substance is deposited, either as molecules or atoms on a semiconductor/metal surface, it forms a superstructure with a periodicity that differs from the one of the host sub-

strates. In this case, the substance's chemical symbol is also mentioned in the wood's notation. For example $\text{Si}(111) - \sqrt{3} \times \sqrt{3} - \text{R}30^\circ - \text{Sn}$ ($\text{Sn}-\sqrt{3}$) superstructure indicated in Fig. 2.1.

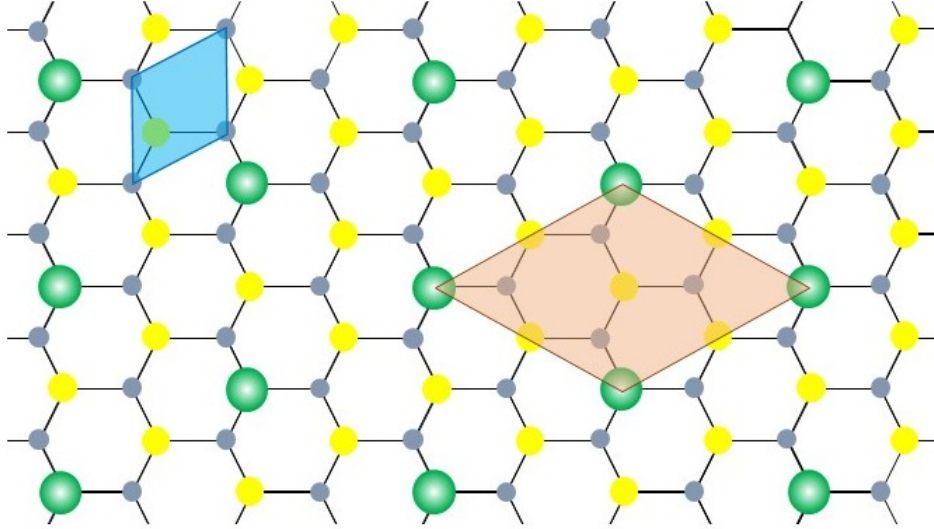


Fig. 2.1 Top-view of the $\text{Si}(111) - \sqrt{3} \times \sqrt{3} - \text{R}30^\circ - \text{Sn}$. Small Yellow (grey) circles represent first (second) atomic layer of the $\text{Si}(111)$ substrate and the large green circles represent the Sn atoms adsorbed on the $\text{Si}(111)$ substrate. As it can be seen the $\sqrt{3} \times \sqrt{3}$ unit cell (orange filling) corresponding to Sn atoms is 30° rotated with respect to the 1×1 unit cell (blue filling) corresponding to Si atoms.

It should be noted that woods notation can only be used if the superstructure and the unreconstructed surface have the same symmetry, otherwise the matrix notation should be used.

2.3 Low Energy Electron Diffraction (LEED)

In this Thesis, LEED is used as a useful tool in addition to STM in order to have a quick check to see if the sample preparation parameters are optimized enough to have our desired samples. We start the section by giving an introduction to LEED and then we will present our LEED results on our samples. Davisson and Germer were among the first scientists who observed the electron diffraction process by exposing a nickel crystal to a monochromatic electron beam [34]. They have found that the distribution-in-angle of the scattered electrons shows sharp peaks at certain angles. They have realized that these peaks are indeed interference patterns following Bragg's law (a schematic figure is shown in Fig. 2.2)

$$n\lambda = a \sin\theta \quad (2.3)$$

Where n is an integer number indicating the diffraction order, λ is the wavelength of the electron, a is the lattice periodicity, and θ is the angle of the incident diffracted (or reflected) beam. This is one of the first experiments that shows the wave like behaviour of electrons which awarded Davison and Germer with a Nobel prize in 1937 for the discovery of electron diffraction by crystals. An electron of momentum p can be seen as a wave with wavelength of $\lambda = h/p$ [35]. To probe the surface using LEED, electrons with the energy range of 20

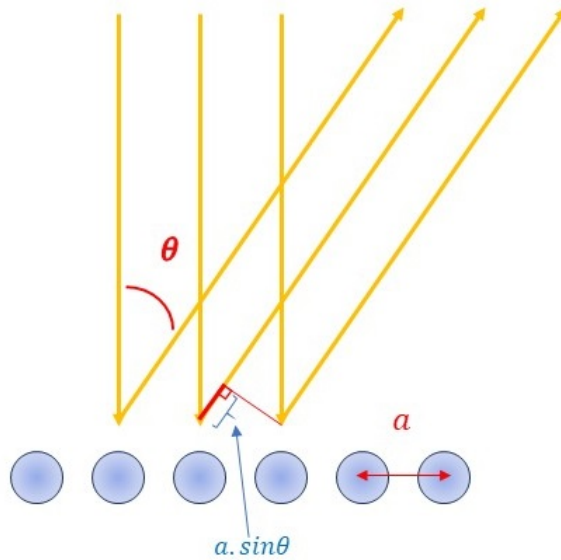


Fig. 2.2 Schematic picture showing electron diffraction and Bragg's law.

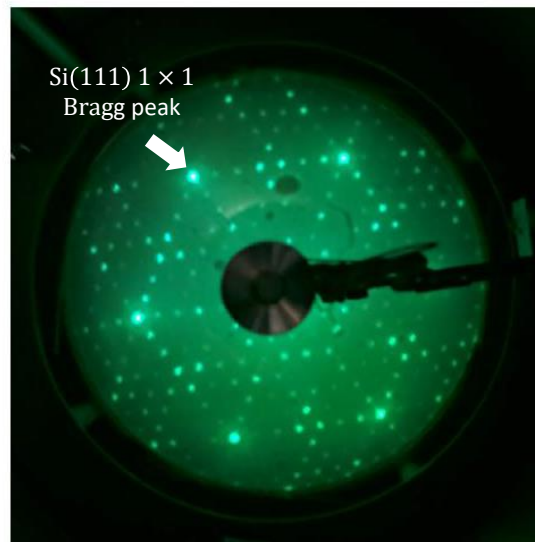
to 200 eV are typically being used because the penetration depth in this case will be around 10 Å. The diffracted electrons impact on a fluorescent screen and form a pattern of bright spots, which is a scale of the reciprocal lattice of the surface reconstruction. The LEED patterns of the Si(111) – 7×7 and Sn- $\sqrt{3}$ are shown in Fig. 2.3.a and Fig. 2.3.b respectively.

As can be seen in the LEED pattern Fig. 2.3.b, the Sn/Si(111) reconstruction is rotated 30 degrees with respect to the 1×1 (2.3.a) unreconstructed surface as expected. In both cases, the spots of the bulk Si and the superstructure can be seen. If the periodicity of the superstructure is longer in the real space, its periodicity should be smaller in the reciprocal space, as can be seen in 2.3.a For example, in the case of the Si(111) – 7×7 superstructure, since the periodicity of the surface is 7 times higher than that of the 1×1 lattice, the periodicity of this superlattice will be 7 times smaller than that of the 1×1 lattice in the reciprocal space. It can be seen that the sides of the hexagon formed by 1×1 are divided by 7 parts by the extra spots.

A typical diagram of the LEED is shown in Fig 2.4. As can be seen in this figure, the LEED consists of an electron gun that sends an electron beam from behind a transparent fluorescent screen to the surface of the sample. The electron beams are produced by heating a cathode and afterward by a Wehnelt and a set of electrostatic lenses the parallelism, energy and focus of the electron beams are adjusted. The electron beam will go towards the surface, become diffracted and it will reflect on the screen. A high positive voltage is applied to the fluorescent screen in order to accelerate the diffracted electron to make them visible.

In this study LEED has been used to check the quality of crystallographic growth of the prepared samples. In particular, when the surface is clean and well reconstructed the LEED pattern shows sharp, well-defined peaks; however, if the sample contains defects, disorder or contaminations the peaks of the LEED will become broader. It is also worth noting that if the surface contains contamination another technique that can be used by LEED setup is Auger spectroscopy which allows probing the exact elements present close to the surface of the sam-

a



b

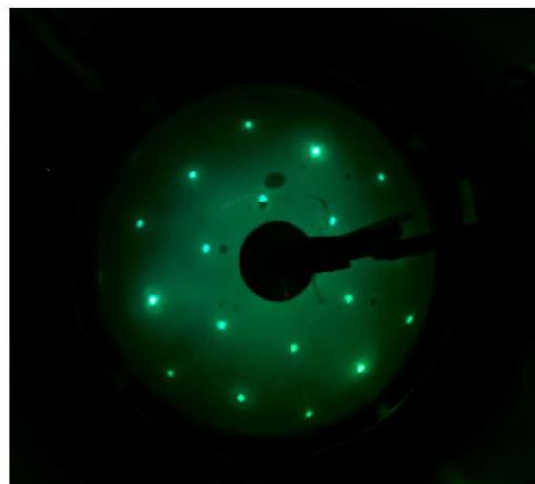


Fig. 2.3 a. Leed image of Si(111)- 7×7 reconstruction and b. Leed image of Sn- $\sqrt{3}$ reconstruction

ple, which can be useful in case LEED is not showing the desired reconstruction. Even with sharp peaks of a desired surface reconstruction, it is always better to verify the quality of the reconstruction using STM since LEED is not accurate enough for determining the amount of contamination, disorder and other non-local structural perturbations. It is quite common in practice that a surface that looks nice by LEED appears as pretty bad in STM due to the fact that STM is local while LEED is an integral probe that averages over many different areas. In particular the presence of tens of nm wide domains separated by twin boundaries will not affect much the LEED pattern.

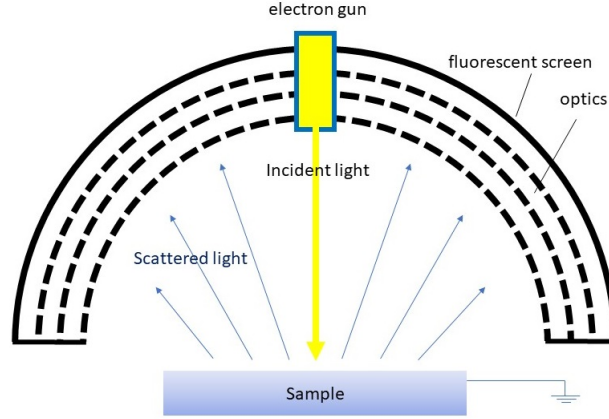


Fig. 2.4 Simplified schematic picture of LEED components.

2.4 Scanning Tunneling Microscopy/Spectroscopy

Scanning tunnel Microscopy (STM) is a near field probing tool that is used to characterize the electronic and structural properties of materials at their surfaces. Its invention in 1982 by Gerd Binnig, Heinrich Rohrer, and Christophe Gerber [36, 37] awarded a Nobel Prize in 1986 for Rohrer and Binnig. This near field microscope utilizes a well-known phenomenon called the quantum tunneling effect. This technique is the main experimental tool that has been used in this thesis and all the results are obtained using this technique. In this chapter the principle of STM and the different techniques it can perform are presented in the following order: First, in this section, the surface imaging procedure using STM is explained. In Section 2.4 the principles of scanning tunneling spectroscopy (STS) are introduced, explaining how this technique can measure the (LDOS) of the samples. The lock-in technique and the spin-polarized STM technique are introduced in Sections 2.5 and 2.6, respectively. In Section 2.7, it will be shown how the Fourier transform combined with STS measurements can extract Quasi Particle Interference (QPI) information which can help to have a clearer picture of the band structure. In Section 2.8, we introduce the experimental setup and sample preparation techniques.

2.4.1 Surface topography imaging

We consider two metallic electrodes separated by a vacuum barrier of width d . If we consider an electron on one of the electrodes, there is an energy barrier of height W for this electron to move to the other electrode (Fig. 2.5). The time independent Schrödinger equation for the wave function $\psi(x)$ in a 1D potential barrier is as follows:

$$\left(-\frac{\hbar^2}{2m_e} + W\right)\psi(x) = E\psi(x) \quad (2.4)$$

Now if we consider an incident wave function e^{ikx} and energy E , which can be transmitted or reflected through the barrier, its probability of being transmitted is:

$$T = \exp(-\kappa(E)d) \quad (2.5)$$

where $\kappa(E)$ is [38]:

$$\kappa(E) = \frac{2\sqrt{2m_e(W - E)}}{\hbar} \quad (2.6)$$

The probability is decreasing exponentially in terms of barrier width d . κ is in the order of a few \AA^{-1} ; if d changes by around one \AA the tunneling current will change by one order of magnitude [1]. This current-height dependence is very sensitive and is what enables us to have atomic resolution extremely localized around the atom at the apex of the tip, which makes it possible to have a high atomic resolution.

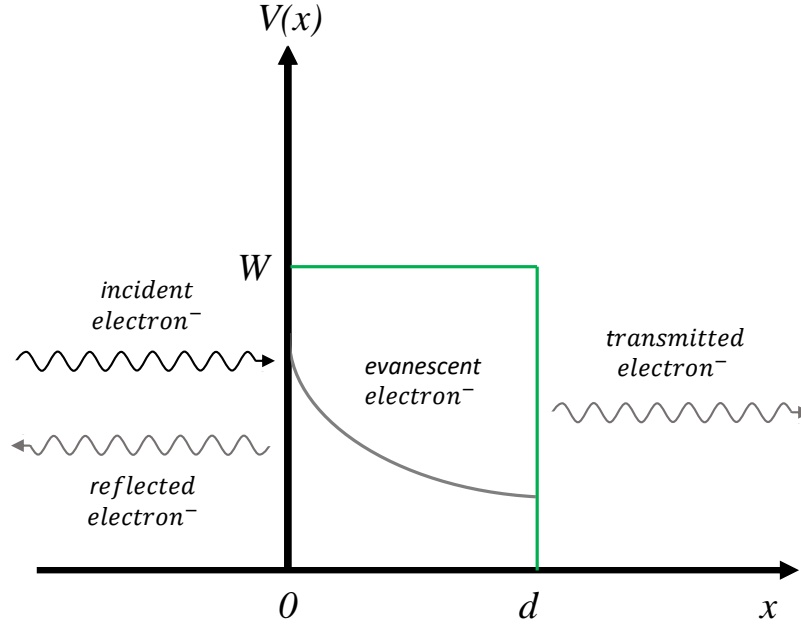


Fig. 2.5 propagating wave in a one-dimensional potential barrier of height W and width d

Now, considering that one of the electrodes is a metallic tip and the other one is the sample. If a positive bias is applied to the sample the electrons will tunnel from the tip to the sample and vice versa. If the voltage is fixed the tunneling current depends only on the distance between the sample and the tip. If we consider the applied voltage to be V , the probability of the electrons to be transmitted through the barrier at absolute zero temperature can be written as follows [38]:

$$I_T \propto \int_0^{eV} \rho_s(r, E) \rho_t(r, eV - E) T(d, E, eV) dE \quad (2.7)$$

and:

$$T(d, E, eV) = \exp\left(-\frac{2d\sqrt{2m}}{\hbar} \sqrt{\frac{\Phi_{\text{tip}} + \Phi_{\text{sample}}}{2} + \frac{eV}{2} - E}\right) \quad (2.8)$$

Where $T(d, E, eV)$ is the probability of the electron to be transmitted, $\rho_s(r, E)$ and $\rho_t(r, E)$ are the density of states of the sample and the tip and Φ_{tip} and Φ_{sample} are the work functions of the tip and the sample, respectively. E represents one generic energy level of the electrons transmitted through the barrier in the energy interval eV from the Fermi level. As can be seen in Eqn. 2.8 the tunneling current is a convolution of the density of states of the sample and the

density of states of the tip integrated in an interval of E_f and $E_f + eV$.

By scanning the surface in $x - y$ using a Piezo-tube, with a fixed tunneling voltage, a feedback loop can be used to regulate the height of the tip in a way that the current always remains constant and equal to a defined set-point (Fig. 2.7.a). In this way, The transmission probability, $T(d,E,eV)$ is considered constant for scanning voltages around the Fermi level $V \ll \Phi$ and since the tip is modeled as a simple metal with a constant density of states around the Fermi level, the tunneling current mainly depends on the density of states of the sample. In this way scanning with a positive or negative bias enables us to measure the filled or empty states of the sample as indicated in Fig. 2.6.a and Fig. 2.6.b, respectively.

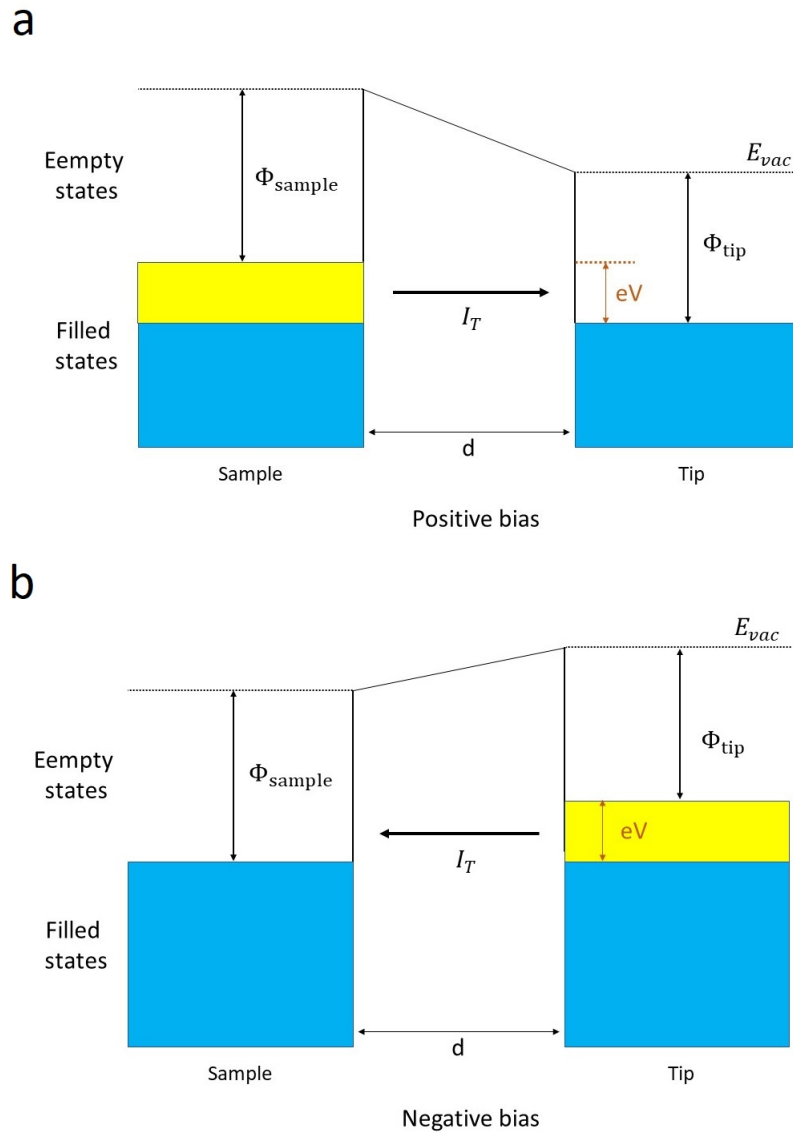


Fig. 2.6 a(b) A schematic figure showing positive(negative) bias voltage applied to the tip creating unfilled (filled) states within an interval of eV from the Fermi level making it possible for the electrons to tunnel from yellow stripes to the Tip (sample).

With this method, one can construct topographic images by plotting the variation of the

height of the tip as a function of $x - y$. All the topographic images in this thesis are taken using this constant current mode. An STM image taken from Si(111) - $\sqrt{3} \times \sqrt{3}$ - R30° - Sn (for simplicity this phase is going to be called Sn - $\sqrt{3}$) surface is shown in Fig. 2.7.b. It should be noted that the tip has an arbitrary shape at the apex, however for simplicity it is considered to be locally spherical, for more information see [39].

2.5 Scanning Tunneling Spectroscopy

As we have seen scanning tunneling microscopy allows measuring topographic features of the material at a given tunneling voltage. But we can also play with the voltage as a parameter to get a much wider set of information. Indeed, using scanning tunneling spectroscopy (STS) we can measure the Local Density of States (LDOS) of a material, which can give us information about the spatial electronic structure down to the atomic scale.

2.5.1 Local Density of States Measurements

To measure the density of states, the tip is first fixed at a certain point. Then the feed-back loop is turned off and the tip is fixed at a certain distance from the sample depending on the set points of the voltage and the current. Then, by sweeping the voltage between a desired range, the tunneling current $I_T(V)$ is recorded. If we differentiate the tunneling current with respect to the voltage, we obtain the differential conductance dI_T/dV and the density of states of the sample can be obtained by differentiating the relation in Eqn. 2.7. Since the density of states of the tip is uniform, the ρ_t is evaluated at the Fermi $eV = 0$.

$$\frac{dI_T}{dV} = \rho_s(r, eV)\rho_t(r, 0)T(d, eV, eV) + \int_0^{eV} \rho_s(r, E)\rho(r, eV - E)\frac{dT(d, E, eV)}{dV}dE \quad (2.9)$$

The second term can be neglected if the I_T curve is measured in a low range close to the Fermi level, however, it can bring a smooth background if the voltage range is in the order of 1-2 V which can also be neglected, leaving only the first term that makes a relation between the tunneling conductance (dI_T/dV) and the density of states of the sample $\rho_s(r, eV)$:

$$\frac{dI_T}{dV} \propto \rho_s(r, eV)T(d, eV, eV) \quad (2.10)$$

Equation 2.9 only holds true at absolute zero temperature where the derivative of the current is directly proportional to the density of states of the sample, however, it should be noted that at finite temperature since the derivative of the tunneling current is a convolution of the density of states of the studied material with the derivative of the Fermi-Dirac function, the spectral features are broadened by a factor of $\approx 3.5K_B T$. That is why we try to perform our measurements at the lowest possible temperature, 300 mK. At 300 mK and 4.2 K this broadening factor will be equal to 100 μeV and 1.4 meV. While STS measurements on samples with broad spectral features (like an insulating gap of several hundreds of meV) can be performed at Helium temperature (4.2 K) with a negligible thermal broadening, for very small spectral features like a BCS superconducting gap which is in the range of several meV it is necessary to perform

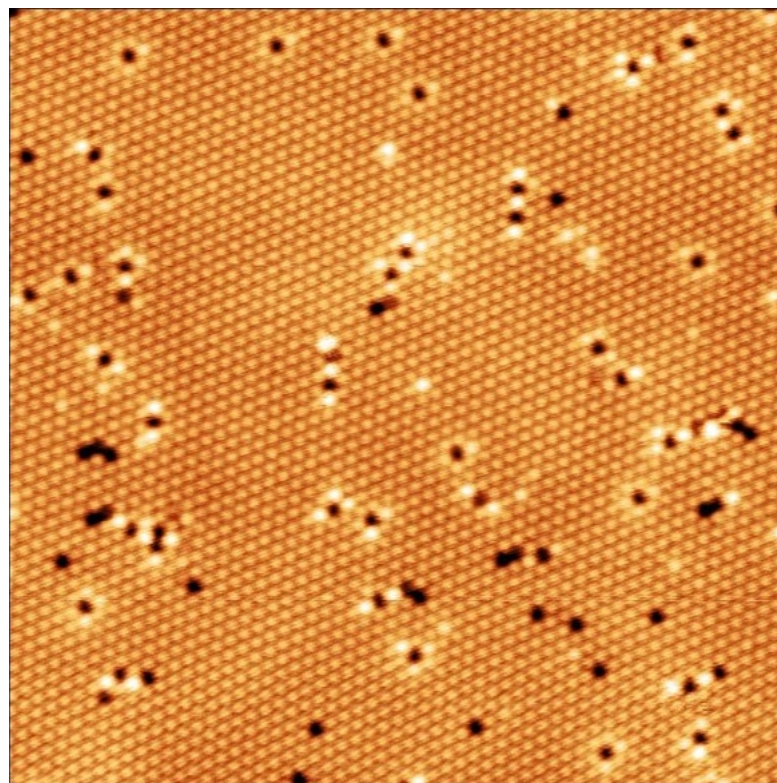
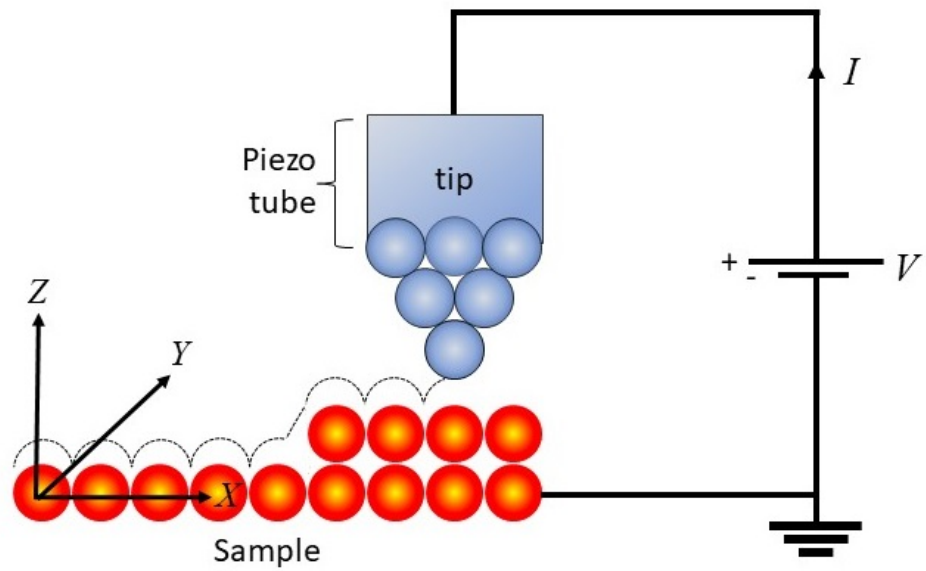


Fig. 2.7 a. Schematic view of the principle of the STM b. a $30 \times 30 \text{ nm}^2$ Atomic resolution image taken from the surface of $\text{Sn} - \sqrt{3}$

STS measurements at mK range. One example would be the thermal broadening of the measured superconducting gap between a Nb tip and Au(111) sample at elevated temperatures. Nb has a T_c of 9K and a superconducting gap of 1.47 meV at zero temperature. We can see in Fig. 2.8 that while at 300 mK the superconducting gap features are very sharp, increasing the temperature to higher values while staying below the T_c broadens these features because of reduced spectroscopic resolution and also because the gap becomes smaller above $T_c/3$ [40].

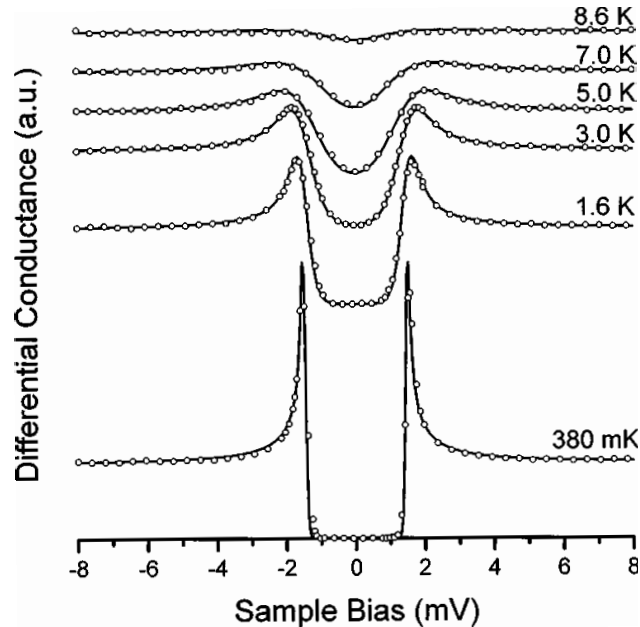


Fig. 2.8 Measured differential conductance spectra (circles) for tunneling between a Nb tip and a Au surface at several temperatures. The spectra are displaced vertically from each other for clarity. The solid lines are the calculated conductance using a BCS DOS with $\Delta_{\text{tip}}(0) = 1.47$ meV and the temperatures shown [40].

While measuring the I_T curves normally, there is a certain amount of noise that is also acquired. Since the LDOS is measured by differentiating the I_T curves with respect to V , a noise in $I(V)$ is strongly enhanced in dI/dV . Moreover, in the case of mechanical noise on the z axis, we obtain a noise on $I(V)$ which is proportional to I , this manifest in the dI/dV as a butterfly shape of noise that is almost negligible at low bias but quite problematic at high bias. During my thesis we have been fighting with this kind of noise that at some times was so large that we couldn't exploit the data for several months. Suddenly it almost disappeared with no explanation. Some amount of mechanical noise was still there and by changing some cables we recently obtained a big improvement on the noise level. In order to remove the noise we normally use a smoothing procedure using Gaussian filtering.

2.5.2 Spectroscopic Grid Measurement

Here we will explain the procedure used to measure the spectroscopic grids that are used to measure the spatial dependence of the density of states of the samples. To illustrate it better a schematic figure is presented in Fig. 2.9 which shows the grid spectroscopy measurement and data treatment procedure. The $I(V)$ curves are measured at each point of an $N \times N$ grid. This

grid is a reciprocal grid which is illustrated as green circles on top of the topographic image. All the $I(V)$ curves are measured at the same bias range $[V_{min}, V_{max}]$. After performing data treatment as mentioned before, differential conductance curves are obtained at each point of the $N \times N$ grid for the bias range. Now, if we choose a voltage V_i between V_{min} and V_{max} we can obtain the spectroscopic map by defining a $N \times N$ matrix that contains the $dI/dV(V_i)$ at each point. By doing this procedure for all the voltages we can find the local density of state maps at all the energies in the range of the measurement.

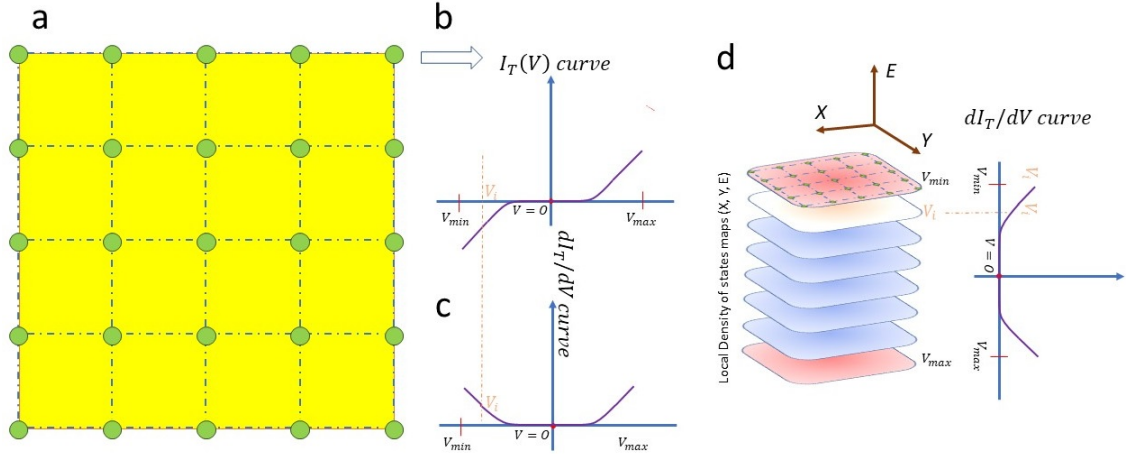


Fig. 2.9 a. Grid of spectroscopic measurements, $I(V)$ curves are taken at the grid nodes of a square grid. b. $I(V)$ curve measured at a node in the range of $[V_{min}, V_{max}]$. c. Derivative of the $I(V)$ curve corresponding to a. d. The density of states map constructed at different energies in the range of $[V_{min}, V_{max}]$.

2.6 Lock-in Technique

Lock-in amplifiers are common in experimental measurements as a technique in a noisy environment. Generally, a reference signal is introduced to an experimental parameter and a filter is used to extract the signal with the same modulation frequency. The working principle is explained as follows: A small high frequency sinusoidal signal, V_{ac} , is imposed to the constant DC bias voltage, which will then cause a sinusoidal response in the tunneling current. The amplitude of the modulated current is dependent on the slope of the $I-V$ curve. Fig. 2.10 shows how the convolution of the applied sinusoidal voltage and the resulting current can detect the changes in the $I - V$ curve.

For a small lock-in sinusoidal signal $V_{ac} = V_{max}\sin(\omega)$, the modulated current expressed in a Taylor series is as follows:

$$I(V_{bias} + V_{max}\sin(\omega t)) \approx I(V_{bias}) + \frac{dI(V_{bias})}{dV} \times V_{max}\sin(\omega t) + \frac{1}{2} \frac{d^2I(V_{bias})}{dV^2} \times V_{max}^2 \sin^2(\omega) + \dots \quad (2.11)$$

And by means of the lock-in amplifier which can demodulate and extract the first harmonic frequency, which is proportional to the differential conductance dI/dV . The inelastic modes

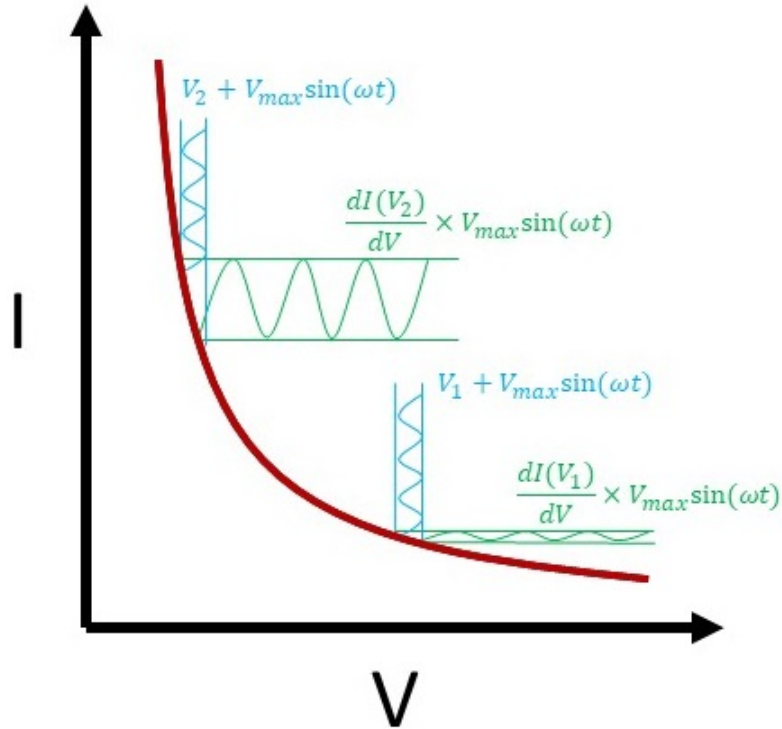


Fig. 2.10 schematic figure showing the dependence of the amplitude of the current on the slope of the I-V curve.

manifest by a peak in the second derivative d^2I/dV^2 and can be extracted from the second harmonic.

2.7 Spin polarized STM

If the tip that is being used to do STM is magnetized, the electrons with spins matching the tip's magnetization have a higher chance of tunneling, this effect is called tunnel magnetoresistance and the tip or the surface will act as a spin valve. The LDOS of the sample and the tip are different for different spin orientations, the tunneling can only occur between the states with the same spin orientation (without considering the spin flip). If the spin of the tip and the sample are parallel there are many available states for the electrons to tunnel resulting in a large tunneling current, however, if they are antiparallel most of the available states are already occupied resulting in a low tunneling current as it can be seen in Fig 2.11.

So, with spin-polarized STM (SP-STM) it is possible to probe the spin dependence of the LDOS and probe if a magnetic order is present. The lock-in technique is a convenient way to perform SP-STM since it can measure the LDOS at a specific energy, however, the energy range in which the lock-in is working should be in the range the spin contrast of the density of states is the highest. The spin texture of the sample's surface can be studied down to the atomic scale using this technique if the tip is chosen properly. There are several ways to prepare a spin polarized tip, in which the two most common ones are to either use a bulk magnetic tip or to deposit several layers of magnetic atoms on a non-magnetic tip (W tip). The bulk magnetic

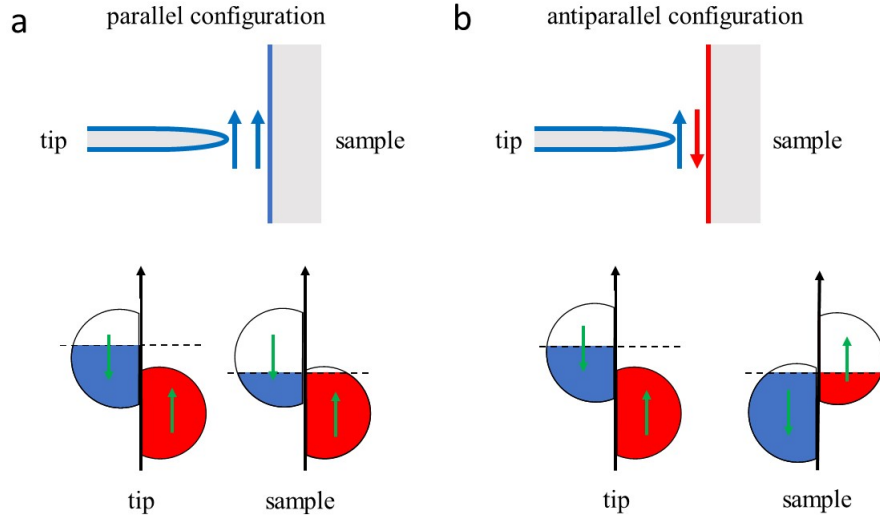


Fig. 2.11 schematic of density of states of the tip and the sample in a. Parallel spin configuration and b. Antiparallel spin configuration.

tip can be either ferromagnetic (Fe or Ni tip) or antiferromagnetic (Cr tip). Bulk Ni or Fe tips work very well as spin-polarized tips since the magnetization can be easily controlled, although Fe-coated W tips fulfill the same conditions however the magnetization can be easily lost due to crashes or bias pulses and these tips are also hard to make. It should be noted that since bulk ferromagnetic tips create a strong stray field compared to other types of spin polarized tips, they are suitable for systems that are robust against external magnetic fields like antiferromagnetic materials with strong exchange coupling. The magnetization in antiferromagnetic Cr tips cannot be easily controlled however they don't create any stray field and the magnetization of the sample is preserved [41]. During my thesis, we tried to perform some spin-polarized measurements with an electrochemically etched tip, but we couldn't get convincing results. Our goal was to be able to observe some predicted striped antiferromagnetic ordering in Sn/Si(111) monolayers where we expected to observe a doubling of periodicity with a magnetic tip.

2.8 Quasiparticle interferences and Fourier Transform STS

In this section the use of Fourier transform Scanning tunneling spectroscopy FT-STs to obtain information about Quasiparticle interference patterns is explained. This method is used to extract information about the band structure of the materials being investigated. In condensed matter physics, the electron inside a perfect crystal propagates with a wavefunction that contains a plane wave part and a periodic part:

$$\psi_k = e^{ikr} u_k(r) \quad (2.12)$$

Where $u(r)$ is a periodic function with the same periodicity as the Ionic lattice. However, if there are defects in the lattice structure the electrons will be scattered by the defects and the Bloch wave function will no longer belong to the basis for the wave functions of electrons

in crystalline solids. If we only consider elastic scattering, since, the energy of the electron is conserved after being scattered by a defect, the wave function of the electrons ψ_e is the interference of ψ_{k_i} and ψ_{k_f} , which are the electronic wavefunction before and after scattering, so:

$$\psi_e = \psi_{k_i} + \psi_{k_f} = e^{ik_i \cdot r} u_{k_i}(r) + e^{ik_f \cdot r} u_{k_f}(r) \quad (2.13)$$

And the local density of states, which is calculated by STS measurements as mentioned before is as follows:

$$|\psi_e|^2 = (e^{ik_i \cdot r} u_{k_i}(r) + e^{ik_f \cdot r} u_{k_f}(r))(e^{-ik_i \cdot r} u_{k_i}^*(r) + e^{-ik_f \cdot r} u_{k_f}^*(r)) \quad (2.14)$$

By multiplication:

$$|\psi_e|^2 = |u_{k_i}(r)|^2 + |u_{k_f}(r)|^2 + 2\text{Re} \left(e^{i(k_f - k_i) \cdot r} u_{k_i}^*(r) u_{k_f}(r) \right) \quad (2.15)$$

QPIs are plotted by calculating the Fourier transform of the density of the states map. So, by calculating the Fourier transform of $|\psi_e|^2$ (Eqn 2.15) we can quantify the QPIs. After some calculations, we will find that QPIs give a signal at scattering wave vector q up to a reciprocal lattice vector G and that the interference of the incoming and final state gives rise to the standing wave patterns of wave vector q . More details about the calculation are explained well in the thesis of Raphael Leriche [7]. Due to Fermi's golden rule, the probability of a scattering happening between the state k_i and the state k_f is as follows:

$$\Gamma_{i \rightarrow f} = \frac{2\pi}{\hbar} |V(q)|^2 \rho(k_i, E_i) \rho(k_f, E_f) \quad (2.16)$$

Where V_s is the scattering potential and $\rho(k_i)$ and $\rho(k_f)$ are the density of states of initial and final states, so, the more the density of states of the initial and the final states, the highest the probability of the scattering to happen. However, if there are a couple of initial and final states with the same scattering vector q , then the probability of the standing waves occurring at this energy will also be high.

By calculating the auto-correlation of the energy contour at a specific energy we can find the QPIs which is equivalent to joint density of states (JDOS).

In Fig. 2.12 and Fig. 2.14 some examples of QPIs are presented; in all of them the Brillouin zone is hexagonal since our system also exhibits hexagonal Brillouin zone.

Fig. 2.12 presents a circular energy contour centered at the center of the Brillouin zone (the Γ point). The wave vector \vec{q} shows good nesting properties since the points it connects are tangential to each other, the same is true about all the \vec{q} vectors with the same amplitude and different directions. The QPIs contour will be a circle with the radius $|\vec{q}|$ and centered at Γ .

One of the examples of such QPIs with circular pattern is the surface of Cu (111) [42]. The band structure of surface states of Cu (111) is parabolic as presented in Fig. 2.12. In the STM study done by Crommie et al. the interference of quasi-electrons leads to the formation of standing waves around defects (single atom, step edges) that manifests by ripples of periodicity $2\pi/|\vec{q}|$. If the ripples are formed around a point defect, the ripples will be circular and if they

are at a step edge, they will have a linear shape as illustrated in Fig. 2.12.

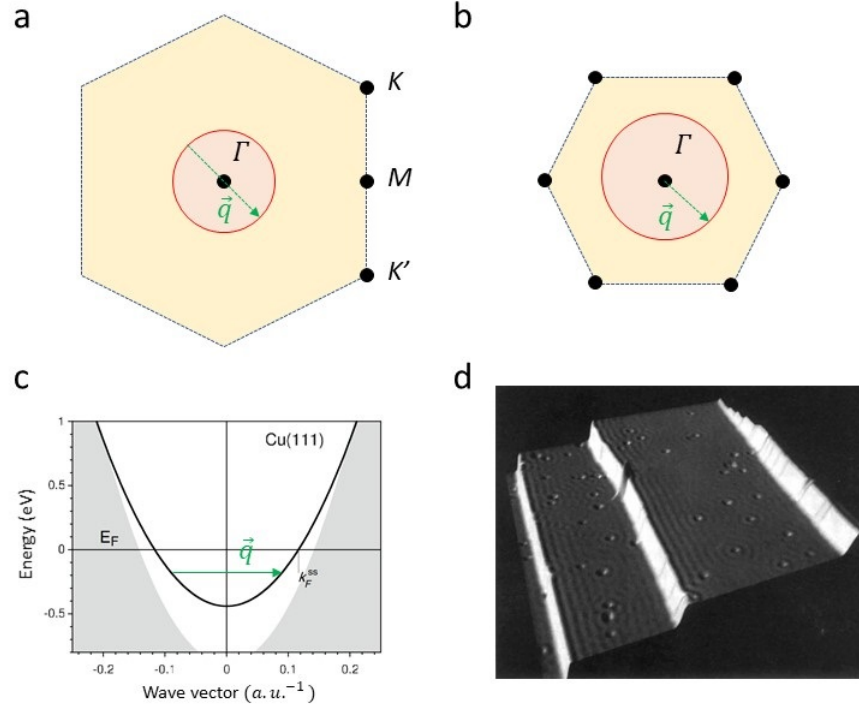


Fig. 2.12 a. The red circle is the energy contour of diameter q and centered at Γ . b. The expected QPIs pattern for 'a' which is the red circle with radius q and centred at Γ . c. The energy dispersion of the surface state of Cu (111). d. Constant current 50 nm \times 50 nm image of the Cu (111) surface showing standing waves around monoatomic steps and point defects.

The scattering channels depend on the symmetry and also on its spin properties. If there is a magnetic impurity on the sample it can change the spin of the incident electron. In this case, the incoming and outgoing electrons cannot interfere because they are orthogonal to each other so the QPIs will not occur. For example, the Rashba spin-orbit coupling splits the spin states of the surface states of Au(111). Thus the Fermi contour will split in two with two different spin directions as indicated in Fig. 2.13.a In this case the scattering only happens between the inner and outer Fermi contours with wave-vector, q_{intra} and there will be no intra-band scattering processes with q_{inter} and q'_{inter} , thus instead of having QPIs with 3 circles corresponding to the 3 wave-vectors indicated in Fig. 2.13.a will have only one allowed QPI pattern corresponding to

This was recently measured using Spin resolved ARPES but it can also be observed indirectly by QPIs measurements [43]. One way to see the Rashba band splitting is to measure QPIs scattering channels between epitaxially grown graphene flakes on Au (111) and the surface of Au(111) [44].

When the band structure is anisotropic the QPIs pattern becomes more complex. For instance, let us consider a hexagonal energy contour. As it can be seen in Fig. 2.14, \vec{q}_1 is the vector that connects two vertical lines of the energy contour which gives a stripe with a maximum intensity (in the middle of the stripe) positioned at q_1 in the reciprocal lattice. The middle

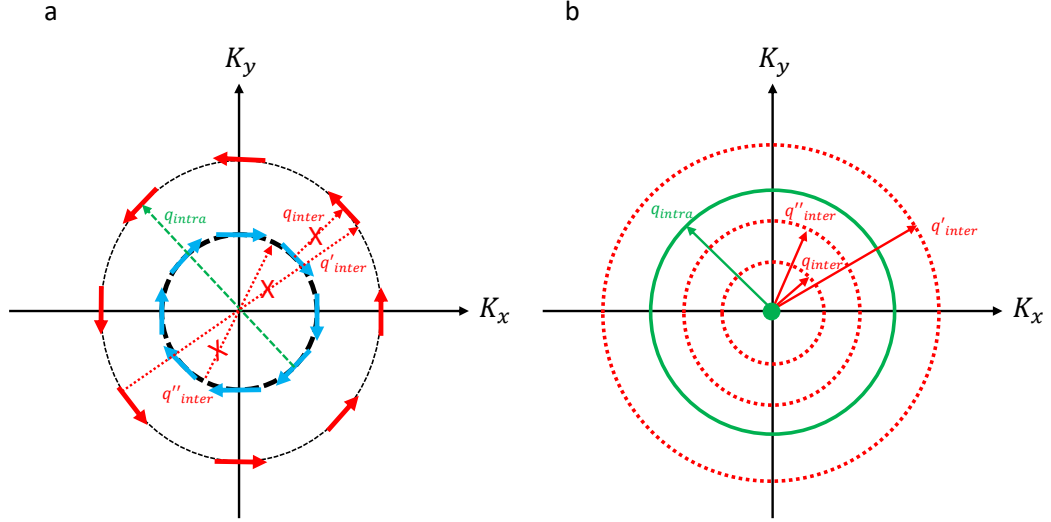


Fig. 2.13 a. Schematic Spin-split Fermi contour of Au(111) with two orthogonal spin directions showing an allowed scattering process with wave-vector q_{intra} and three unallowed scattering processes with wave-vectors q_{inter} , q'_{inter} and q''_{inter} b. The QPIs patterns correspond to allowed (green solid line) and un-allowed (red dashed line) scattering processes. The filled circle in the middle corresponds to the tangential scattering process close to $q = 0$.

of the stripe is of high intensity due to lots of $|\vec{q}|$ points that connect these two vertical lines, it's a kind of nesting effect. The intensity of the stripe fades by going away from the center of the stripe. The reason is that q_1 is the smallest wave vector that connects the vertical lines of the Fermi contour, thus it can bridge more points between them compared to other nesting wave vectors like q_R that are longer and have a rotation with respect to q_1 , as indicated in Fig. 2.14. The same is also true for $|\vec{q}_2|$ and $|\vec{q}_3|$ vectors. In addition to these scattering vectors on each line of the energy contour there are also allowed scattering processes, indicated in Fig. 2.14.a as $|\vec{q}_4|$, $|\vec{q}_5|$ and $|\vec{q}_6|$, here the wave-vector can take any length smaller than the straight line of the Fermi-contour that the scattering is happening, the smaller the wave vector the higher the intensity of the QPP due to more possible scattering processes, thus normally in the QPP pattern we should see a star like a feature with a maximum size of $|\vec{q}_4|$, $|\vec{q}_5|$ and $|\vec{q}_6|$ with an intensity that fades towards the end of the star.

In general, the band structure is more complex than just a circular or hexagonal shape and DFT calculations are needed to understand the complicated QPIs pattern. For instance, some experimental data for the system Pb/Si(111) – 3×3 reconstruction [45] are shown in Fig. 2.15. It shows an almost circular ring with a little bit of hexagonal modulation. It corresponds to the scattering between the inner and outer Rashba split Fermi surface. Indeed, due to the Rashba spin orbit coupling the back-scattering of outer-outer and inner-inner are not contributing to QPI signal due to the spin orthogonality. Note that there is also a star-shape pattern at low q that corresponds to intra-pocket (inner-inner and outer-outer) scattering for small scattering vectors, because here for small q transfer the spin are almost parallel in the inner band and also in the outer band. These QPI measurements are in perfect agreement with those estimated by DFT calculations, and hence it was used to validate that the DFT+U band structure calculation

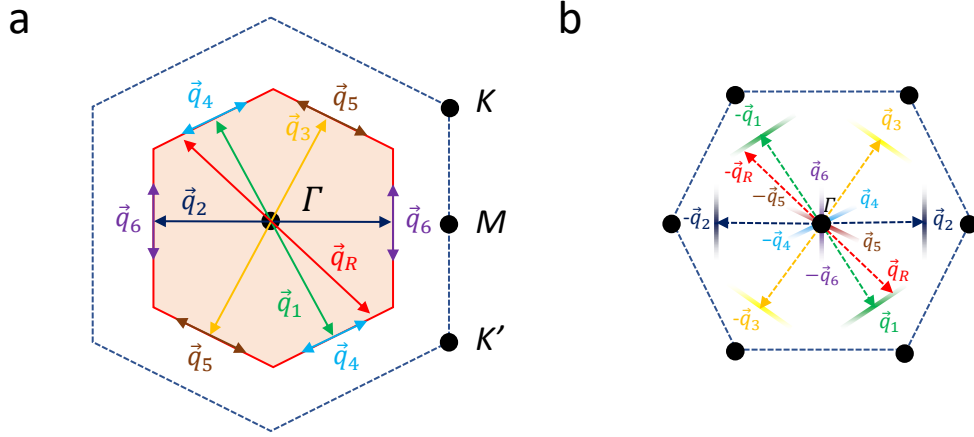


Fig. 2.14 a. The red hexagon is an energy contour with \vec{q}_1 , \vec{q}_2 and \vec{q}_3 being nesting vectors and \vec{q}_4 , \vec{q}_5 and \vec{q}_6 being an indication of nesting vectors on each line of the energy contour. b. The stripes positioned at \vec{q}_1 , \vec{q}_2 and \vec{q}_3 show the corresponding QPIs patterns of energy contour of a. And the star shape feature which is rotated 30° corresponds to the QPIs patterns of \vec{q}_4 , \vec{q}_5 and \vec{q}_6 .

was accurate in a much debated topic where some authors pretended that instead of DFT+U, dynamical mean field theory (DMFT) should be more accurate due to strong Mott-Hubbard interaction.

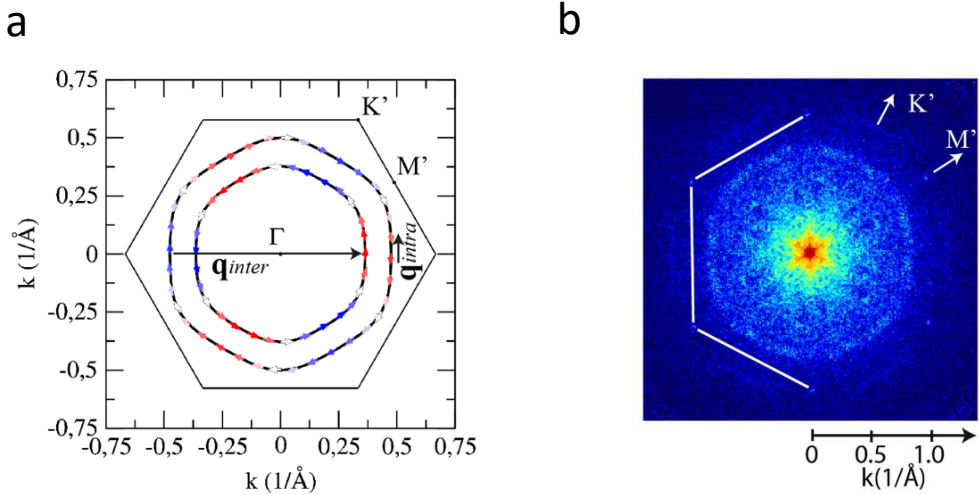


Fig. 2.15 a. DFT + U Fermi surface of Pb-3x3 / Si (111) including polarization (arrows). The out-of-plane component of the spin is 1% of the in-plane one. White arrows have 100 in-plane polarization. Blue and red arrows are opposite out of plane components. b. Symmetrized Fourier transform of a $60 \times 60 \text{ nm}^2$ dI/dV ($V = 0$) map measured by STS at $T = 0.3 \text{ K}$ and $B = 0.5 \text{ T}$, corresponding to quasiparticle interference at $E = E_F$ [45].

2.9 Experimental setups

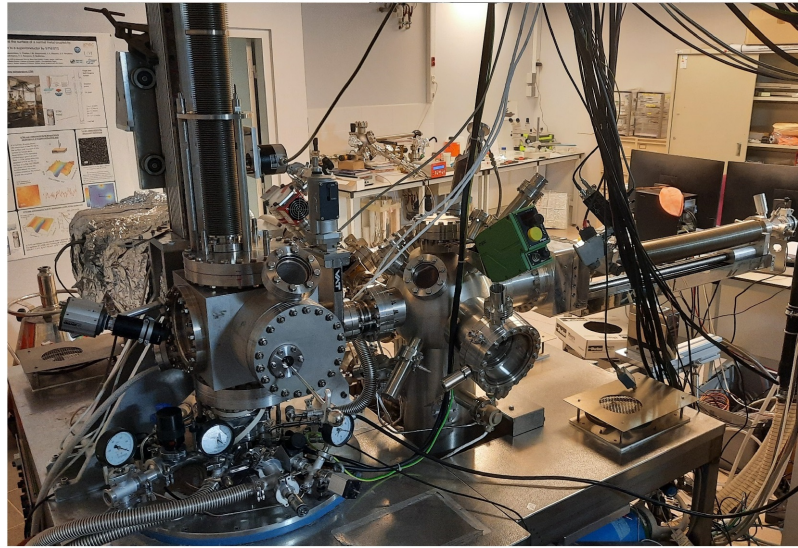
In this section, two experimental setups on which all the scanning tunneling measurements have been performed and presented in this manuscript are described. First, the M3 setup in which most of the measurements have been done is presented and after LT-STM in which sample preparations have been checked and verified is presented.

2.9.1 M3 setup

Fig. 2.16 presents photographs and a schematic picture of the M3 STM setup. This experimental setup is home-made and allows to perform STM/STS measurements under ultra-high vacuum, very low temperature (down to 300 mK) and under strong magnetic field (7T). This equipment is composed of two main chambers, a preparation chamber in which the samples can be prepared and an STM chamber in which the tips and the sample can be stored or put in the STM, cleaving the samples is performed in this chamber. Both chambers are under ultra-high vacuum and the base pressure inside them is around 10^{-11} mbar, which can be achieved after a bakeout at 150 °C and it is maintained over time through a combination of pumping systems that includes primary, turbomolecular, ionic, and titanium sublimation pumps. The whole setup is isolated from the mechanical vibrations by compressed air legs. High frequency noise is eliminated by means of dedicated electronic fibres. In order to transfer the samples and the tips to the UHV an extra chamber is attached to the preparation chamber called the load-lock. It is linked to a primary pump (which allows to reach a pressure of around 10^{-2} at first) and a turbo pump which further reduces the pressure down to 2×10^{-8} . A magnetic manipulator is used to transfer the samples/tips to the preparation chamber when the pressure is low enough. The load-lock can be only opened under an over pressure of nitrogen in order not to pollute the preparation chamber. There is a valve that separates the STM and the preparation chamber in order to keep the STM chamber clean while preparing samples in the preparation chamber. The preparation chamber contains among other components, a quartz microbalance (QCM) and a triple electron beam (omicron). It possesses three independent cells of high purity crucibles. The crucible is heated by electron bombardments and therefore a fraction of ionized atoms is produced during the evaporation. The evaporator thus, is equipped with a high voltage suppressor in order to suppress the ions created while the ionic bombardment, which helps to have less defects on the surface. The QCM is used to calibrate the deposition. A water-cooling system is used to stabilize the temperature of the evaporator during the deposition.

The preparation chamber is also equipped with a 4 axes Cryomanipulator which consists of two separated heating modules. One of them can heat the sample by means of direct heating (up to 1200 °C) and the other by means of resistive heating (up to 800 °C). The manipulator is also used to move the samples/tips from the preparation chamber to STM chamber. There is a carousel inside the STM chamber which allows the storage of several tips and samples. Those samples/tips can be moved inside the STM chamber by a wobble stick. The approach of the tip to the sample is controlled by the help of a camera filming the reflection of the tip and the sample. It is essential to approach the tip as close as possible to the sample in order to gain time on the fine approach which is done automatically by piezoelectric motors.

a



b

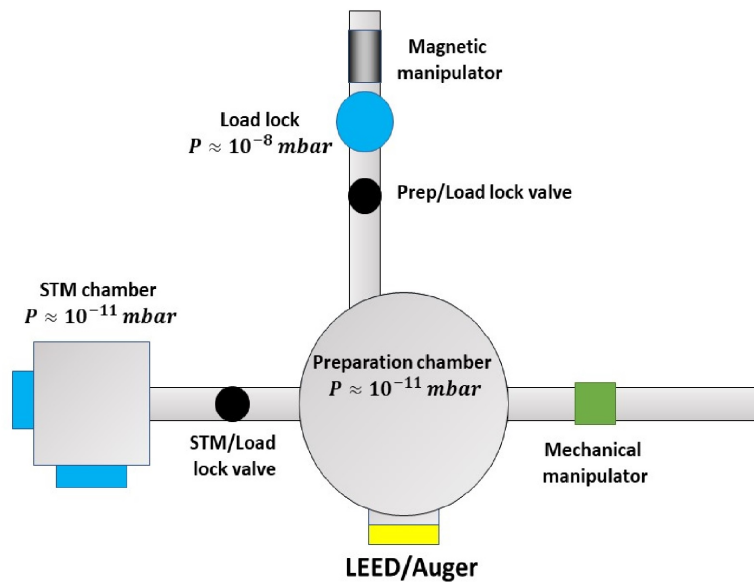


Fig. 2.16 a. Photograph and b. Schematic picture of the M3 setup

2.9.2 Cooling system

Once the tip approached near the surface the microscope is transferred down to a cryostat by means of a transfer rod (1.8 m) which is moved by a motor. The transfer rod is centered on the outer tube by means of several springs. The cryostat has a capacity of 60 liters and it can be either filled by nitrogen or helium. When it is filled by nitrogen it can be thermalized at 77 K or it can be stabilized at around 50 K by pumping on the cryostat. To reduce the temperature of the microscope to 4.2 K it is necessary to first pre-cool the microscope by nitrogen and then to remove all the nitrogen by means of gaseous ^4He . After, the cryostat can be filled with liquid

^4He . During the cooling procedure, the ^4He gas is put inside the IVC (internal vacuum can) in order to make a thermal contact between the ^3He pot and the cryostat. The ^3He pot is in thermal contact with the bottom of the microscope (^3He tail). Below 50 K the ^3He is absorbed by a sorption pump which consists of activated carbon, the pressure of the IVC thus, should be adjusted in order to have an exchange gas between the IVC and the ^3He pot allowing the microscope to stabilize at 4.2 K. next to the sorption pump is a pot which is connected to the ^4He bath through a capillary with a valve, called 1K pot. The reason why it is called a 1K pot is that, by means of pumping, its temperature can be reduced to around 1K.

Now the procedure to cool the microscope down to 300 mK is described. Before starting the cooling, all the ^3He is absorbed on the wall of the sorption pump. The sorption pump is then heated by means of a resistive heater to reach a temperature of around 50K. At this temperature all the ^3He is evaporated into the ^3He chamber. The temperature of the 1K pot is lowered by adjusting the valve down to 1.4-1.5 K. At this temperature the ^3He will start to liquidity in contact with the 1K pot and when the sorption pump temperature reaches 40 K it will start to absorb the ^3He , thus, lowering the pressure inside the ^3He chamber which consequently will lower the temperature of the condensed ^3He to 300 mK by means of cryocooling. The different elements of the cooling system are shown in the schematic Fig. 2.17.

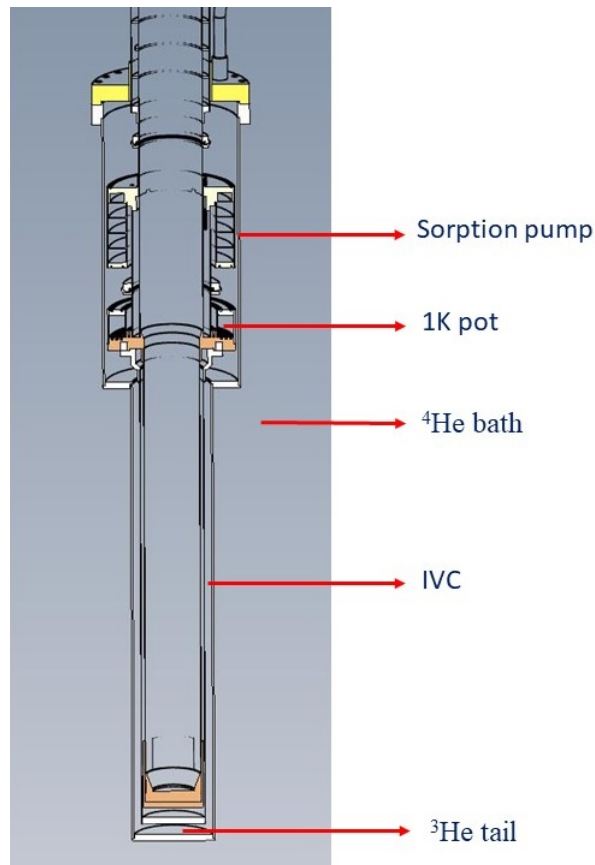


Fig. 2.17 Schematic image of M3 cooling system

2.9.3 variable temperature STM

In addition to the M3 setup another STM setup was used in this study called the VT-STM. The purpose of using this setup was mainly to perform structural study in parallel to the experiments on the M3 setup in order to optimize the best parameters of sample growth and preparation to be later used in M3 to do further study of the system. The reason for this arrangement is that growth studies are normally very time consuming and it is not reasonable to use very low temperature setup (M3) for these studies.

A picture of the VT-STM is shown in Fig. 2.18.a. Like M3, the experimental apparatus consists of two main chambers, the preparation and the STM chambers which both are under ultra-high vacuum. The samples are introduced to the preparation chamber by means of the load-lock. The base pressure of the two chambers is at 10^{-10} mbar which is possible after a bake-out at 150 °C and it is maintained with a combination of turbopumps, ionic pumps, and titanium sublimation. The same e-beam evaporation systems is also used here in order to deposit pure Sn and pure Pb on top of Si (111) and Ge (111) respectively. The chambers are also equipped with a manipulator which makes it possible to perform resistive and direct heating of the samples. The preparation chamber is also equipped with a LEED-Auger (SPEC). The manipulator also permits cooling the samples to nitrogen temperature by pumping liquid nitrogen inside it. The STM chamber hosts a variable temperature STM (Omicron VT-STM) whose head is shown in Fig. 2.18.b. This microscope can work in a range of temperatures from around 30 K to around 500 K and controlled pressures ranging from 10^{-10} mbar to 10 mbar.

The fact that this setup can work in environmental conditions, high temperatures and high pressure makes it a great tool to study physicochemical processes like the growth of materials and catalysts. As it has been mentioned before the STM is very sensitive to the tip-surface distance, thus having vibrations in the system can highly affect the results of the STM, that is why the VT-STM is mechanically isolated from the rest of the setup by means of copper support suspended by springs. The copper support is embedded in a magnetic field generated by fixed magnets. In these conditions, the oscillatory displacement of the conductor will induct current which according to Faraday's law can reduce the oscillatory displacements.

2.10 preparation of the samples

In this study all the samples were prepared in an ultrahigh vacuum, however, all types of tips were prepared outside the setup without any further preparation in an ultra-high vacuum. In the following, the different preparation procedures for samples and the tips are explained.

2.10.1 $(\text{TMTSF})_2\text{ClO}_4$

$(\text{TMTSF})_2\text{ClO}_4$ single crystals were obtained from our colleagues Denis Jérôme and Claire Marrache from Paris-Sud University. They were grown by the group of Patrick Batail from Angers laboratory. The crystals are small (length up to 1cm, width less or much less than 1mm, thickness few tens of microns) and extremely fragile. They should be manipulated very carefully. The surface of this sample should be cleaved inside the ultra-high vacuum to avoid any kind of contamination on the surface. The crystals were glued on a clean stainless-steel sample

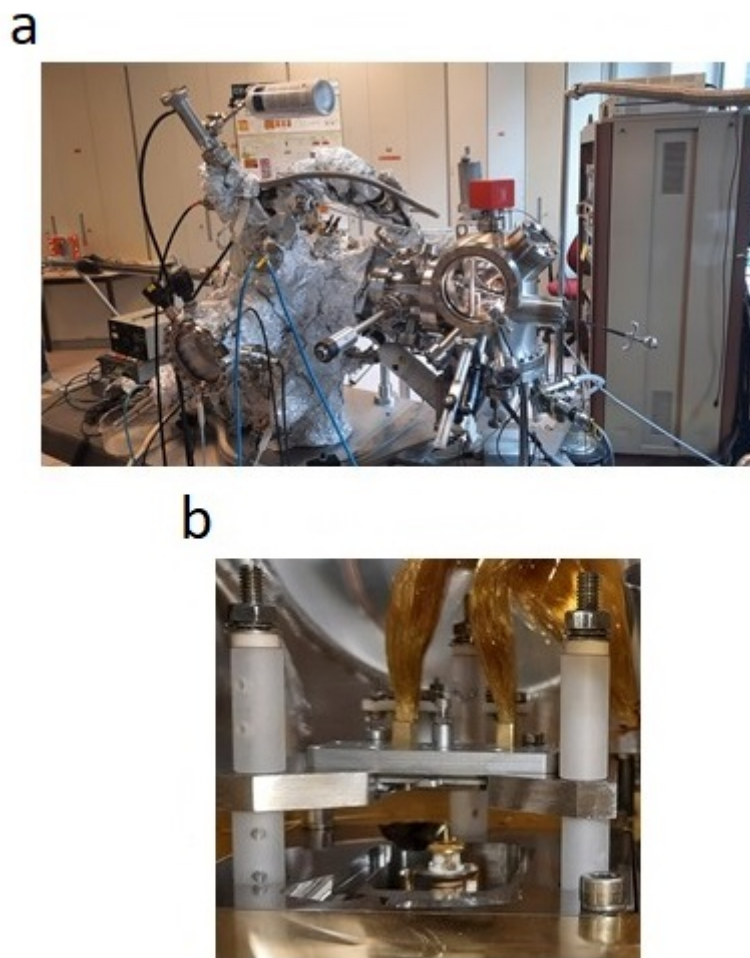


Fig. 2.18 a. A photograph of the VT-STM and b. The head of the VT-STM.

holder with a silver epoxy hardening at room temperature after one day. Then a flat piece of stainless steel is glued on top of the sample with the same silver epoxy and introduced in the load lock chamber. The sample was further transferred inside the STM chamber through the preparation chamber. The crystal surface was cleaved at room temperature in $P \sim 4 \times 10^{-11}$ mbar by removing the cleavage support with the wobble stick of the STM chamber. (Fig. 2.19)

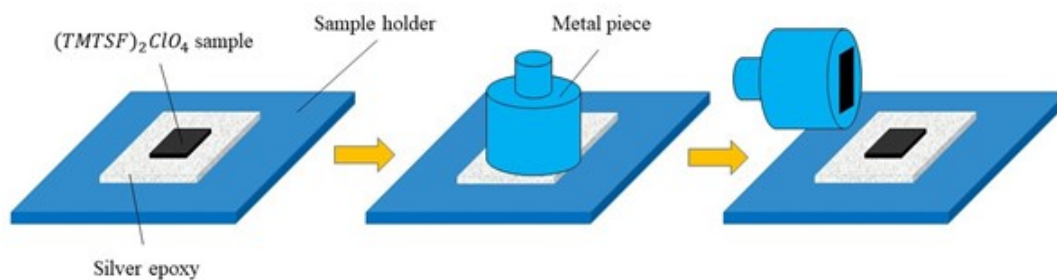


Fig. 2.19 Schematic picture explaining the cleavage procedure of the $(\text{TMTSF})_2\text{ClO}_4$ sample.

2.10.2 Sn/Si(111) (highly n doped)

In order to prepare a clean Sn/Si (111) surface, clean Si (111) surface should be first prepared. The n-doped Si wafer (111) highly doped with As with a resistivity of $0.003\text{-}0.004 \Omega \cdot \text{cm}^{-1}$ is cut to obtain a small piece after it is fixed between two electrodes. The sample is introduced into the preparation chamber and out-gassed at 600°C in the resistive stage to not exceed the pressures above 2×10^{-10} during the sample preparation process. After the sample is repeatedly flashed at $1150\text{-}1200^\circ\text{C}$ for $5 - 20$ seconds by means of direct heating. This will remove the covering oxide on the surface together with other contaminants. Finally, the reconstruction $\text{Si} - 7 \times 7$ is prepared by a last quick flash at 1000°C and cooling to 800°C and then further cooling down to 600°C . In about 20 minutes in order to obtain a large monoatomic terrace. After, in order to obtain the $\text{Si} - 7 \times 7$ reconstruction the sample is cooled down to room temperature. The Sn deposition is done by keeping the sample at 600°C . This is deposited while the ion suppressor of the e-beam evaporator is on. The flux is kept at $4 \mu\text{A}/\text{min}$ and the deposition is done in 2 minutes, in order to have slightly higher than $1/3$ ML of Sn over layer in order to ensure full coverage of the Sn. After the deposition has finished, the sample is annealed at 600°C for around 1 minute.

The excess Sn atoms will form other phases which are the $\text{Si}(111) - 2\sqrt{3} \times 2\sqrt{3} - \text{R}30^\circ - \text{Sn} (\text{Sn} - 2\sqrt{3})$ reconstruction and a glassy phase. While the first one is not well known the latter got a denser $4/3$ ML density and it is very well studied in the literature [46]. Both of these phases have semiconducting electronic properties.

The coexistence of these three phases is shown in Fig. 2.20.a The atomic resolution of $\text{Sn}-\sqrt{3}$ and $\text{Sn}-2\sqrt{3}$ are shown in Fig. 2.20.b and Fig. 2.20.c. As it can be seen the $\text{Sn} 2\sqrt{3}$ is grown either on the step edges or around the glassy phase and also $\text{Sn}-2\sqrt{3}$ contains fewer defects than the $\text{Sn}-\sqrt{3}$ phase. The number of defects on the $\sqrt{3}$ phase account for 2-3 % of the total Sn atoms. As it can be seen in Fig. 2.20.b the defects consist of Sn atom vacancies, Si substitutional atoms and dopant substitutional atoms. The properties of these defects are very well studied in the literature and will be discussed in more detail in Chapter 3. As can be seen in Fig. 2.20 the domains have an average size of around 200 nm, which makes them a perfect area to measure spectroscopic maps.

Note: if the sample is annealed at temperatures lower than 600°C (around 550°C) the structural domains are smaller as can be seen in Fig. 2.22.a, this can pose problems for further QPI calculations since in this kind of measurement large domains are required. At higher temperatures (around 700°C) the domains are larger (Fig. 2.22.b) however the number of defects is higher (Fig. 2.21.b), for this reason, it is very important to optimize the deposition parameters in order to have the least number of atomic defects together with largest domains which was observed for annealing temperature of around 600°C as it can be seen in Fig. 2.22.c and Fig. 2.21.c.

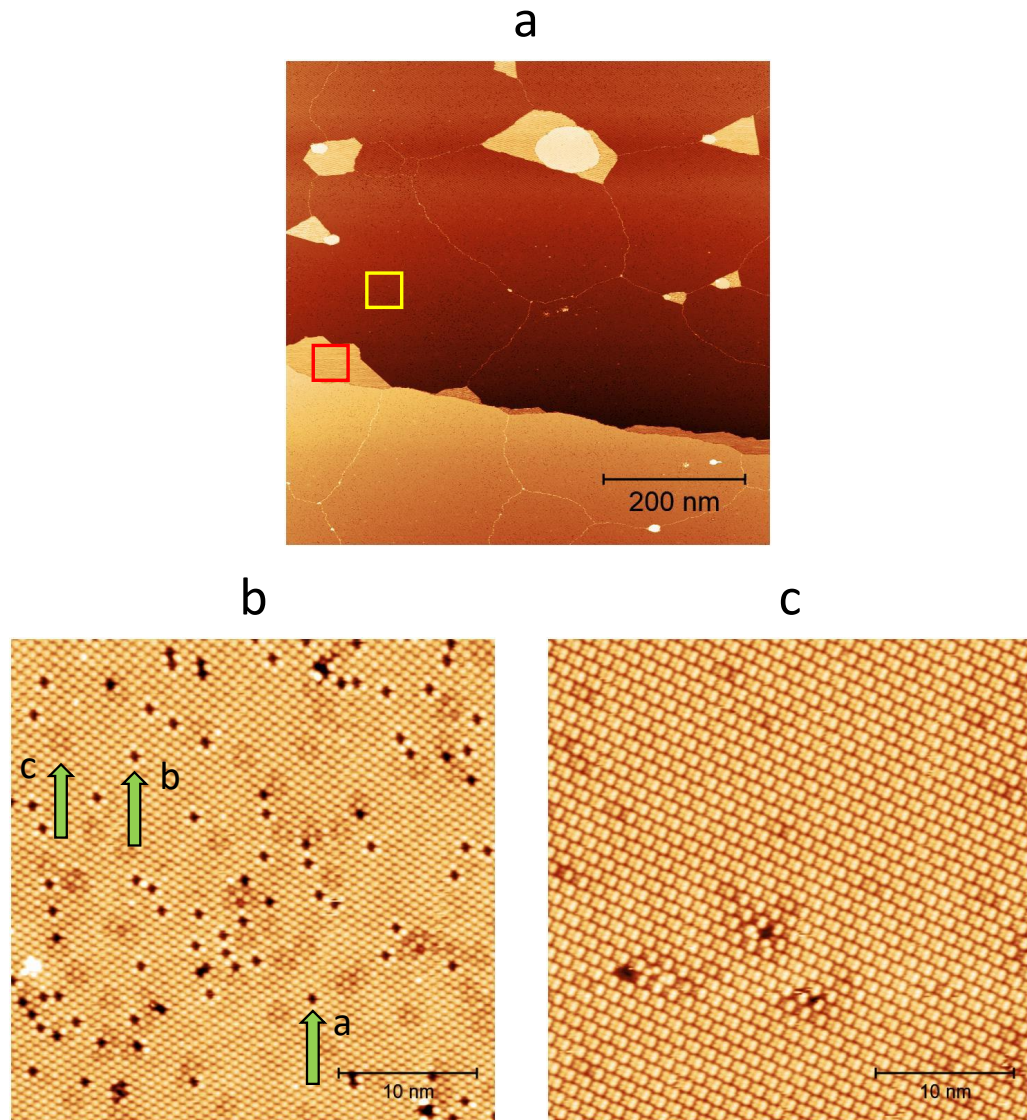


Fig. 2.20 a. Large scale topographic image of Sn/Si(111) showing different reconstructions b. Atomic resolution of Sn - $\sqrt{3}$ showing different defects (a) Sn vacancy, (b) Si substitution, and (c) dopant substitution c. Atomic resolution on Sn - $2\sqrt{3}$

Another parameter that plays an important role is whether the annealing was done at the same time as the Tin deposition or if it has been done only afterward. We have observed that to have the least amount of defects, annealing should be done at the same time as the Tin deposition, as can be seen in Fig. 2.23 we have also observed that extended annealing in both cases will not change the quality of the sample in terms of domain size and also the number of defects.

2.10.3 Shadowing effect

One of the problems that usually is faced in thin layer depositions is the shadowing effect which means that close to the electrodes that connect to the sample there will be no deposition because of the angle of the incident beam of the atoms as is shown in Fig. 2.24.a.

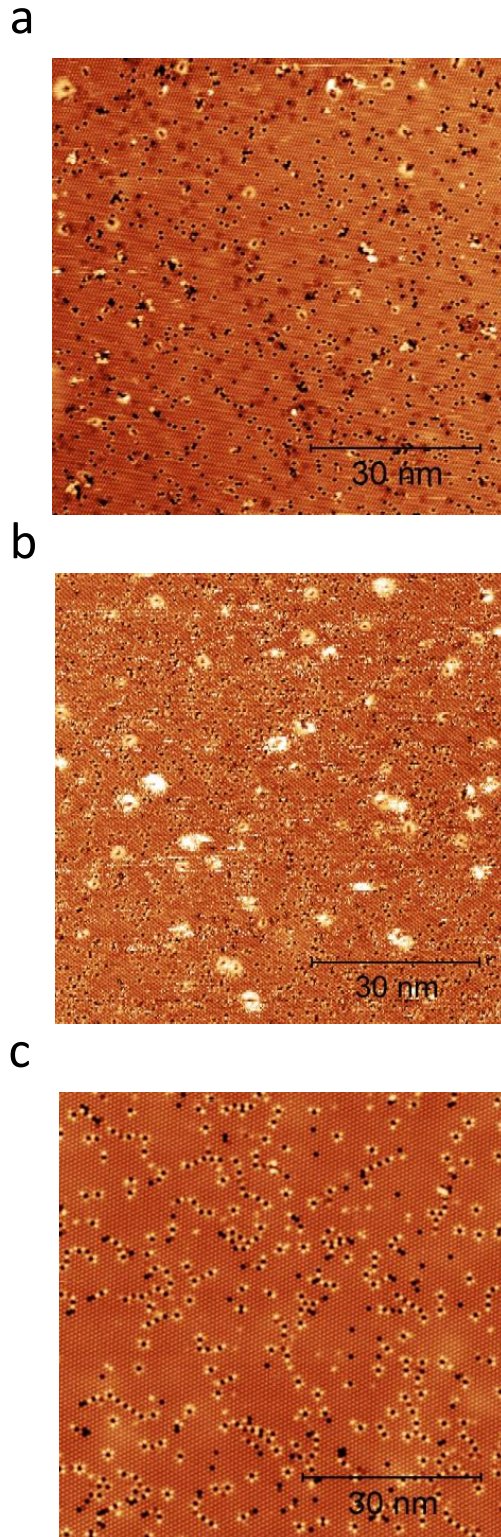


Fig. 2.21 Atomic resolution of $\text{Si}(111) - \sqrt{3} \times \sqrt{3} - \text{R}30^\circ - \text{Sn}$ phase annealed at different temperatures of a. 550°C , b. 700°C and c. 600°C

This situation can make a problem, especially in the case of n-doped silicon at low temperatures. The reason for this is that after the flashing the dopants will migrate from the surface

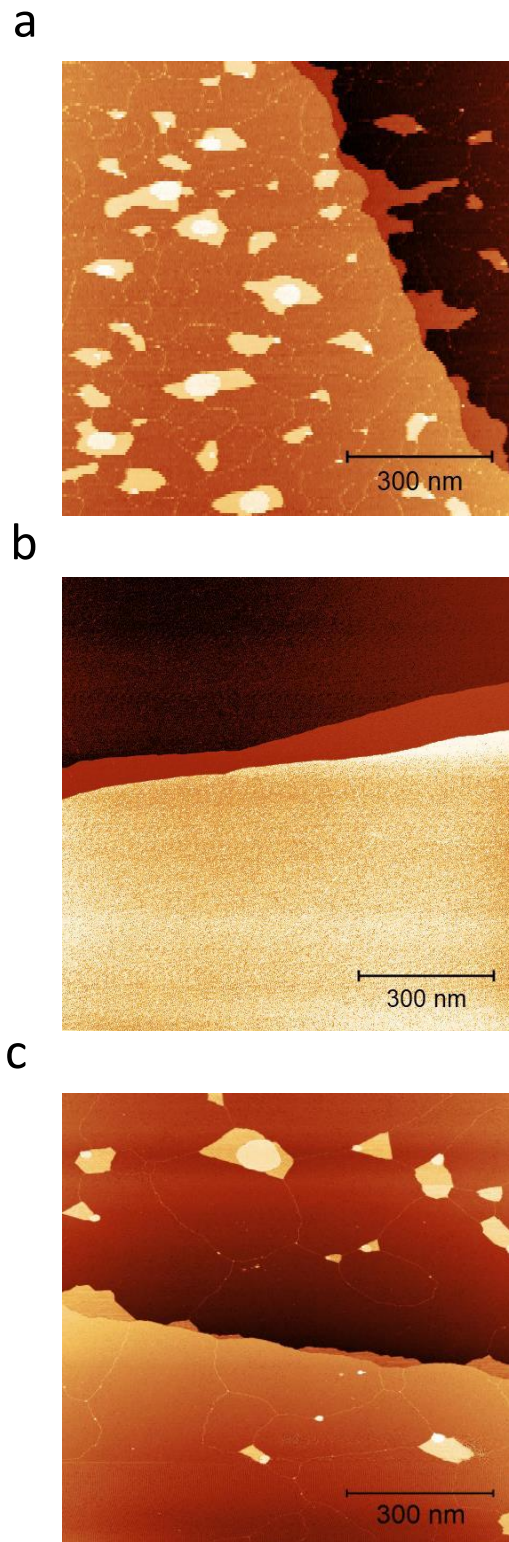


Fig. 2.22 Large scale images of $\text{Si}(111) - \sqrt{3} \times \sqrt{3} - \text{R}30^\circ - \text{Sn}$ phase with the same amount of deposition but annealed at different temperatures of a. 550°C , b. 700°C and c. 600°C

to the bulk of the sample leaving the surface with a very low number of dopants, which makes the surface insulating with a very large gap at very low temperatures, thus, having electrodes connected to the surface of the Si (111) and not to the deposited Sn atoms makes it impossi-

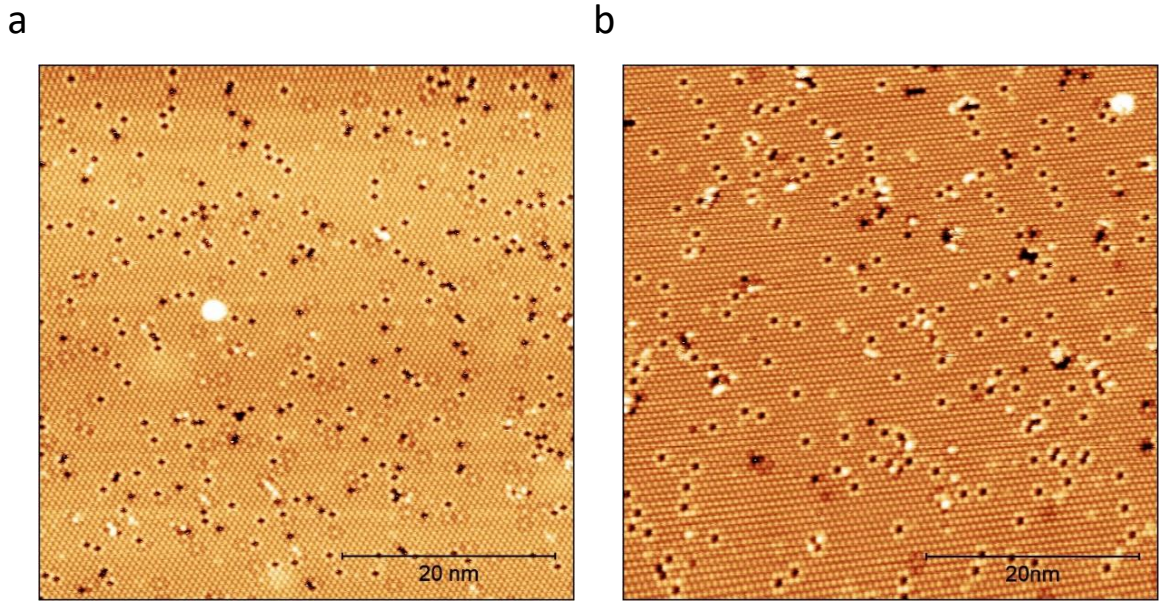


Fig. 2.23 Atomic resolution images of $\text{Sn} - \sqrt{3}$ phase annealed at 600°C in two different modes: a. At the same time as Tin deposition (for 1 min) and b. After the Tin deposition (for 2 mins)

ble to perform STM. This is especially true for the case of Si with low N doping. In order to solve this problem and anticipate electrical conductivity problems at low temperatures we have tried two different approaches, one of the electrodes which is connected to the colder part of the sample (to prevent evaporation) is connected to a region between the middle of the sample and the electrode through either a Pt wire (Fig. 2.24.b) or by depositing tantalum on one side of the sample (Fig. 2.24.c).

However, we have realized that by using either of these two configurations, the sample will be prone to contamination since the Pt and Ta ions will migrate over the whole surface of the sample making a different reconstruction and different electronic properties at the surface. As it can be seen in Fig. 2.25 in the case of the Pt wire a stream of Pt ions has created a silver line on the sample which depends on the polarity of the voltage applied while flashing the Si samples. The topographic image in Fig. 2.25 shows the regions with a new reconstruction related to this contamination that differs from the underlying 7×7 reconstruction, therefore it should be noted that this kind of contacts are not recommended in our studies.

2.10.4 Sn/Si (111) (highly P doped)

The goal is to prepare a $\text{Si}(111) : \text{B} - \sqrt{3} \times \sqrt{3} - \text{R}30^\circ - \text{Sn}$ ($\text{Sn} - \sqrt{3} - \text{B}$) sample which means the surface contains 1/3 ML of Sn on top of Boron doped Si (111) surface. The first step is to prepare $\text{Si} - \sqrt{3} - \text{B}$ samples, in order to do so highly P-doped samples (doped with Boron) with a resistivity of $0.001\text{-}0.003 \Omega \cdot \text{cm}^{-1}$ are outgassed in the preparation chamber and they are flashed at $1150\text{-}1200^\circ\text{C}$ for several times for about 5 to 20 seconds. After this procedure, the Boron dopants will segregate to the surface and a proper $\text{Si} - \sqrt{3} - \text{B}$ reconstruction can be seen on the surface. It should be noted that the top layer, in this case, is the Si atoms and not the

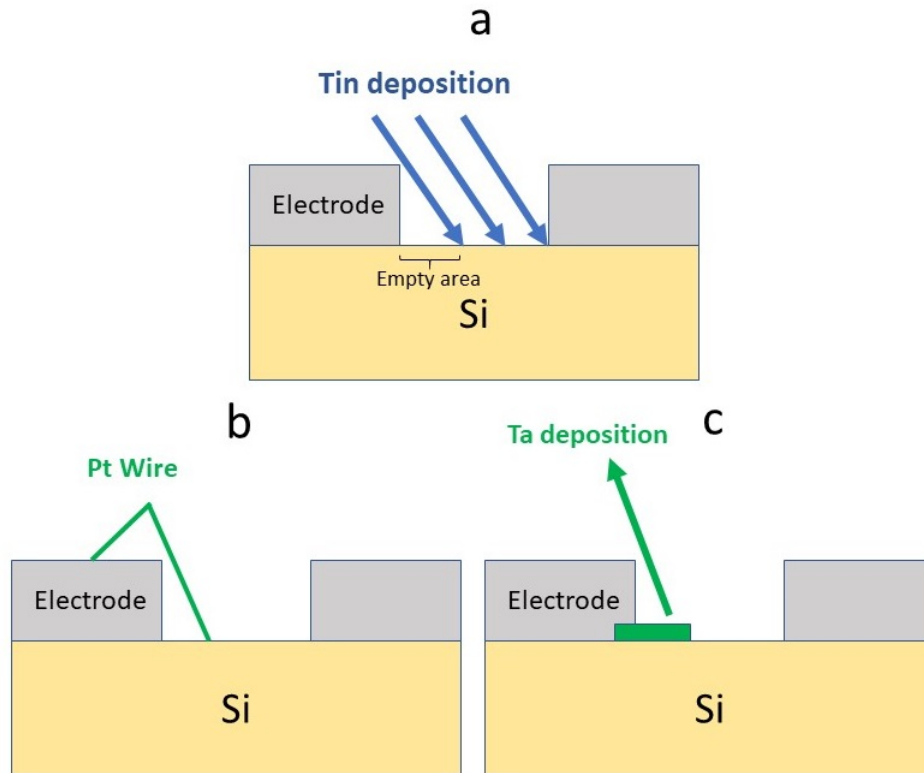


Fig. 2.24 schematic figure showing a.the shadowing effect close to an electrode and using b. Pt/Ir wire or c. Tantalum deposition reinforces the electrical connection between a deposited layer and the electrodes in order to surpass the shadowing effect

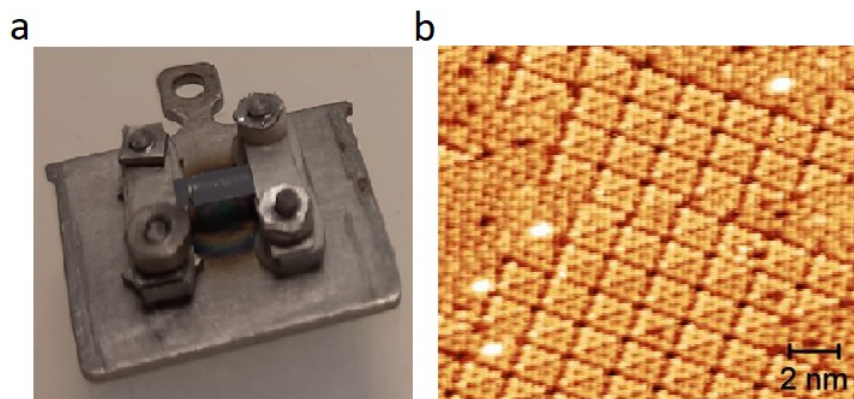


Fig. 2.25 a. Stream of Pt ions migrated over the sample leaving a silver line on the surface b. The new reconstruction on the Si(111) surface made by the Pt contamination on the surface

B atoms. A topographic image of the sample is shown in Fig. 2.27. After the flashing is done the sample is annealed and the deposition of Sn is done the same way that has been discussed for the highly N-doped sample.

On this sample, the $\text{Sn} - \sqrt{3}$ reconstruction is less stable than that of the highly n-doped samples. To solve this, we have tried to stabilize the $\text{Sn} - \sqrt{3}$ structure with the help of $\text{Sn} - 2\sqrt{3}$ regions because we have observed that close to the $\text{Sn} - 2\sqrt{3}$ regions the $\text{Sn} - \sqrt{3}$ reconstruction is more stable with much fewer defects, as can be seen in Fig. 2.27.b. It should

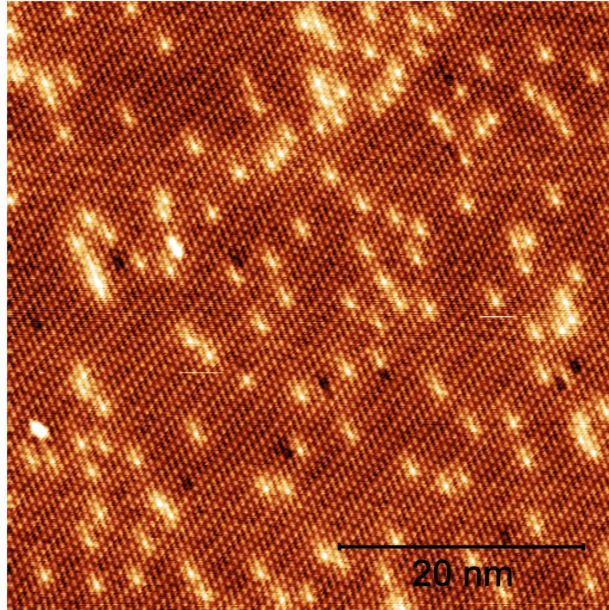


Fig. 2.26 Atomic resolution of Si(111) : $B - \sqrt{3} \times \sqrt{3} - R30^\circ$

be noted that in this case the deposition is done at the same flux as for the highly n-doped samples but for a longer time in order to have most of the sample being covered by the $Sn - 2\sqrt{3}$ regions. A large-scale topographic image is shown in Fig. 2.27.a.

Note: the time of the deposition should be adjusted carefully in order not to have excess Sn which can render the whole surface being covered by the $Sn - 2\sqrt{3}$ regions.

2.10.5 Pb/Ge(111)

To deposit 1/3 monolayer of Pb/Ge(111) we started by preparing a clean Ge(111) surface. To do that a p-doped Ge(111) wafer was mounted on a sample holder and fixed by welding Tantalum ribbons to the sample holder and on the sides of the Ge(111) sample. The sample was then introduced into the prep chamber and out-gassed at around 700 °c. we have started by preparing the Ge(111) sample in the VT-STM by several cycles of 1.5 KeV Ar^+ for 20 mins sputtering together with annealing at 750 °c for 5 mins (5-10 times) which resulted in a clean Ge(111)-c(2×8) reconstructing.

Then we tried to reproduce the same results in M3 setup. However due to the different geometry of the sputter gun (the distance to the sample was higher) we used a higher voltage for sputtering. By several cycles (5-10 times) of 3.0 KeV Ar^+ sputtering for 20 min and annealing at 800 °c for 5 mins in UHV, the Ge(111)-c(2×8) reconstruction was observed again. Fig. 2.28.a and Fig. 2.28.b show the large-scale and atomic resolution of the sample for 3.0 KeV Ar^+ sputtering which are the parameters we used at the beginning of the preparations. However, as can be seen in Fig. 2.28.a the size of the terraces is not large enough, which is due to the high voltage used for sputtering. So we have reduced the sputtering voltage to 1KV which resulted in larger terraces as can be seen in Fig. 2.29.

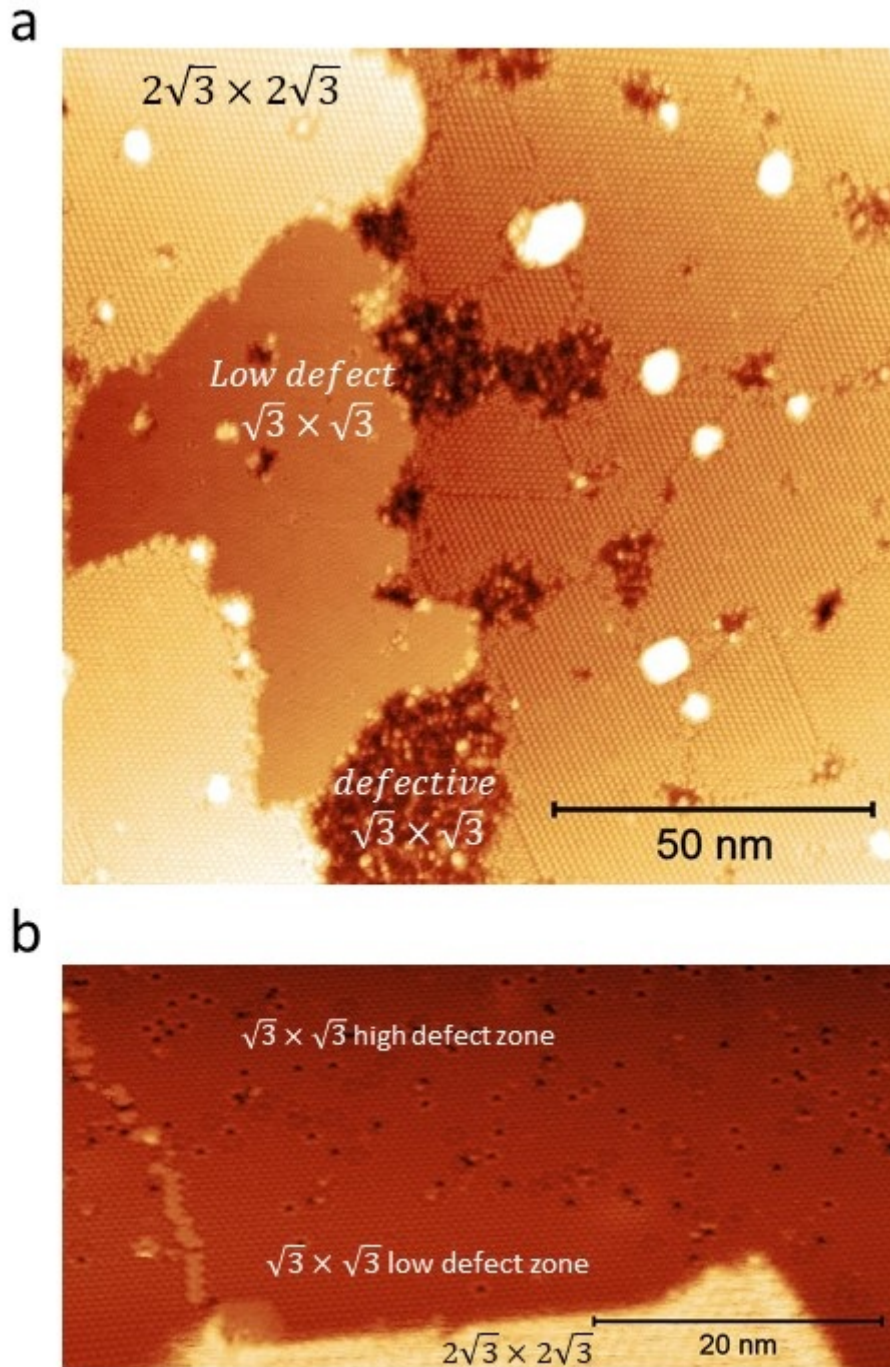
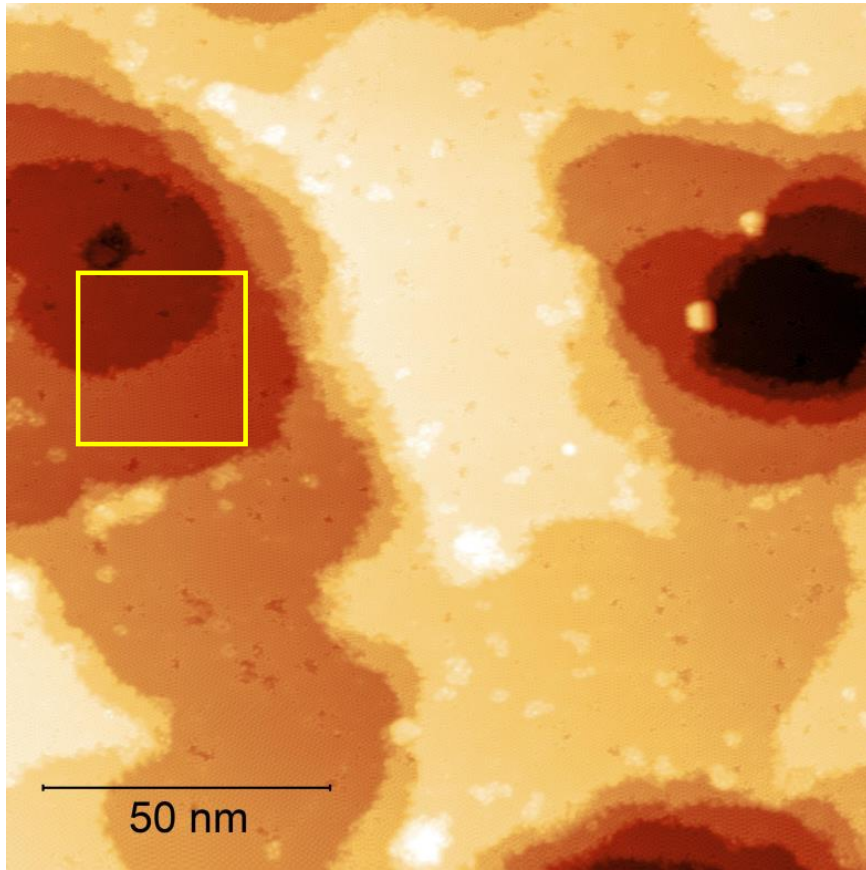


Fig. 2.27 a. Topographic image showing zero to no defects on the $\text{Sn} - \sqrt{3}$ regions which are grown next to the $\text{Sn} - 2\sqrt{3}$ regions b. Large scale topographic image of the $\text{Sn} - \sqrt{3} - \text{B}$ reconstruction

Pb was deposited on the clean $\text{Ge}(111)\text{-c}(2 \times 8)$ surface using an e-beam evaporator at room temperature (RT). The amount of deposition was determined by the deposition duration time at a constant evaporation rate. After that, the samples were annealed to get the desired reconstruction. Fig. 2.30 shows the phase diagram of the Pb/Ge(111) phase. As can be seen, there are two types of $\sqrt{3} \times \sqrt{3}$ reconstruction, the $\alpha - \sqrt{3} \times \sqrt{3}$ and the $\beta - \sqrt{3} \times \sqrt{3}$,

a



b

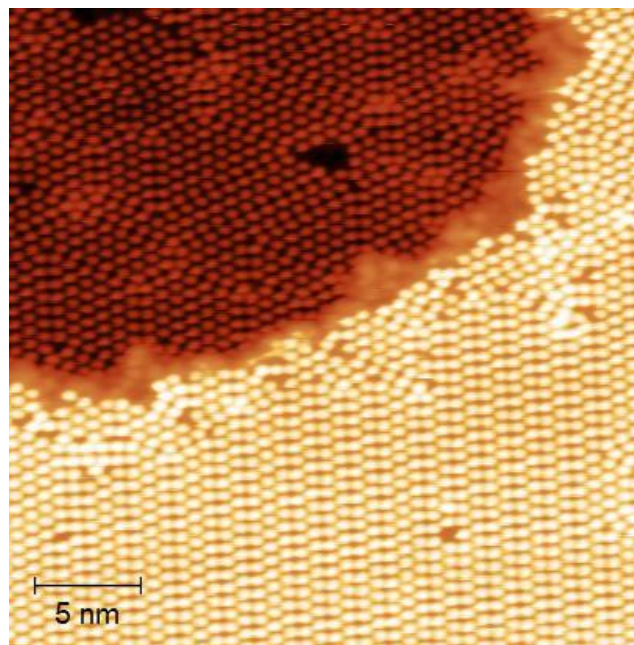


Fig. 2.28 a. Large scale and b. Atomic resolution of the yellow window shown in a of Ge(111)-c(2 × 8) surface prepared using 3KV as sputtering voltage

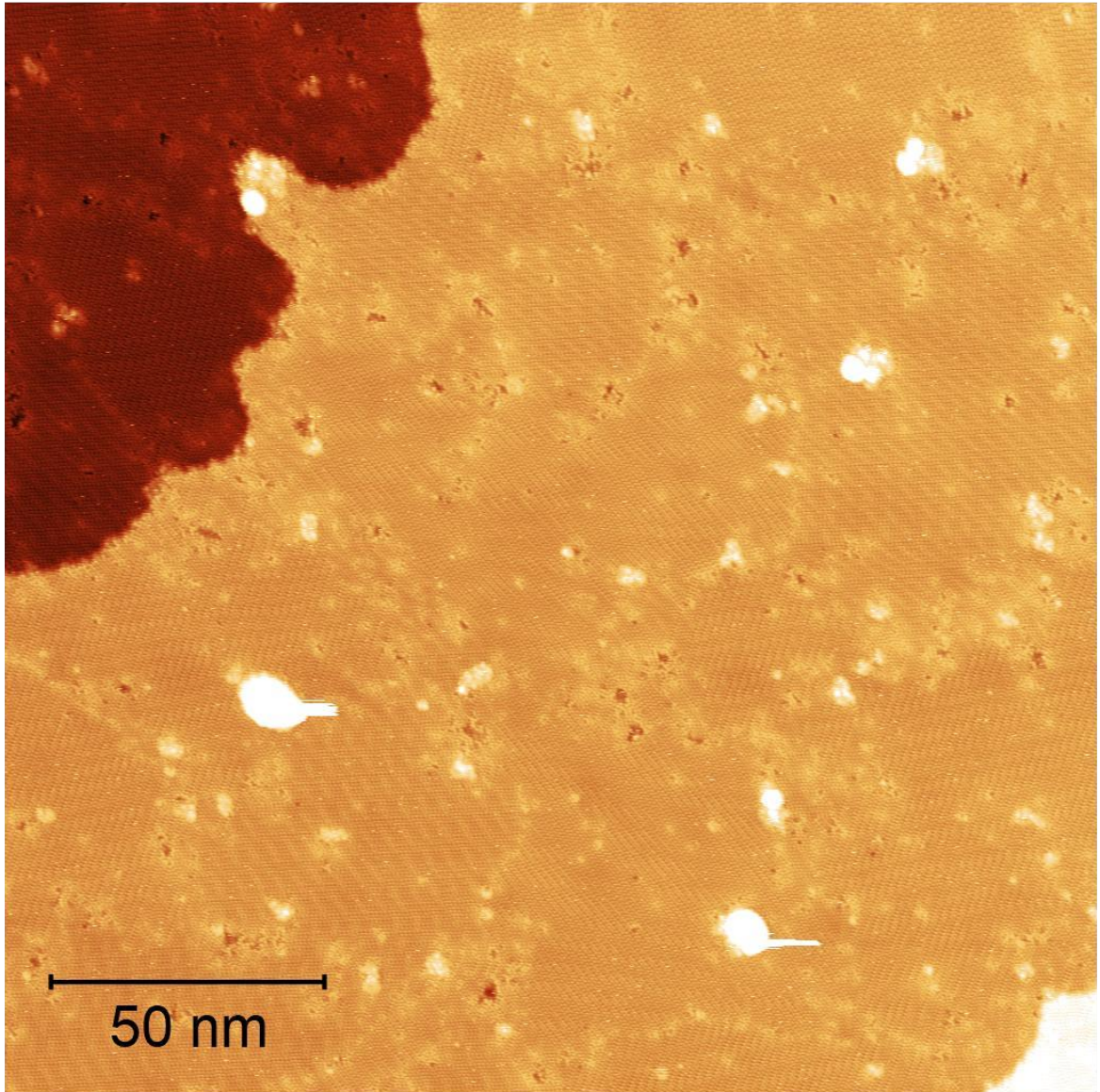


Fig. 2.29 Large scale image of Ge(111)-c(2 × 8) surface prepared using 1KV as sputtering voltage

which correspond to 1/3 and 4/3 monolayer of Pb/Ge(111). The aim of this thesis is to study the $\alpha\sqrt{3} \times \sqrt{3}$ structure. We deposited 1/3 ML of Pb on Ge(111)-c(2 × 8) at room temperature and annealed the sample at 200 - 250 °C afterward. Fig. 2.31 shows a large scale image of the $\alpha - \sqrt{3} \times \sqrt{3}$ structure in coexistence with denser $\beta - \sqrt{3} \times \sqrt{3}$ phase which means that the deposition is slightly in excess. The atomic resolution of the $\alpha - \sqrt{3} \times \sqrt{3}$ structure is shown in Fig. 2.32.

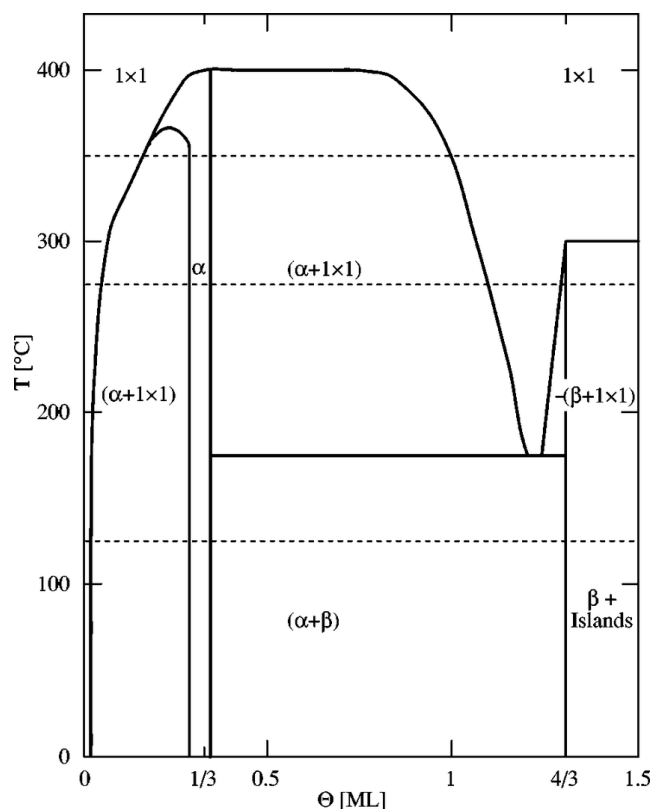


Fig. 2.30 Phase diagram of Pb/Ge(111) proposed by Grey [47]

2.10.6 Tip preparations

There are two main kinds of tips used in this study, $\text{Pt}_{0.8}\text{Ir}_{0.2}$ tips and Bulk Cr tips, while the latter is a spin polarized tip with antiferromagnetic order.

The $\text{Pt}_{0.8}\text{Ir}_{0.2}$ tips were simply cut with scissors to make their apex sharp enough, $\text{Pt}_{0.8}\text{Ir}_{0.2}$ are known to be a good choice for both topography and spectroscopic measurements. While the $\text{Pt}_{0.8}\text{Ir}_{0.2}$ tips are prepared easily the preparation of Cr tips are quite complex. In order to prepare the Cr tips first a solution of NaOH is prepared with the concentration of 1 mol/l. Then a circular shaped copper wire is put in the solution together with a Cr rod, which is put in the middle of the circle. After a voltage is applied between the copper wire electrode and the tip, which will etch the tip.

The tip is then sharpened by means of the etching and taken out from the solution before the part of the tip which is inside the solution is fully etched and after it is rinsed with water. To check if the tip is spin polarized it has been checked on a Co/Au (111) sample. The Co is known to form islands on top of the Au (111) surface and these islands are known to have a strong magnetic anisotropy which makes them to stabilize different magnetic in-plane directions. A topographic image of Co islands grown on Au(111) surface is shown in Fig. 2.33.a. However, while probing the surface of this sample using the lock-in technique, we couldn't see a magnetic contrast between the islands in the absence and presence of an external magnetic field. Fig. 2.33.b, Fig. 2.33.c and Fig. 2.33.d show dI/dV images taken at 600 meV and at external perpendicular magnetic fields of 1T, -1T and 3T, respectively. It can be seen that the magnetic

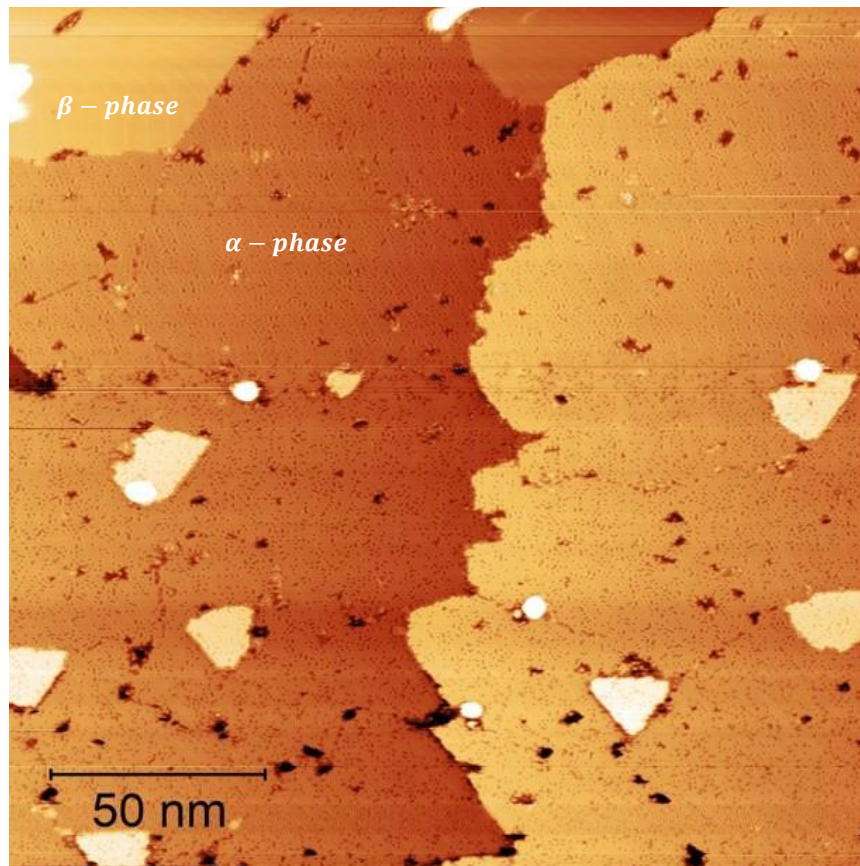


Fig. 2.31 Large scale image of $\alpha - \sqrt{3} \times \sqrt{3}$ phase in coexistence with the $\beta - \sqrt{3} \times \sqrt{3}$ phase

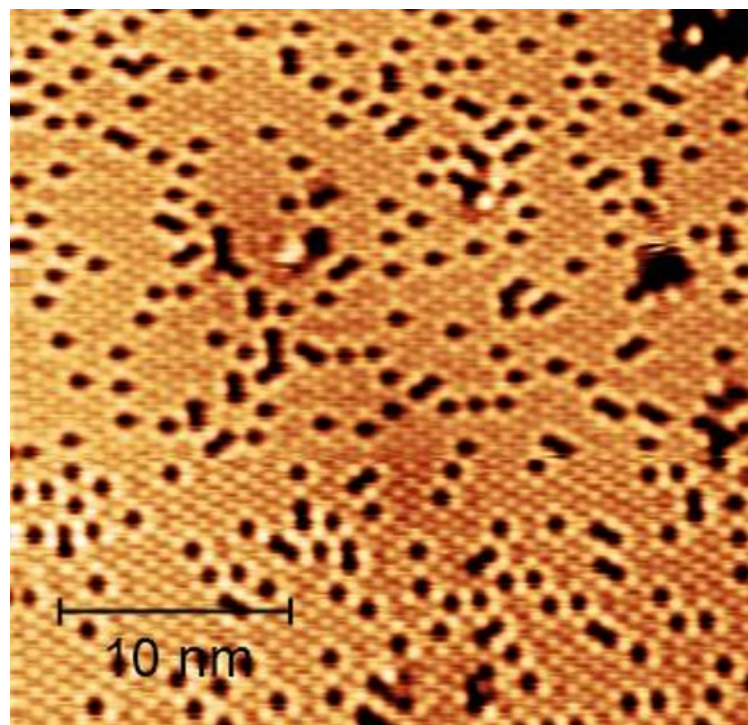


Fig. 2.32 Atomic resolution of $\alpha - \sqrt{3} \times \sqrt{3}$ phase

contrast can not even be seen in different magnetic fields and the dI/dV maps look all the same. This might be due to the fact that either our Co islands were too small to exhibit a stable magnetization at 4K, or our tip was not well prepared enough (i.e. pulsed) to exhibit a well-defined spin polarization at its atomic apex.

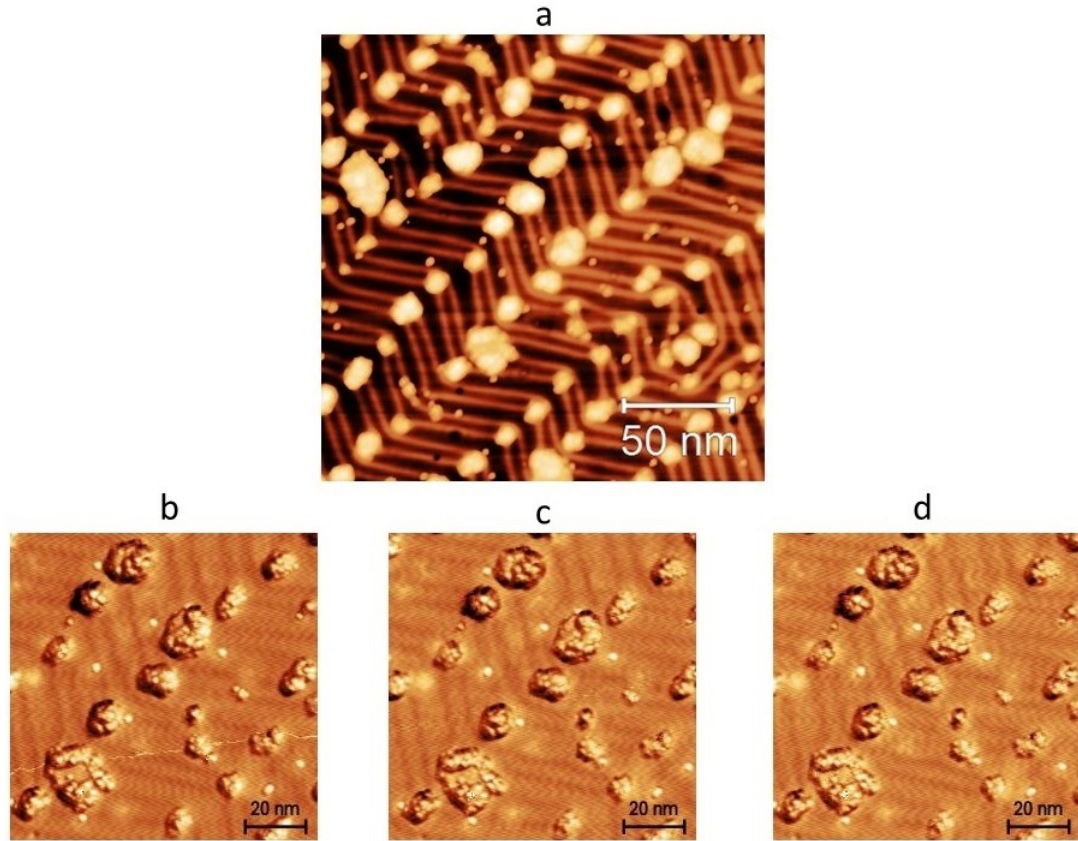


Fig. 2.33 a. Topographic image taken from the Co/Au(111) surface showing islands grown on the edges of the Au(111) herringbone structure and dI/dV map taken at 600 meV using the lock-in technique at external magnetic fields of b. 1T, c. -1T and d. 3T.

2.10.7 Nanonis electronics calibration

Since the electronics that control the M3 setup have been changed from Matirx to Nanonis, we have decided to calibrate the energy resolution of the electronics using a system that is the 2d grown Pb islands on Ge(111) and has a well-known superconducting gap dependence on temperature. Toyama et al. [48] have shown that different coverage of Ge(111) surface with islands shows different superconducting behavior. While 1 ML Pb/Ge(111) sample has a wetting layer with small clusters without any sign of superconductivity, 3 ML Pb/Ge(111) has a wetting layer with unconnected Pb islands with a T_c of 4K. However, if the surface is fully covered by a Pb thin film in the case of 10 ML coverage the superconducting temperature will be 6K.

For our purpose, we have used the more than 10 ML coverage of Pb/Ge(111). To produce the sample we have prepared 1 ML Pb/Ge(111) sample with the same procedure as described

before and shown in Fig. 2.31. Then more than 10 ML of Pb have been deposited on the sample at room temperature forming a continuous film of Pb/Ge(111) with different heights (Fig. 2.34). The different phases of the 1 ML Pb/Ge(111) sample can be seen as a "moire" on the continuous Pb film.

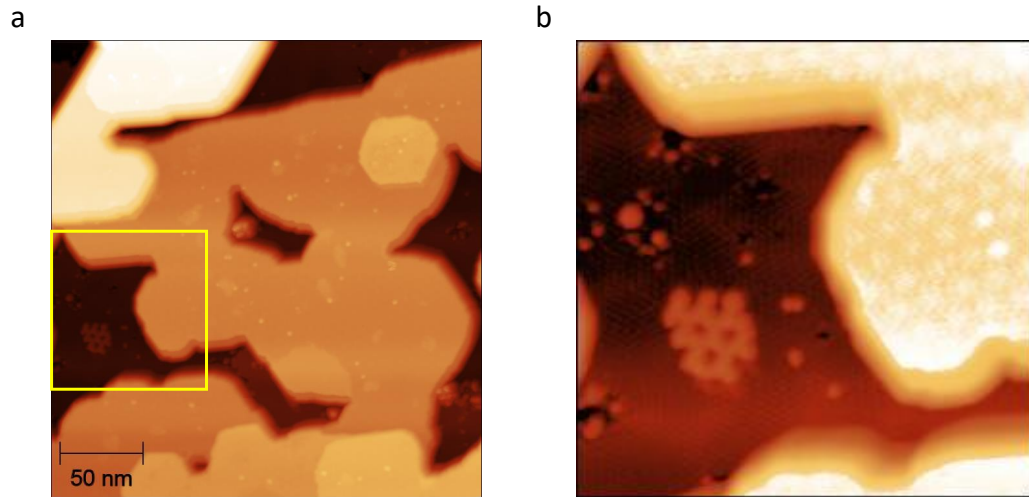


Fig. 2.34 a. continuous film of Pb/Ge(111) showing islands with different height and b. zooming in the window shown in a, to show a small patch of 4×4 on the left and the "moire" of the $\sqrt{3} \times \sqrt{3}$ structure that can be seen on the right part of the panel

In order to calibrate the energy resolution of the microscope we have performed spectroscopic measurements on the continuous Pb/Ge(111) film in an energy range close to the superconducting gap, as shown in Fig. 2.35 which exhibits spectroscopy measurements at approximately 380 mK. Note that this is a Superconductor-Insulator-Superconductor (S-I-S) measurement with a PtIr tip covered with a thin layer of Pb that was formed by digging Pb into the Pb film several times before the experiment. We have found that the STM was not very well grounded and that can induce a lot of voltage noise (jitter) and thus a lower energy resolution. The superconducting gap after improving the grounding of the STM is shown in orange in Fig. 2.35. The superconducting gap is now sharper. However the spectra shown on figure 2.35 are still not as sharp as one could expect for S-I-S spectroscopy. The best conductance peaks are only about 3 times higher than the normal conductance background while we would expect more than 5 if we consider the usual jitter of the apparatus which was measured to be around $30 \mu\text{eV}$ prior to my thesis. The base temperature of 300 mK was not achieved due to some change in the length of a tube that have been broken during my thesis and which length control the pressure of the STM cone and 1K cone. Too much pressure is applied on the STM cone and not enough on the 1K cone, this result in a bad thermalization of the wiring at the 1K cone. This might lead to a strong thermal load on the STM and a bad electron temperature which could lead to some broadening of the conductance spectra. Additional measurements in S-I-N and S-I-S will be needed once the fine tuning of the pressures on the cones will be properly achieved.

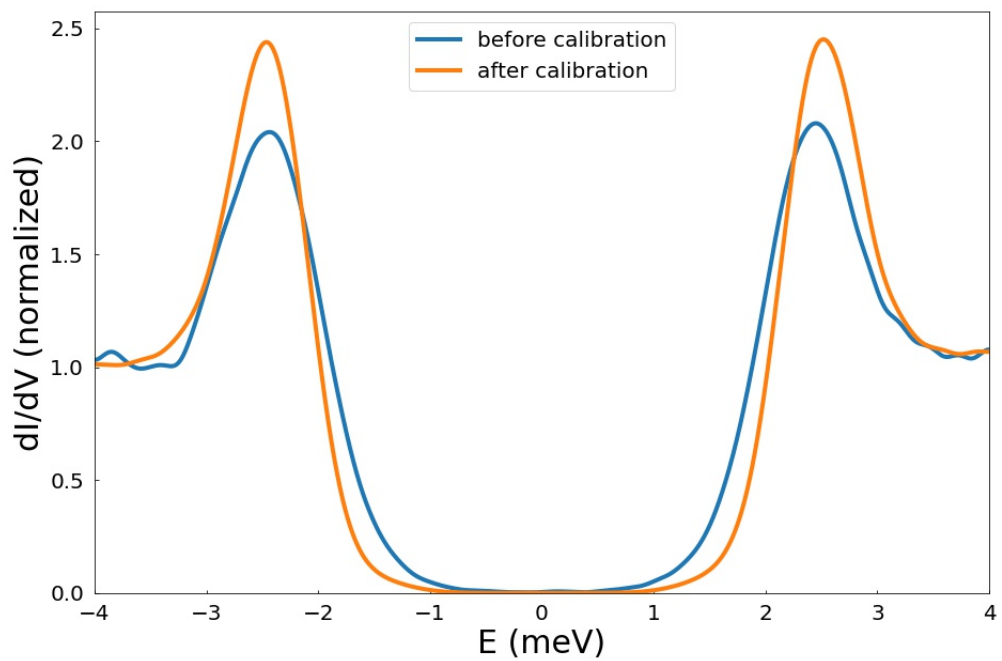


Fig. 2.35 S-I-S point spectroscopy at 380 mK on Pb/Ge(111) islands with a superconducting tip Pb/PtIr. The blue spectrum was measured before the appropriate grounding of the STM and the orange was performed with the correct grounding.

CHAPTER 3

Electronic properties of correlated diluted 2d layers of tetravalent metals on semiconducting surfaces

3.1 Introduction

In this chapter we are going to share our measurements on two remarkable phases of matter which are α -phase of Sn and Pb on Si(111) and Ge(111), respectively, with more emphasis on the former one. The reason for that is that there are many unanswered questions about the α -Sn/Si(111) for many years. One of them is: what is the ground state of this material in undoped regime, a Mott insulator or a band insulator? The reason why we think this is an important question is because recently on this phase an interesting superconducting state was observed upon hole doping. Such a doped Mott insulator that becomes a superconductor upon hole doping might be a model system for probing the physics of high-temperature superconductivity in Cuprates but with a much simpler structure that can pave the way to better understanding this exotic phase transition. That is why we think that understanding the ground state of the insulating α -Sn/Si(111) phase and confirming that it is related or not to a Mott insulating state is of fundamental importance.

We are going to shed more light to understand better the electronic properties of α -Sn/Si(111) by scanning tunneling spectroscopy at low temperatures which led us to propose that this material is in fact a magnetic band-insulator and not a Mott insulator, which is one of the most important result in this thesis, even if a bit deceptive.

unfortunately we couldn't perform measurements on the superconducting phase of this material because of technical problems and lack of time.

In this chapter first we will discuss the literature and give a general picture about 1/3 ML of Pb and Sn metals on top of Si(111) and Ge(111) which exhibit α phase and then we see how and why Sn - $\sqrt{3}$ was thought to be a Mott insulator and how it can transition to a superconducting state upon doping. Then we will expose our results in detail while comparing them to previous studies. Then, we will discuss some exotic phenomenon that we have observed on this material like: surface "molecules", edge state and multifractality.

At the end of the chapter we are going to also show some of our interesting measurements on the α -Pb/Ge(111) surface.

3.2 Previous studies

There is a huge on-going interest both from fundamental and applications perspectives to search for two-dimensional magnetic materials and in particular for antiferromagnets. One interesting way of getting antiferromagnets is to look for the low temperature ground state of correlated electronic materials exhibiting Mott physics [49], the cuprates materials being a characteristic example [50]. In the search for true two-dimensional materials, surface crystals appear very appealing as reference materials, as it was shown for instance recently in the context of two-dimensional superconductivity [51].

In this context attention was drawn to a class of correlated surface crystals, the so-called α -phase. It consists in a low density single-layer ($1/3$ Monolayer) of metal atoms (Pb or Sn) grown on semiconducting substrates like Si(111) or Ge(111), occupying the T4 sites of their surface [52, 53, 54]. The atoms are organized in a triangular lattice forming a $\sqrt{3} \times \sqrt{3} - R30^\circ$ reconstruction (the so-called α phase) in the high-temperature phase. Each tetravalent metal atom leaves a free electron leading to a narrow single half-filled electronic band confined at the surface and isolated from bulk bands, the DFT calculation without considering any correlations in this system shows a half filled band as can be seen in Fig. 3.1.

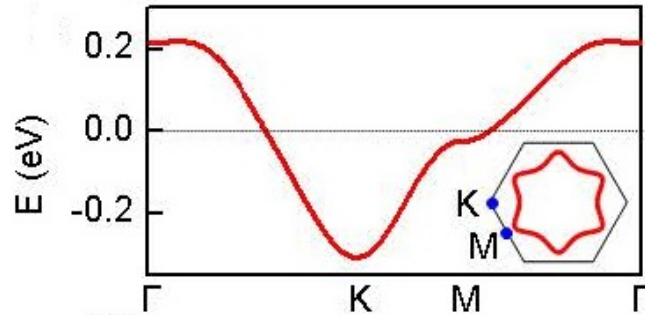


Fig. 3.1 Non-interacting dispersion of the dangling-bond surface state. The inset shows the Fermi surface in the hexagonal surface Brillouin zone. The high symmetry points are indicated [55, 56].

Due to the large nearest neighbor distance between Sn or Pb atoms, inducing an on-site Coulomb repulsion U larger than the electronic bandwidth, these materials were believed to be a well suited platform for the realization of the single band Hubbard model.

Experimentally a 3×3 reconstruction is observed at low temperature for all α -phase compounds except Sn/Si(111). While the Sn/Si(111) and Sn/Ge(111) show insulating behaviour at low temperatures, Pb/Ge(111) and Pb/Si(111) remain a metal with a pseudo-gap at low temperatures.

The origin of this 3×3 phase transition was under the debate and several model have been proposed, one suggesting the formation of a charge density wave triggered by the Fermi nesting at low temperatures for Pb/Ge (111) or by the correlation effects in the case of Sn/Ge(111) [57]. However, the defects play an important role [58] since the 3×3 phase nucleates around the defects even at the room temperature.

Several experiments have been done to reveal if there is indeed any difference in the elec-

tronic band structure of 4d core levels of Sn at RT and LT. However there has been no difference between the measurements at those temperatures and photo-emission spectroscopy didn't show any sign of Charge Density Wave (CD) at low temperatures [59, 60].

Surface diffraction patterns show that in the case of 3×3 both Pb/Ge (111) [59] and Sn/Ge (111) [61] show two different types of atoms with different heights. One atom top and two atoms down per unit cell.

In fact, in the less correlated materials Pb/Ge(111) and Pb/Si(111) that remain metallic, this aspect has been recently questioned by us [8, 9]. Our theoretical and experimental works showed that an accurate description of their metallic ground state with the 3×3 charge order should include the significant exchange interaction with the substrate atoms induced by the strong vertical hybridization between Pb and Si or Ge valence orbitals, in addition to the on-site repulsion term U in addition to the surface lattice degrees of freedom. In the more correlated materials Sn/Ge(111) and Sn/Si(111) that become insulating, the well-accepted theoretical description in terms of Mott-Hubbard physics was challenged by Lee et al. [62]. These authors argued that the strong vertical hybridization between Sn and Si or Ge valence orbitals renders the Mott-Hubbard modeling not appropriate as the exchange interaction with the substrate atoms plays a crucial role in determining different electronic and magnetic properties of the insulating ground state. This contradicting state-of-the-art requires a careful experimental characterization of the ground state regarding the charge, spin and lattice degrees of freedom, in order to finally enable deciding which theoretical description is most appropriate between DMFT-like methods only considering surface atoms and advanced DFT-like methods including substrate atoms.

3.3 Sn/Si(111) (highly n-doped)

In the following Chapter we focus on the more studied Sn/Si(111). Structure-sensitive measurements reported the absence of structural transition at helium temperature [63]. Angular-resolved photoemission (ARPES) results [64, 55] and STM/STS studies [65, 66] reported a strong reduction of density of states (DOS) at the Fermi level between room temperature and 77 K or 30 to 40 K, typically by a factor close to ten, accompanied by a transfer of spectral weight to lower binding energies. Nevertheless the DOS was found to remain finite at E_F in all these works.

Only two works, to our knowledge, reported spectroscopic results below 30 K at helium temperature by STS [65, 67], suggesting the possible opening of true energy gap of less than 100 meV at E_F . Modesti et al. [65] have done spectroscopy measurements at 5 K and they have shown a gap opening of around 40 meV in the dI/dV curves which they consider to be a phase transition to a Mott insulating phase as can be seen in Fig 3.2 (b and c). However, the validity of this measurement is under question since there is no large scale STM images shown in this work proving the purity and lack of any contamination on the samples, also, the best STM image, which is shown in Fig. 3.2.a is taken from a very small scale which contains defects. In fact as mentioned in Chapter 2 some of our Sn - $\sqrt{3}$ samples were contaminated by either Ta or Pt, and surprisingly in these contaminated sample we have observed a gap similar to the one reported by Modesti et al. [65].

As mentioned in Chapter 2, we have tried to improve the contact to the electrodes using either Ta deposition or Pt wire, which, resulted in a contaminated sample. While performing

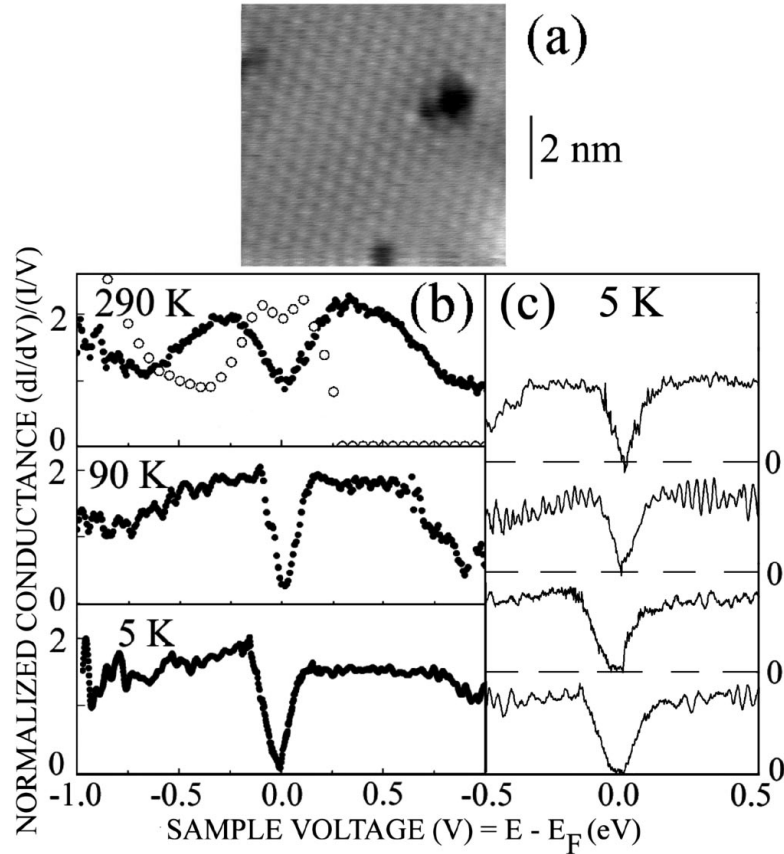


Fig. 3.2 a. Filled state STM image of the $\text{Sn} - \sqrt{3}$ at 5 K, sample bias -1.9 V, tunneling current 0.3 nA. b. Average tunneling spectra of the same surface measured far from the defects at different temperatures c. Single conductance spectra at 5 K [65].

spectroscopy measurements on this sample we have observed that the electronic structure and the gap looks similar to the aforementioned measurement at 5 K by Modesti et al. [65] as it can be seen in Fig. 3.3.b. The Fig. 3.3.a shows the surface of this $\text{Sn} - \sqrt{3}$ highly contaminated phase.

Also as can be seen in Fig. 3.4, in the work of Odobescu [67] a similar energy gap was measured but at 30 K, however we are going to see later in this chapter that indeed a phase transition to an insulating phase can happen at temperatures lower than 30 K. These two aforementioned works are the basis to some misleading interpretations, one example would be the recent work by Weitering [66], in which they assert that the $\text{Sn} - \sqrt{3}$ is a Mott insulator. The authors note that they could not perform measurement in the case of highly n-doped samples at 4 K, but only at 77 K, due to the fact, according to them, the system was experiencing and Anderson localization at low temperature making it unsuitable for scanning tunneling spectroscopy. We will see that this Anderson localization on top of a Mott insulating phase is not a correct interpretation as we are going to explain in the next subsection. We will also explain why we believe that their assumption of a Mott insulating ground state for this system is wrong.

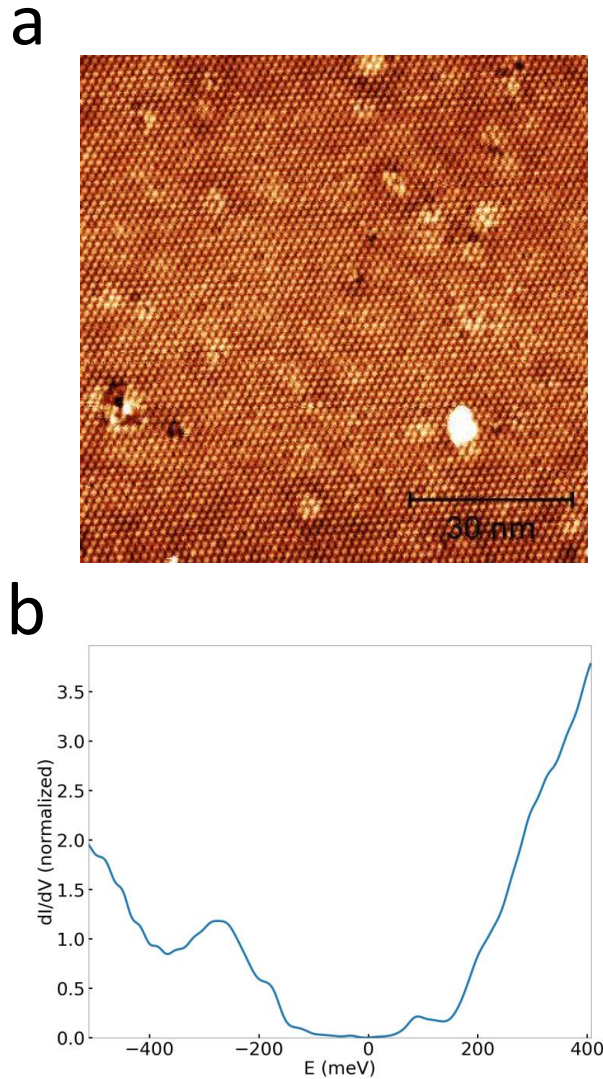


Fig. 3.3 a. Topographic image taken from the $\text{Sn} - \sqrt{3}$ surface in a $100 \times 100 \text{nm}^2$ window b. Average spectra of the map taken in the area shown in a.

3.3.1 Is $\text{Sn}/\text{Si}(111)$ a Mott insulator?

As can be seen in Fig. 3.5 Weitering et al. [66] have shown that by doping the $\text{Sn} - \sqrt{3}$ systems with holes, starting from the undoped sample (n-0.002 corresponding to highly n-doped $\text{Si}(111)$ substrate), subsequently to a saturated hole doped sample (indicated by $\text{B} - \sqrt{3}$ corresponding to a highly P-doped $\text{Si}(111)$ substrate) at 77 K a pick in DOS starts to appear. In this figure the DOS curves are fitted using several Gaussians corresponding to the Si edge band, higher and lower energy Upper/Lower Hubbard Bands (UHB/LHB) and also a Quasi Particle Peak that becomes bigger at higher dopings.

The UHB and LHB look very similar, however the spectral weight of the UHB decreases with hole doping of the substrate, while the relative spectral weight of the LHB remains constant. At the same time, the spectral weight of the QPP increases monotonically with increased hole doping. A similar behaviour was predicted by Menders et al. [32] and was discussed in Chapter

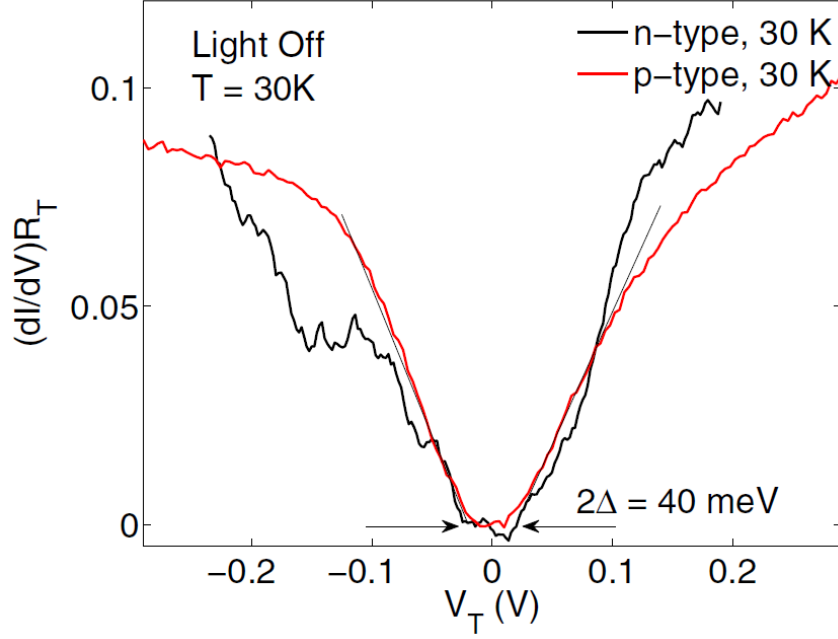


Fig. 3.4 STS spectra in the vicinity of the energy gap developed at the Fermi level on the $\text{Sn} - \sqrt{3}$ surface for n- and p-type samples. Set point parameters are $V_T = -2\text{V}$, $I_T = 50\text{pA}$ for the n type and $V_T = 1.8\text{V}$, $I_T = 50\text{pA}$ for the p type [66].

1, however, the correctness of this assumption is questionable since in the calculations [32, 33] it has been predicted that the UHB is detached from the QPP and also the QPP should be positioned at the Fermi level. In the measurements of Weitering et al. the QPP appears at about 100 meV, and the putative UHB is overlapping with the QPP while we would expect an overlap of LHB with the QPP in the case of a hole doped Mott insulator as shown in Chapter 1.

Another contradictory point is that in the case of a hole (electron) doped Mott insulator, the QPP intensity should only be considered at the energies higher(lower) than the Fermi level, while they have considered the intensity of the whole peak to calculate the amount of doping.

Also, there is one point that still remains unclear, Weitering et al. [68] used DMFT measurements of Meinders et al. [32] as reference to calculate the amount of doping, which they showed that the normalized spectral weight, S of the QPP is equal to the amount of doping in local limit ($t = 0$) and can be overestimated by a factor of 2 if hopping is considered. Weitering et al. [68] have calculated the normalized spectra S of QPP, LHB and UHB by dividing the area of the associated Gaussians by the sum of the total spectral intensity (i.e., LHB+QPP+UHB). The results of their DCA calculations of the spectral weight transfer indicate that $S = 0.1$ for 5% hole doping (which is twice the amount of doping). They used the same way to calculate the amount of doping of the p-doped $\text{Sn} - \sqrt{3}$ samples.

What we think is wrong is that they verified this with the results of DMFT calculations [32] that doesn't have the same LHB and UHB structure and the position of the QPP is not the same as in the work of Weitering et al as mentioned before.

In the present work, we have performed new measurements in order to elucidate these questions that were raised by the state-of-the-art work. We reveal for the first time the nature of the

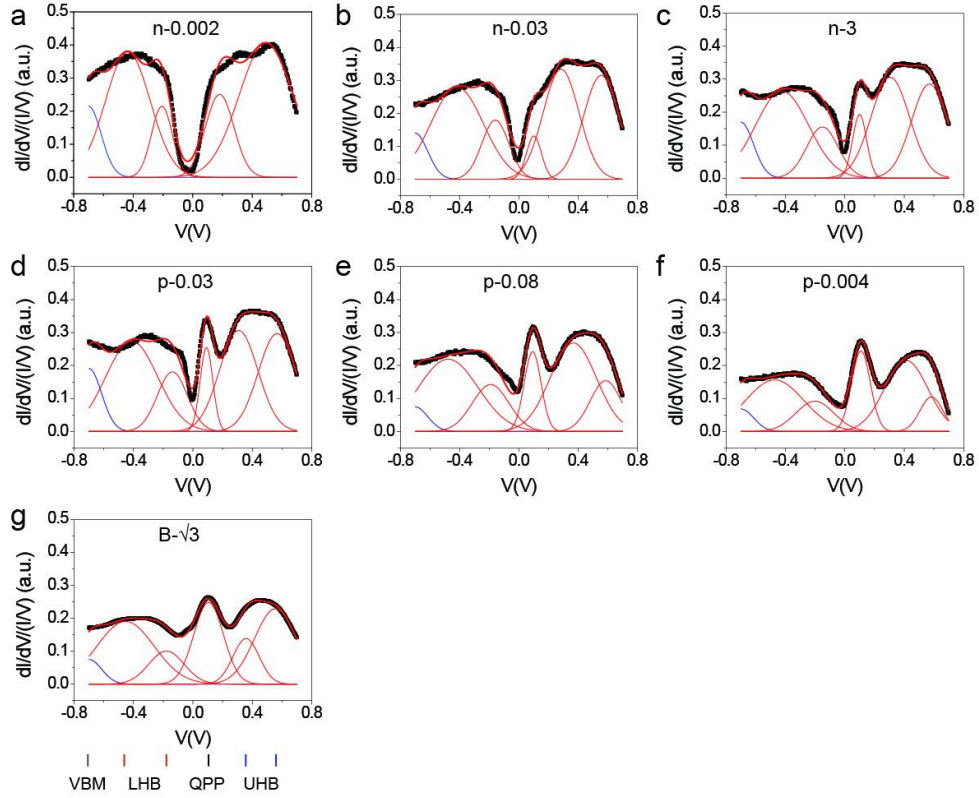


Fig. 3.5 Determination of the relative spectral weight of the QPP, UHB and LHB. (a) Fitting of the spectra using six (or five for the n-0.002 sample) Gaussian peaks. The solid bars below (g) mark the centers of the Gaussian peaks: one peak for the bulk VBM (indicated in blue), two peaks for the LHB, one peak for the QPP, and two peaks for the UHB (all indicated in red)[66].

$S_n - \sqrt{3}$ ground state. Using spatial and spectral STM/STS measurements, we show that below 20 K an insulating state develops with a large energy gap of about 650 meV at 4 K. This value is about ten times more than previously suggested both experimentally and theoretically. Signature of the magnetic order existing at 4 K is revealed using quasiparticle interference measurements in single structural domains.

3.3.2 possible spin ordering in $\text{Sn} - \sqrt{3}$

Regarding the possible spin ordering, a spin-resolved ARPES study performed at 40 K claimed to have measured a very small spin polarization consistent with a collinear antiferromagnetic order [69]. However, the high temperature of this study, the complexity induced by the presence of three possible orientational domains together with the absence of spectroscopic signatures at the expected $2\sqrt{3}$ period render this study questionable to our opinion regarding the eventual presence of a magnetic order.

Different possible magnetic ordering of the spin 1/2 lattice at low temperature are presented in Fig. 3.6 [62].

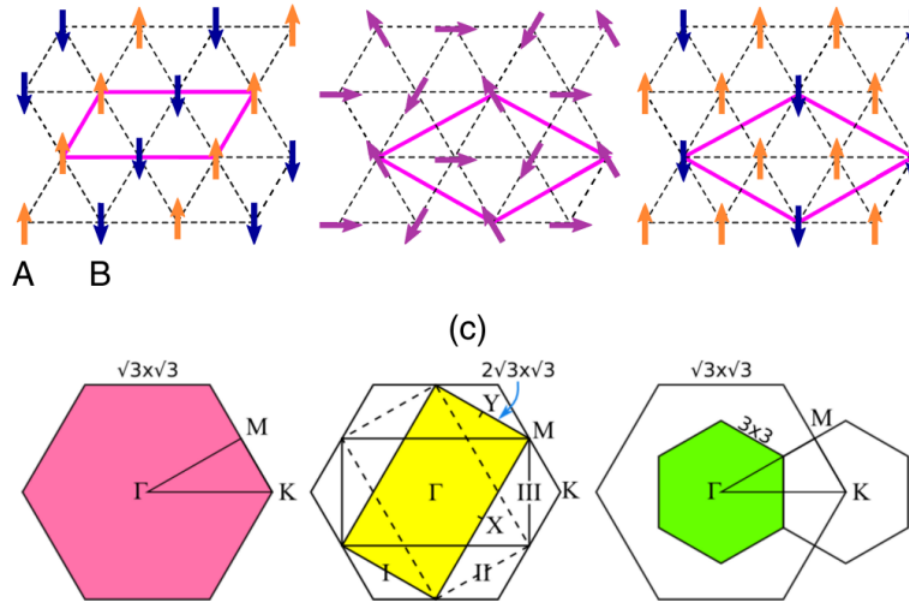


Fig. 3.6 Three different magnetic structures with the AFM, 120° spiral, and FI spin orders are schematically drawn in (b), where the corresponding $2\sqrt{3} \times \sqrt{3}$, 3×3 , and 3×3 unit cells are indicated by the solid lines. The Brillouin zones (BZs) of various unit cells are drawn in (c). The rectangular I represents the BZ of the AFM structure shown in (b), while the rectangular II and III represent the BZs of other AFM spin alignments [62].

3.3.3 Chiral superconductivity observed in $\text{Sn}/\text{Si}(111)$ (highly p-doped)

In this subsection the results of Weitering et al. on the Chiral superconducting state of $\text{Sn}/\text{Si}(111)$ (highly p-doped) is presented. As mentioned before we couldn't perform these measurements ourselves because of technical problem of our STM setup and also lack of time, however, we have some insights regarding the previous results on this interesting phase transition. We think that while the discovery of the superconductivity and its properties under magnetic field is quite convincing, the results and the discussions in this paper must be confirmed with more scientific studies. In the future the same experiments are going to be carried out in our group to verify what is the nature of the superconducting phase. Recently Weitering et al. [70] have reported that $\text{Sn} - \sqrt{3}$ can be modulation hole doped and becomes a superconductor at low temperatures.

They have found that for a Si(111) sample with $0.008 \Omega \cdot \text{cm}$, the T_c of the superconducting state becomes 9K and that the T_c of this systems is dependent on the hole doping concentration and they compare this system with high temperature Cuprates which are the state of the art high T_c superconductors which have a Mott-insulating initial state and become superconductor upon doping. We have discussed before in this chapter why their calculation for the amount of doping for this system is not accurate and also we will prove in the next pages that this system is in fact not a Mott-insulator but a Band-insulator before doping and can not be trivially compared to the high temperature superconductors. However, the evidence of the superconducting state is quite clear. Fig. 3.7.a shows the lattice structure of the $\text{Sn} - \sqrt{3}$ and the dependency of the superconducting gap to the doping level (Fig. 3.7.b), position (Fig. 3.7.c) and temperature (Fig. 3.7.d). They have argued that the nature of this superconducting state can be either S-wave or chiral d-wave by fitting the data, while the latter is more in favour because by inducing non-magnetic defects (Sn ad-atoms or Si substitution defects) they see scattering patterns which can only happen if the order parameter is chiral d-wave superconductor, however the non-magnetic properties of this defects are not proven accurately. It means that if the defects are magnetic there is a chance for the possibility of a s-wave superconducting order parameter and the scattering pattern reminds us of the Yu-Shiba-Rusinov (YSR) states as discussed in chapter 1.

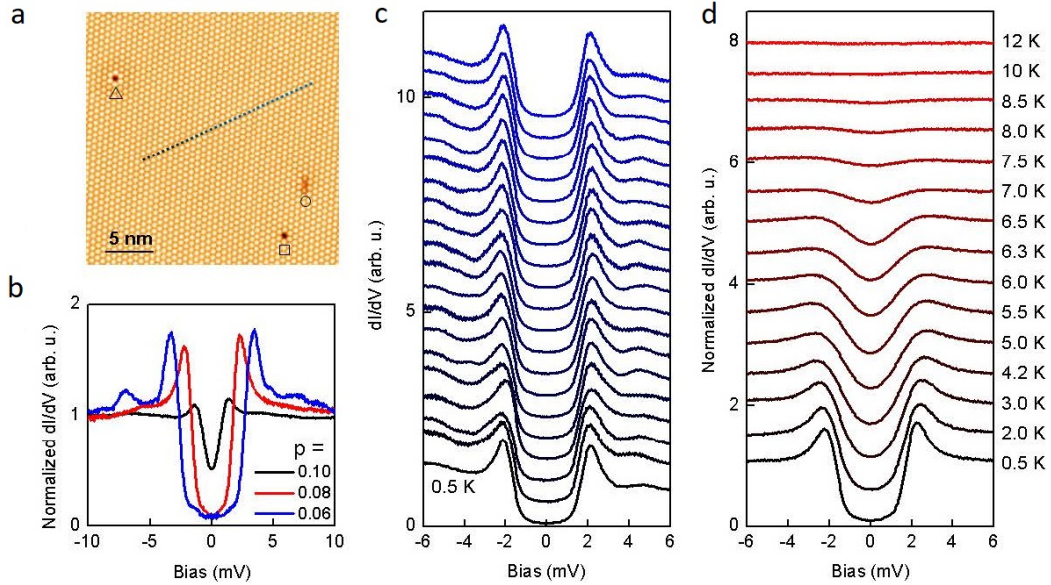


Fig. 3.7 a. Topographic STM image ($V_s = -0.1 \text{ V}$, $I_t = 0.1 \text{ nA}$) showing a near perfect Sn adatom lattice, along with a substitutional Si defect, vacancy, and other defect, labelled with a triangle, square and a circle, respectively ($p = 0.08$). b. Normalized STS spectra for three different hole concentrations, revealing a clear doping dependence of the superconducting gap. c. A Set of raw dI/dV spectra taken at equidistant locations along the dotted line shown in panel d, starting on the left. ($p = 0.08$). d, Normalized dI/dV spectra as a function of temperature ($p = 0.08$). The spectra in panels f and g are offset vertically for clarity.

3.3.4 Spectroscopy measurements

The STS spectroscopy measurements were performed on $\text{Sn} - \sqrt{3}$ single domains having a lateral size larger than 50-100 nm at $T = 4.2$ K with metallic Pt-Ir tips. For such domain sizes we have found that the spectral characteristics presented hereafter are well established and reproducible. The $I(V)$ spectra were measured far enough from the boundaries with neighboring $\text{Sn} - 2\sqrt{3}$ to neglect any interaction with this phase and to probe intrinsic electronic properties of the $\text{Sn} - \sqrt{3}$ phase. The $dI/dV(V)$ spectra were obtained by numerical derivation of the raw $I(V)$ curves. Representative tunneling conductance spectra are shown in panel a of Fig. 3.8 at room temperature, 77 K and 4 K. Negative (positive) bias voltage corresponds to occupied (empty) sample states.

The room temperature spectrum is in good agreement with previous STS [65], ARPES [64, 65] and inverse photoemission results [71]. It features LDOS maxima around -0.3 eV and +0.35 eV and suggests an experimental bandwidth larger than 1 eV. The strong spectrum modification seen at 77 K also agrees with the large changes reported in previous STS [65, 66] or ARPES [55, 65, 69] results. The spectral weight across most of the bandwidth is depleted and appears to be transferred to lower binding energies and larger unoccupied energies. The DOS around E_F is lowered by a factor close to ten. At 4 K we see that a large energy gap has set-in, reaching true zero conductance and being equal to about 650 meV. The gap has been calculated by measuring the energy range around the Fermi level ($E = 0$ meV) in which the LDOS becomes zero.

This value is much larger than the ones reported in [65, 72] or theoretically predicted using many-body approaches based on the Hubbard model [55, 73], or DFT calculations assuming a DFT+U approach with a PBE functional [54].

To gain more insight into the opening of the energy gap, we have followed its temperature dependence presented in Fig. 3.8b. At 40 K the LDOS is still finite at E_F . Below around 30 K, the LDOS gets progressively strongly depleted in the energy range [-400;+500] meV. Within our experimental resolution, the tunneling conductance reaches zero around 25 K. It should be noted that as can be seen in Fig. 3.8.b, changing the sample and the tip doesn't change the value of the energy gap at 4K. Also, the value of the energy gap changes negligibly at different positions of the $\text{Sn} - \sqrt{3}$ phase, especially on the defects, as can be seen in Fig. 3.9 which shows the spectra of the different defects together with the average spectra of the map.

Another important note that should be discussed is that the energy gap that we have observed for the $\text{Sn} - \sqrt{3}$ phase can not be attributed to band bending or coming from the underlying $\text{Si}(111) - 7 \times 7$ surface. As can be seen in Fig. 3.10 it has been shown by Myslivecek et al. [74] that by lowering the temperature at 7K changing the set current (I_t^0) can change the value of the energy gap, however, it should be noted that while this has an effect on the positive side of the gap it doesn't change the position of the gap edge on the negative side of the energy gap meaning that band bending can not explain such a large gap at the negative side of the band gap.

We now present how to rationalize and successfully model our surprising spectroscopic results using advanced DFT calculations and further discuss in detail the theoretical investigations of the $1/3$ ML $\text{Sn} - \sqrt{3}$ phase.

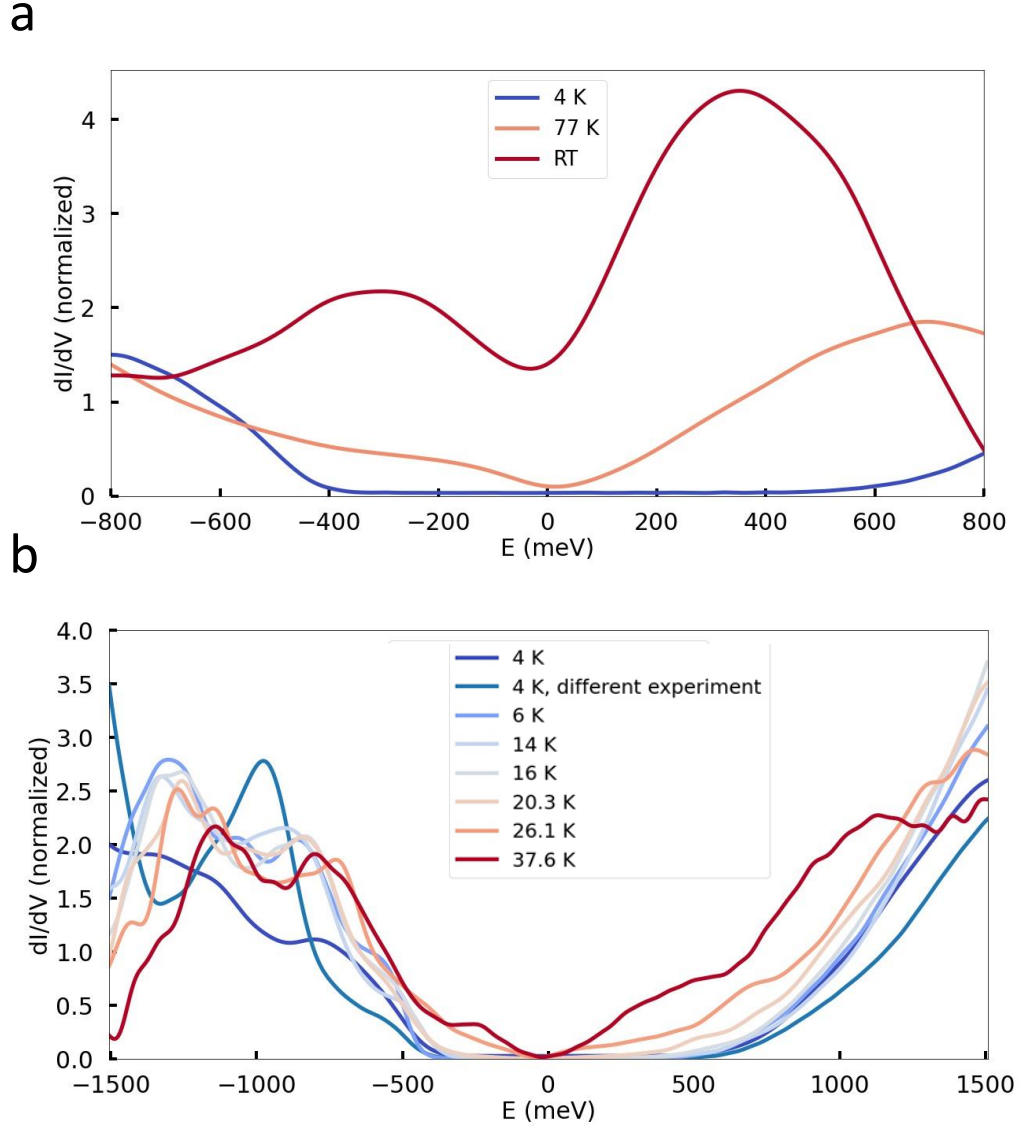


Fig. 3.8 (color online) Temperature dependent dI/dV ($E = eV_{\text{bias}}$) spectra acquired by scanning tunneling spectroscopy in single Sn $-\sqrt{3}$ domains. a. Comparison between tunneling spectra acquired at room temperature (RT), 77 K and 4 K. A large energy gap has set in at 4 K. These spectra are measured between [-1;1] V using a set-point at $I = 200$ pA for $V_{\text{bias}} = -1$ V. b. Temperature evolution of the dI/dV tunneling spectra between 37.6 K and 4 K. The energy gap opening starts around 25-30 K. These spectra are measured between -2V and 2V using a set-point at $I = 200$ pA for $V_{\text{bias}} = -2$ V. Note that the spectrum at 4K is also given for another experiment with a different sample and different tip.

3.3.4.1 Computational details

As in [75] we model the Sn/Si(111) surfaces by considering a layer of Sn atoms on top of 3 Si bi-layers. Hydrogen atoms are bonded to the dangling bonds of the bottom Si surface fixed to the relaxed positions obtained by capping one side of the pristine Si surface. The Sn atoms are placed on the T_4 sites above the Si(111) and the position of the atoms of the top two Si bilayers together with the Sn atoms were optimized to reduce any residual forces introduced by adding

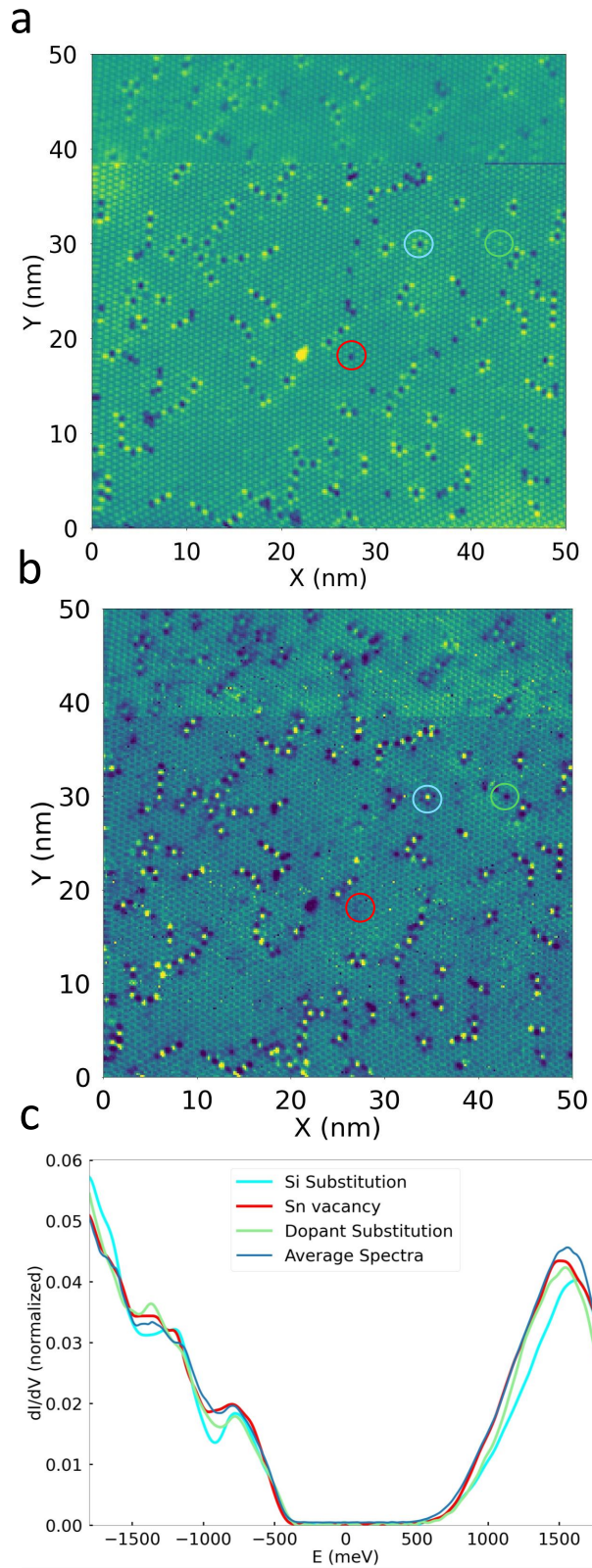


Fig. 3.9 a. Atomic resolution image taken from a window of $50 \times 50 \text{ nm}^2$ b. spectroscopic map recorded at $E = 1600 \text{ meV}$ at the same window as a, c. spectra showing the total average and local density of states averaged on the circles on different defects shown in a and b.

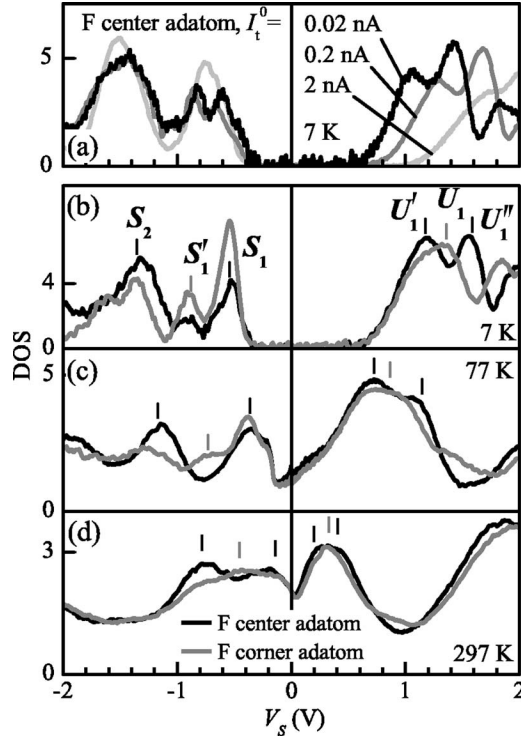


Fig. 3.10 a. Dependence of the STS spectra on I_t^0 at $T = 7\text{K}$. b, c and d. Spectroscopic measurements at $T = 7, 77$ and 297 K (RT), respectively (all the measurements has been done on a highly n-doped $\text{Si}(111) - 7 \times 7$ sample). By lowering the temperature at 7K , the measured energy gap becomes dependent on the spectroscopy set-point. This points out that part of this energy gap is due to a voltage drop across the sample. For more information please see [74].

Sn ad atoms. A vacuum of 16\AA is considered to simulate a slab and prevent the interaction between the slab in z-direction. Calculations has been done by the master student Amitayush Thakur, helped by Cesare Tresca and Matteo Calandra, using QUANTUM ESPRESSO code with GGA exchange-correlation functional (PBE). The calculation was done using ultra-fast pseudo-potential with an energy cutoff of 45 Ry or by using HSE functional from CRYSTAL17 package (using 25 % mixing parameter) and calculating accurate values for exchange part of the energy performed in Gaussian basis set.

3.3.4.2 Determination of the ground state and comparison to experimental results

It has been shown that the $\text{Sn} - \sqrt{3}$ with a $2\sqrt{3} \times \sqrt{3}$ AFM super-lattice in the presence of a Hubbard repulsion $U = 2.12\text{ eV}$ has a band gap of 70 meV as is shown together with the band structure in Fig. 3.11.a and Fig. 3.11.b respectively. However, while this calculation estimates very well what is measured at low temperature in our contaminated samples it can not account for the band structure in clean system at 4 K which shows a gap of approximately 650 meV. However, using exchange interaction with the substrate in the case of HSE calculation it has been observed that the calculated band gap matches very well with the experimental data as it can be seen in Fig. 3.12 with a calculated band gap of around 600 meV. This very good agreement with HSE calculation supports the fact that the electronic orbitals of the Sn atoms, as predicted before by Lee et al. [62], has an exchange interaction with the $\text{Si}(111)$ top layer.

This means that the Mott-Hubbard scheme is not appropriate for this systems in contrary to the conclusions of most of the previous researches.

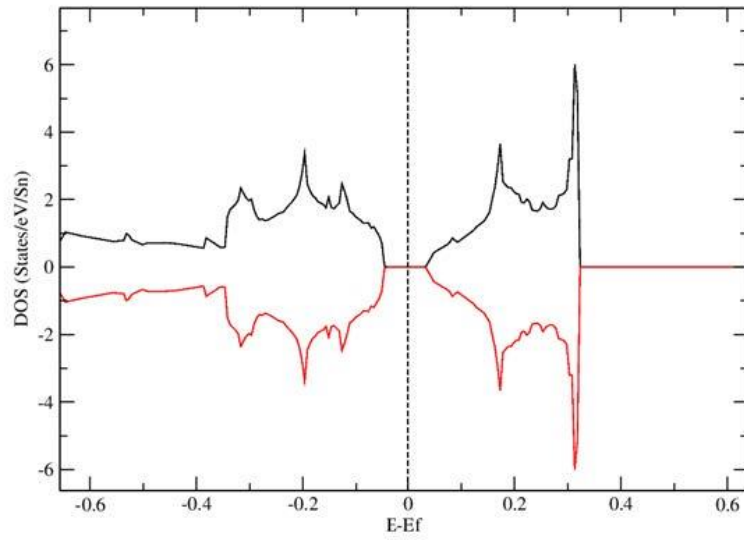
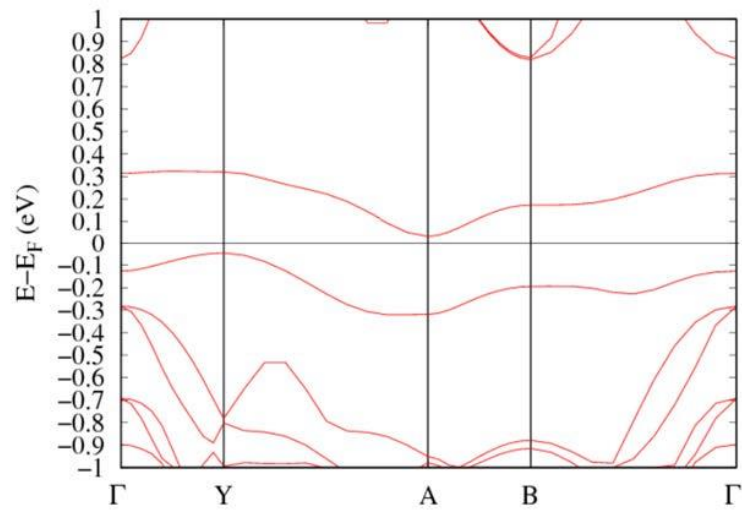
a**b**

Fig. 3.11 a. DOS in the presence of $U=2.12$ eV with a gap of 70 meV. b. Band structure of the AFM configuration $2\sqrt{3} \times \sqrt{3}$ with U

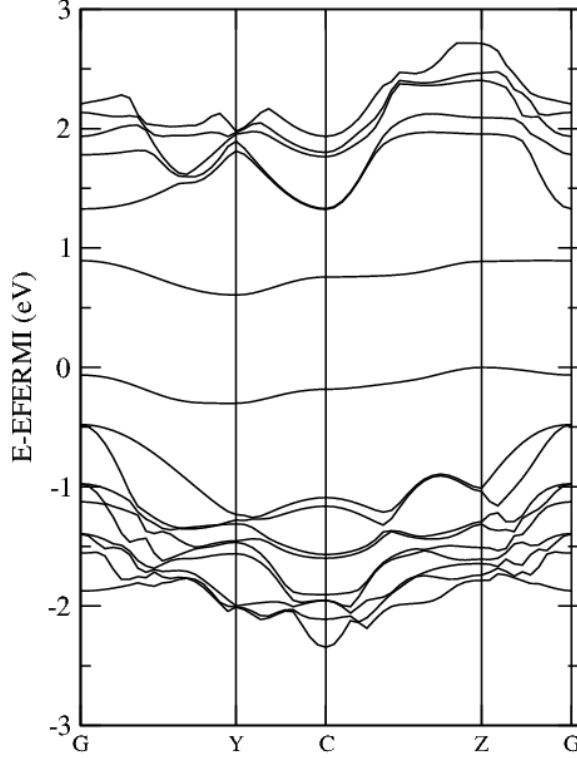


Fig. 3.12 HSE band structure for AFM configuration with default range of interactions, the insulating gap is around 0.7 eV

3.3.4.3 Experimental signature of the colinear antiferromagnetic order and theoretical modeling

An elegant and efficient way to infer information about order parameter symmetry, topology, spin and band-structure properties is to use quasi-particle interference (QPI) STS measurements. QPI are a phase-coherent manifestation of the scattering of elementary electron or hole excitations by defects [76, 77, 78]. These QPI measurements are typically obtained by performing the Fourier transform of a $dI/dV(V, x, y)$ map measured for a given energy $E = eV$. In the neighboring material Pb/Si(111)- $\sqrt{3} \times \sqrt{3}R^\circ 30$ the team had shown that this technique could be successfully used to map out the main elastic scattering vectors of the Fermi surface and hence reveal the under-lying Rashba spin-orbit coupling and shape/size of the Fermi surface [79]. As recently explained [80], care should be taken in acquiring such constant energy tunneling conductance maps and full STS mode where full spectra are taken at each point of a large grid should be privileged as I did during my thesis work. In previous work some wrong conclusions were drawn based on scanning at a given voltage while recording some dI/dV signal with the lock-in, however this technique can remove LDOS the signal from the lock-in sector if it is contained principally in the z-regulation channel, i.e. the topography, which is particularly the case at low voltage in a metal or at gap edge in a semiconductor [80].

In the present work we again followed a careful procedure in order to obtain reliable spectroscopic maps with a minimum of STM z-regulation artifacts. We directly acquired a complete set of dI/dV maps between -2V and +2V numerically derivated from a dense $I(V)$ 256×256

grid on a $60 \times 60 \text{ nm}^2$ area. A proper normalization condition for all spectra was found for $V_{bias} = 2 \text{ V}$ and $I = 200 \text{ pA}$. In the context of determining the ground state of the $\text{Sn} - \sqrt{3}$ phase, QPI are particularly interesting due to the band gap opening and the possibility of having a magnetic ordering of the spin 1/2 lattice. The topographic image, the Energy-dependent dI/dV maps and the Energy-dependent QPI measurements acquired at 4K in a single structural domain are presented in Fig. 3.13, Fig. 3.14 and Fig. 3.15, respectively.

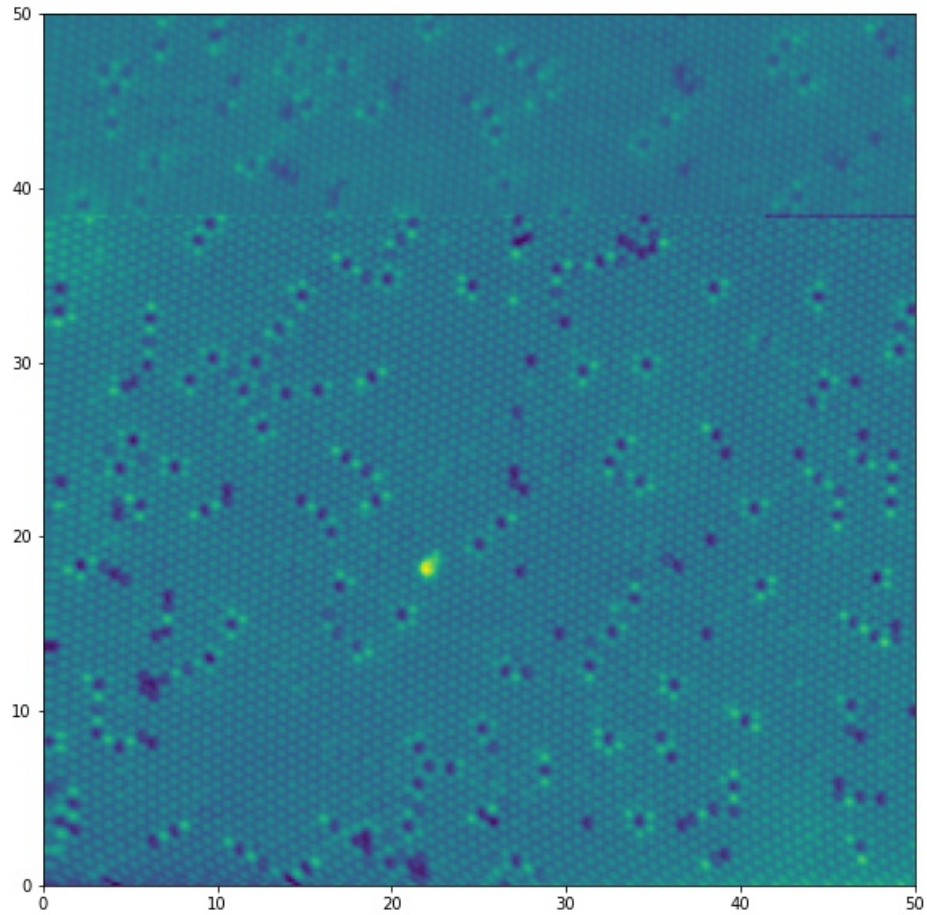


Fig. 3.13 A $50 \times 50 \text{ nm}^2$ area of a single $\text{Sn} - \sqrt{3}$ domain in which, further spectroscopic measurements have been done

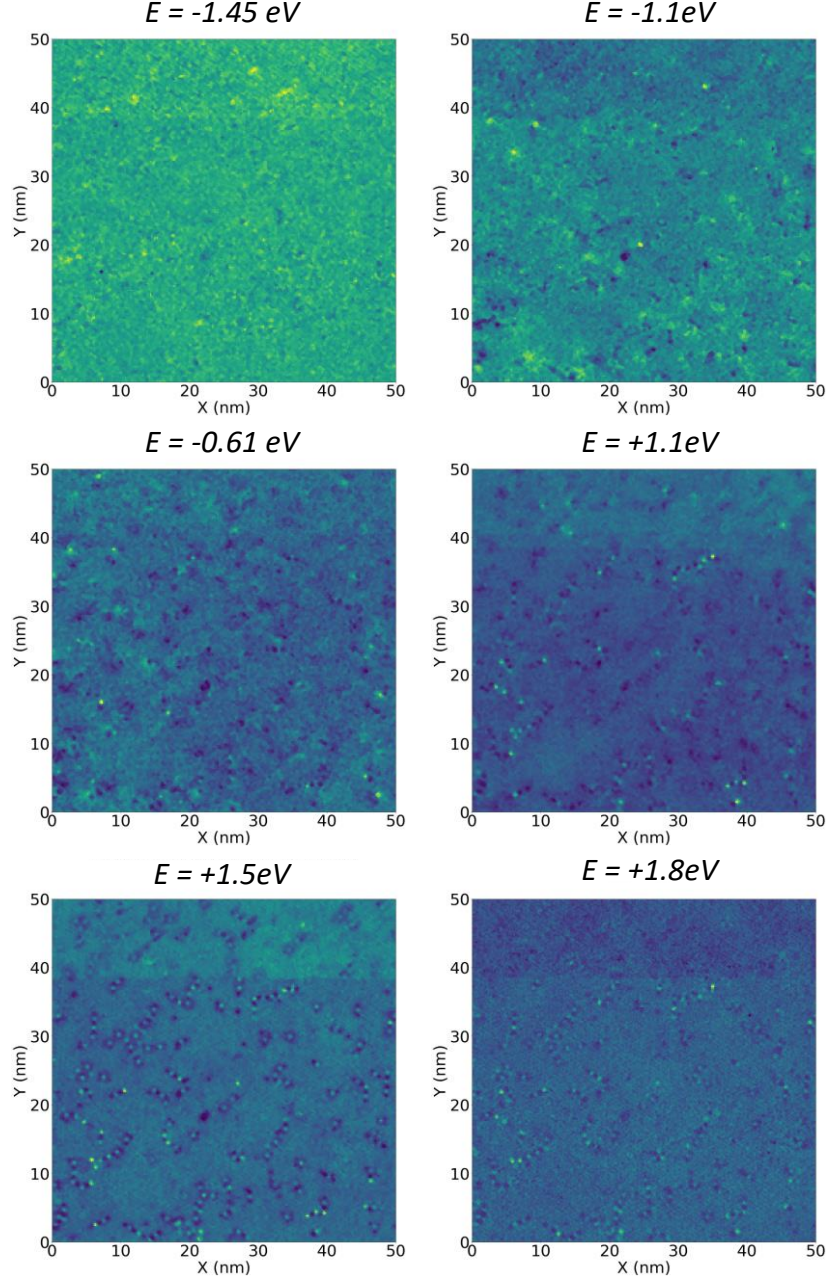


Fig. 3.14 Energy dependent dI/dV maps. Each panel represents the dI/dV ($E = eV_{\text{bias}}$) map acquired at the indicated energy. All dI/dV (E) maps were acquired at 4 K in the same 50×50 nm² area of a single $\text{Sn} - \sqrt{3}$ domain shown in Fig. 3.13, by derivation a grid of 256×256 individual $I(E = eV_{\text{bias}})$ spectra acquired using a set-point for spectroscopy of $V_{\text{bias}} = -2$ V and $I = 200$ pA, together with a constant current STM topography measured at $V_{\text{bias}} = -2$ V and $I = 50$ pA.

Three energies cover the occupied states (-1.45 eV, -1.00 eV, -0.61 eV) and three others the unoccupied ones ($+1.1$ eV, $+1.5$ eV, $+1.8$ eV). The Bragg peaks associated to the structural $\text{Sn} - \sqrt{3}$ unit cell are nicely visible for all energies and one of them is indicated by the arrow labeled $Q_{\sqrt{3}}$ for $E = -1.45$ eV. Starting from $E = -1.45$ eV, a diffuse disk-like signal is observed for the wave vector modulus smaller than $|Q_{\sqrt{3}}|$. This signal gets reorganized for

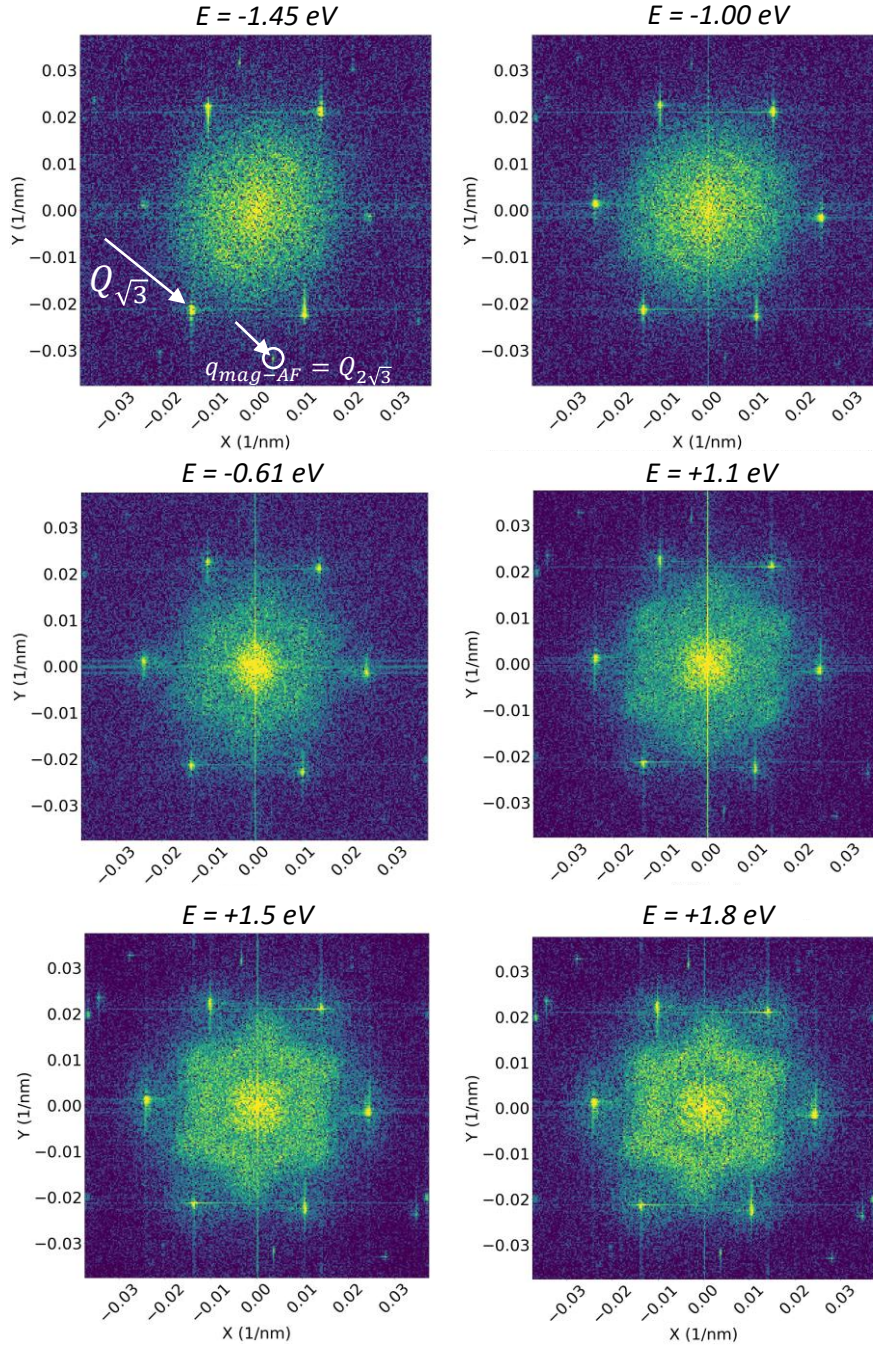


Fig. 3.15 (color online) Revealing the magnetic superstructure in Energy dependent quasiparticles interference maps. Each panel represents the numerical Fourier transform of a dI/dV ($E = eV_{\text{bias}}$) map acquired at the indicated energy. All dI/dV (E) maps were acquired at 4 K in the same $50 \times 50 \text{ nm}^2$ area of a single $\text{Sn} - \sqrt{3}$ domain shown in Fig. 3.13, by derivation a grid of 256×256 individual I ($E = eV_{\text{bias}}$) spectra acquired using a set-point for spectroscopy of $V_{\text{bias}} = -2 \text{ V}$ and $I = 200 \text{ pA}$, together with a constant current STM topography measured at $V_{\text{bias}} = -2 \text{ V}$ and $I = 50 \text{ pA}$. The Bragg peaks associated to the $\sqrt{3} \times \sqrt{3}$ atomic structure form an hexagon consisting in 6 sharp bragg spots. Along a particular direction, one of the Bragg peaks is labelled $Q_{\sqrt{3}}$. At a vector $q_{\text{maf-AF}} = Q_{\sqrt{3}}/2 = Q_{2\sqrt{3}}$ sharp superlattice spots of weaker intensities are seen, associated to the antiferromagnetic ordering of the spin 1/2

-0.61 eV in a more hexagonal shape and a strong component has developed close to $q = 0$. For $E = 1.1$ eV the hexagonal signal is better defined and additional pockets are seen faintly near the corners of the hexagon. Simultaneously, the signal close to $q = 0$ has grown in diameter. For $E = 1.5$ eV the hexagonal shape has turned into a star-like shape with curved edges. A darker corona has appeared between the external star and the brighter disk located near $q = 0$. Simultaneously, diffuse signal forms around each Bragg peak. At $E = 1.8$ eV, these patterns are even clearer and keep the same shapes.

In addition to these spectroscopic signatures, sharp Bragg-like spots but of smaller intensities, are seen for all the QPI maps and are indicated by the vector $q_{\text{mag-AF}}$. This set of additional spots are located as satellites of the main Bragg peaks with the vector $q_{\text{mag-AF}}$. They correspond precisely to the expected $2\sqrt{3} \times \sqrt{3}$ supercell in real space, that is predicted by our advanced DFT calculations to be associated to the antiferromagnetic ground state. We thus interpret our findings as an experimental hint of the existence of the ordering of the spin $1/2$ triangular lattice in a colinear row-wise $2\sqrt{3} \times \sqrt{3}$ antiferromagnetic superlattice using a normal tip. It might be surprising that a normal tip may be sensitive to a spin contrast, we don't have the explanation yet. Non magnetic tip have been shown to give magnetic contrast; for instance, in the presence of a strong Rashba spin-orbit one has a spectroscopic contrast directly in the LDOS between an in plane spin and a out-of-plane, this is called Tunneling Anisotropic Magnetov Resistance (TAMR). But, two opposite spin both in plane or both out-of-plane would not give any TAMR signal. One possible explanation could be that the tip picked up some magnetic impurities, but where these impurities could come from is not clear.

In order to confirm this measurement and ascertain the magnetic origin of the $2\sqrt{3} \times \sqrt{3}$ supercell, I tried to directly measure the spin polarisation using spin polarized STM with an antiferromagnetic Cr tip. Unfortunately, as mentioned earlier, the attempt to use Cr tip to measure the spin order was not successful.

3.3.4.4 Discussion

In this work we could reveal for the first time the nature of the $S_n - \sqrt{3}$ ground state, which was long thought as a natural implementation of the two-dimensional Mott-Hubbard model on a triangular lattice because very few experimental work are available that do not correspond to the accurate nature of this system due to either contamination or not the right conditions for the experiments specially measurements that are not being done at low enough temperatures to reveal the true ground state of this system.

We show that below 30 K an insulating state develops with a large energy gap of about 650 meV at 4 K. This value is about ten times more than previously suggested both experimentally and theoretically, however, when doing measurement on this sample with contamination either Pt or Ta we have seen the small gap that was reported in the literature.

Signatures of a colinear antiferromagnetic order existing at 4 K are revealed using quasi-particle interference measurements in single structural domains, leading to a sharp non-dispersive superstructure associated to a $2\sqrt{3}$ period, consistent with the establishment of a $2\sqrt{3} \times \sqrt{3}$ super-cell. These experimental results are fully supported by advanced DFT calculations emphasizing the crucial role played by the Sn-Si exchange interaction, concerning the energy gap's

size and ordering of the magnetic state. Our work definitely supports, for the two-dimensional α -phase surface materials, the super-exchange model as being much more appropriate to describe this antiferromagnetic insulating state than the canonical on-site Mott-Hubbard model because of the important role played by the surface substrate atoms and in particular their important exchange interaction that stabilize a non-colinear magnetic order.

In my opinion this findings can create more opportunities for researcher to design superconductors based on doped band-insulators and not be restricted to only a Mott-insulating phase.

Now in the next subsections we are going to present other interesting experimental measurements and also calculations that has been done for the Sn/Si(111) and also the Pb/Ge(111)

3.3.5 Artificial molecules induced by defects

An interesting phenomenon that has been observed on the surface of Sn – $\sqrt{3}$ is the interaction of substitutions defects which leads to bonding interaction between them and create artificial molecules. As can be seen from Fig. 3.16 which shows an atomic resolution of this structure, there are white spots in between the defects that correspond to electronic orbitals. These electronic orbitals bond the defects together to form artificial molecules on the surface. The structure of the molecules changes when the scanning voltage is changed. As indicated by yellow arrows in Fig. 3.16.a and Fig. 3.16.b corresponding to scanning voltages of -1 V and -2 V, respectively, the white spots have disappeared and reappeared between other defects. These modifications are pure LDOS effects and are not associated to any moving atoms. Depending on the bias voltage, different orbitals appears that exhibit different kind of bonding. For instance, the vertical up arrow point to a pattern, in image b at -2 V, that evokes an antibonding link with a node (dark region) surrounded by two lobes (white spots). This interpretation is still speculative and DFT simulations would be needed in order to ascertain this molecular scenario.

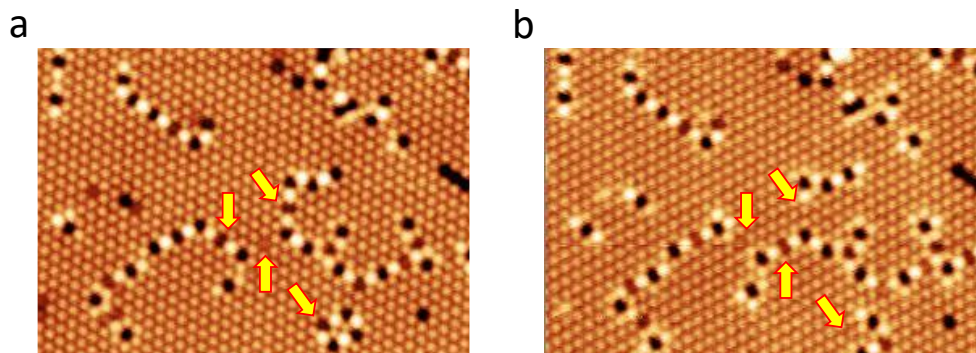


Fig. 3.16 Atomic resolution of Sn – $\sqrt{3}$ Reconstruction recorded at 4K scanned with two different voltages: a. -1 V and b. -2 V the white arrows show the area in which a switching of the artificial molecules appeared.

Some switching of electronic orbitals were also observed on the boundaries of the Sn – $\sqrt{3}$ domains. As can be seen in Fig. 3.17 on the domain boundaries several triplets of white spots corresponding to electronic orbitals can be seen. Here the STM images are done at the same voltage and they show some triplets that tend to switch back and forth to another configuration

as it has been indicated in Fig. 3.17 with yellow arrows. This switching of the white spots corresponds to the switching of electronic orbitals. The additional white spot cannot be due to an additional adatom since at different voltages the shape and intensity of the white spots changes as can be seen in Fig. 3.17(a and b) at -2V and Fig. 3.17.c at -1V. Also, the switching of these white spots is changing the electronic configuration at other parts of the surface as indicated by the red arrows, white spots appear in Fig. 3.17.b (shown by the red arrow) that can only be an electronic effect. It seems quite likely that these switching are linked to an atom that slightly moves around its position and depending on its precise positioning its orbitals are redistributed as well as those of neighbouring atoms.

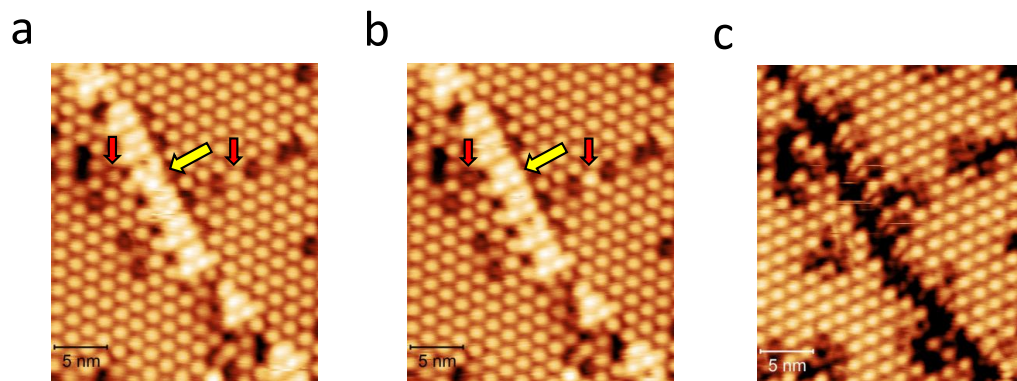


Fig. 3.17 a and b. Triplets of electronic orbitals observed on the domain boundaries of $\text{Sn} - \sqrt{3}$ switching randomly while scanning using the STM with the same voltage (-2 V) as indicated with the yellow arrows c. Atomic resolution at the same position as a and b but at scanning bias of -1 V

3.3.6 Edge states

While measuring the spectroscopic maps in an area involving both the $S_n - \sqrt{3}$ and $S_n - 2\sqrt{3}$ as shown in Fig. 3.18 we have observed that at the energies inside the $S_n - 2\sqrt{3}$ gap, there is a high density of state region close to the domain boundary, on the $S_n - 2\sqrt{3}$ side with an evanescent decaying when we move away from the domain boundaries (Fig. 3.18.c). This features can only be seen in the gap edge of the $S_n - 2\sqrt{3}$ and might thus correspond to a Tamm state.

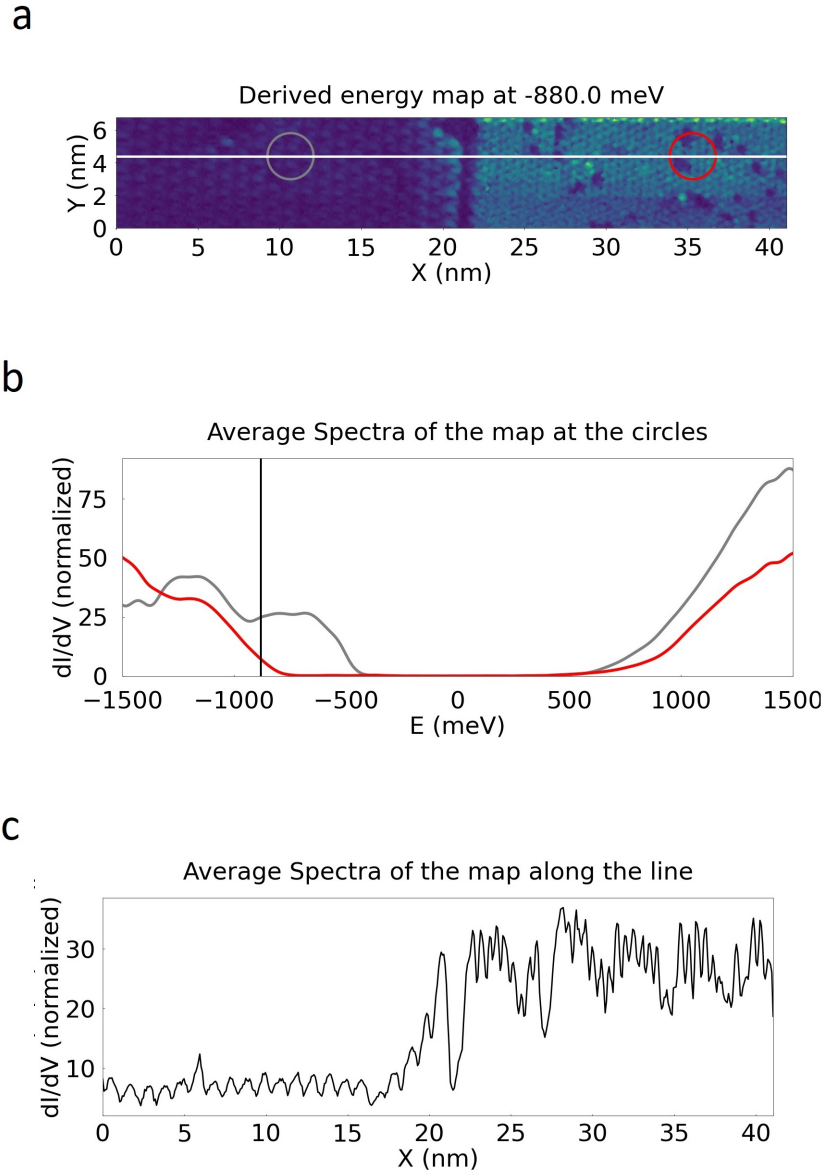


Fig. 3.18 a. Spectroscopic map taken from the intersection of $S_n - 2\sqrt{3}$ and $S_n - \sqrt{3}$ phases, in the window of $41 \times 7 \text{ nm}^2$ and energy range of -880 meV b. Average spectra taken from the circles indicated in a and c in an energy interval of $[-1500, 1500] \text{ meV}$. c. Spectra profile taken from the white line shown in a.

Tamm states named after the Russian physicist Igor Tamm [81] are surface states which are calculated in the framework of tight bonding model and describes well the edges of transition

metals and wide gap semiconductors [82]. More explanation about this topic can be found in the mentioned references and is beyond the purpose of this thesis.

3.3.7 Multifractal electronic wave functions at the gap edge of $\text{Sn} - \sqrt{3}$

In this section we are going to discuss a very interesting character of electronic wave functions: they behave like a multifractal at the intersection of extended and localized state. We will see why it is related to our system and how we can characterize multifractality using box counting method. While performing STM measurements we have observed that by reducing the scanning bias, from -2 V till -550 mV (close to the gap edge) we start to see a transition from extended states to localized electronic states. Fig. 3.19 shows that close to the gap edge (around -550 meV) there are some areas with high intensity corresponding to localized states with high density of states and there are some areas depleted from electronic states with low or zero density of states.

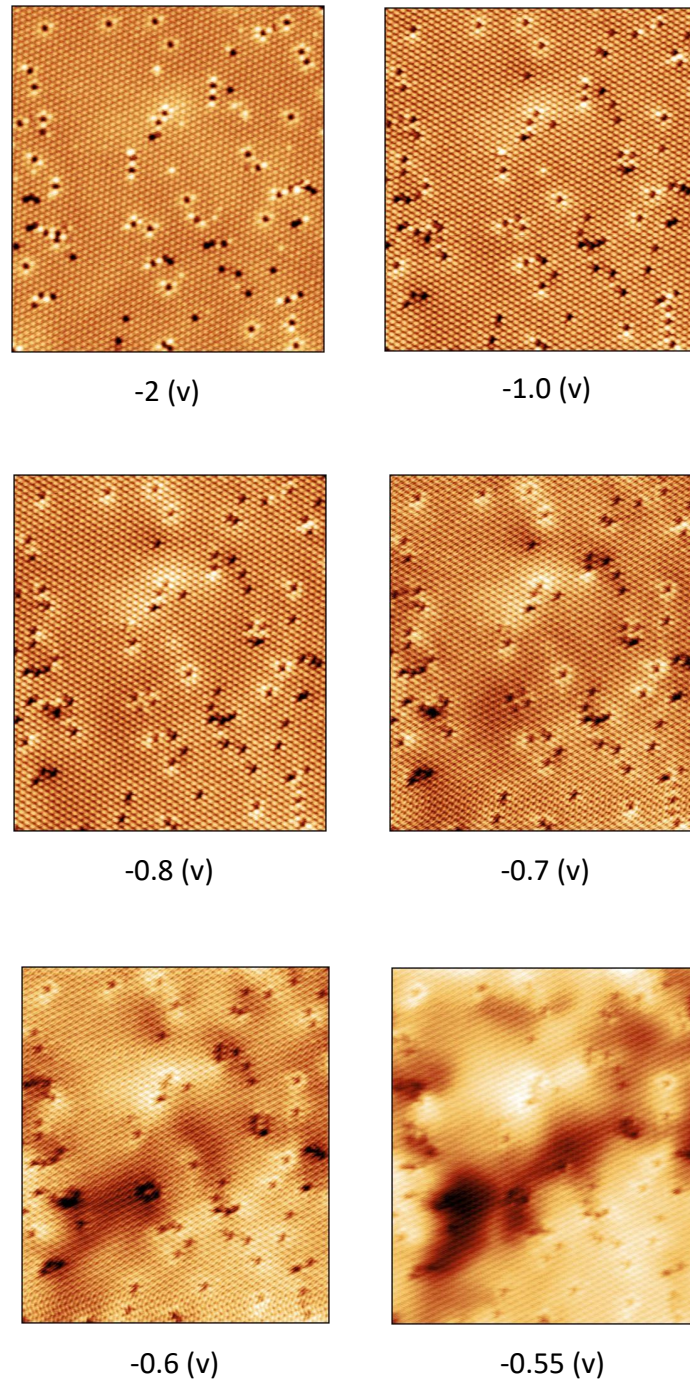


Fig. 3.19 Atomic resolution topographic images taken at different energies from -2 eV down to -0.55 eV from $\text{Sn} - \sqrt{3}$ phase

Large scale topographic images are shown at -2 V (Fig. 3.20) which shows some extended metallic states and at -600 meV in Fig. 3.21 which shows some localized states as it can be observed.

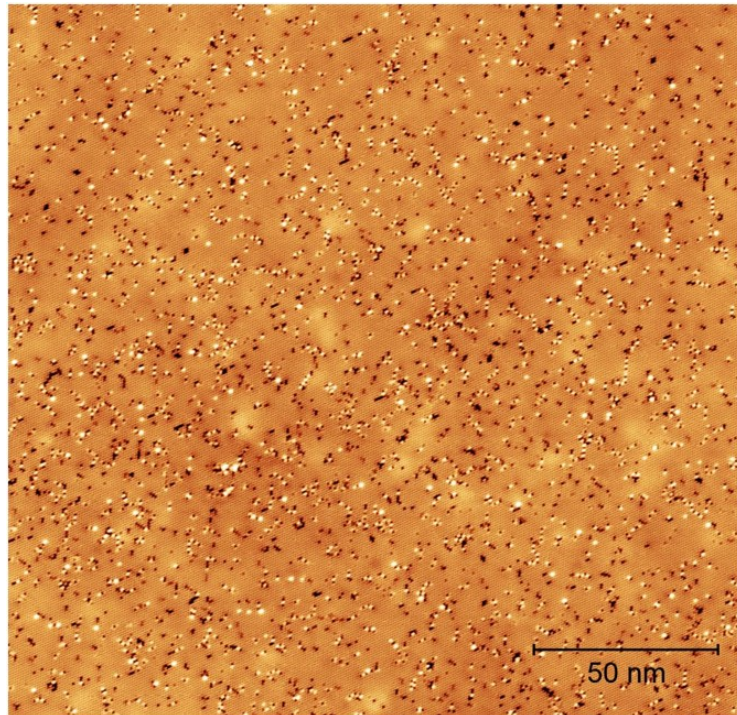


Fig. 3.20 $300 \times 300\text{nm}^2$ image taken from $\text{Sn} - \sqrt{3}$ phase with a scanning bias of -2 V

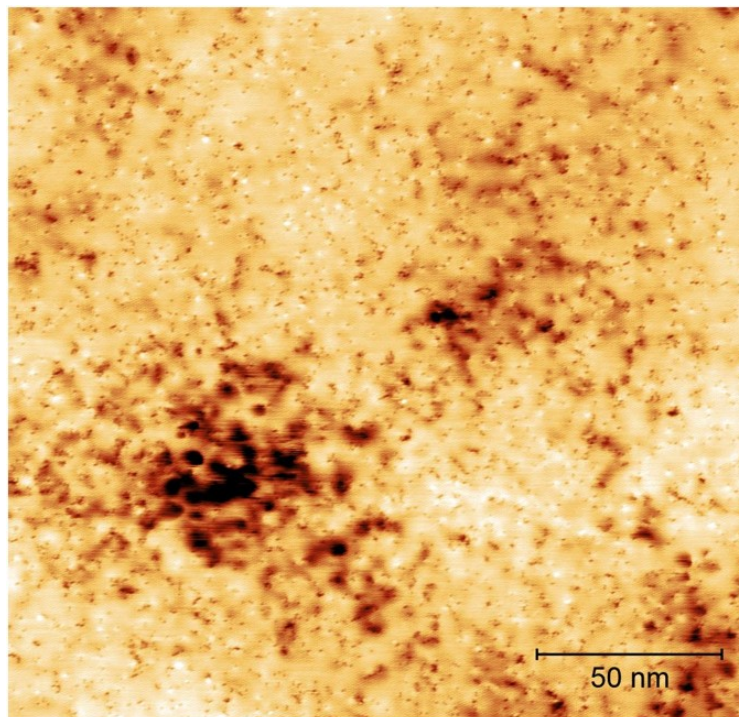


Fig. 3.21 $300 \times 300\text{nm}^2$ image taken from $\text{Sn} - \sqrt{3}$ phase with a scanning bias of -600 meV

In addition to topographic images we have also observed the same characteristics in spectroscopic maps as it can be seen in Fig. 3.22.a in the case of extended states and away from the gap (Fig. 3.22.b) and in Fig. 3.22.c in the case of localized states at the gap edge (Fig. 3.22.d).

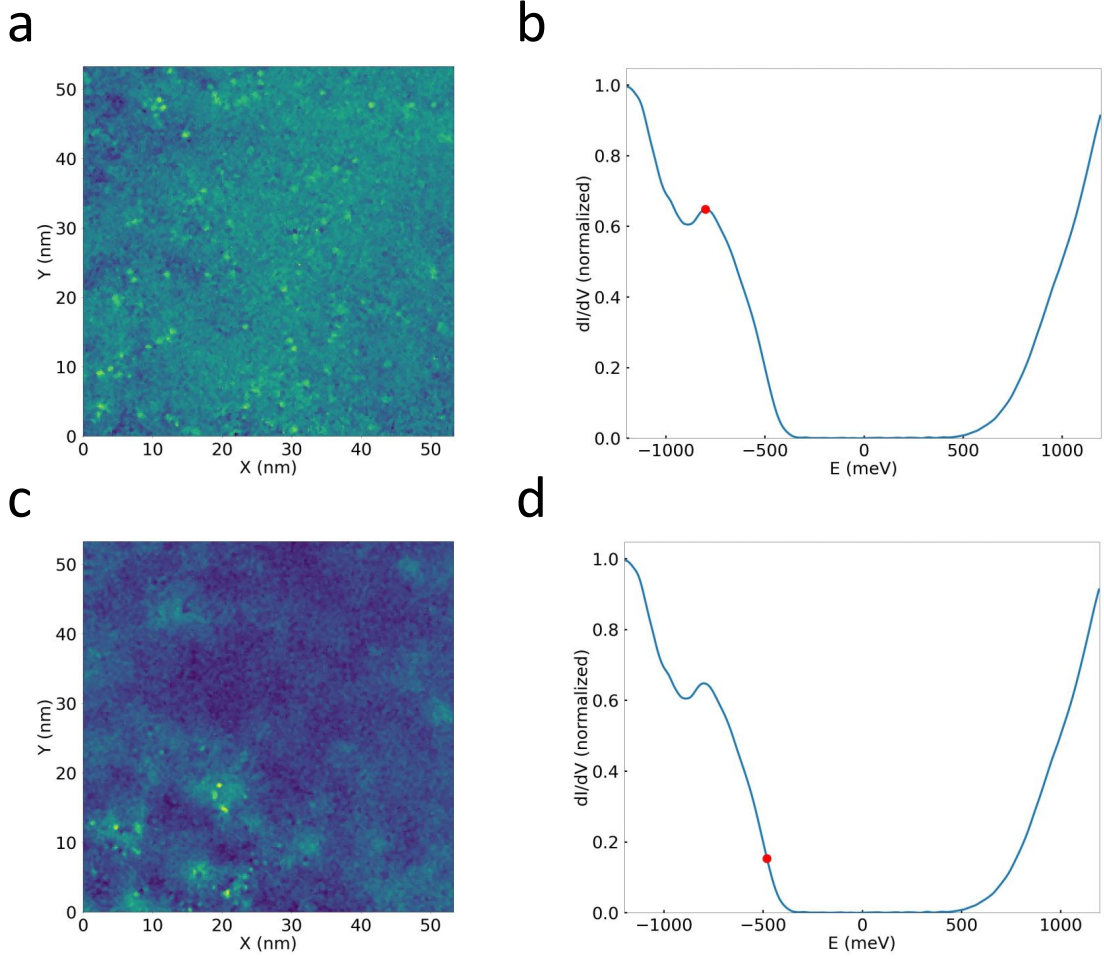


Fig. 3.22 a and c. Spectroscopic maps recorded at the energies corresponding to extended states (-800 meV) and localized states (-480 meV) respectively in a window of $50 \times 50 \text{ nm}^2$, b and d. Average spectra of the map with the red circle showing the energies that the maps at a and c are shown.

In the Fourier transform images we have seen that the Bragg peaks are present even very close to the gap at about 450 meV. But when entering the gap, in the tail states that we can detect between -350 mV and -450 mV, the Bragg peaks disappear as well as the QPIs due to the localization. The tail states are coming from Sn orbitals at the gap edge and are localized because of the defects in the disordered monolayer. The scattering by defects induces Anderson localization in the tail states and this manifests by a multifractal aspect of the LDOS. In the following we will delve deeper in multifractal concept and we will show how these states near localization can be described and characterized by multifractal analysis tools.

A multifractal system is a generalized concept of a fractal system in which a single exponent is not enough to describe its dynamics and a continuous spectrum of exponents is needed to describe it well [83]. Multifractal systems are very common in nature. We can encounter multifractality in mountain topography [84], fully developed turbulence, human heart beat dynamics [85] and many other examples. Multifractality is also found in the physics of Anderson quantum phase transition in disordered systems, which happens in the phase transition from An-

erson localized states with localized electronic wave functions (insulating phase) to a metallic phase in the extended electronic wave functions. At the Anderson critical point, which separates the localized systems from the metallic ones, the real space distribution of the local density of states (LDOS) is multifractal [86, 87].

Multifractal analysis is based on the standard box-counting procedure. The following calculations are adopted from a paper written by Schreiber et al. [88]. We start by dividing the system into N_L sub-systems of lateral linear size L and measuring the average of the modulus squared of the wave function in the k_{th} box:

$$\mu_k(L) = \sum_{n=1}^{L \times L} |\Psi_n|^2, k = 1, \dots, N_L \quad (3.1)$$

Multifractality can be completely characterized with the singularity strength of the fractal, given by the Lipschitz-Holder exponent α , and the corresponding singularity spectrum $f(\alpha)$. In the k_{th} box the singularity strength α is given by:

$$\mu_k(L) = const.L^{\alpha_k} \quad (3.2)$$

The spatial distribution of subsets $N(\alpha)$ for whose this relation holds is a fractal itself, with the Hausdorff dimension $f(\alpha)$:

$$N(\alpha) = const.L^{-f(\alpha)} \quad (3.3)$$

The singularity spectrum can be obtained by means of a Legendre transform [89, 90, 91] which suffers from inaccuracies, here a parametric representation of f and α in terms of q is presented:

$$f(q) = \lim_{L \rightarrow 0} \sum_k \mu_k(q, L) \ln(\mu_k(q, L)) / \ln(L) \quad (3.4)$$

and

$$\alpha(q) = \lim_{L \rightarrow 0} \sum_k \mu_k(q, L) \ln(\mu_k(1, L)) / \ln(L) \quad (3.5)$$

with $\mu_k(q, L)$ the q_{th} moment of the measure:

$$\mu_k(q, L) = \mu_k^q(L) / \sum_k \mu_k^q(L) \quad (3.6)$$

From these relations $f(q)$ and $\alpha(q)$ one can deduce the relation between the f and α : $f(\alpha)$ which is the so-called singularity spectrum. In the presence of multifractality at the Anderson localization, the singularity spectrum $f(\alpha)$ describes a continuous set of scaling exponents. In the case of extended metallic states, $f(\alpha)$ shows only a delta Dirac distribution positioned at $\alpha = 2$ as it can be seen in Fig. 3.23. In case of a multifractal wave function induced for instance by Anderson localization one expect the $f(\alpha)$ function to broaden and shift towards higher values of α .

Previous STM measurements on disordered Two-dimensional quantum Hall systems [92,

93], on the surface of bulk GaAsMn [94], and on 2d layers of transition metal Dichalcogenides [95] reported $f(\alpha)$ spectra, calculated from density of states maps whose broadened characteristics were consistent with interpretation of a Multifractal scaling at criticality (Fig. 3.23). Christian Ast et al. [96] have shown that a disordered 2d electron gas of mixed alloys at the Anderson criticality shows Multifractal behaviour. They have found that for $\text{Bi}_x\text{Pb}_{(1-x)}/\text{Ag}(111)$ there is a good agreement between measured dI/dV maps and the LDOS calculated by the Anderson tight binding model, with some deviation which comes from the simplified tight binding model (only considering nearest neighbour hopping) and neglecting any interaction to the Au(111) substrate. While Multifractality was observed in disordered metallic systems it has never been observed in an insulator in the vicinity of the gap, here we report a continuous amplification of the multifractal behaviour while entering into the tail states at gap edge of $\text{Sn} - \sqrt{3}$.

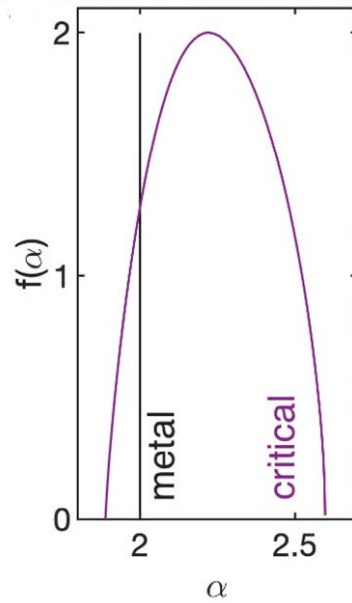


Fig. 3.23 Schematic plot of the singularity spectrum $f(\alpha)$ for a $d = 2$ dimensional system with multifractal (purple) and metallic (black) scaling behavior

We have measured the multifractal singularity spectrum, $f(\alpha)$, which can be directly obtained from the LDOS maps as a function of singularity strength α . The parabolic appearance of $f(\alpha)$ is broadened while going from the extended states (-700 meV) to the gap edge (-520 meV) as can be seen in Fig. 3.24 and it shrinks while going further and inside the gap (-450 meV), The position of the maxima of the parabolas corresponding to α_0 is close to 2 for extended states and it becomes higher than 2 when the multifractality is stronger as can be also seen in Fig. 3.24.

To illustrate this point better we have measured α_0 in all the energies of the measured maps. Fig. 3.25 shows the average spectra of the spectroscopic maps together with the α_0 curve, as it can be seen in this Figure, α_0 is around 2 in the extended state (at -700 meV), it rises at the transition energy (-520 meV) and it reduces again inside the gap to around 2. Note that the latter doesn't have a physical meaning, since it correspond to a very weak LDOS in tail states that is dominated by white noise. The bad noise to signal ratio results in a ill defined α_0 values.

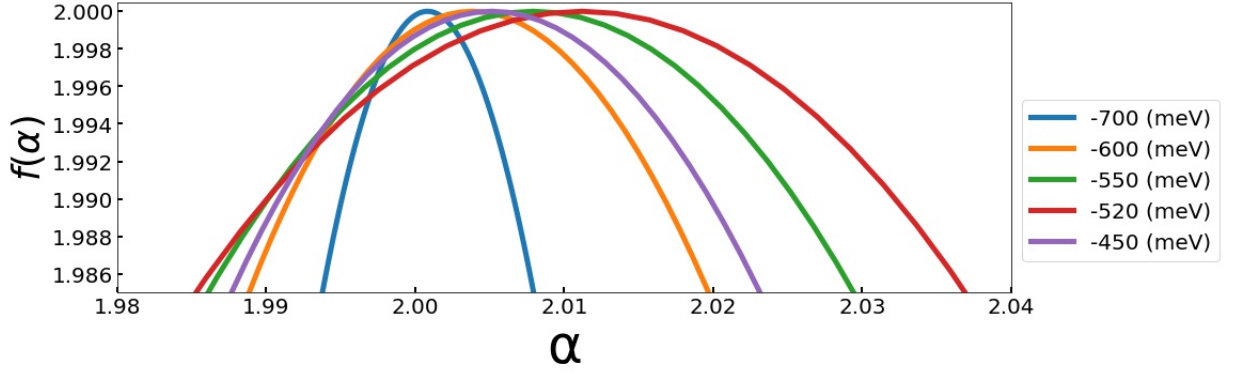


Fig. 3.24 $f(\alpha)$ spectrum measured for spectroscopic maps with different energies

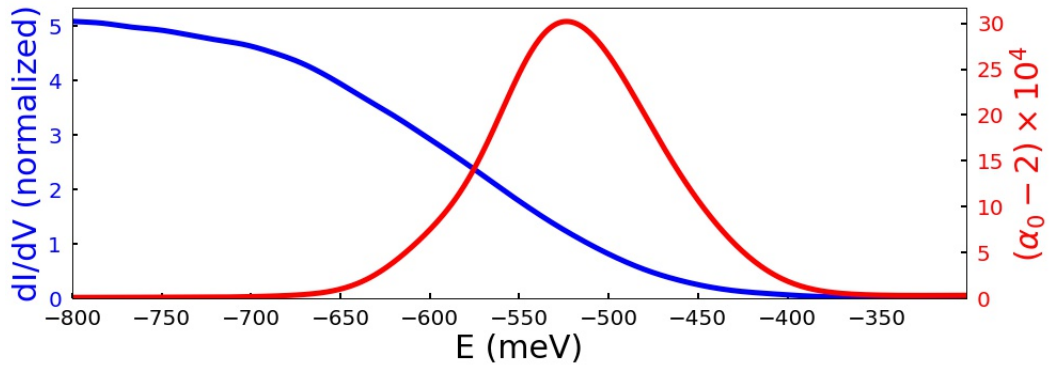


Fig. 3.25 Average spectra of the spectroscopic maps together with the α_0 curve shown in an energy interval of $[-800, -300]$ meV

The $f(\alpha)$ is a parabola in the weak multifractality regime and close to be a parabola with some anti-symmetric feature in strong multifractality regime which can approximately be quantified by this formula: $f(\alpha) = 2 - (\alpha - 2 - \gamma)^2 / (4\gamma)$, where γ is a measure for the strength of multifractality and defines both the position of the maximum at $\alpha = 2 + \gamma$ and the opening angle of the parabola [97]. Applying a quadratic fit to the $f(\alpha)$ spectrum at the extended state (-700 meV) and at the gap edge (-520 meV) yields a γ value of $11.2 \pm 0.1 \times 10^{-3}$ and $0.85 \pm 0.1 \times 10^{-3}$ respectively. Christian Ast et al. [96] attributed this small values of γ to be due to weak multifractality. Our observations can be further quantified by investigating the distribution of the probability distribution of LDOS in a given area [86, 87]. While the LDOS of extended states follows a Gaussian distribution the LDOS of insulating states shows a log-normal distribution, related to the broad distribution of the LDOS in this state [89].

The lognormal distribution is defined by the following formula:

$$P(x) = \frac{1}{x\sigma\sqrt{2\pi}} \exp\left(-\frac{(\ln(x) - \mu)^2}{2\sigma^2}\right)$$

The normal distribution is defined by the usual:

$$P(x) = \frac{1}{\sigma\sqrt{2\pi}} \exp\left(-\frac{(x - \mu)^2}{2\sigma^2}\right)$$

Applying this analysis to the measured spectroscopic maps reveal a transformation from the Gaussian distribution in the extended states to a lognormal distribution at the gap edge, Fig. 3.26 shows the distribution of the $LDOS/\langle LDOS \rangle$ for 4 different energies in the range of metallic to insulating states together with the Gaussian fit for metallic states ($E = -700, -650$ meV) and lognormal fit for the insulating states ($E = -520, -550$ meV). Table 3.1 shows the parameters related to the fits.

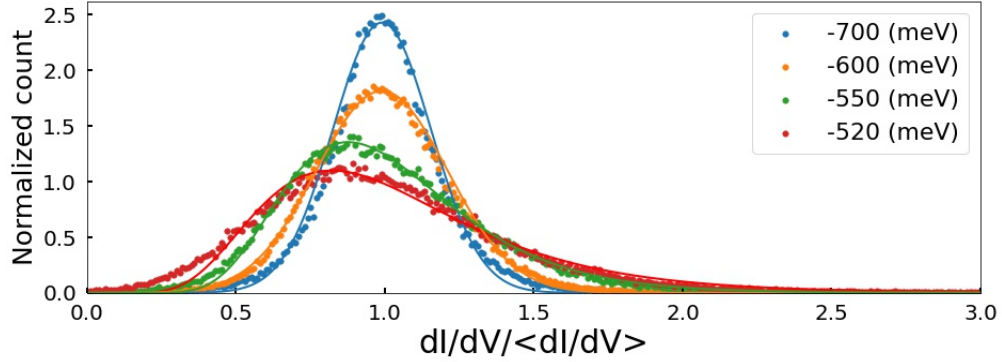


Fig. 3.26 The distribution of the $LDOS/\langle LDOS \rangle$ for 4 different energies in the range of metallic to insulating states indicated with scatter points together with the Gaussian fit for metallic states ($E = -700, -650$ meV) and lognormal fit for the insulating states ($E = -520, -550$ meV) indicated in solid lines.

Table 3.1 Fitting parameters of the $LDOS/\langle LDOS \rangle$ histograms of the maps at different energies

Energies (meV)	σ	μ
-700	0.164	1.0
-600	0.221	1.0
-550	0.324	$\ln(0.968)$
-520	0.408	$\ln(0.970)$

3.3.8 Conclusion

While nice QPIs are observed well inside the conduction band of Sn/Si(111), the LDOS near the gap edge seems to show some clear signature of localization. We have thus used some tools devoted to the study of multifractality in order to study that tail state at gap edge as such tools are adequate for Anderson localization. It seems that the multifractality is indeed observed both by the broadening of $f(\alpha)$ and the shift of the maximum of this curve toward values higher than $\alpha = 2$ in the tail states. Conversely, well in the conduction band one recovers a sharp parabolic $f(\alpha)$ well centered at $\alpha = 2$. We also observed that the distribution of the LDOS values is well accounted for the states well inside the conduction band while close to the band edge the distribution is stretched and well fitted by a lognormal distribution as expected for localization. Note, however, that the LDOS should exhibit multifractality in the Anderson localization only at criticality. In a three-dimensional system, there is indeed a critical disorder threshold at which the system transits from delocalized to localized states. Just at this point, the system is

critical and its LDOS is expected to manifest multifractality. While disorder strength plays an important role in criticality in the crossover from extended states to localized states in 3d systems, in an infinite 2d system localization happens regardless of disorder strength. Hence our two dimensional system Sn/Si(111) should be localized whatever the strength of the disorder. However, the coherence length of the localization can be affected by the disorder's strength and depends on the considered energy range. We assume that well inside the conduction band the localization length is way larger the size of the sample however, close to gap edge, in the tail states the localization length is expected to be much shorter. Indeed imagine the case of a punctual disorder (dopants) with some impurity localized states below the conduction band, such states are by construction perfectly localized. We have seen in this section that for the same amount of disorder the localization appeared at a certain energy, meaning that not all the eigenstates of the system experience the Anderson localization the same and there should be a criticality in the energy that distinguishes between localized and extended states, at the gap edge, but we didn't expect such property in this crystalline material and additional studies are necessary to prove the multifractality and the assumptions discussed here.

3.4 Pb/Ge(111)

The system studied here is 1/3 Monolayer of Pb/Ge(111) (α -phase) which undergoes a reversible phase transition from a $\sqrt{3} \times \sqrt{3}$ to a 3×3 phase at around 250 K [98]. The 3×3 phase is the result of a reconfiguration of Pb atoms which is an ordered super-lattice of 1 atom up and 2 atoms down as shown in Fig. 3.27.

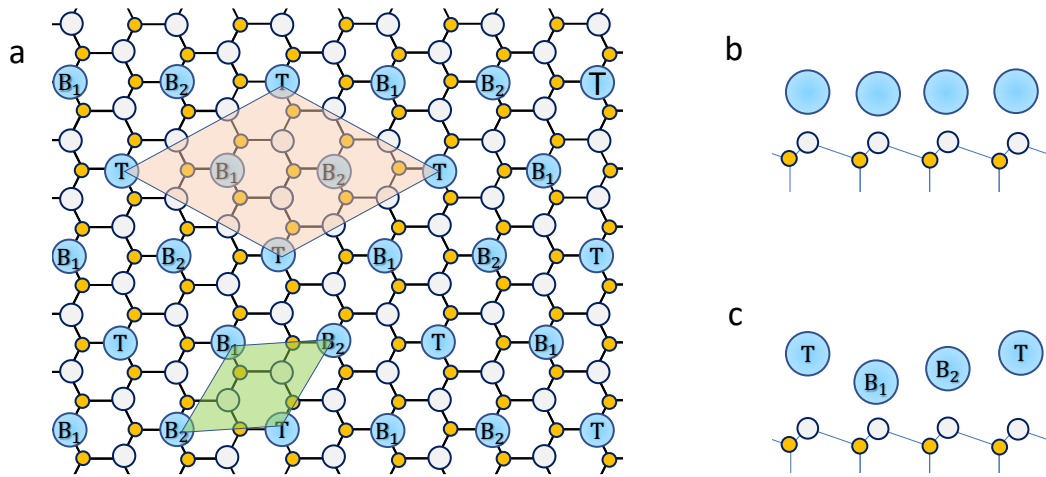


Fig. 3.27 a. Top view of α - Pb/Ge(111) phase showing the 1 atom top and 2 atoms down concept, Pb atoms are shown in blue while Si top and down atoms are shown in white and yellow circles respectively. 'T', 'B₁' and B₂ notes on the circles refers to Pb 'Top', 'Lower Bottom' and 'Upper Bottom' atoms respectively. The different reconstruction are shown, including $\sqrt{3} \times \sqrt{3}$ unit cell in green and a 3×3 unit cell in orange. b and c are the side view of the $\sqrt{3} \times \sqrt{3}$ and 3×3 reconstructions respectively. It can be seen in c that the two Pb bottom atoms do not have the same height.

The low-temperature metallic phase exhibits a pseudogap, the nature of this phase is char-

acterized by a charge-density waves (CDW) which gives rise to a 3×3 structure [99, 52]. Only few works theoretical works are present in the literature on this system [52, 100]. They assert that, due to strong correlations, the low-temperature ground state cannot be explained using the density functional theory which only predicts a metallic state. However, recently Cesare Tresca and Matteo Calandra [75] showed by DFT calculations that the driving force behind the 3×3 CDW structure is the non-local exchange interaction between the Pb and the substrate atoms and the electronic structure of this phase is mainly determined by two factors: the magnitude of the Pb distortion and the large spin-orbit coupling.

Guo et al. have reported a new phase transition on $\alpha - \text{Pb}/\text{Ge}(111)$ at lower temperatures ($T_c \approx 76\text{K}$) from the (3×3) to a glassy (labyrinth-like) phase (Fig. 3.28) [101]. This phase transition was characterized only by filled-state STM imaging and was proposed to occur as a result of a balance between two driving forces: the long-range electron-mediated interaction and the elastic stress imposed on the substrate [102].

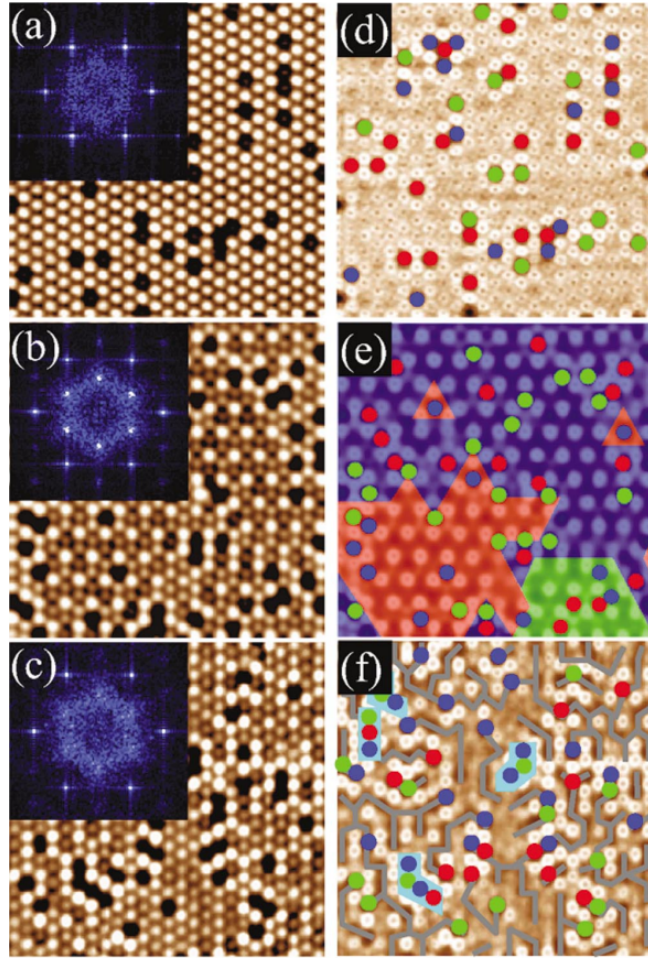


Fig. 3.28 STM images ($14 \times 14 \text{nm}^2$ of the Pb/Ge interface at (a) RT, (b) 90K, and (c) 41 K. STM images presented were obtained with the tip bias at +1.5 V and feedback current at 3 nA. The Fourier Transform images are shown as insets of the corresponding real space images. (d)-(f) show the perpendicular distortion by filtering out the $\sqrt{3} \times \sqrt{3}$ symmetry from images (a)-(c), respectively. Ge substitutions defects are marked with red, green, or blue circles depending on their coordination relative to the three nonequivalent sites in a (3×3) lattice. In (e), the (3×3) domains are highlighted in colors following the up sites. Three or more neighbouring defects are marked in light blue in (f), and the ad atoms distorted downwards are connected with gray lines [101].

While cooling down the sample with Pb/Ge(111) $\sqrt{3} \times \sqrt{3}$ we have also observed a similar coexistence of the (3×3) and Labyrinth phase at 77 K and also at 4 K. We have thought this might be due to thermal quenching of the sample while cooling down from room temperature after sample preparation, which is not true since we have observed that even while cooling down the sample slowly we still see that a large portion of the $1/3$ ML is covered by the Labyrinth phase. Fig. 3.29 shows an STM image showing empty states (Fig. 3.29.a) and filled states (Fig. 3.29.b) of 4 different phases taken at 4 K, the $\beta\sqrt{3} \times \sqrt{3}$, 3×3 , 4×4 and the Labyrinth phase. Our initial purpose was to produce large areas of 3×3 reconstruction (around $50 \times 50 \text{nm}^2$) in order to perform QPIs measurements. However, due to this phase's very small domain size, we have decided to perform point spectroscopy on all 4 different phases mentioned before at 4 K. Fig. 3.30 shows the point spectroscopy measurement in the range of $[-200, 200]$ meV for all the

different mentioned phases.

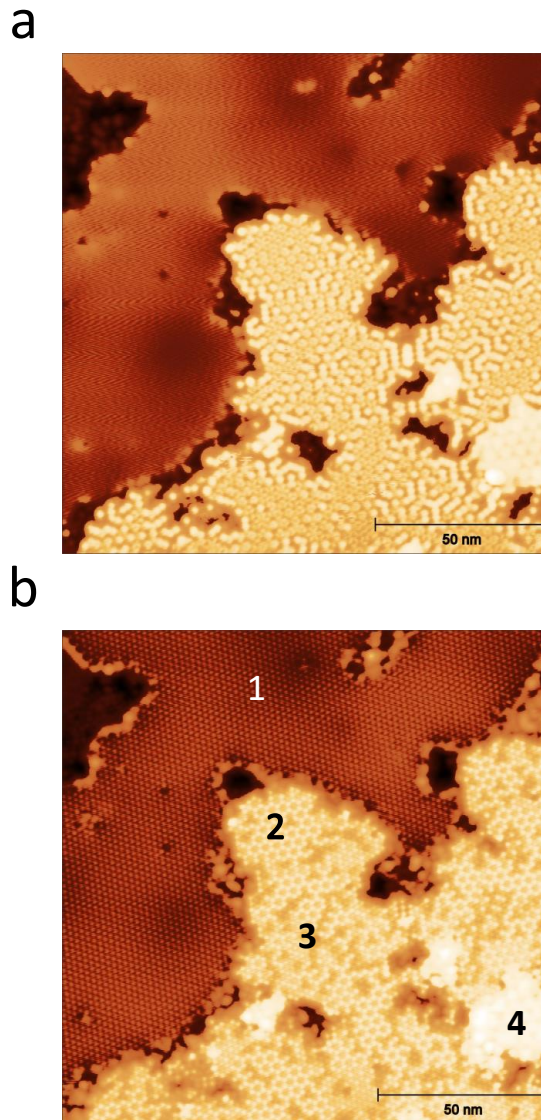


Fig. 3.29 STM images taken from a. Filled (-500 mV) and b. Empty (+800 mV) states of Pb/Ge(111) taken in a window of $140 \times 140 \text{ nm}^2$ showing 4 different reconstructions as indicated in the empty states images by numbers: 1. $\beta\sqrt{3} \times \sqrt{3}$, 2. 3×3 , 3. Defective 3×3 (Labyrinth) and 4. 4×4 .

As it can be seen from Fig. 3.30 the $\beta - \sqrt{3} \times \sqrt{3}$ is a metallic phase while the 4×4 phase has a vanishing density of state above E_F with a totally gapped dos between 50 meV and 200 meV.

Both the 3×3 and the 3×3 (Labyrinth) phases are metallic at low-temperature but show a depletion around the Fermi level, a characteristic of electronic correlations as mentioned before while the density of states is lower in 3×3 (labyrinth) phase at the Fermi level. This phase is probably less metallic due to the localization induced by the intrinsically high disorder of the labyrinth structure.

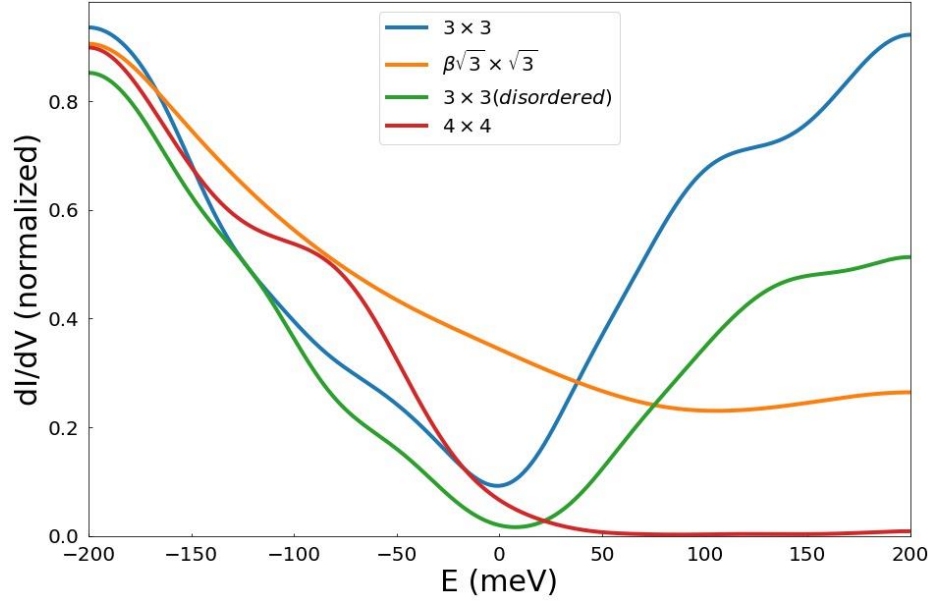


Fig. 3.30 Spectroscopic measurement of different reconstruction of Pb/Ge(111) at 4K

3.4.0.1 conclusion

While our main intention was to perform QPIs measurements on the 3×3 phase of Pb/Ge(111) samples we couldn't find large homogeneous regions of this phase due to the stabilization of a labyrinth phase appearing at temperatures below 78 K. However, we have measured the LDOS at different phases of the Pb/Ge(111), we have found that on the normal and disordered 3×3 phases we see a depletion around E_F as was predicted by previous theoretical works [99, 52, 75] while the disordered phase has a slightly lower DOS at the Fermi level probably due to its intrinsic disorder.

CHAPTER 4

Granular superconductivity at cleaved $(\text{TMTSF})_2\text{ClO}_4$

4.1 Bechgard salts

Among the various families of materials presenting unconventional superconductivity, organic materials occupy a very noticeable place thanks to their strong quasi-one dimensional electronic properties and close proximity to a quantum critical point where superconductivity is found to emerge on the brink of antiferromagnetism, as pressure is tuned either hydrostatically or chemically, by substitution of anion X [103, 104]

Among organic crystals there are two types that exhibit superconductivity, $(\text{TMTSF})_2\text{ClO}_4$ or “Bechgaard salts” and the (BEDT – TTF) salts, where TMTSF is the tetramethyl-tetrafulvalent electron donor molecule, (BEDT-TTF) is bisethylenedithio-tetrathiafulvalene and X is a mono-valent anion [105, 106].

Bechgaard salts are quasi-one-dimensional systems (Q-1D) that show unconventional superconductivity together with a competition between a spin density wave ground state (having an insulating ground state) and a superconducting state [105, 106, 107].

$(\text{TMTSF})_2\text{PF}_6$ is the prototype of Bechgard salts that shows superconducting behavior under pressure greater than 9 kbar, the ground state being a spin density wave (SDW) state at lower pressure [108, 109].

The aim of this part of the thesis is to study the exotic low temperature properties of $(\text{TMTSF})_2\text{ClO}_4$, which is the only ambient pressure superconductor of the family of $(\text{TMTSF})_X$ with $T_c = 0$, discovered shortly after $(\text{TMTSF})_2\text{PF}_6$ [110]. The single crystals of $(\text{TMTSF})_2\text{ClO}_4$ can be obtained by electrochemical oxidation of TMTSF the chemical reaction is as follows [111]:



The crystal structure of $(\text{TMTSF})_2\text{ClO}_4$ is the triclinic space group P1 with the unit cell parameters: $a = 7.27\text{\AA}$, $b = 7.7\text{\AA}$, $c = 13.38\text{\AA}$, $\alpha = 84.58^\circ$, $\beta = 86.73^\circ$ and $\gamma = 70.43^\circ$ [111, 112, 113]. Fig. 4.1 shows a schematic figure of the direction perpendicular to the a-b, b-c and a-c planes of this material. The a-b plane is the most conducting plane, with 'a' being the most conducting axis, while the “c” direction is the least conducting axis [113].

At ambient pressure in $(\text{TMTSF})_2\text{PF}_6$ there is a strong anisotropy in resistivity with respect to the direction of the applied current: the minimum is along the chain direction with a typical value similar to a normal conductor which is $10^{-3} - 10^{-2}\Omega\cdot\text{cm}$ (along a in Fig. 4.2), 100 times higher perpendicular to the chain (along b' in Fig. 4.2) and 10000 times higher perpendicular to

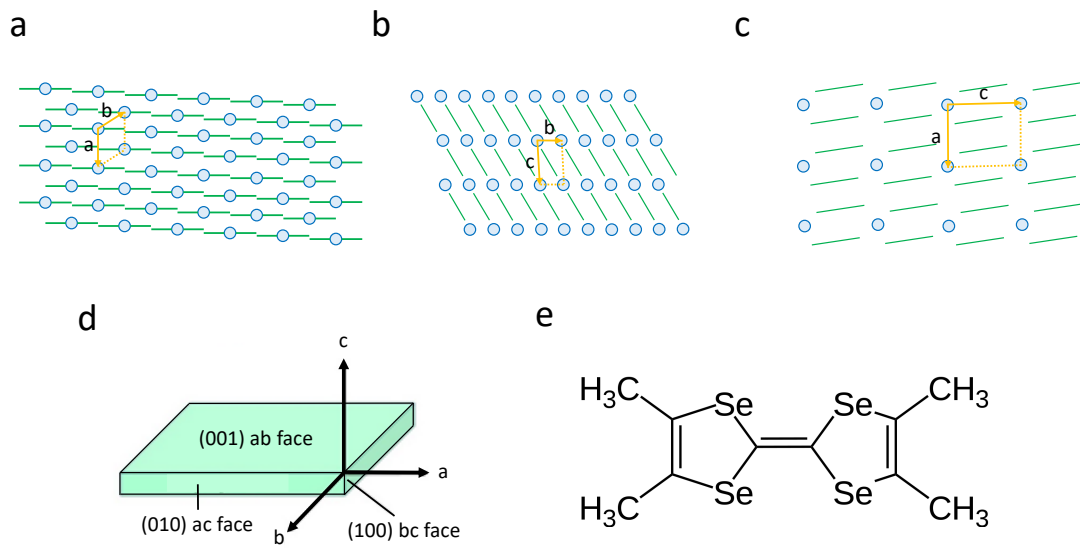


Fig. 4.1 a,b and c are top views of ab, bc and ac planes. d. Is showing different crystallographic planes and e displays the TMTSF molecule, adopted from [112]

the ab plane (c^* in Fig. 4.2). The transition to a SDW ground state is seen between 10 and 20 K by a large increase in resistivity in this material.

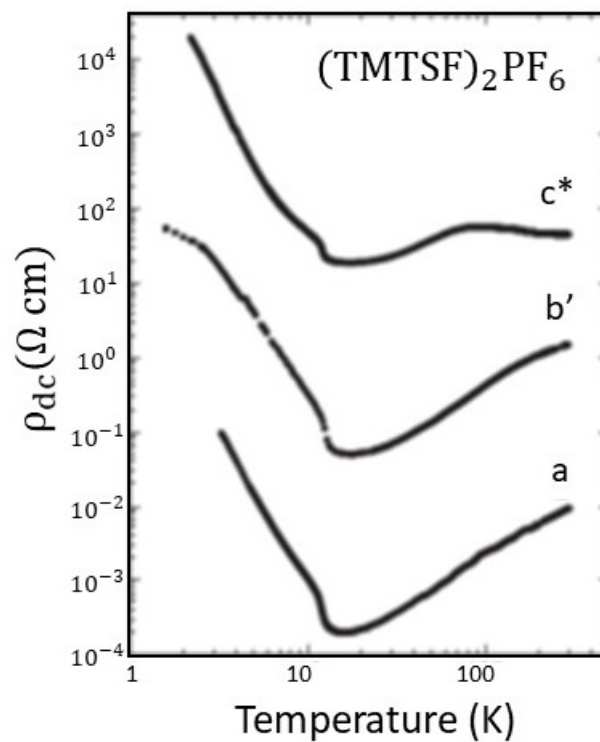


Fig. 4.2 Resistivity measurement along different crystallographic directions of $(\text{TMTSF})_2\text{PF}_6$ [114]

In the $(\text{TMTSF})_2\text{X}$ family the SDW instability at low temperature is favored and stabilized by a one-dimensional Fermi surface with small warping, together with electron-electron repulsion at quarter filling due to correlations. The quarter filling originates from one electron being taken by the counterion (PF_6^- or ClO_4^-) from two nearest-neighbour TMTSF molecules. The resulting Q-1D fermi surface is shown in Fig. 4.3 and clearly explains the quasi-1D properties.

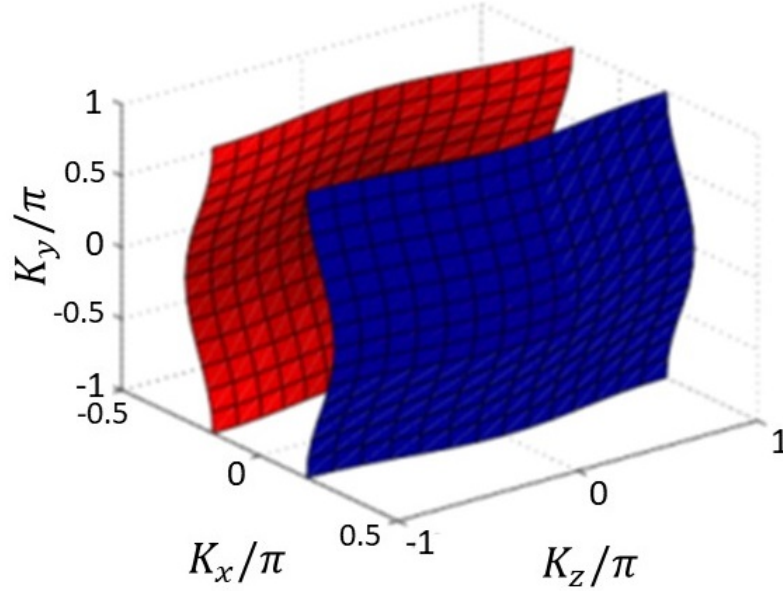


Fig. 4.3 calculated fermi surface of $(\text{TMTSF})_2\text{PF}_6$ [115]

The isomorphous compound $(\text{TMTSF})_2\text{PF}_6$ based on the sulfur-based fulvalene donor molecule has allowed the construction of a generic phase diagram (T - P) for $(\text{TM})_2\text{X}$ (TM = TMTSF or TMTTF) in which the one-dimensional character of these materials is dominant for all of their physical properties. In addition, the close proximity between the antiferromagnetic and superconducting ground states of the materials $(\text{TM})_2\text{X}$, the deviation from the metallic phase from the traditional Fermi-liquid behavior, was recognized in the early 1980s. The possibility of a pairing mechanism involving carriers on neighboring chains in these Q1D conductors avoiding the Coulomb repulsion has been proposed by Emery in the context of the phonon exchange mechanism [116]. Subsequently, the possibility for the pairing emerging from antiferromagnetic fluctuations has been suggested, although, superconducting pairing would in turn emerge with the exchange of charge density waves proposed by Kohn and Luttinger in the context of a new pairing mechanism in low-dimensional conductors [117].

Furthermore, the quasi-one-dimensionality of these conductors should manifest itself not only in the nature of the SC pairing but also in the behavior of various properties of the normal state, differing from those of a regular Fermi liquid. This is supported by experimental evidence of a power law temperature dependence followed by the resistivity of conducting $(\text{TMTSF})_2\text{X}$ compounds below room temperature, which is reminiscent of the theoretical expectation of weakly coupled Luttinger chains [118, 119]. Regarding the low temperature regime, the possibility of non conventional pairing mechanism has been investigated by thermodynamic mea-

surements and also by a determination of the density of states at the Fermi level through various junction devices. $(\text{TMTSF})_2\text{ClO}_4$ being the only member of the $(\text{TMTSF})_2\text{X}$ family displaying a superconducting ground state below 1.2 K under ambient pressure, it is the reason why this is the material on which most sophisticated experiments have been conducted. The temperature dependence of the spin lattice relaxation rate in its superconducting state under zero applied magnetic field using a field cycling experiment was consistent with either an anisotropic s-singlet or a p triplet superconducting gap. While the s-wave scenario had received some support from early specific heat data looking like a BCS behaviour [120], NMR Knight shift experiments tended to favor a triplet coupling [121].

This experimental controversy has been settled after new experimental results in the superconducting phase came out, specific heat and Se^{77} NMR relaxation [122] establishing conclusively the singlet nature of the pairing and a linear energy dependence of the superconducting gap in the vicinity of line nodes on the Fermi surface. In addition, a field-angle-resolved calorimetry of $(\text{TMTSF})_2\text{ClO}_4$ succeeded in mapping the nodal gap structure [123].

A very direct way to access the quasi-particle density-of-states of the superconducting phase is given by tunneling spectroscopy [124]. Several attempts have been performed using different tunneling setups. Early experiments used a n-doped GaSb Schottky barrier evaporated onto a $(\text{TMTSF})_2\text{PF}_6$ single crystal down to 50 mK under a pressure of 11 Kbar [125]. It provided evidence of a well developed gap $2 \approx 3.6$ meV at the Fermi level, interpreted as a superconducting gap, persisting above T_c . Subsequent $(\text{TMTSF})_2\text{ClO}_4$ studied at ambient pressure revealed similar results and evidenced also the role of the cooling speed. An estimation of the SDW gap of $2\Delta_{\text{SDW}} \approx 6\text{meV}$ was given [126]. Further SIS experiment using $(\text{TMTSF})_2\text{ClO}_4$ -amorphous Si-Pb junctions, revealed a much smaller superconducting energy gap in the ordered state of $2\Delta \approx 0.8\text{meV}$ and an SDW gap of $2\Delta_{\text{SDW}} \approx 3\text{meV}$ [127].

At low temperature, the SDW transition is derived from a $2k_F$ exchange interaction between conducting electrons. There are subtle differences among the behaviors of $(\text{TMTSF})_2\text{PF}_6$ and $(\text{TMTSF})_2\text{ClO}_4$. The reason for this is that the PF_6^- ion is centrosymmetric and the ClO_4^- ion is noncentrosymmetric. This will result in ClO_4^- ions occupying two equivalently stable positions in the crystal structure, while PF_6^- can only occupy one. Thus, at high temperature, the ClO_4^- ion will continuously switch between the two stable positions. However, while the material is cooled down, the ClO_4^- ions will choose a particular position below 25K, resulting in an order. The formation of large domains of ordered ions is subject to the speed of cooling. While slow cooling will stabilize large domains of the ordering with the same positions, fast cooling helps to retain disorder in the anion ordering at low temperature. More details can be found in the literature . [105, 128, 115, 129, 130]

Different orderings of the ClO_4^- ions have a profound effect on the ground state of the material. It has been shown that if $(\text{TMTSF})_2\text{ClO}_4$ is cooled slowly, it will show unconventional superconducting properties at temperatures bellow $T_c = 1.3\text{K}$ [110, 131, 132]. This is because of the fact that new ions will strongly dimerize the TMTSF molecules, which will result in a doubling of the bands and will completely reshape the Fermi surface. However, when the sample is sufficiently fast cooled at temperatures below 25K, the material will transition to an SDW state, with an insulating ground state stabilized at temperatures below 4-5 K [128, 133, 134].

In this situation, due to the ion disorder, the band structure is not reconstructed and the Fermi surface remains similar to the one shown in Fig. 4.3. Here the origin of the SDW instability is the same as the $(\text{TMTSF})_2\text{PF}_6$ system. A schematic figure of the resistivity versus temperature dependence of $(\text{TMTSF})_2\text{ClO}_4$ in three different cooling rate regimes, including fast, intermediate and slow rate, is shown in Fig. 4.4.

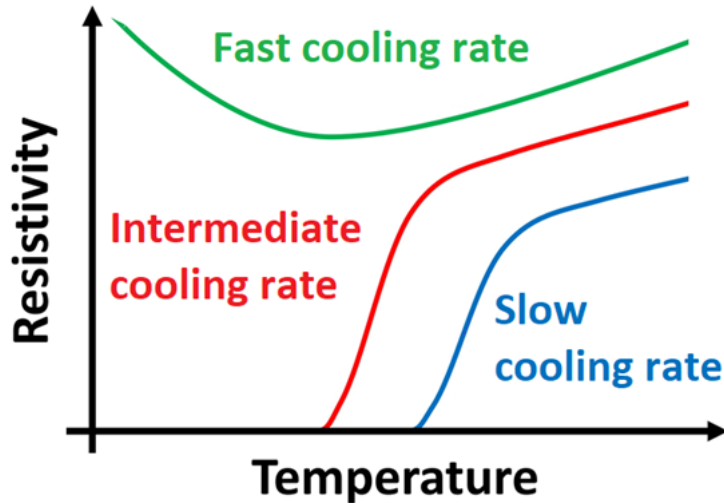


Fig. 4.4 Schematic picture showing different cooling rate regimes (adapted from [130])

Interestingly, the local electronic properties of this material are expected to change a lot depending on the cooling rate. That is, even for a slow-cooled material, one expects to find few regions with disordered regions, thus insulating phase. The opposite is true for the fast-cooled sample, ordered regions with superconducting character that should exist. In a study done by Claire Marrache and Denis Jérôme, it has been shown that when the disorder in the system increases (upon fast cooling), a crossover from a homogeneous 'd-wave' superconducting state at low cooling rates to a granular superconducting state at faster cooling rates (intermediate cooling) also occurs. Granular superconductivity means that superconducting puddles are embedded in a normal or poorly metallic background and are connected through the proximity effect [105]. The motivation behind our project is to search for inhomogeneous local electronic properties showing the interplay between superconducting and SDW regions in the moderate cooling rates.

4.2 Results and discussion

Topographic images of the $(\text{TMTSF})_2\text{ClO}_4$ sample will be presented in this chapter together with structural analysis. The local density of states (LDOS) and also LDOS maps at different energies have also been measured.

Measurements were made at two different temperatures, 300 mK and 2.2K. The sample was cooled to these temperatures at a very low cooling rate (around 0.02 K/min) below 45K to reach a very good anion ordering, allowing us to reach a superconducting state below T_c . The typical

cooling of the sample is quantified in a graph in Fig. 4.4 down to around 5K, then the sample is cooled faster to 2.2K but was cooled slower to 300mK.

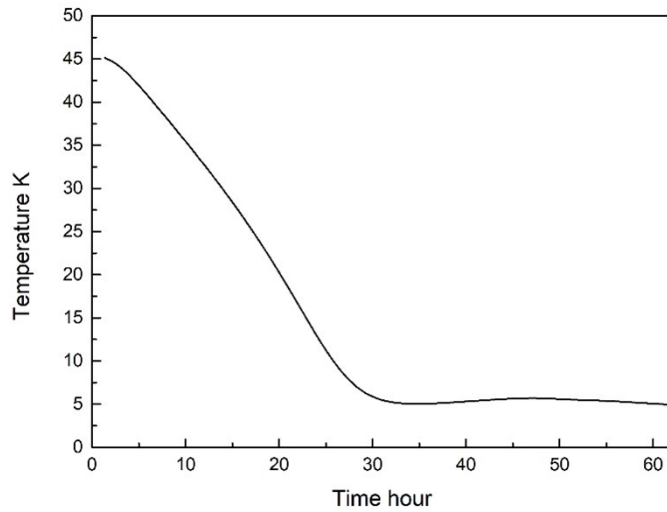


Fig. 4.5 Typical cooling rate curve between 45 K and 5 K

When probing the electronic structure of the sample using the LDOS measurements technique with STS in a low bias range, we found conducting and insulating types of regions. There are regions in the sample where the tip does not change nor interact with the surface plane of the sample. In these regions, the spectroscopic measurements have been performed in the top plane of the surface of the sample. Additionally, we found that there are other regions of the sample in which the tip changes the surface by digging into the sample because these regions are not well connected to the electrodes and/or are insulating. In these regions, while performing spectroscopic measurement, the tip digs several tens of nanometers below the surface plane in order to find conducting or superconducting planes. The mechanism behind these different regions might be due to i) the cleavage process locally removing a large fraction of the anions and ii) there might exist regions where anions are disordered, thus insulating. In the following, these two different behaviors are presented.

4.2.1 surface spectroscopy

Fig. 4.6 shows a large-scale topographic image that corresponds to the a-b plane of the sample (area $410 \times 325 \text{ nm}^2$) at 300mK. The monoatomic steps separating flat terraces of size 100 nm in width can be well seen. The height of the steps was measured to be 1.49 nm on average from the profile taken from the topographic image (Fig. 4.6), which is in agreement with the value reported for the lattice constant along the c direction ($c = 1.33 \text{ nm}$) with an error of slightly larger than 10%)

Subsequently, a 64×64 grid of $I(V)$ curves was measured in this region on a flat atomic terrace of size $8 \times 8 \text{ nm}^2$ area at 300mK and later at 2K. The average of all dI/dV curves was measured in an energy range of $[-4, +4] \text{ meV}$. Filtering of the data is performed as discussed in

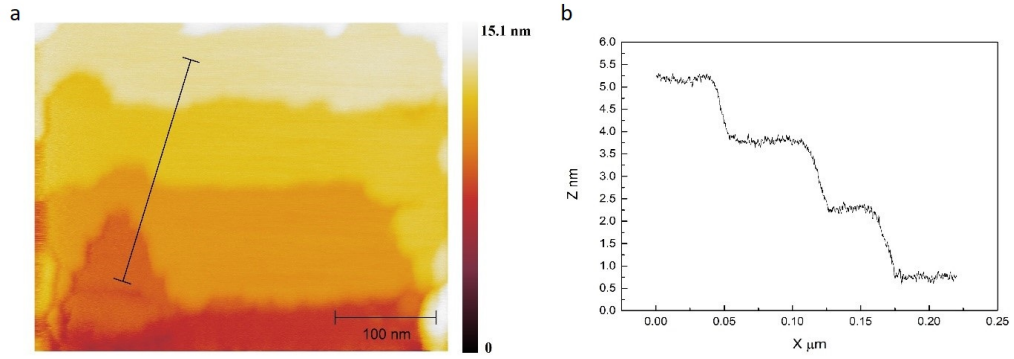


Fig. 4.6 a) large scale $410 \times 325 \text{ nm}^2$ topographic image measured in constant current mode with $V = -0.1 \text{ V}$ and $I=50 \text{ pA}$, b) profile measured along the direction shown in a.

Chapter 1.

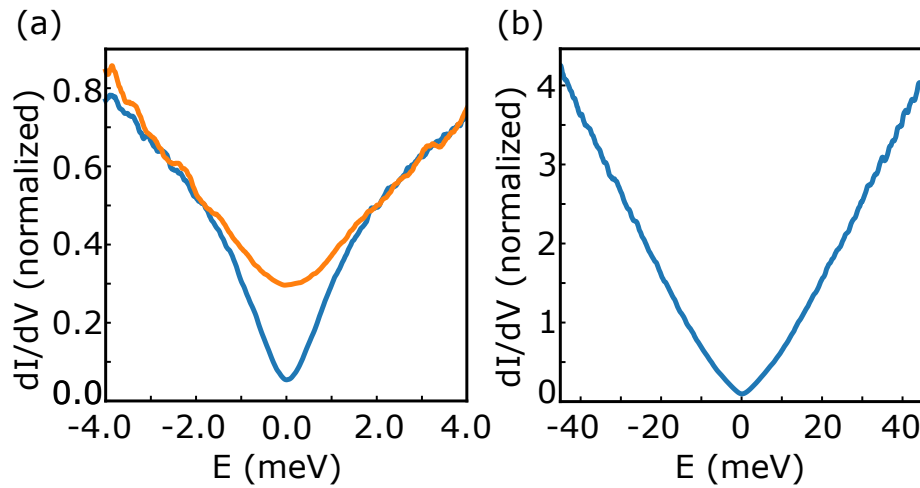


Fig. 4.7 a. Differential tunneling conductance dI/dV spectra measured in the energy range $[-4;+4] \text{ mV}$ with the following set-point for STS: $I = 300 \text{ pA}$ and $V = -9 \text{ mV}$. Each presented spectrum is the average of a 60×60 STS grid measured at $T = 300 \text{ mK}$ (yellow spectrum) or $T = 2.13 \text{ K}$ (blue spectrum) over the same homogeneous area of $8 \times 8 \text{ nm}^2$.

From the resistivity measurement presented in the literature, the sample should be in the normal state at 2K. As can be seen in the orange curve in Fig. 4.7a, there is also a depletion of DOS near the Fermi surface, which is an indication of a bad metal due to the strong electron correlation existing in this material. At 300 mK the average LDOS shows a larger depletion in the density of states near the Fermi level, which remains also finite at the Fermi level, as can be seen in Fig. 4.7a. By comparing the behaviors of LDOS at 2K and also 300 mK, a change in the slope can be seen in the density of states at 1K and around 1 meV. This energy is compatible with what might be expected from the superconducting gap of this material. The shape of dI/dV spectra that shows no coherence peaks and an almost linear dependence below 1 meV is consistent with the d-wave superconductivity expected for this material [135]. The ratio of $\Delta/k_b T_c$ is estimated to be 10. Indeed, as discussed in chapter 1 the superconducting gap is much larger in d-wave superconductors than the theoretical value calculated on the basis of the

BCS theory.

In addition to the low-energy scale dI/dV measurements, the dI/dV curves of the normal and superconducting states were also measured at the same area as shown before in Fig. 4.7a in larger scale $[-40, 40]$ meV which is 50 times the superconducting energy gap. (see Fig. 4.7b). The LDOS shows a strong V-shaped behavior with a close to linear energy dependence. This points out the strongly correlated quasi-1D character of the LDOS due to quantum criticality that links anti-ferromagnetism with superconductivity in this material [104].

Bulk experiments suggested that maybe the electronic structure at the whole sample should be rather homogeneous of the surface, but other regions revealed that, in fact, the sample surface is showing near-insulating behavior. The region shown in Fig. 4.8 has been studied at 300 mK and has an area of 12×40 nm² and an energy interval of $[-10, 10]$ meV. When grid spectroscopy measurements are performed, the dI/dV map at -1.90 meV is presented in Fig. 4.8.a. The Fig. 4.8.b shows spectroscopy data measured at the three different areas indicated in Fig. 4.8.a.

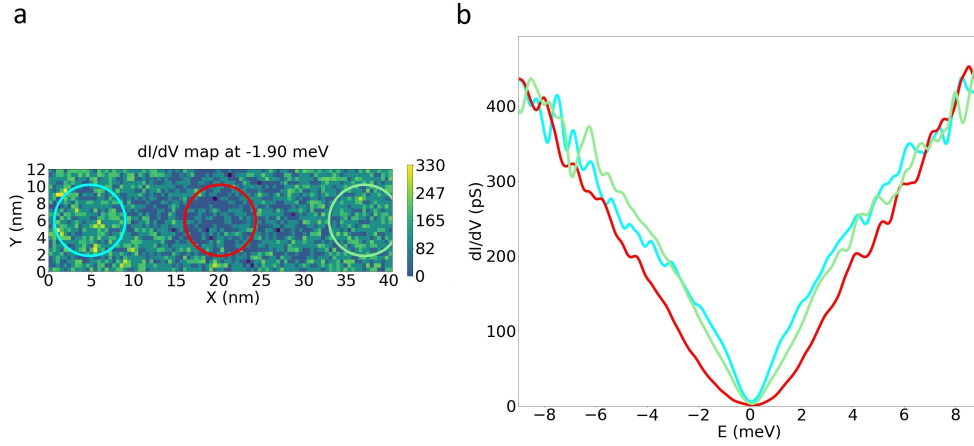


Fig. 4.8 (color online) Measurements performed at $T = 300$ mK. a. Differential tunneling conductance map dI/dV (at -1.90 meV) measured over an area of size 12×40 nm² in the energy range $[-9; +9]$ mV with the following set-point for STS: $I = 300$ pA and $V_{\text{bias}} = -9$ mV. b. Selected $dI/dV(E)$ spectra averaged locally in the conductance map presented in panel 'a'. Three different neighboring regions are seen: left superconducting area (blue spectrum), middle spin-density-wave area (red region), right superconducting area (green spectrum). Each spectrum is the average of about 100 single spectra.

As can be seen in Fig. 4.8 the dI/dV spectra in the two circle-shaped areas on the left part and the right part of the area show a V-shaped DOS below -2 meV, reminding us of the superconducting features observed above.

Strikingly, the middle area also in the circular shape shows a close-to-insulating phase accompanied by a U-shaped spectra. This shows that different parts of the material can have different electronic properties. It can also be inferred from Fig. 4.8 that the length of the superconducting phase is around 10 nm along b' in this region.

4.2.2 near bulk spectroscopy

Another large-scale topographic image with an area of $328 \times 328 \text{ nm}^2$ is presented in Fig. 4.9.a. It has been measured in a different region of the sample with a distance of several hundreds of micrometers from the previous area described previously. Flat atomic terraces with a size of 20 nm can be observed in Fig. 4.9.b. The profile through several atomic terraces is also presented. The average height of the terraces is measured to be 1.57 nm, which is larger than previously reported and is greater than 10 % of error with respect to the lattice parameter c . This suggests a symmetric increase of the c lattice parameter at the surface with respect to the bulk reference value.

The periodic unit cell is presented in topographic image in Fig. 4.9.c. This area was measured in the yellow window shown in Fig. 4.9.a. The lattice constant along the a and b directions was determined to be 8.1 and 8.9 Å, respectively, with an angle of approximately $\gamma = 70^\circ$. Although the angle is consistent with the crystallographic value, the lattice constants a and b are larger by 11 % and 16% respectively with respect to what has been reported in the literature: $a = 7.27$ and $b = 7.7$ Å [136]. The STM is well calibrated, and since the angle between the lattice directions is the same as that reported before, this enlargement in the lattice constant cannot be due to the measurements but seems intrinsic to the material. The reason for this behavior is still not well known, but it might be due to an increase in lattice constants resulting from expansion of the crystal in every direction because of the ultrahigh vacuum or because charge transfer is affected after cleavage. Another reason might be due to a distortion in the crystal structure after the cleavage process.

Fig. 4.9.d shows the topographic image taken after a measurement of a grid spectroscopy map in the low-energy range in the area shown by a black square in Fig. 4.9.a. From the profile in Fig. 4.9.e taken through the center of this area, it can be seen that the tip has dug into the surface, leaving a hole with a depth of 18 nm behind. This behavior was not seen in previous spectroscopic measurements because the sample surface remained unchanged. This new effect is interpreted as revealing the areas of the sample that are strongly insulating below the sample surface. When the resistance of such areas is higher than the tunnel resistance required by the STM feedback loop, the tip digs into the surface to find conducting regions. For the low bias set-point spectroscopy that has been used, such as $V = -10\text{mV}$ and $I = 100\text{-}200 \text{ pA}$, the tip must be displaced at minimum (10-15 layers) to obtain the set-point tunneling current. It should be noted that these experiments are also done at UHV and since the spectroscopic features are very similar to the ones that which the tip did not dig into the surface, we believe that the tip is still in tunneling condition while doing spectroscopic measurements despite digging to the surface.

In this kind of region, since the tip is digging into the surface, the grid spectroscopy at low bias does not correspond to that of the surface but to the interior of the sample (typically between several nanometers and 15-20 nanometers deep). Interestingly, it has been found that the dI/dV curves show local signatures with different spectroscopic properties: superconducting, metallic, or insulating.

This shows that the interior of the sample also has inhomogeneous regions that can be probed by penetrating the surface of the sample. The following spectroscopic map was taken at 300mK and in the energy range of $[-10,10] \text{ meV}$ in a $20 \times 20\text{nm}^2$. It shows three different behaviors.

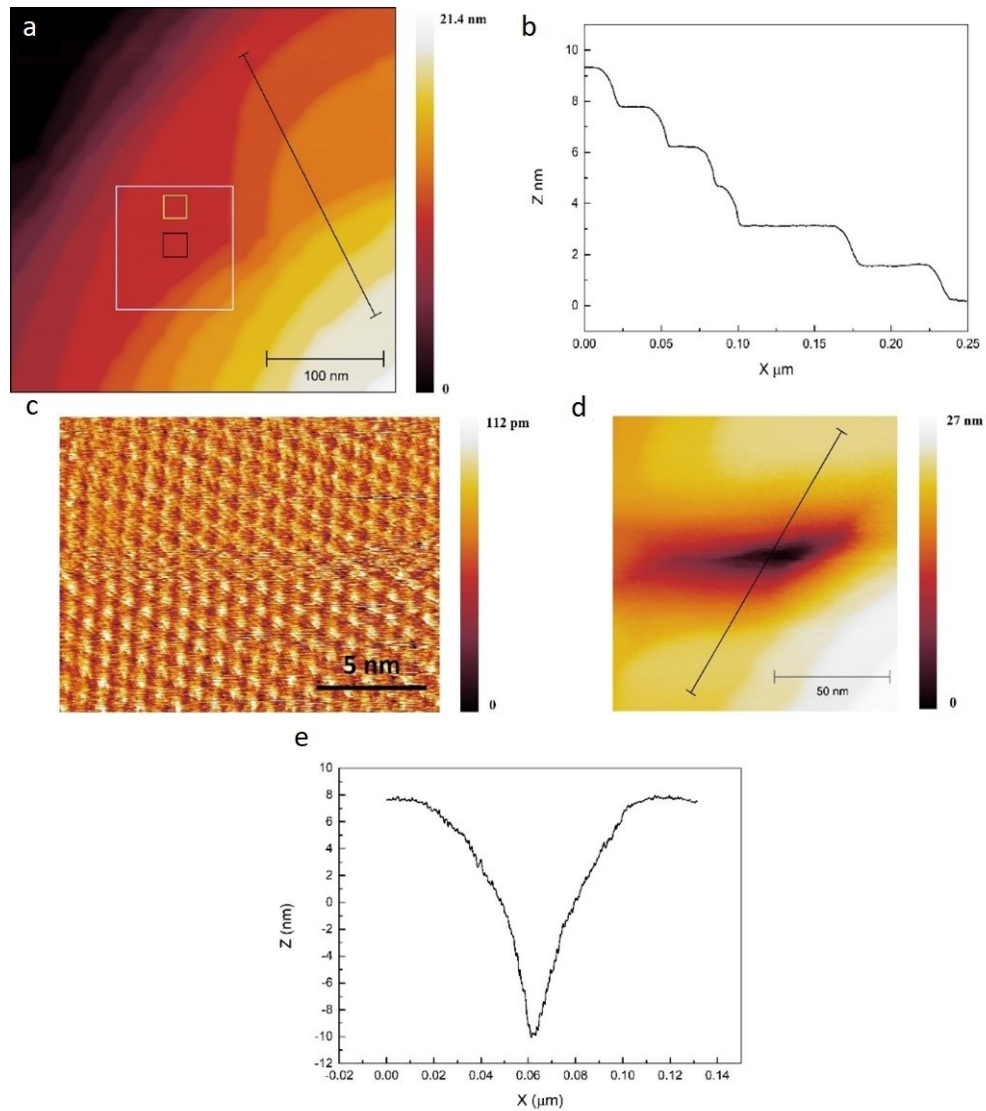


Fig. 4.9 a. Large scale $328 \times 328 \text{ nm}^2$ topographic image measured at $V = -0.05 \text{ V}$ and $I = 50 \text{ nA}$. b Z profile taken along the direction shown in a. c. Atomic resolution of a periodic unit cell pattern measured at $V = -0.1 \text{ V}$ and $I = 50 \text{ nA}$ in the blue window shown in d. Large scale topographic image taken at $V = -0.1 \text{ V}$ and $I = 50 \text{ nA}$ in the large green area after grid spectroscopy was performed in the black window shown in a. and e Z-profile taken along the line shown in d.

These regions can be displayed by showing an LDOS map at -2.2 meV . The three different circles are shown in Fig. 4.10a and their corresponding average spectra are shown in Fig. 4.10b. Superconducting, insulating, and bad metal behaviors can be seen in these different regions. Because the tip dug into the surface of the sample during this measurement, all the individual dI/dV measurements were not necessarily done at the very same sample plane below the surface.

While the low-energy scale spectroscopy leaves a hole on the sample surface because of its low set-point current and voltage, larger energy-scale spectroscopies leave the surface unchanged, meaning that above $+50 \text{ meV}$ the surface plane is always probed. However, also at larger energy scale, local spectroscopy measurements can also show inhomogeneous electronic properties. An example is shown in Fig. 4.11.a measured at 300 mK between $[-100, 100] \text{ meV}$

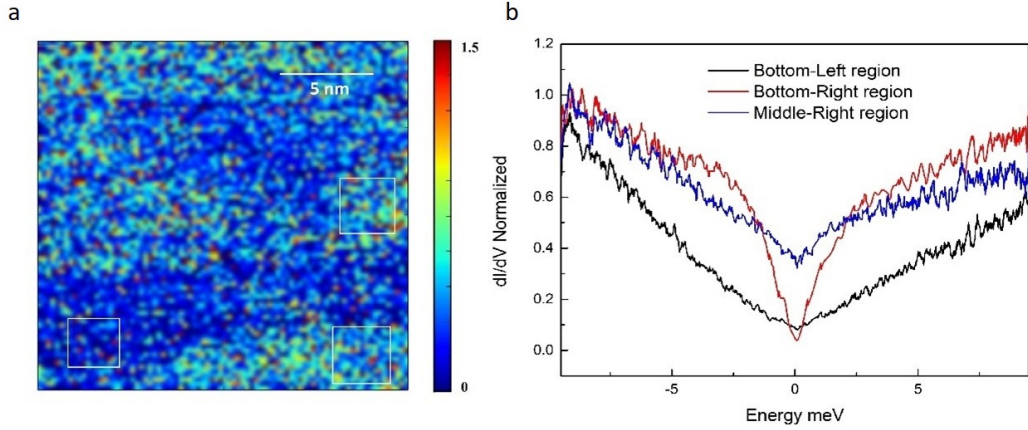


Fig. 4.10 a. dI/dV map taken at -2.2 meV at 300 mK while digging in a window of $20 \times 20 \text{nm}^2$ and b. corresponding average dI/dV curves measured between $[-10,10]$ meV in each different square region indicated in a.

on a $32 \times 32 \text{nm}^2$ area. Four different regions with a V-shaped behavior and slightly different dependence are observed (Fig. 4.11.b). This is consistent with the fact that the electronic properties are inhomogeneous on most samples, such as those on the surface of the sample.

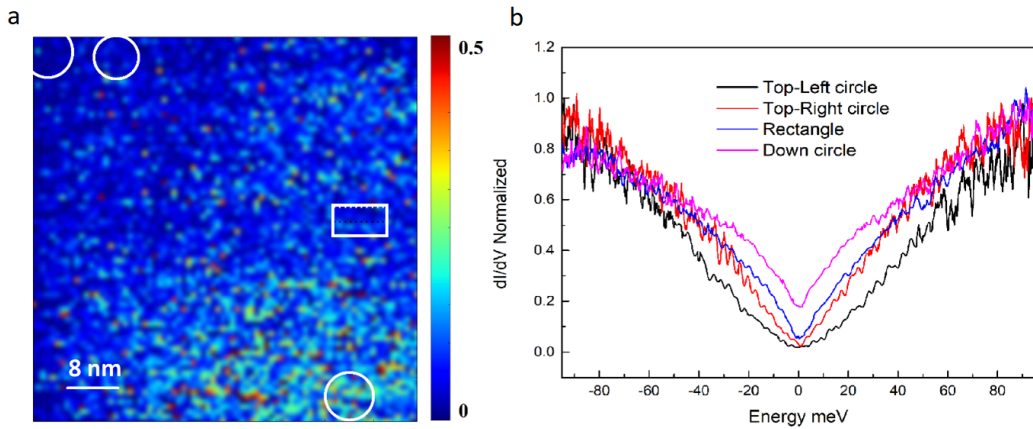


Fig. 4.11 a. Spectroscopy map taken at 0.4 meV at 300 mK while digging and b. dI/dV curve measured and averaged in an interval of $[-100,100]$ meV in four regions as indicated in a.

Now in this same sample region where the large energy scale measurement was performed, the grid spectroscopy map was also measured for a low energy scale of $[-10, 10]$ meV at 300 mK. Insulating, close to insulating, and metallic regions can be seen in this area and are presented in Fig. 4.12. In this measurement again the surface was altered and the tip dug in to the surface.

As can be seen in Fig. 4.12 and the blue curve shows a close to insulating behavior while the red and violet curves show metallic and close to metal behavior. we anticipated that by depositing lead on top of the sample surface, the conductivity of the sample will increase, because of a charge transfer between the lead adatoms and the surface. However, due to the very low wettability of the surface by the lead atoms, they form large drop-shaped islands on top of the surface, leaving the space between the lead atoms empty. This configuration of the lead atoms

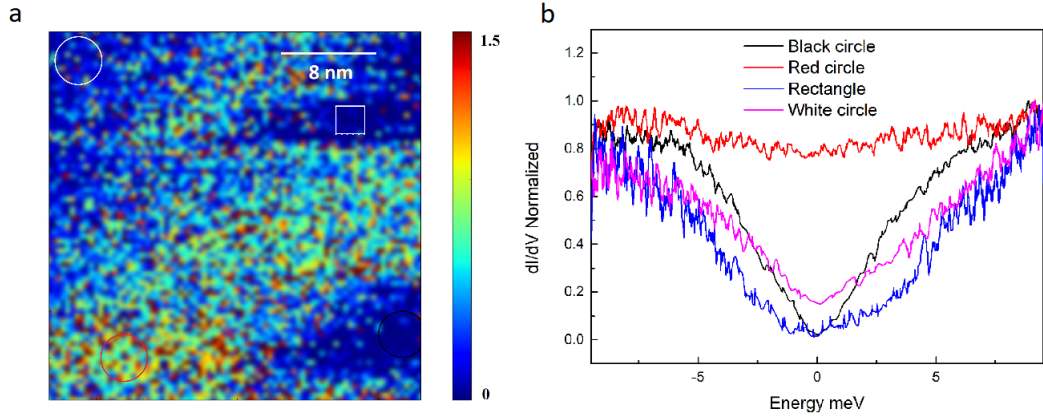


Fig. 4.12 a. dI/dV map measured from a grid STS performed on the same area as in Fig. 4.11. The dI/dV map is taken at E_f (0 meV) at 300 mK while digging and b. dI/dV curve measured and averaged in an interval of $[-10,10]$ meV in the four different regions indicated in a.

does not help to make the surface of the sample conduct, and it was observed that the lead deposition did not change the electronic structure of the system after the deposition. A similar behavior as presented above was again observed.

4.2.3 Magnetic field dependence

To confirm that the gap that we saw while measuring the $TMTSF_2ClO_4$ sample corresponds to a superconducting gap, spectroscopy measurements under magnetic field has been conducted as follows: a very small scale spectroscopic grid was launched and at the same time the magnetic field was turned on and increased with a ramp of 0,05 T/hr. The results of the magnetic field measurements are shown in Fig. 4.13 which shows the averaged density of states in three different magnetic fields. As can be seen in Fig. 4.13 the gap starts to fill and the LDOS at the Fermi level increases with increasing the magnetic field which is another indication of a superconducting gap which is consistent with the bulk critical field along c^* which is between 0.1 a,d 0.2 T depending on the experiment.

4.2.4 discussion

The energy dependence of the STS spectra associated with superconducting regions is linear-like in the energy gap region and always presents a finite LDOS. This is not consistent with an s-wave order parameter but reminds what is observed in d-wave Cuprates superconductors by STS [137]. On the other hand, non-magnetic disorder in the ClO_4 anions lattice can be expected as a result of the cleaving process to create local defects. A more natural explanation compatible with point group symmetry could then be a d-wave symmetry where line nodes would give a linear energy dependent DOS in the superconducting energy gap, consistent with angular specific heat measurements [20]. Moreover, for a d-wave symmetry nonmagnetic point defect would behave as a pair breaker leading to additional gap filling as observed in our experiments.

From electronic bandstructure calculations, a strongly V-shaped LDOS is not expected around E_F [138]. The existence of a quasi-1D bandstructure could lead to a k-parallel tun-

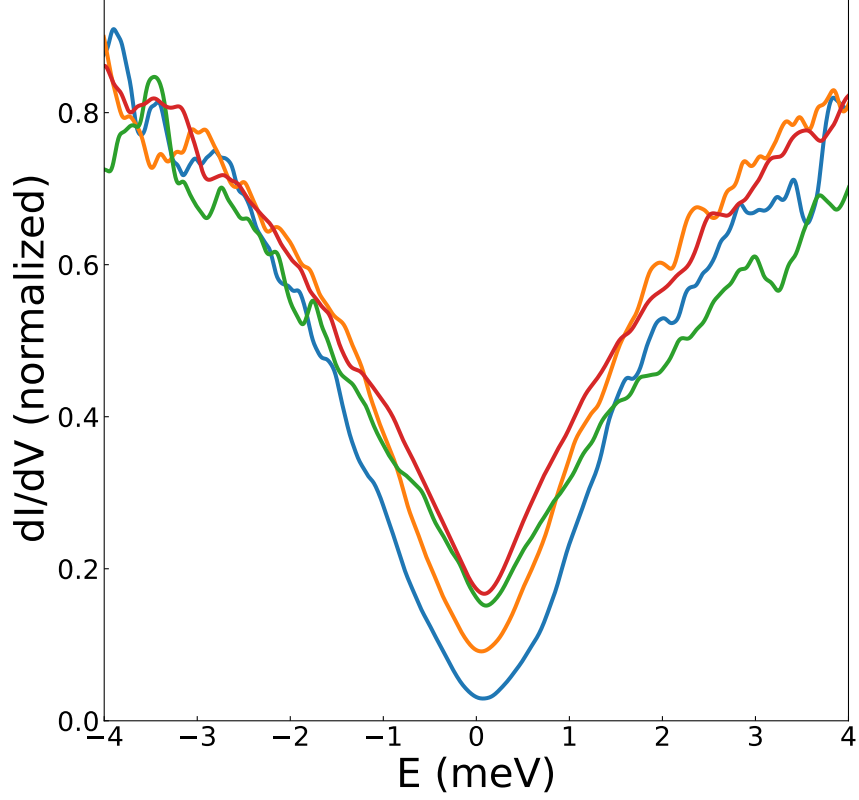


Fig. 4.13 magnetic field dependence of the density of states which corresponds to, blue line: 0T, orange line: 0.1T, green line: 0.2 T and red line: 0.3 T.

neling dependence but not as strong as to induce such a fast increase as observed in our case over only 40 meV assuming a reasonable sample work function of at least one eV. A more reasonable explanation is that we measure an intrinsic V-shaped LDOS due to the quasi-1D correlated electronic LDOS not described by DFT calculations accompanied by an additional Altshuler-Aronov component [139, 140].

This latter component is likely to be linked with an increase in the anions disorder as well as with possible other types of structural defects induced by the cleavage process which would lead to highly resistive surface planes having a resistance not negligible anymore with respect to the resistance quantum. As to correlation component to the density of states, one can look at the results of the renormalization group approach to the density of states of the quasi-1D electron gas model of a d-wave superconductor [104]. The expression for the differential tunneling conductance at temperature T is given by:

$$\frac{dI}{dV} = G_{nn} \int_{-\infty}^{+\infty} \bar{N}_s(E) \left[-\frac{\delta f(E + eV)}{\delta(eV)} \right] dE, \quad (4.2)$$

Where G_{nn} is the normal conductance of the junction and $f(E)$ is the Fermi distribution. The normalized density of states of the d-wave quasi-1D superconductor can be put in the form

$$\bar{N}_s(E) = \bar{N}_n(E) \left\langle \text{Re} \frac{|E + i\Gamma|}{\sqrt{(E + i\Gamma)^2 - \Delta^2(k_{\perp})}} \right\rangle_{k_{\perp}} \quad (4.3)$$

Where $\Delta(K_{\perp}) = \Delta \cos K_{\perp}$ is the d-wave SC gap for an open quasi-1D Fermi surface, K_{\perp} the transverse wave vector, Γ is the scattering rate on impurities; $\langle \dots \rangle_{K_{\perp}}$ stands for an average over the transverse wave vector and $v\bar{N}_n(E)$ is the metallic state density of states for $vE > \Delta$. The latter is formally related to the one-particle Green function, namely $v\bar{N}_n(E) = \frac{-2}{N_0} \frac{1}{V} \sum_K \text{Im}G(K, E)$. Following a renormalization group calculation carried out by Claude Bourbonnais and Abdelouahab Sedeki at the two-loop level for the coherent part of the Green function G in the framework of the quasi-1D electron gas model, the expression for the coherent contribution to the normal density of states, $v\bar{N}_n = \langle z(k_{\perp}, E) \rangle_{k_{\perp}}$, is related to an effective energy scale dependent quasiparticle weight z . The RG calculations show a V-shape reduction of the density of states as a function of energy for $|E| > \Delta$, as a result of strong quantum fluctuations that emerge close to the QCP tied to the succession antiferromagnetic and superconducting ground states under pressure [104]. This reduction is followed at lower $|E| < \Delta$ by the characteristic dip in the density of states for a d-wave superconductor in Eqn. 4.3.

We have calculated These theoretical features in collaboration with Claude Bourbonnais and Abdelouahab Sedeki and they are displayed in Fig. 4.14 in the low energy range where they are confronted to experiments at $T = 200$ mK. The calculations are obtained with $T_c = 0.7K$ ($\sim \Delta/1.76$), a value for T_c close to the QCP in the quasi-1D electron gas model and reduced from its optimal values (1K) by impurities scattering $\Gamma/\Delta = 0.4$.

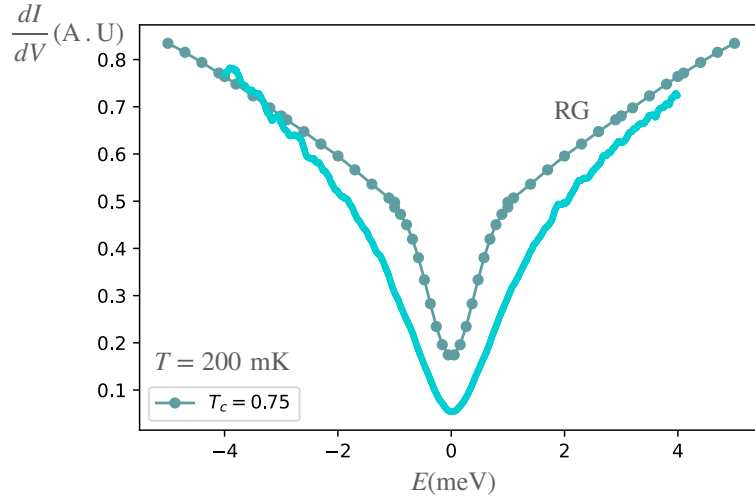


Fig. 4.14 Comparison of the renormalization group prediction(dotted line) and STM experiments for the density of states at $T = 300$ mK.

4.2.5 conclusion

The LDOS measurement of the surface of this material shows regions that are more conducting and regions that are less conducting, which in the latter the tip digs into the surface leaving a hole with a height of around 18 nm. Topographic images of the sample show lattice parameters that are larger than those reported in the literature by 10 % or even higher than 10 % in regions that are less conducting. We suggest that this change in the lattice parameter is due to an expan-

sion inside the ultra-high vacuum plus the charge transfer effect linked to the cleavage process. It has been found that different regions of the sample have different ground state properties with superconducting, metallic bad metal, and near-insulating phases appearing during LDOS measurements. The superconducting gap was found to be around 1 meV and the coherence length of the superconducting phase was found to be around 10 nm along b' . Since the deposition of lead on the sample did not change the electronic properties, it is highly recommended to deposit lead in a controlled way to better contact the surface with the electrodes.

CHAPTER 5

Superconductivity in $\text{KTaO}_3/\text{Al}_2\text{O}_3$

5.1 Introduction

Heterostructures based on KTaO_3 gained a lot of interest after the discovery of superconductivity in two-dimensional electron gases (2-DEG) at the interfaces of KTaO_3 and various overlayers in the beginning of the year 2021, like: EuO [141], LaAlO_3 [142] and AlO_x [143] with a T_c that can go as high as 2.2 K for a doping level of $\approx 1.04 \times 10^{14} \text{e}^- \cdot \text{cm}^{-2}$ [141]. Like SrTiO_3 [144], KTaO_3 can be used in many applications like spintronics [145], orbitronics [146, 147] and in topological quantum computing [148].

In this chapter we are going to present some rare tunneling spectroscopy measurement on a superconducting in the two-dimensional electron gas that forms at the interface of two insulators, KTaO_3 (substrate) and Al_2O_3 (top layer) at low temperatures. Such system is generally not suitable for STM and up to now only one experiment of planar tunneling has been reported so far in a similar system $\text{LaAlO}_3/\text{SrTiO}_3$. We have tried to develop a method that made it feasible for us to measure the superconducting gap using STS on this material for the first time. However due to bias voltage noise due to a bad grounding, that was discussed in chapter 2, the gap was strongly broadened. We will start our discussion by giving a general introduction on this type of materials and then we will give our temperature and magnetic dependent STS results.

5.2 Buried 2-d superconductivity in $\text{KTaO}_3/\text{Al}_2\text{O}_3$

It was recently discovered that superconductivity is found at the surface of Potassium Tantalate, KTaO_3 where a 2DEG forms. KTaO_3 is a band insulator with a large gap of 3.6 eV with a cubic perovskite structure even at very low temperatures [149]. Recently S. Malik et al. have shown that 2-DEG can be generated at the surface of a (111)-oriented KTaO_3 crystal by simply sputtering a very thin Al layer. Evidenced by X-ray photoelectron spectroscopy (XPS) the Ta ions will be reduced by deposition of Al leading to an interfacial gate tunable in-plane superconducting 2-DEG. While different thickness ratios of Al and KTaO_3 can lead to different formulation of $\text{AlO}_x/\text{KTaO}_3$ [143], in this study the deposition and the sample thickness ratio was tuned to have $\text{Al}_2\text{O}_3/\text{KTaO}_3$, samples are provided by UMR CNRS-THALES and more details about sample preparation is given in ref. [143]. It should be noted that the thickness of the Al layer in our sample is 8\AA the T_c and B_c of this material are reported to be around 1 K and 1 T respectively. Although there are transport measurement available in the literature for

this material it has never been measured using scanning tunneling spectroscopy which can give a clearer resolution of the electronic properties and reveal the nature of superconducting phase.

5.2.1 Topography and Point spectroscopy measurement

We have started our measurements by performing topography images at 4 K. As it can be seen in Fig. 5.1, the STM image shows an amorphous surface which corresponds to the insulating Al_2O_3 overlayer. To perform point spectroscopy measurement we have to dig the tip into the sample to pass some current throughout the insulating overlayer to reach the buried 2-DEG superconducting phase.

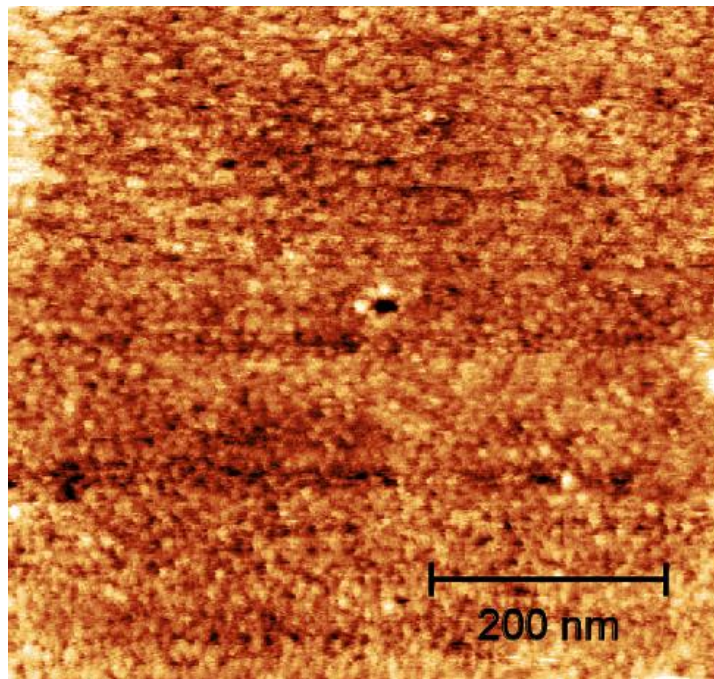


Fig. 5.1 600×600 topographic image taken from the surface of the $\text{AlO}_x/\text{KTaO}_3$ sample

We have performed point spectroscopy measurement at various temperatures and we have found a V shape depletion around the Fermi level at 600 mK as can be seen Fig. 5.2 which might correspond to a broadened superconducting gap. The main reason for the broadening might be because at the time of this measurement the Nanonis electronics that we use for M3 setup were not well grounded as was mentioned in chapter 2, thus the differential conductance doesn't go to zero. Indeed performing measurement from 600 mK at the superconducting state up to the normal state at 1.6 K shows an increase in the value of the density of states at the Fermi level meaning the gradual disappearance of the superconducting gap. Unfortunately, such a poor energy resolution does not give access to pertinent information on the symmetry of the order parameter.

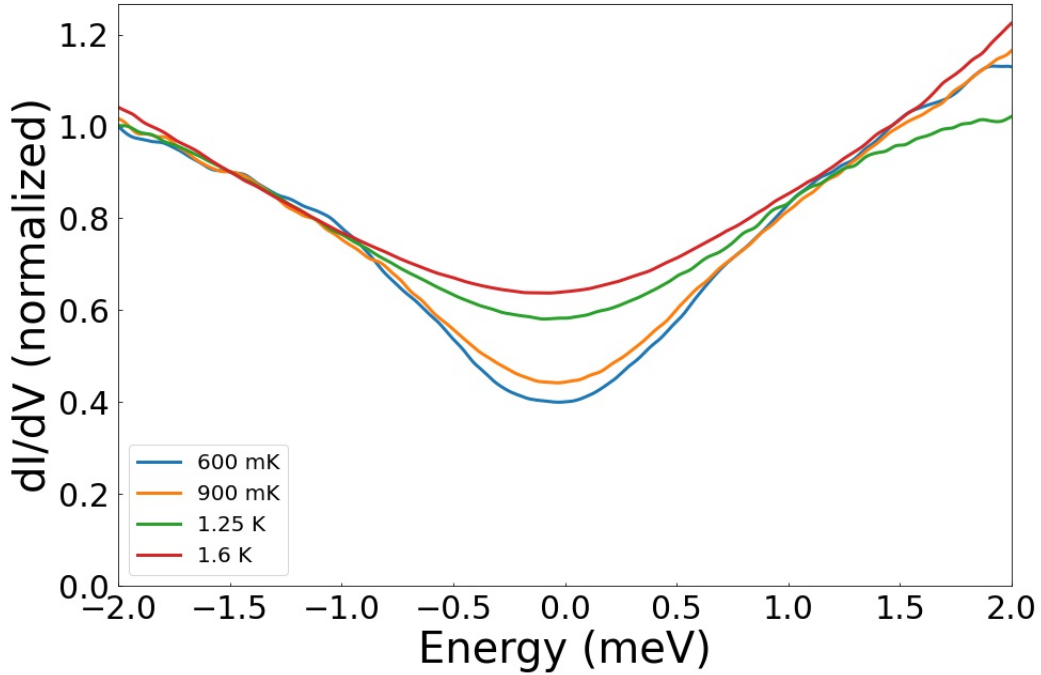


Fig. 5.2 point spectroscopy measurement in an interval of $[-2, 2]$ meV at different temperatures ranging from 600 mK to 1.6 K.

5.2.2 spectroscopic map

Despite the thick oxide layer covering the two-dimensional electron gas we could manage to perform scanning tunneling spectroscopy experiments. Fig. 5.3 shows the way that these measurements have been performed. The tip is gently moving right above the sample while scanning between the grid points of the spectroscopic map. Then, in order to perform spectroscopic measurements at the grid points, the tip is dig into the sample as discussed in the previous subsection. This sewing machine mode seems not to destroy the sample which is quite resilient.

Fig. 5.4 shows a spectroscopic map measured on this sample and as it can be seen in the average spectra of the circles that there are regions that show superconductivity while others show a wider depletion corresponding to a normal state. This can be interpreted as the fact that the Al deposition was not homogeneous over the $\text{KTaO}_3(111)$ surface leading to an inhomogeneous 2-DEG layer due to the fact that the Ta ions are not reduced in the same way over the sample. We have also performed magnetic field dependence spectroscopic measurements on this sample by acquiring spectroscopic maps at different magnetic fields, however we couldn't preserve the same position to perform these measurements. The reason is because the sample holder was made from stainless steel, so by changing the magnetic field the sample holder was subject to a huge magnetostriction which prevented us from following a given region as a function of the magnetic field. Thus taking into account the inhomogeneity of the sample and the fact that the superconducting gap will not have the same feature at different areas it was hard to perform a precise magnetic field dependence study on this sample. The average spectra of the maps at zero and 0.2 T are

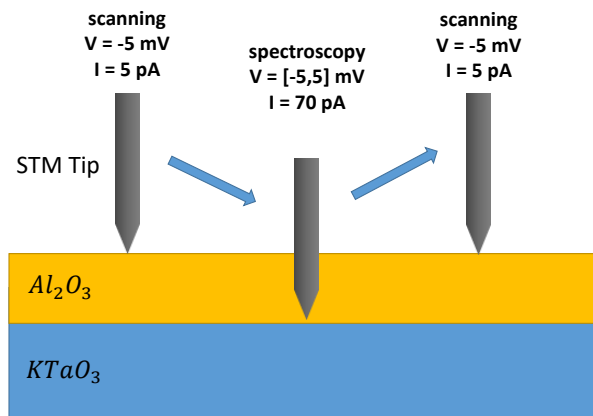


Fig. 5.3 Schematic figure a new method for spectroscopic map measurements by scanning at low current between the grid points of the spectroscopic map and measuring the spectra at higher current by digging the tip to the sample to reach the 2-DEG at the grid points of the spectroscopic map.

shown in Fig. 5.5, it can clearly be seen that the zero energy density of states in the vicinity of the gap will start to rise at higher magnetic field.

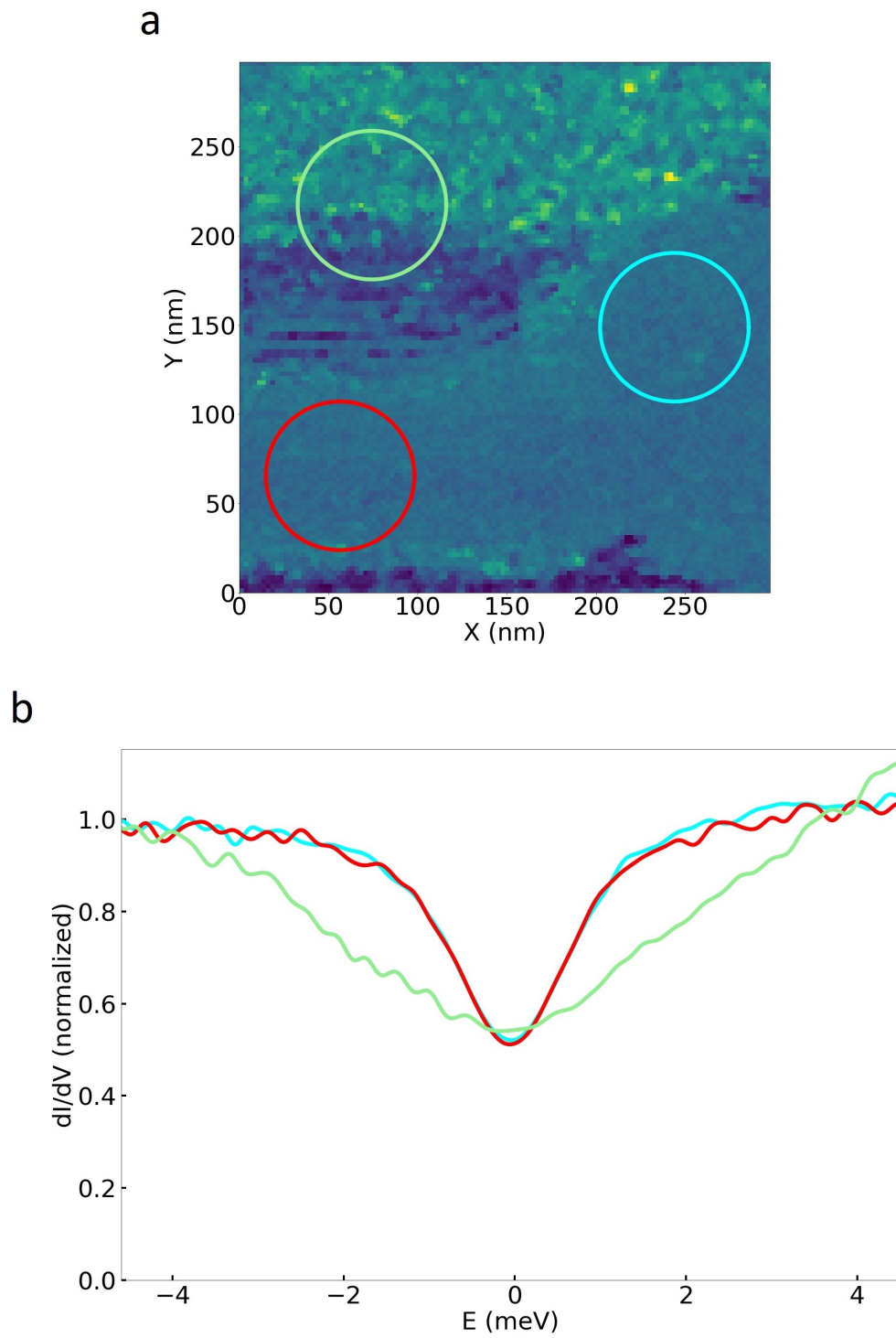


Fig. 5.4 a. Spectroscopic map at the Fermi level b. Average spectra of the map in an energy interval of $[-4.5, 4.5]$ meV (the color of the curves in b corresponds to color of the circles in a)

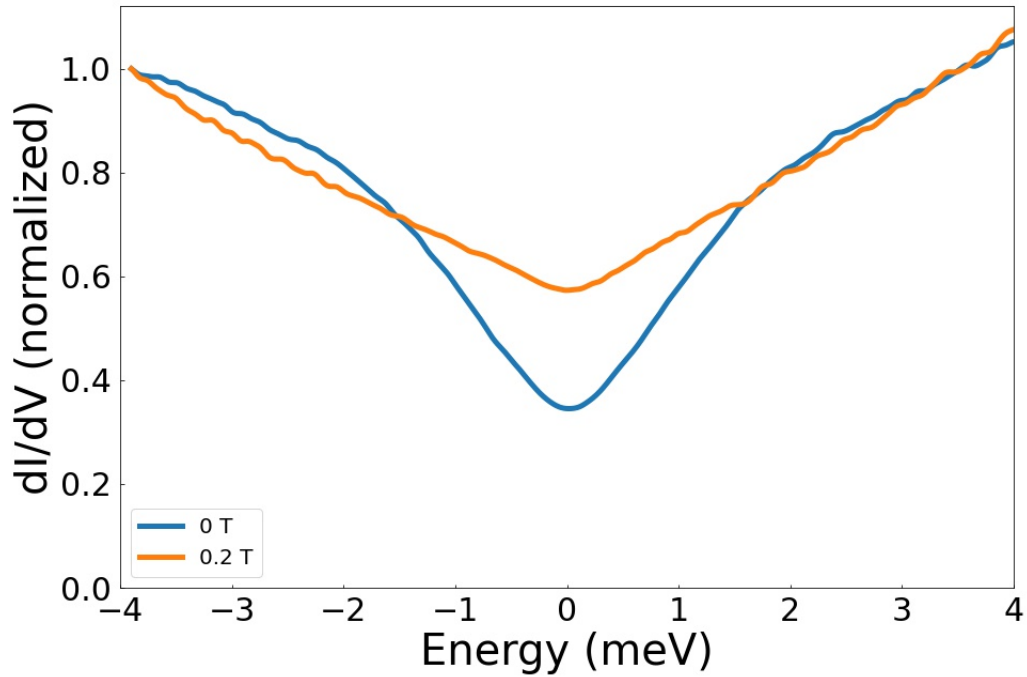


Fig. 5.5 LDOS measured at 0 and 0.2 Tesla, an increase in the density of state at the Fermi level can be observed.

5.2.3 discussion

For the first time, STM and STS measurements were performed on the superconducting 2-DEG layer at the interface of two insulating materials ($\text{KTaO}_3/\text{Al}_2\text{O}_3$). The superconducting gap couldn't be measured properly because of the experimental broadening. Due to the heterogeneous distribution of the Aluminum overlayer the superconducting phase is not homogeneously spread over the 2-DEG layer. For future work it is suggested to use a thinner overlayer in order to have more accuracy in measuring the 2-DEG by not digging to deep into the insulating layer. It is also suggested to use non-magnetic sample holders in order to have precise magnetic field dependence measurement of the superconducting gap over a fixed region.

Conclusion

In the framework of studying systems that show correlation effects and unconventional superconductivity, I will give a summary of the results that have been obtained during this thesis. The studied systems are as follows: Sn/Si(111), Pb/Ge(111), (TMTSF)₂ClO₄ and KTO/Al₂O₃.

In the first part of this thesis, we have explained our most important results which is on the α -Sn/Si(111). Our first aim was to study its transition to a superconducting state while hole doping by segregation of Boron atom to the surface upon heating a highly P-doped sample. Unfortunately, because of problems of both vibrations/noise in our STM and of a large delay induced by studying the clean undoped phase, it was not possible to study this part of our project. However, we have observed that in the undoped regime for α -Sn/Si(111) a large gap of 650 meV develops at temperatures below about 20 K. The results of QPI measurements show a spot corresponding to a row-wise antiferromagnetic order with a $2\sqrt{3} \times \sqrt{3}$ super lattice structure. These results together with the DFT calculation considering exchange-interaction between Sn and Si atoms indicates a Slater-type of ground state for this system.

Weitering et al. have performed experiments on doped α -Sn/Si(111) and have found a chiral d-wave superconducting state. However, their previous assumption of a small gap Mott-insulating phase in the undoped regime (n-doped Sn/Si(111)) was not correct. Another point in their study that is unclear is that they have assumed that the superconductivity is of chiral d-wave nature by assuming the fact that it can be suppressed by non-magnetic Sn adatoms and Si substitutional defects. However, the non-magnetic nature of these defects is not very clear since it should be true if the system is in a Mott insulator, which we have proven to be incorrect. Using other defects such as 'K', which can only be non-magnetic for future work is recommended. Furthermore, we have also studied other interesting phenomena like edge states and artificial molecules. The artificial molecules showed bonding and anti-bonding orbitals, further DFT calculations are suggested to prove these results. Finally, we have done a Multifractal analysis on the α -Sn/Si(111) and we have seen that the defects induced Anderson localization on the electronic states situated close to the gap edge of α -Sn/Si(111). We believe that the localization coherence length can be changed by changing the energy of the electrons; however, our results can be improved by studying larger scale images and also different densities of defects.

Another system we have studied is the α -Pb/Ge(111), which has been shown to have a transition to a 3×3 structure at low temperatures. Although our goal was to obtain spectroscopic maps in this phase and study the properties of QPIs, due to the stabilization of a disordered phase called the labyrinth phase, it was not possible to find homogeneous regions of α -Sn/Si(111) with a size more than $10 \times 10 \text{ nm}^2$. However, we have performed point spectroscopy measurements on 4 different phases of Pb/Ge(111), which are the 3×3 , the disordered 3×3 , 4×4 and β - $\sqrt{3} \times \sqrt{3}$. For future work, it is suggested to make the Pb deposition at low temperatures and do the annealing at temperatures no more than the room temperature, this can help to have larger areas of 3×3 reconstruction.

In addition, we have performed STS measurements for the first time on two types of unconventional superconductors, the cleaved (TMTSF)₂ClO₄ and the interfacial 2-DEG devel-

oped at the interface of KTaO_3 and Al_2O_3 . We have observed a V-shape pseudo-gap for $((\text{TMTSF})_2\text{ClO}_4)$ which does not go exactly to zero. We believe this is due to the nodal behavior of d-wave superconductivity and also due to the suppression of the gap due to non-magnetic surface disorder (induced by cleavage). In addition to the superconducting state, we have observed several other phases such as metallic, bad metal, and spin-density-wave insulating phases. We attribute this to either the granular nature of this material or the disorder induced by the cleavage process. The result of renormalization group calculations of the excitation spectra in the superconducting state fits very well with our experimental results. Since the deposition of lead on the sample did not change the electronic properties, it is highly recommended to deposit lead in a controlled way to better contact the surface with the electrodes, i.e. at low temperature.

Our results on the superconducting 2-DEG at the interface of KTaO_3 and Al_2O_3 , also showed a V shape pseudo-gap which does not go to zero; however, it gets suppressed at temperatures higher than $T_c \approx 1\text{K}$ and higher magnetic fields. Unfortunately, at the time of our measurements, we have switched our electronics from MATRIX to NANONIS and since the new electronics was not very well calibrated yet on a reference superconducting sample, we could not have enough resolution on the superconducting gap. Also, the sample holder was made from stainless steel, and while performing continuous magnetic field measurements the sample was moving, making it difficult for us to have an exact magnetic field dependent measurement. It is suggested to perform the measurements again, since the calibration problem of the NANONIS electronics is solved, and to use molybdenum sample holders instead of stainless steel.

REFERENCES

- [1] J. G. Bednorz and K. A. Müller. Possible high T_c superconductivity in the BaLaCuO system. *Zeitschrift für Physik B Condensed Matter*, 64(2):189–193, 1986.
- [2] M. K. Wu, J. R. Ashburn, C. J. Torng, P. H. Hor, R. L. Meng, L. Gao, Z. J. Huang, Y. Q. Wang, and C. W. Chu. Superconductivity at 93 k in a new mixed-phase y-ba-cu-o compound system at ambient pressure. *Physical Review Letters*, 58(9):908–910, 1987.
- [3] N F Mott. The basis of the electron theory of metals, with special reference to the transition metals. *Proceedings of the Physical Society. Section A*, 62(7):416–422, 1949.
- [4] Michael Tinkham. *Introduction to Superconductivity*. Courier Corporation, 2004.
- [5] J. Bardeen, L. N. Cooper, and J. R. Schrieffer. Microscopic theory of superconductivity. *Physical Review*, 106(1):162–164, 1957.
- [6] N. N. Bogoljubov. A new method in the theory of superconductivity. i. *Sov. Phys. JETP*, 7:41–46, 1958.
- [7] Raphael Leriche. *Unconventional superconductivity in quasi-2D materials with strong spin-orbit coupling*. PhD thesis, 2019. Thèse de doctorat dirigée par Cren, Tristan et Brun, Christophe Physique de la matière condensée Sorbonne université 2019.
- [8] Md Atikur Rahman, Md Zahidur Rahaman, and Md Nurush Samsuddoha. A review on cuprate based superconducting materials including characteristics and applications. *American Journal of Physics and Applications*, 3(2):39, 2015.
- [9] P.W. Anderson. Theory of dirty superconductors. *Journal of Physics and Chemistry of Solids*, 11(1):26–30, 1959.
- [10] A. A. Abrikosov and L. P. Gor'kov. Contribution to the theory of superconducting alloys with paramagnetic impurities. *Zhur. Eksptl'. i Teoret. Fiz.*, 39, 1960.
- [11] L Yu. Bound state in superconductors with paramagnetic impurities. *Acta Physica Sinica*, 21(1):75, 1965.
- [12] A I Rusinov. Superconductivity near a paramagnetic impurity. *JETP Lett. (USSR) (Engl. Transl.); (United States)*, 9:85–87, 1969.
- [13] W. Bauriedl, P. Ziemann, and W. Buckel. Electron-tunneling observation of impurity bands in superconducting manganese-implanted lead. *Physical Review Letters*, 47(16):1163–1165, 1981.

- [14] Hiroyuki Shiba. Classical spins in superconductors. *Progress of Theoretical Physics*, 40(3):435–451, 1968.
- [15] K. J. Franke, G. Schulze, and J. I. Pascual. Competition of superconducting phenomena and kondo screening at the nanoscale. *Science*, 332(6032):940–944, 2011.
- [16] Gerbold C. Ménard, Christophe Brun, Raphaël Leriche, Mircea Trif, François Debontridder, Dominique Demaille, Dimitri Roditchev, Pascal Simon, and Tristan Cren. Yu-shiba-rusinov bound states versus topological edge states in Pb/Si(111). *The European Physical Journal Special Topics*, 227(15-16):2303–2313, 2019.
- [17] Gerbold C. Ménard, Sébastien Guissart, Christophe Brun, Stéphane Pons, Vasily S. Stolyarov, François Debontridder, Matthieu V. Leclerc, Etienne Janod, Laurent Cario, Dimitri Roditchev, Pascal Simon, and Tristan Cren. Coherent long-range magnetic bound states in a superconductor. *Nature Physics*, 11(12):1013–1016, 2015.
- [18] A. V. Balatsky, I. Vekhter, and Jian-Xin Zhu. Impurity-induced states in conventional and unconventional superconductors. *Reviews of Modern Physics*, 78(2):373–433, 2006.
- [19] A. J. Millis, Subir Sachdev, and C. M. Varma. Inelastic scattering and pair breaking in anisotropic and isotropic superconductors. *Physical Review B*, 37(10):4975–4986, 1988.
- [20] R. J. Radtke, K. Levin, H.-B. Schüttler, and M. R. Norman. Predictions for impurity-induced t_c suppression in the high-temperature superconductors. *Physical Review B*, 48(1):653–656, 1993.
- [21] Ali Yazdani, B. A. Jones, C. P. Lutz, M. F. Crommie, and D. M. Eigler. Probing the local effects of magnetic impurities on superconductivity. *Science*, 275(5307):1767–1770, 1997.
- [22] Catherine Kallin and John Berlinsky. Chiral superconductors. *Reports on Progress in Physics*, 79(5):054502, 2016.
- [23] Annica M Black-Schaffer and Carsten Honerkamp. Chiralid/i-wave superconductivity in doped graphene. *Journal of Physics: Condensed Matter*, 26(42):423201, 2014.
- [24] R. Peierls, R.E. Peierls, and R.E. Peierls. *Quantum Theory of Solids*. International series of monographs on physics. Clarendon Press, 1955.
- [25] G. Grüner. The dynamics of charge-density waves. *Reviews of Modern Physics*, 60(4):1129–1181, 1988.
- [26] D. E. Moncton, J. D. Axe, and F. J. DiSalvo. Neutron scattering study of the charge-density wave transitions in $2H - TaSe_2$ and $2H - NbSe_2$. *Physical Review B*, 16(2):801–819, 1977.
- [27] J.A. Wilson, F.J. Di Salvo, and S. Mahajan. Charge-density waves and superlattices in the metallic layered transition metal dichalcogenides. *Advances in Physics*, 24(2):117–201, 1975.

- [28] S. van Smaalen. The peierls transition in low-dimensional electronic crystals. *Acta Crystallographica Section A: Foundations of Crystallography*, 61(1):51–61, 2005.
- [29] Wen Wen, Chunhe Dang, and Liming Xie. Photoinduced phase transitions in two-dimensional charge-density-wave $1t\text{-}2a_2^*$. *Chinese Physics B*, 28(5):058504, 2019.
- [30] Jeffrey G. Rau, Eric Kin-Ho Lee, and Hae-Young Kee. Spin-orbit physics giving rise to novel phases in correlated systems: Iridates and related materials. *Annual Review of Condensed Matter Physics*, 7(1):195–221, 2016.
- [31] X. Y. Zhang, M. J. Rozenberg, and G. Kotliar. Mott transition in the $d=1$ hubbard model at zero temperature. *Physical Review Letters*, 70(11):1666–1669, 1993.
- [32] M. B. J. Meinders, H. Eskes, and G. A. Sawatzky. Spectral-weight transfer: Breakdown of low-energy-scale sum rules in correlated systems. *Phys. Rev. B*, 48:3916–3926, 1993.
- [33] A. Camjayi, R. Chitra, and M. J. Rozenberg. Electronic state of a doped mott-hubbard insulator at finite temperatures studied using the dynamical mean-field theory. *Physical Review B*, 73(4), 2006.
- [34] C. Davisson and L. H. Germer. Diffraction of electrons by a crystal of nickel. *Physical Review*, 30(6):705–740, 1927.
- [35] K.W. Kolasinski. *Surface science: Foundations of catalysis and nanoscience*, 2002.
- [36] Gerd Binnig and Heinrich Rohrer. Scanning tunneling microscopy—from birth to adolescence. *Reviews of Modern Physics*, 59(3):615–625, 1987.
- [37] G. Binnig, H. Rohrer, Ch. Gerber, and E. Weibel. 7×7 reconstruction on Si(111) resolved in real space. *Physical Review Letters*, 50(2):120–123, 1983.
- [38] Dawn Bonnell. *Scanning probe microscopy and spectroscopy: theory, techniques, and applications*. John Wiley and Sons, 2000.
- [39] J. Tersoff and D. R. Hamann. Theory and application for the scanning tunneling microscope. *Phys. Rev. Lett.*, 50:1998–2001, Jun 1983.
- [40] S. H. Pan, E. W. Hudson, and J. C. Davis. Vacuum tunneling of superconducting quasiparticles from atomically sharp scanning tunneling microscope tips. *Applied Physics Letters*, 73(20):2992–2994, 1998.
- [41] Masahiro Haze, Hung-Hsiang Yang, Kanta Asakawa, Nobuyuki Watanabe, Ryosuke Yamamoto, Yasuo Yoshida, and Yukio Hasegawa. Bulk ferromagnetic tips for spin-polarized scanning tunneling microscopy. *Review of Scientific Instruments*, 90(1):013704, 2019.
- [42] M. F. Crommie, C. P. Lutz, and D. M. Eigler. Imaging standing waves in a two-dimensional electron gas. *Nature*, 363(6429):524–527, 1993.

- [43] C. Brand, S. Muff, M. Fanciulli, H. Pfnür, M. C. Tringides, J. H. Dil, and C. Tegenkamp. Spin-resolved band structure of a densely packed Pb monolayer on Si(111). *Physical Review B*, 96(3):035432, 2017.
- [44] Philipp Leicht, Julia Tesch, Samuel Bouvron, Felix Blumenschein, Philipp Erler, Luca Gragnaniello, and Mikhail Fonin. Rashba splitting of graphene-covered au(111) revealed by quasiparticle interference mapping. *Physical Review B*, 90(24):241406, 2014.
- [45] C. Tresca, C. Brun, T. Bilgeri, G. Menard, V. Cherkez, R. Federicci, D. Longo, F. Debontridder, M. D'angelo, D. Roditchev, G. Profeta, M. Calandra, and T. Cren. Chiral spin texture in the charge-density-wave phase of the correlated metallic Pb/Si(111) monolayer. *Physical Review Letters*, 120(19):196402, 2018.
- [46] Seho Yi, Fangfei Ming, Ying-Tzu Huang, Tyler S. Smith, Xiyou Peng, Weisong Tu, Daniel Mulugeta, Renee D. Diehl, Paul C. Snijders, Jun-Hyung Cho, and Hanno H. Weitering. Atomic and electronic structure of doped Si(111)- $2\sqrt{3} \times 2\sqrt{3}$ R30°-Sn interfaces. *Physical Review B*, 97(19):195402, 2018.
- [47] S. A. de Vries, P. Goettkindt, P. Steadman, and E. Vlieg. Phase transition of a pb monolayer on Ge(111). *Physical Review B*, 59(20):13301–13308, 1999.
- [48] Haruko Toyama, Hong Rui Huang, Tomonori Nakamura, Leonid V. Bondarenko, Alexandra Y. Tupchaya, Dimitry V. Gruznev, Akari Takayama, Andrey V. Zotov, Aleksandr A. Saranin, and Shuji Hasegawa. Superconductivity of Pb ultrathin film on Ge(111) surface. *Defect and Diffusion Forum*, 386:80–85, 2018.
- [49] Etienne Janod, Julien Tranchant, Benoit Corraze, Madec Querré, Pablo Stoliar, Marcelo Rozenberg, Tristan Cren, Dimitri Roditchev, Vinh Ta Phuoc, Marie-Paule Besland, and Laurent Cario. Resistive switching in mott insulators and correlated systems. *Advanced Functional Materials*, 25(40):6287–6305, 2015.
- [50] Patrick A. Lee, Naoto Nagaosa, and Xiao-Gang Wen. Doping a mott insulator: Physics of high-temperature superconductivity. *Reviews of Modern Physics*, 78(1):17–85, 2006.
- [51] Christophe Brun, Tristan Cren, and Dimitri Roditchev. Review of 2d superconductivity: the ultimate case of epitaxial monolayers. *Superconductor Science and Technology*, 30(1):013003, 2016.
- [52] Joseph M. Carpinelli, Hanno H. Weitering, E. Ward Plummer, and Roland Stumpf. Direct observation of a surface charge density wave. *Nature*, 381(6581):398–400, 1996.
- [53] Giuseppe Santoro, Sandro Scandolo, and Erio Tosatti. Charge-density waves and surface mott insulators for adlayer structures on semiconductors: Extended hubbard modeling. *Physical Review B*, 59(3):1891–1901, 1999.
- [54] G. Profeta and E. Tosatti. Triangular mott-hubbard insulator phases of Sn/Si(111) and Sn/Ge(111) surfaces. *Phys. Rev. Lett.*, 98:086401, 2007.

- [55] Gang Li, Philipp Höpfner, Jörg Schäfer, Christian Blumenstein, Sebastian Meyer, Aaron Bostwick, Eli Rotenberg, Ralph Claessen, and Werner Hanke. Magnetic order in a frustrated two-dimensional atom lattice at a semiconductor surface. *Nature Communications*, 4(1):1620, 2013.
- [56] F. Ming, X. Wu, C. Chen, K. D. Wang, P. Mai, T. A. Maier, J. Stroockoz, J. W. F. Venderbos, C. Gonzalez, J. Ortega, S. Johnston, and H. H. Weitering. Evidence for chiral superconductivity on a silicon surface, 2022.
- [57] J M Carpinelli, H H Weitering, M Bartkowiak, R Stumpf, and E W Plummer. Surface charge ordering transition: a phase of Sn/Ge(111). *Physical Review Letter*, 79(15):4, 1997.
- [58] A. V. Melechko, J. Braun, H. H. Weitering, and E. W. Plummer. Role of defects in two-dimensional phase transitions: An STM study of the Sn/Ge(111) system. *Physical Review B*, 61(3):2235–2245, 2000.
- [59] A. Mascaraque, J. Avila, J. Alvarez, M. C. Asensio, S. Ferrer, and E. G. Michel. Nature of the low-temperature 3×3 surface phase of Pb/Ge(111). *Physical Review Letters*, 82(12):2524–2527, 1999.
- [60] R. I. G. Uhrberg and T. Balasubramanian. Electronic structure of the $\alpha - \sqrt{3} \times \sqrt{3}$ and 3×3 periodicities of Sn/Ge(111). *Phys. Rev. Lett.*, 81:2108–2111, 1998.
- [61] Jiandi Zhang, Ismail, P. J. Rous, A. P. Baddorf, and E. W. Plummer. Periodic lattice distortion accompanying the charge-density-wave transition for Sn/Ge(111). *Physical Review B*, 60(4):2860–2863, 1999.
- [62] Jun-Ho Lee, Xiao-Yan Ren, Yu Jia, and Jun-Hyung Cho. Antiferromagnetic superexchange mediated by a resonant surface state in Sn/Si(111). *Physical Review B*, 90(12):125439, 2014.
- [63] Harumo Morikawa, Iwao Matsuda, and Shuji Hasegawa. STM observation of Si(111)- $\alpha - \sqrt{3} \times \sqrt{3}$ -Sn at low temperature. *Phys. Rev. B*, 65:201308, 2002.
- [64] J. Lobo, A. Tejada, A. Mugarza, and E. G. Michel. Electronic structure of Sn/Si(111)- $(\sqrt{3} \times \sqrt{3})R30^\circ$ as a function of sn coverage. *Physical Review B*, 68(23), 2003.
- [65] S. Modesti, L. Petaccia, G. Ceballos, I. Vobornik, G. Panaccione, G. Rossi, L. Ottaviano, R. Larciprete, S. Lizzit, and A. Goldoni. Insulating ground state of Sn/Si(111)- $(\sqrt{3} \times \sqrt{3})R30^\circ$. *Phys. Rev. Lett.*, 98:126401, 2007.
- [66] Fangfei Ming, Steve Johnston, Daniel Mulugeta, TylerS. Smith, Paolo Vilmercati, Geunseop Lee, ThomasA. Maier, PaulC. Snijders, and HannoH. Weitering. Realization of a hole-doped mott insulator on a triangular silicon lattice. *Physical Review Letters*, 119(26):266802, 2017.

- [67] A. B. Odobescu, A. A. Maizlakh, N. I. Fedotov, and S. V. Zaitsev-Zotov. Electronic correlation effects and coulomb gap in the Si(111)-(3×3)-Sn surface. *Physical Review B*, 95(19):195151, 2017.
- [68] F. Ming and *et al.* Realization of a hole-doped mott insulator on a triangular silicon lattice. *Phys. Rev. Lett.*, 119:266802, 2017.
- [69] M. Jäger, C. Brand, A. P. Weber, M. Fanciulli, J. H. Dil, H. Pfnür, and C. Tegenkamp. -sn phase on Si(111): Spin texture of a two-dimensional mott state. *Physical Review B*, 98(16):165422, 2018.
- [70] Xuefeng Wu, Fangfei Ming, Tyler S. Smith, Guowei Liu, Fei Ye, Kedong Wang, Steven Johnston, and Hanno H. Weiering. Superconductivity in a hole-doped mott-insulating triangular adatom layer on a silicon surface. *Physical Review Letters*, 125(11), 2020.
- [71] A. Charrier and *et al.* Contrasted electronic properties of sn-adatom-based($\sqrt{3} \times \sqrt{3}$)R30° reconstructions on Si(111). *Phys. Rev. B*, 64:115407, 2001.
- [72] A. C. Ferrari and J. Robertson. Interpretation of raman spectra of disordered and amorphous carbon. *Phys. Rev. B*, 61:14095–14107, 2000.
- [73] P. Hansmann, T. Ayrál, L. Vaugier, P. Werner, and S. Biermann. Long-range coulomb interactions in surface systems: A first-principles description within self-consistently combined *gw* and dynamical mean-field theory. *Physical Review Letters*, 110(16), 2013.
- [74] J. Mysliveček, A. Stróžeczka, J. Steffl, P. Sobotík, I. Ošťádal, and B. Voigtländer. Structure of the adatom electron band of the Si(111)–7 × 7 surface. *Phys. Rev. B*, 73:161302, Apr 2006.
- [75] Cesare Tresca and Matteo Calandra. Charge density wave in single-layer Pb/Ge(111) driven by Pb-substrate exchange interaction. *Physical Review B*, 104(4), 2021.
- [76] L Simon, C Bena, F Vonau, M Cranney, and D Aubel. Fourier-transform scanning tunnelling spectroscopy: the possibility to obtain constant-energy maps and band dispersion using a local measurement. *Journal of Physics D: Applied Physics*, 44(46):464010, 2011.
- [77] Lan Chen, Peng Cheng, and Kehui Wu. Quasiparticle interference in unconventional 2d systems. *Journal of Physics: Condensed Matter*, 29(10):103001, 2017.
- [78] C.-L. Lin, N. Kawakami, R. Arafune, E. Minamitani, and N. Takagi. Scanning tunneling spectroscopy studies of topological materials. *J. Phys.: Condens. Matter*, 32:243001, 2020.
- [79] C. Tresca and *et al.* Chiral spin texture in the charge-density-wave phase of the correlated metallic Pb/Si(111) monolayer. *Phys. Rev. Lett.*, 120:196402, 2018.
- [80] Prabhakar P Singh. Effects of disorder in FeSe: an *ab – initio* study. *Journal of Physics: Condensed Matter*, 22(13):135501, 2010.

- [81] I.E. Tamm, R. Peierls, B.M. Bolotovskii, and V.Y. Frenkel. *Selected Papers*. Springer Berlin Heidelberg, 2012.
- [82] John T. Yates. Surface science: An introduction. *Physics Today*, 57(10):79–80, 2004.
- [83] David Harte. *Multifractals*. Chapman and Hall/CRC, 2001.
- [84] Firas Gerges, Xialong Geng, Hani Nassif, and Michel C. Boufadel. Anisotropic multifractal scaling of mount lebanon topography: Approximate conditioning. *Fractals*, 29(05):2150112, 2021.
- [85] Plamen Ch. Ivanov, Luís A. Nunes Amaral, Ary L. Goldberger, Shlomo Havlin, Michael G. Rosenblum, Zbigniew R. Struzik, and H. Eugene Stanley. Multifractality in human heartbeat dynamics. *Nature*, 399(6735):461–465, 1999.
- [86] I.V. Lerner. Distribution functions of current density and local density of states in disordered quantum conductors. *Physics Letters A*, 133(4-5):253–259, 1988.
- [87] Alexander D. Mirlin and Yan V. Fyodorov. Distribution of local densities of states, order parameter function, and critical behavior near the anderson transition. *Physical Review Letters*, 72(4):526–529, 1994.
- [88] Michael Schreiber and Heiko Grussbach. Multifractal wave functions at the anderson transition. *Physical Review Letters*, 67(5):607–610, 1991.
- [89] Thomas C. Halsey, Mogens H. Jensen, Leo P. Kadanoff, Itamar Procaccia, and Boris I. Shraiman. Fractal measures and their singularities: The characterization of strange sets. *Physical Review A*, 33(2):1141–1151, 1986.
- [90] Jens Feder. *Fractals*. Springer US, 1988.
- [91] Ashvin Chhabra and Roderick V. Jensen. Direct determination of the $f()$ singularity spectrum. *Physical Review Letters*, 62(12):1327–1330, 1989.
- [92] M. Morgenstern, J. Klijn, Chr. Meyer, and R. Wiesendanger. Real-space observation of drift states in a two-dimensional electron system at high magnetic fields. *Physical Review Letters*, 90(5), 2003.
- [93] K. Hashimoto, C. Sohrmann, J. Wiebe, T. Inaoka, F. Meier, Y. Hirayama, R. A. Römer, R. Wiesendanger, and M. Morgenstern. Quantum hall transition in real space: From localized to extended states. *Physical Review Letters*, 101(25), 2008.
- [94] Anthony Richardella, Pedram Roushan, Shawn Mack, Brian Zhou, David A. Huse, David D. Awschalom, and Ali Yazdani. Visualizing critical correlations near the metal-insulator transition in $\text{Ga}_{1-x}\text{Mn}_x\text{As}$. *Science*, 327(5966):665–669, 2010.
- [95] Kun Zhao, Haicheng Lin, Xiao Xiao, Wantong Huang, Wei Yao, Mingzhe Yan, Ying Xing, Qinghua Zhang, Zi-Xiang Li, Shintaro Hoshino, Jian Wang, Shuyun Zhou, Lin Gu, Mohammad Saeed Bahramy, Hong Yao, Naoto Nagaosa, Qi-Kun Xue, Kam Tuen

- Law, Xi Chen, and Shuai-Hua Ji. Disorder-induced multifractal superconductivity in monolayer niobium dichalcogenides. *Nature Physics*, 15(9):904–910, 2019.
- [96] Berthold Jäck, Fabian Zinser, Elio J. König, Sune N. P. Wissing, Anke B. Schmidt, Markus Donath, Klaus Kern, and Christian R. Ast. Visualizing the multifractal wave functions of a disordered two-dimensional electron gas. *Physical Review Research*, 3(1), 2021.
- [97] Ferdinand Evers and Alexander D. Mirlin. Anderson transitions. *Reviews of Modern Physics*, 80(4):1355–1417, 2008.
- [98] J. Avila, A. Mascaraque, E.G. Michel, and M.C. Asensio. Phase transition of submonolayer Pb/Ge(111): α - $3\times 3R30^\circ \leftrightarrow 3 \times 3at \sim 250$ k. *Applied Surface Science*, 123-124:626–630, 1998.
- [99] E. Tosatti and P.W. Anderson. Spin-density-wave anomaly at 140 k in the ternary iron arsenide bafe_2as_2 . *Jpn. J. Appl. Phys.*, 2S2:381, 1974.
- [100] A. Mascaraque, J. Avila, J. Alvarez, M. C. Asensio, S. Ferrer, and E. G. Michel. Nature of the low-temperature 3×3 surface phase of Pb/Ge(111). *Physical Review Letters*, 82(12):2524–2527, 1999.
- [101] Jiandong Guo, Junren Shi, and E. W. Plummer. Low temperature disordered phase of α -Pb/Ge(111). *Physical Review Letters*, 94(3), 2005.
- [102] Junren Shi, Biao Wu, X. C. Xie, E. W. Plummer, and Zhenyu Zhang. Surface phase transitions induced by electron mediated adatom-adatom interaction. *Physical Review Letters*, 91(7), 2003.
- [103] Denis Jerome and Shingo Yonezawa. Novel superconducting phenomena in quasi-one-dimensional bechgaard salts. *Comptes Rendus Physique*, 17(3-4):357–375, 2016.
- [104] A. Sedeki, D. Bergeron, and C. Bourbonnais. Extended quantum criticality of low-dimensional superconductors near a spin-density-wave instability. *Physical Review B*, 85(16), 2012.
- [105] Shingo Yonezawa, Claire A. Marrache-Kikuchi, Klaus Bechgaard, and Denis Jérôme. Crossover from impurity-controlled to granular superconductivity in $(\text{TMTSF})_2\text{ClO}_4$. *Physical Review B*, 97(1):014521, 2018.
- [106] H. R. Ott. *Ten Years of Superconductivity: 1980–1990*. Springer Science and Business Media, 2012.
- [107] V. J. Emery. Theory of the one-dimensional electron gas. In Jozef T. Devreese, Roger P. Evrard, and Victor E. van Doren, editors, *Highly Conducting One-Dimensional Solids*, Physics of Solids and Liquids, pages 247–303. Springer US, 1979.
- [108] D. Jérôme and H.J. Schulz. Organic conductors and superconductors. *Advances in Physics*, 31(4):299–490, 1982.

- [109] D. Jérôme, A. Mazaud, M. Ribault, and K. Bechgaard. Superconductivity in a synthetic organic conductor $(\text{TMTSF})_2\text{PF}_6$. *Journal de Physique Lettres*, 41(4):95–98, 1980.
- [110] Klaus Bechgaard, Kim Carneiro, Malte Olsen, Finn Berg Rasmussen, and Claus S. Jacobsen. Zero-pressure organic superconductor: Di-(tetramethyltetraselenafulvalenium)-perchlorate $[(\text{TMTSF})_2\text{ClO}_4]$. *Phys. Rev. Lett.*, 46:852–855, 1981.
- [111] A. N. Bloch, D. O. Cowan, K. Bechgaard, R. E. Pyle, R. H. Banks, and T. O. Poehler. Low-temperature metallic behavior and resistance minimum in a new quasi one-dimensional organic conductor. *Physical Review Letters*, 34(25):1561–1564, 1975.
- [112] Shulong Li, Henry S. White, and Michael D. Ward. Scanning tunneling microscopy of the organic conductors $(\text{TMTSF})_2\text{X}$ ($\text{X} = \text{ClO}_4^-$, ReO_4^-). *The Journal of Physical Chemistry*, 96(22):9014–9021, 1992.
- [113] K. Bechgaard, K. Carneiro, F. B. Rasmussen, M. Olsen, G. Rindorf, C. S. Jacobsen, H. J. Pedersen, and J. C. Scott. Superconductivity in an organic solid. synthesis, structure, and conductivity of bis(tetramethyltetraselenafulvalenium) perchlorate, $(\text{TMTSF})_2\text{ClO}_4$. *Journal of the American Chemical Society*, 103(9):2440–2442, 1981.
- [114] SE Brown. Organic superconductors: The bechgaard salts and relatives. *Physica C: Superconductivity and its Applications*, 514:279–289, 2015.
- [115] D. U. Gubser, W. W. Fuller, T. O. Poehler, J. Stokes, D. O. Cowan, M. Lee, and A. N. Bloch. Resistive and magnetic susceptibility transitions in superconducting $(\text{TMTSF})_2\text{ClO}_4$. *Molecular Crystals and Liquid Crystals*, 79(1):581–590, 1982.
- [116] V.J Emery. The mechanisms of organic superconductivity. *Synthetic Metals*, 13(1-3):21–27, 1986.
- [117] W. Kohn and J. M. Luttinger. New mechanism for superconductivity. *Physical Review Letters*, 15(12):524–526, 1965.
- [118] J. Moser, M. Gabay, P. Auban-Senzier, D. Jérôme, K. Bechgaard, and J.M. Fabre. Transverse transport in organic conductors: possible evidence for a luttinger liquid. *The European Physical Journal B*, 1(1):39–46, 1998.
- [119] David Logan. Quantum physics in one dimension. *Journal of Physics A: Mathematical and General*, 37(19):5275–5276, 2004.
- [120] P. Garoche, R. Brusetti, D. Jérôme, and K. Bechgaard. Specific heat measurements of organic superconductivity in $(\text{TMTSF})_2\text{ClO}_4$. *Journal de Physique Lettres*, 43(5):147–152, 1982.
- [121] I. J. Lee, S. E. Brown, W. Yu, M. J. Naughton, and P. M. Chaikin. Coexistence of superconductivity and antiferromagnetism probed by simultaneous nuclear magnetic resonance and electrical transport in $(\text{TMTSF})_2\text{PF}_6$ system. *Physical Review Letters*, 94(19), 2005.

- [122] J. Shinagawa, Y. Kurosaki, F. Zhang, C. Parker, S. E. Brown, D. Jérôme, J. B. Christensen, and K. Bechgaard. Superconducting state of the organic conductor $(\text{TMTSF})_2\text{ClO}_4$. *Physical Review Letters*, 98(14), 2007.
- [123] Shingo Yonezawa, Yoshiteru Maeno, Klaus Bechgaard, and Denis Jérôme. Nodal superconducting order parameter and thermodynamic phase diagram of $(\text{TMTSF})_2\text{ClO}_4$. *Physical Review B*, 85(14), 2012.
- [124] E.L. Wolf. *Principles of Electron Tunneling Spectroscopy: Second Edition*. International Series of Monographs on Physics. OUP Oxford, 2011.
- [125] P.G. de Gennes. Some effects of long range forces on interfacial phenomena. *Journal de Physique Lettres*, 42(16):377–379, 1981.
- [126] A. Fournel, C. More, G. Roger, J. P. Sorbier, and C. Blanc. TUNNELING IN ORGANIC SUPERCONDUCTORS. *Le Journal de Physique Colloques*, 44(C3):C3–879–C3–884, 1983.
- [127] Hiroshi Bando, Koji Kajimura, Hiroyuki Anzai, Takehiko Ishiguro, and Gunzi Saito. Superconducting tunneling in $(\text{TMTSF})_2\text{ClO}_4$ /a – Si/Pb junctions. *Molecular Crystals and Liquid Crystals*, 119(1):41–44, 1985.
- [128] S. Tomić, D. Jérôme, P. Monod, and K. Bechgaard. EPR and electrical conductivity of the organic superconductor di-tetramethyltetraselenafulvalenium-perchlorate, $(\text{TMTSF})_2\text{ClO}_4$ and a metastable magnetic state obtained by fast cooling. *Journal de Physique Lettres*, 43(23):839–844, 1982.
- [129] Jean-Paul Pouget. Structural aspects of the bechgaard and fabre salts: An update. *Crystals*, 2(2):466–520, 2012.
- [130] H. Schwenk, K. Andres, and F. Wudl. Resistivity of the organic superconductor ditetramethyltetraselenafulvalenium perchlorate, $(\text{TMTSF})_2\text{ClO}_4$, in its relaxed, quenched, and intermediate state. *Physical Review B*, 29(1):500–502, 1984.
- [131] H. Schwenk, K. Neumaier, K. Andres, F. Wudl, and E. Aharon-Shalom. Meissner anisotropy in deuterated $(\text{TMTSF})_2\text{ClO}_4$. *Molecular Crystals and Liquid Crystals*, 79(1):633–638, 1982.
- [132] P. Garoche, R. Brusetti, D. Jérôme, and K. Bechgaard. Specific heat measurements of organic superconductivity in $(\text{TMTSF})_2\text{ClO}_4$. *Journal de Physique Lettres*, 43(5):147–152, 1982.
- [133] T. Ishiguro, K. Murata, K. Kajimura, N. Kinoshita, H. Tokumoto, M. Tokumoto, T. Ukachi, H. Anzai, and G. Saito. Superconductivity and metal-nonmetal transitions in $(\text{TMTSF})_2\text{ClO}_4$. *Le Journal de Physique Colloques*, 44:C3–838, 1983.
- [134] T. Takahashi, D. Jérôme, and K. Bechgaard. Observation of a magnetic state in the organic superconductor $(\text{TMTSF})_2\text{ClO}_4$: influence of the cooling rate. *Journal de Physique Lettres*, 43(15):565–573, 1982.

- [135] Shingo Yonezawa, Yoshiteru Maeno, Klaus Bechgaard, and Denis Jérôme. Nodal superconducting order parameter and thermodynamic phase diagram of $(\text{TMTSF})_2\text{ClO}_4$. *Physical Review B*, 85(14):140502, 2012.
- [136] K Bechgaard, K Carneiro, FB Rasmussen, M Olsen, G Rindorf, CS Jacobsen, HJ Pedersen, and JC Scott. Superconductivity in an organic solid. synthesis, structure, and conductivity of bis (tetramethyltetraselenafulvalenium) perchlorate, $(\text{tmtsf})_2\text{ClO}_4$. *Journal of the American Chemical Society*, 103(9):2440–2442, 1981.
- [137] Øystein Fischer, Martin Kugler, Ivan Maggio-Aprile, Christophe Berthod, and Christoph Renner. Scanning tunneling spectroscopy of high-temperature superconductors. *Reviews of Modern Physics*, 79(1):353–419, 2007.
- [138] Pere Alemany, Jean-Paul Pouget, and Enric Canadell. Electronic structure and anion ordering in $(\text{TMTSF})_2\text{ClO}_4$ and $(\text{TMTSF})_2\text{NO}_3$ a first-principles study. *Physical Review B*, 89(15), 2014.
- [139] B. L. Altshuler, A. G. Aronov, and P. A. Lee. Interaction effects in disordered fermi systems in two dimensions. *Physical Review Letters*, 44(19):1288–1291, 1980.
- [140] C. Carbillet, V. Cherkez, M. Skvortsov, M. Feigel’Man, F. Debontridder, L. Ioffe, V. Stolyarov, K. Ilin, M. Siegel, D. Roditchev, T. Cren, and Christophe Brun. Spectroscopic evidence for strong correlations between local superconducting gap and local Altshuler-Aronov density of states suppression in ultrathin NbN films. *Physical Review B*, 102(2), 2020.
- [141] Changjiang Liu, Xi Yan, Dafei Jin, Yang Ma, Haw-Wen Hsiao, Yulin Lin, Terence M. Bretz-Sullivan, Xianjing Zhou, John Pearson, Brandon Fisher, J. Samuel Jiang, Wei Han, Jian-Min Zuo, Jianguo Wen, Dillon D. Fong, Jirong Sun, Hua Zhou, and Anand Bhattacharya. Two-dimensional superconductivity and anisotropic transport at KTaO_3 (111) interfaces. *Science*, 371(6530):716–721, 2021.
- [142] Zheng Chen, Yuan Liu, Hui Zhang, Zhongran Liu, He Tian, Yanqiu Sun, Meng Zhang, Yi Zhou, Jirong Sun, and Yanwu Xie. Electric field control of superconductivity at the $\text{LaAlO}_3/\text{KTaO}_3$ (111) interface. *Science*, 372(6543):721–724, 2021.
- [143] S. Mallik, G. C. Ménard, G. Saïz, H. Witt, J. Lesueur, A. Gloter, L. Benfatto, M. Bibes, and N. Bergeal. Superfluid stiffness of a KTaO_3 -based two-dimensional electron gas. *Nature Communications*, 13(1), 2022.
- [144] Yun-Yi Pai, Anthony Tylan-Tyler, Patrick Irvin, and Jeremy Levy. Physics of SrTaO_3 -based heterostructures and nanostructures: a review. *Reports on Progress in Physics*, 81(3):036503, 2018.
- [145] Felix Trier, Paul Noël, Joo-Von Kim, Jean-Philippe Attané, Laurent Vila, and Manuel Bibes. Oxide spin-orbitronics: spin–charge interconversion and topological spin textures. *Nature Reviews Materials*, 7(4):258–274, 2021.

- [146] Annika Johansson, Börge Göbel, Jürgen Henk, Manuel Bibes, and Ingrid Mertig. Spin and orbital edelstein effects in a two-dimensional electron gas: Theory and application to SrTiO₃ interfaces. *Physical Review Research*, 3(1), 2021.
- [147] Sara Varotto, Annika Johansson, Börge Göbel, Luis M. Vicente-Arche, Srijani Mallik, Julien Bréhin, Raphaël Salazar, François Bertran, Patrick Le Fèvre, Nicolas Bergeal, Julien Rault, Ingrid Mertig, and Manuel Bibes. Direct visualization of rashba-split bands and spin/orbital-charge interconversion at KTaO₃ interfaces. *Nature Communications*, 13(1), 2022.
- [148] A. Barthelemy, N. Bergeal, M. Bibes, A. Caviglia, R. Citro, M. Cuoco, A. Kalaboukhov, B. Kalisky, C. A. Perroni, J. Santamaria, D. Stornaiuolo, and M. Salluzzo. Quasi-two-dimensional electron gas at the oxide interfaces for topological quantum physics. *EPL (Europhysics Letters)*, 133(1):17001, 2021.
- [149] Yoshimasa Fujii and Tunetaro Sakudo. Dielectric and optical properties of KTaO₃. *Journal of the Physical Society of Japan*, 41(3):888–893, 1976.